SIMULATING DIVERTOR DETACHMENT IN THE TCV AND JET TOKAMAKS

PAR

Marco WISCHMEIER

Diplom-Physiker, Heinrich-Heine-Universität
de nationalités allemande et italienne

acceptée sur proposition du jury:

Dr R. Pitts, directeur de thèse
Dr W. Fundamenski, rapporteur
Dr Ch. Hollenstein, rapporteur
Prof. D. Reiter, rapporteur
Prof. N. Tatsuya, rapporteur

Lausanne, EPFL
2005

Abstract

Divertor detachment is currently assumed to be a fundamental pre-requisite for the successful operation of future fusion reactors. Only by partially detaching the divertor in the regions of highest power flux density can high performance tokamak operation be made compatible with the technological limits set by the thermo-mechanical properties of surfaces in contact with the plasma. Although the various physics components of the detachment process are thought to be well known, their relative importance and the degree to which each may affect the others, thus determining the final detached state, cannot in general be deduced from any simple analytic approach. Instead, sophisticated two and three dimensional interpretative and predictive code packages have been developed within the fusion community to model the scrape-off layer (SOL) and divertor plasmas of magnetic confinement devices. One of these, the SOLPS code, has for some time been employed as a tool for the design of the divertor in the next step tokamak reactor, ITER. In reality, however, these codes have not, in general, been fully validated against experimental observations from current tokamaks, in particular with regard to divertor detachment.

This thesis aims to contribute to such validation by thorough comparisons between numerical simulations, using the SOLPS5 (plasma fluid, Monte Carlo neutral) code package and experimental characterization of the detachment process in two very different tokamaks, TCV and JET. The approach taken has been to test the code against experiment, not only for two machines with a vast difference in size and divertor geometry, but also for plasma operation with either deuterium or helium fuel. Changing the fuel species in a tokamak containing significant graphite first wall components as do TCV and JET, dramatically modifies the impurity production mechanism but also the important atomic physics processes at work, both of which influence the detachment threshold.

In TCV, divertor detachment in the simplest of situations is experimentally observed to be anomalous and could not be explained by the first attempts at code modeling prior to this thesis. Evidence is presented for the detachment anomaly being directly linked to

enhanced interaction between the graphite main chamber walls at high plasma density due to anomalous convective radial transport. Such interaction is not well modeled by the code and the results presented in this thesis highlight an important area in which the complexities of the real situation are inadequately represented in the numerical model. This work also constitutes the first known application of the SOLPS code to tokamak simulation with consistent modeling of molecular hydrocarbons. Indeed, they are found to be important in producing high degrees of numerical detachment.

In JET, experimental data from high density helium plasma operation have been successfully modeled, constituting the first ever simulations of pure He discharges on this machine. Helium detachment is very different to that in deuterium, due in large part to the absence of carbon chemistry. The simulation results demonstrate this together with strong evidence for conclusions to be drawn concerning the principal mechanisms driving the detachment. Similar good agreement is obtained between code and experiment for helium operation on TCV and a comparison of code results between the two devices demonstrates how divertor geometry can have a significant impact on the detachment behavior.

Version abrégée

Es wird zur Zeit davon ausgegangen, dass Divertor Detachment eine entscheidende Voraussetzung für den erfolgreichen Betrieb eines zukünftigen Fusionsreaktor ist. Nur durch teilweises Detachment in Regionen mit der höchsten Leistungsflussdichte ist der Betrieb eines Hochleistungstokamaks mit den, durch thermomechanische Eigenschaften der mit dem Plasma in Kontakt stehenden Oberflächen bedingten, technologischen Beschränkungen kompatibel. Obwohl man davon ausgeht, dass die einzelnen Komponenten des Detachmentprozesses hinreichend bekannt sind, kann in der Regel ihre relative Bedeutung und der Grad der gegenseitigen Beeinflussung im Zuge des Erreichens des finalen Detachment nicht durch eine simple analytische Vorgehensweise bestimmt werden. Statt dessen sind hoch entwickelte zwei und drei dimensionale interpretative und prediktive Codepakete in der Fusionsgemeinschaft entwickelt worden, um die Plasmarandschicht und Divertorplasmen von Maschinen mit magnetischem Einschluss zu modellieren. Ein solcher Code ist SOLPS, welcher seit geraumer Zeit als Designwerkzeug für den Divertor des Tokamaks der nächsten Generation, ITER, verwendet wird. Allerdings sind diese Codes nicht vollständig auf der Basis experimenteller Daten heutiger Tokamaks validiert worden, insbesondere im Rahmen des Divertor Detachment.

Diese Doktorarbeit möchte, das SOLPS5 (Plasmafluid, Monte Carlo Neutralteilchen) Softwarepaket verwendend, durch einen sorgfältigen Vergleich numerischer Simulationen und experimenteller Charakteristiken während des Detachments zweier sehr verschiedener Tokamaks zu einer solchen Validierung beitragen. Die Herangehensweise war den Code, nicht nur für zwei Maschinen solch unterschiedlicher Grösse sondern auch unter Plasmabetriebsbedingungen mit Deuterium und Helium jeweils als Gas, am Experiment zu testen. Ein Austausch des Füllgases in einem Tokamak welcher signifikante Anteile von Graphit in den Komponenten der ersten Wand enthält, verändert dramatisch den Produktionsmechanismus für Verunreinigungen und zugleich auch die atomphysikalischen Prozesse. Beides beeinflusst den Schwellwert zum Ereichen des Divertor Detachment.

In TCV, ist Divertor Detachment in der einfachsten der experimentellen Bedingun-

gen anomal und konnte, während erster Versuche vor dieser Arbeit, nicht mit Hilfe numerischer Modellierungen erklärt werden. Belege werden in dieser Arbeit vorgelegt, die zeigen, dass diese Anomalie im Zusammenhang mit einer verstärkten Wechselwirkung mit den Graphitwänden der Hauptkammer steht, welche ihre Ursache im anomalen konvektiven radialen Transports bei hohen Plasmadichten hat. Eine solche Wechselwirkung wird durch den Code nicht angemessen modelliert und die Ergebnisse beleuchten ein wichtiges Gebiet in welchem die Komplexität der realen Situation unangemessen im numerischen Modell einbezogen ist. Diese Arbeit stellt zugleich auch die erste bekannte Anwendung des SOLPS Codes mit konsistenter Behandlung von Kohlenwasserstoffen dar. Wie sich zeigt sind diese für das Erreichen eines hohen Grads numerischen Detachments wichtig.

Für JET sind die experimentellen Daten erfolgreich modelliert worden und stellen die ersten jemals durchegeführten Simulationen von Entladungen in reinem He dieser Maschine dar. Insbesondere auf Grund des Fehlens der Kohlenstoffchemie ist Detachment in Helium sehr verschieden von jenem in Deuterium. Die Ergebnisse der Simulationen veranschaulichen dies sehr deutlich und erlauben eindeutige Schlussfolgerungen in Bezug auf die hauptsächlichen Mechanismen, welche Detachment hervorrufen. Eine ähnlich gute Übereinstimmung konnte zwischen Code und Experiment für den Betrieb in Helium in TCV gefunden werden und ein Vergleich von Ergebnissen beider Maschinen liefert ein interessantes Beispiel inwiefern die Geometrie des Divertors einen signifikanten Einfluss auf das Detachment haben kann.

Contents

Part I

An Introduction to Divertor Detachment

Chapter 1

Introduction

1.1   Nuclear fusion: an energy option for the future

The world's economic growth over the past decade, especially in Eastern Asian countries like China or India, and the general increase of the world average standard of living, have led to an increased demand for energy [1]. Even with a more sustained effort in industrially developed countries in limiting their energy consumption, overall demand for relatively cheap energy is certain to increase. Most of the industrialized countries currently rely on non-renewable energy resources such as fossil fuels for their energy supply. In the medium to long term, however, fossil fuel reserves are limited. In addition, especially recent history in particular has demonstrated the sensitivity of industrialized economies to international crises and political instability in the main fossil fuel supplying countries.

There is no scenario for replacing the current dependency on fossil fuels completely. Options include a higher efficiency of energy production and conservation, the expansion of the importance of renewable sources such as solar, wind, water or biomass energy and the construction of new generation fission reactors. In a green hydrogen economy [2], H_2 would need to be produced through electrolysis driven by wind and solar power plants. Due to the low efficiency of solar power production and the large energy consumption in industrialized countries, these economies might still need to rely on the importation

of hydrogen from temperate regions such as northern Africa or the Arab peninsula. If renewable energy sources are not used for H_2 generation, it is unclear that a hydrogen economy offers a better alternative to the current global energy production scheme, since the primary energy source would not be renewable and hydrogen just a form of energy storage. It has been estimated that with the current energy consumption rate and economic growth, renewable energy sources will still only account for at most 20% of the average world wide demand by 2025 [1].

Nuclear fusion is a possible option as a base energy source for the future, probably as part of general energy mix including renewable energy sources and a more decentralized energy production grid. It has a major advantage in any future energy market of rendering a country practically independent of any other on its fuel supply once it has the necessary technology to build a fusion power plant.

The fundamental basis is to fuse two light nuclei to produce a heavier product in a controlled environment, thereby releasing kinetic energy, which can be used to heat water and run electric power producing turbine generators. Currently, the only feasible route is to use the hydrogenic isotopes *deuterium* and *tritium* in the fusion reaction, yielding helium and fast neutrons as reaction products and using the neutrons as in conventional fission plants to heat water. Deuterium is a stable hydrogen isotope found in abundance in water, whilst tritium is radioactive with a short decay time which, in a reactor, will have to be produced in a breeding reaction with lithium, also abundant in nature. The production of energy through fusion using $33mg$ of D is equivalent to burning $260l$ of gasoline [3].

At present, magnetic confinement devices are the most scientifically and technologically advanced concepts with which to achieve fusion in a controlled environment. Two main forms of such devices have been developed over the past decades, Stellarators [4] and Tokamaks [5]. They differ essentially in the magnetic field configuration used to confine the hot plasma fuel. The tokamak concept is the most developed concept of the two and will be the configuration for the next step experimental international fusion machine, ITER [6]. This thesis will be concerned only with results from and simulations of tokamak

plasmas, concentrating on the TCV and JET tokamaks.

1.2   Tokamak and Divertor

A tokamak is essentially a low pressure high temperature toroidal gas discharge. In the tokamak reactor a hot plasma [7] of D and T ions at temperatures of several keV is confined by magnetic fields such that the ions can overcome the repulsive forces due to their Coulomb fields, thereby producing α-particles, the ash of the fusion reaction, and fast neutrons that escape into the surroundings. The basic tokamak principle is shown in figure 1.1. A set of coils wound poloidally around a toroidal vacuum vessel produce a

Coils wound around torus to
produce toroidal magnetic field

Transformer winding
(primary circuit)

Poloidal
magnetic field

Toroidal
magnetic field

Iron transformer core

Plasma current
(secondary circuit)

Helical field

Plasma particles contained
by magnetic field
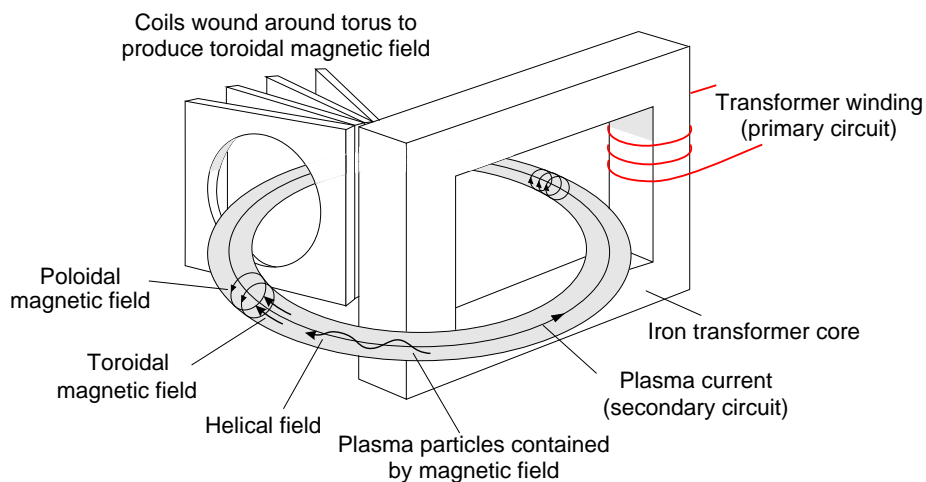
Figure 1.1: *The tokamak configuration.*

toroidal magnetic field, B_Φ. On its own, a pure toroidal field cannot confine the plasma since its natural radial decay ($B_\Phi \propto 1/R$, with R the major radius) produces charge separation, vertical electric fields and subsequent radial drift of the entire plasma column. In the tokamak, this is overcome by using the plasma as a simple turn secondary winding in a transformer circuit and inducing a large current in the plasma. This current produces a poloidal magnetic field, which, combined with the toroidal field, results in a helical total field. Charged particles are constrained to follow these helical field lines, thereby short-

ing out vertical charge separation and increasing confinement times. In practice, further vertical field coils are also required as are additional heating systems to raise the plasma temperature beyond that which can be achieved by ohmic heating alone.

In a reactor the fusion α-particles must be confined within the reacting volume for a time sufficient to transfer their kinetic energy to the fuel ions. If this does not occur, the reaction process cannot be self-sustained. Once this energy transfer has occurred, the helium ions must be removed from the reaction volume to avoid both dilution of the fuel reactants and reduction of the plasma temperature due to enhanced radiation loss. Both processes reduce the reaction rate and prevent ignition conditions from being sustained. Pumping of the helium ash can only take place at the plasma edge where temperatures are low enough for interaction with material structures to occur. In turn, high pumping efficiencies require high neutral pressures in the region in front of the pumping duct. A low temperature, high density region at the plasma boundary can be achieved naturally in a tokamak in the so called divertor configuration.

In the tokamak, magnetic field lines can be pictured as nested on toroidal magnetic flux surfaces. In the poloidal cross-section, there will always be one last such surface upon which field lines never intersect the confining walls of the vacuum vessel. In practice, material objects, known as limiters, are often placed inside the vessel to define the *Last Closed Flux Surface* LCFS (figure 1.2). These objects perform the function of "scraping off" plasma and the region behind the limiter or outside of the LCFS is commonly known as the scrape-off-layer or SOL.

An alternative is shown in figure 1.3 which illustrates the poloidal cross-section of the most common divertor configuration, known as the toroidally symmetric poloidal divertor. In such a configuration, the LCFS is not determined by the interference of a solid surface with the main plasma, but by additional magnetic coils that shape the magnetic flux surfaces such as to create an X-point, where the poloidal field vanishes. This can be obtained using an external conductor whose current is parallel to the main plasma current. The magnetic flux surface passing through this X-point is called the *separatrix*. Inside the separatrix, above the X-point, all magnetic flux surfaces are closed and none

6
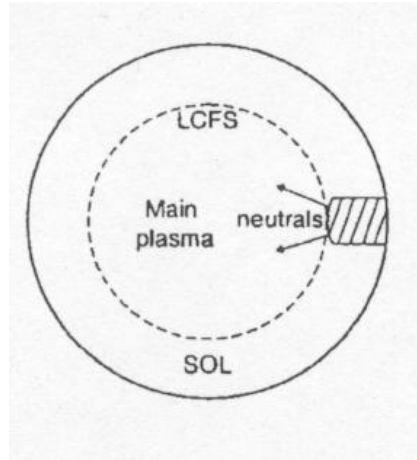
Figure 1.2: *The schematic of a limiter configuration [8].*

intersects a material surface. Any flux surface outside the separatrix intersects the wall at some location and is part of the SOL. The region below the X-point in figure 1.3 may be loosely defined as the divertor. The points at which the separatrix strikes the wall below the X-point are known as the *strike points*. The area in the vicinity of each strike point is the divertor target. In the case shown the divertor has two targets, an inner (left) and an outer (right) target. These target areas are also commonly referred to as the low and high field side (HFS, LFS) divertors.

If the magnetic confinement were perfect, charged particles in the plasma would move only along the magnetic field lines, with their perpendicular motion being limited to the extent of the gyro radius around that field line. In such an ideal situation plasma is confined to the area labeled *main plasma* in figure 1.3. In a real tokamak, however, confinement is not perfect and particles escape readily across the magnetic field lines, leading to a leakage of plasma out of the core plasma region. The origin of such leakage is manifold. Radial drifts, inter-particle collisions and plasma turbulence cause charged particles to move perpendicularly to magnetic field lines. Plasma therefore penetrates from the core plasma region into the scrape-off layer, where it is quickly transported parallel to the magnetic field to the closest material surface. Any such surface is naturally a sink for the plasma, since charged particles reaching the walls will most likely recombine there, with the subsequent possibility of being re-released as a neutral. The process of plasma
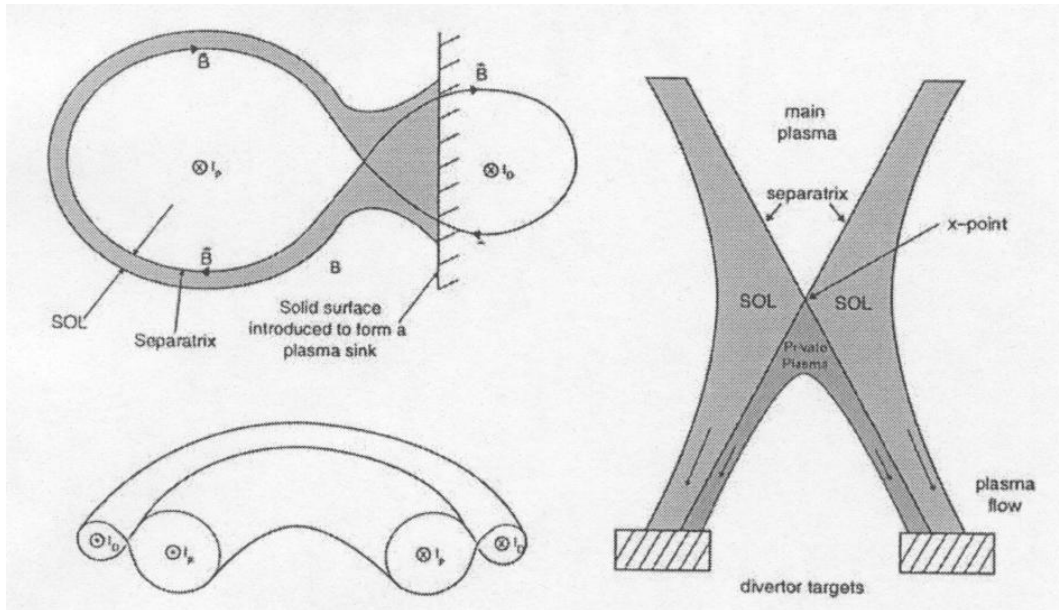
Figure 1.3: *The schematic of a divertor configuration [8].*

recombination on material surfaces and the subsequent neutral release is referred to as *recycling*.

As will be shown later in Chapter 2, parallel transport along field lines is faster than perpendicular transport across them. As a consequence, radial decay lengths outside the LCFS are very short and the SOL can be thought of a very thin layer of plasma enveloping the core region, not extending radially outward more than a few *cm* in the area above the X-point. As a result of the magnetic geometry common to most tokamaks, this SOL undergoes a certain radial expansion below the X-point which is related to the magnetic *flux expansion* in the divertor volume. Of course both particles and energy penetrate into the SOL. Most of the energy reaching the SOL is, like the particles, transported in the parallel direction toward the divertor targets rather than cross-field to the outer walls. In an experimental next step device such as ITER, about $200MW$ of fusion power exhaust will enter the SOL [9] but the maximum continuous peak power load on material surfaces in the divertor should not exceed $\sim 10MW/m^2$.

Magnetic flux expansion is used to spread the extent of divertor over as much an area as possible. Volume not used for the fusion process itself, is, though, an expensive commodity and such expansion cannot be arbitrary. In order to further increase the area

in contact with the plasma (the *plasma wetted area*), field lines are configured such that their angle of incidence with the divertor targets is as shallow as possible, not exceeding a few degrees in general. As a consequence, the deposited heat flux onto target surfaces can be reduced to a fraction of that flowing parallel to magnetic lines further upstream in the main chamber SOL

When plasma is in contact with a solid object, wall material can be eroded by *sputtering* processes. If the plasma ions have sufficient energy, physical sputtering occurs. An ion penetrating the material surface releases its kinetic energy, breaking bonds, such that atoms of the wall material can overcome their surface binding potentials. Below a critical *energy threshold* value, physical sputtering cannot occur. Low target plasma temperatures are therefore advantageous.

If the material surfaces are chemically reactive with the plasma (as is the case in all tokamaks with graphite wall components and hydrogenic fuel), then wall material can be released through processes of *chemical sputtering*. In this case, both ions and neutrals of any energy can release impurities and there is no practical energy threshold.

Particles eroded from the walls by sputtering (and other) processes are *impurities* and will not only dilute the plasma but can, depending on the atomic number, radiate a large amount of power. Such *impurity radiation* will be generally beneficial in the SOL and divertor volume where power fluxes must be reduced, but very counterproductive in the confined region where power loss due to radiation in a burning plasma will be sufficient to extinguish the fusion burn if the impurity content is too high. The release of impurities into the main plasma must therefore be minimized, a natural consequence of divertor operation and the principal reason why a limiter machine is not a serious option for a next step device.

It is not yet clear what material will be chosen for the divertor targets in ITER, though in a first phase graphite, and therefore the chemically reactive carbon, is currently the proposed option [10], with the remainder of the wall being composed of beryllium and tungsten (the latter for the divertor baffle plates). Graphite is a very desirable target material from the point of its thermal properties, but is currently thought to retain too

much radioactive tritium to be of use in a future reactor [10]. Particle flux onto such a target should therefore be minimized or at most be allowed to such an extent as to be beneficial for radiation in the divertor volume.

Summarizing, the requirements for SOL and divertor operation are that:

- high neutral pressures are produced in the divertor to enrich the helium concentration close to the active pumping ducts such as to efficiently pump the helium ash and prevent dilution of the burning plasma in the core

- minimize the penetration of impurities into the main plasma

- reduce the power load onto plasma-facing components

- minimize the plasma flux onto plasma-facing components.

1.3   An introductory picture of divertor detachment

Before discussing divertor detachment itself Fig. 1.4 shows the typical structure of a baffled divertor and introduces some terminology in common use in edge physics. The region inside the separatrix below the X-point is called the *private flux region* (PFR). The divertor, situated below the X-point, is defined in such a way as to minimize the escape of neutrals from the divertor volume to the main SOL. Such a divertor is called a *closed divertor*. The magnetic configuration in the example of Fig. 1.4 is a single null lower (SNL) equilibrium and will be the only configuration in this thesis. In the case of JET, simulations will be performed for comparison with dicharges executed in the MarkIIGB divertor (see Fig. 6.1 in Chapter 6) - a baffled divertor with vertical targets. In contrast, TCV (see Fig. 5.1 in Chapter 5) has no baffle structures and operates with geometrically open diverted equilibria.

The criteria for 'burning plasma' operation mentioned earlier can be matched in current tokamaks if the divertor is operated in the so called *detached regime*. When *divertor detachment* occurs, the particle flux to the targets is drastically decreased, the total
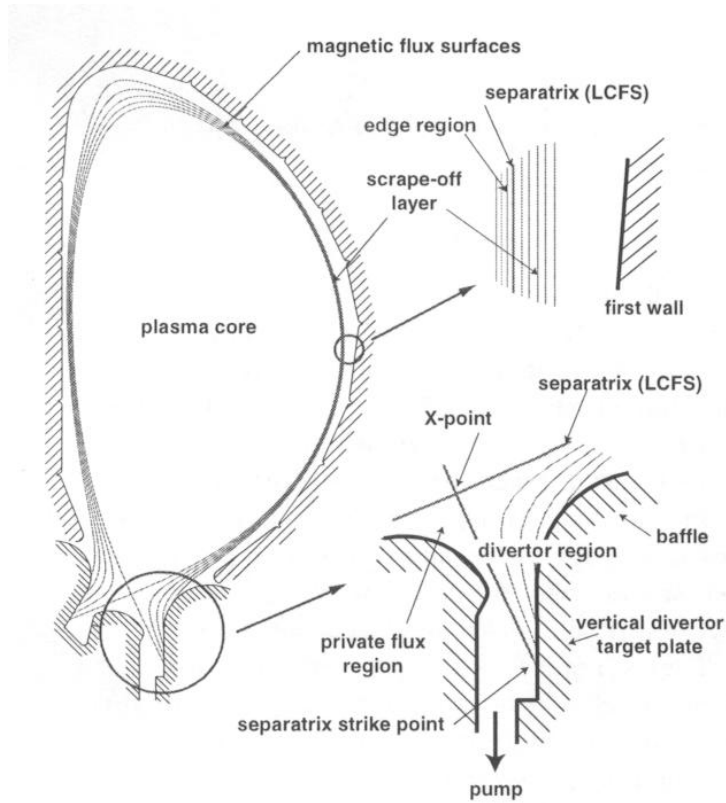
Figure 1.4: *Poloidal cross-section of SOL and baffled divertor, taken from ref. [10]*

plasma pressure along a magnetic field line drops, the plasma temperature is low in front of the target plates and neutral pressures are high enough that neutral particles can be efficiently exhausted with an active pumping system. In addition in a burning plasma, helium, the main plasma minority species, is enriched in the cold divertor, making its removal more efficient. Divertor detachment has been observed in various geometries on all current large experimental devices, such as JET [11], DIII-D [12], CMOD [13], ASDEX-U [14], JT60U [15] and also in some smaller machines such as the tokamak TCV [16] at the CRPP in Lausanne. The much higher power flux densities that ITER will produce during burning plasma operation ($Q_{DT} > 5$) will require detached divertor operation.

The detachment process is extremely complex invoking plasma and material particle physics, magnetic and surface geometries and plasma-surface interaction. It can only really be quantitavely modelled theoretically through the use of large $2D$ simulation codes.

11

Even then, a complete description, matching all experimental observables has not yet been achieved.

Qualitatively, however, divertor detachment is readily explained and an excellent overview on experimental divertor physics has been given by Pitcher and Stangeby [17]. Divertor detachment in deuterium plasmas can be experimentally achieved in two ways (or by a combination of both). It can be obtained by increasing the plasma density until the divertor plasma finds itself in a detached regime, or it can be "forced" through additional impurity seeding by injecting, for example, N_2 or Ne into the SOL and divertor plasmas [18].

It is helpful at this point to define some further useful terminology. The *upstream density*, n_u, is the density above the X-point in the main SOL, usually taken to be at the plasma *midplane*, an imaginary horizontal line passing through the magnetic axis of the main plasma. In the domain of edge physics, one often distinguishes the *inner* and the *outer midplanes*, which are respectively located in region of the SOL with high magnetic field (small major radius) and low magnetic field (large major radius). The line averaged plasma density, $\bar{n}_e$ is the average plasma density usually measured along a vertical diagnostic viewing chord that crosses the core plasma. It is commonly used as a parameter when describing the operating density of any particular plasma discharge.

1.3.1 Sheath and conduction limited regimes

If the plasma density is sufficiently low, the divertor will access the *sheath limited regime*. In a true sheath limited condition, there are no temperature gradients parallel to the magnetic field between the midplane and the divertor targets. Heat and particles are transported only through convection. The power that can be removed from the plasma is then purely determined by the heat that the *sheath*, the region of strong electric field that is established between the plasma and any solid surface, can transmit. In this regime the upstream temperature, T_u, tends to be high, since the density there is low, and thus also the temperature of the plasma in front of the target.

As n_u is increased by increasing $\bar{n}_e$, (for example, by puffing gas into the vessel volume or fueling the core plasma, perhaps by pellet injection), more plasma reaches the targets and the density there increases. Since the recycled neutrals that are released by particle impact on the solid surfaces are re-ionized in the plasma in front of the targets, positive feedback occurs on the local plasma density (and hence the particle flux) such that a zone of *high recycling* develops. In this regime, temperatures are low and densities high in the target vicinity. With increasing plasma density and decreasing temperature the plasma collisionality (see eqns. 2.21, 2.22) becomes larger and heat is conducted rather than convected parallel to $\vec{B}$, such to develop strong parallel temperature gradients, exhausting power entering the SOL to the targets. Parallel heat transport is then determined by heat conduction and this high recycling regime is therefore naturally also a *conduction limited regime*. The phenomena described thus far can be described in a relatively simple one dimensional picture with sources and sinks of particles and power along any given field line.

1.3.2 From high recycling to detachment

If plasma-facing components are made of graphite, as target plates in most of todays tokamaks are, then carbon impurities are released into the plasma due to chemical and physical sputtering. Such impurity release happens not only in the divertor volume but also above the X-point region where plasma may reach the *main chamber* walls of the confining vessel. Depending on plasma parameters encountered in the SOL and core region, this carbon may reach a number of ionization stages. In the stepwise ionization processes, strong volumetric radiation losses may occur, with C^{2+} and C^{3+} (found for $T_e < 100eV$ and typical for the SOL), being powerful radiators. Such radiation losses cool the divertor plasma further, increasing the plasma density.

In a cool divertor a series of different processes may take place: The *ionization front*, the region where most neutrals recycled at the target are ionized inside the divertor volume, moves away from the target toward the X-point as T_e drops in the divertor (re-

ionization is important for $T_e \geq 5eV$). Material surfaces are not the only sinks for plasma - volumetric recombination processes may also occur, including three body recombination, radiative recombination and molecular assisted recombination [19]. If T_e decreases to low enough values, typically below $1.5eV - 2eV$, volumetric plasma recombination can decrease the plasma flux onto the target by decreaing the plasma density. The *recombination front* is located between the ionization front and the target.

Any plasma source (for example an ionization region) and parallel pressure gradient (as a result of $\nabla T_\parallel$) in the divertor volume is a momentum source for the plasma. With material surfaces being particle sinks, the plasma as a fluid is always accelerated toward the divertor targets. Depending on the plasma parameters encountered in the divertor volume, some parallel velocity profile will always be established.

Plasma needs to reside in the divertor volume long enough for ions and electrons to recombine. Any momentum source necessarily reduces the resident, or dwell time of the plasma in front of the target plate. Momentum is removed from the plasma (more specifically the ion fluid) in the divertor volume through ion-neutral friction, as a result of elastic and inelastic collisions with neutral atoms and molecules. But the neutrals can only remove plasma momentum if they are able to escape the region of the divertor plasma after a charge exchange (CX) event, without re-transferring too much momentum back to the plasma at different locations in the divertor. The neutral flux into the plasma must therefore be such that enough CX collisions can occur for plasma to transfer momentum to the neutrals, but at the same time plasma conditions must permit the accelerated neutrals to escale and deposit their momentum on the surrounding surfaces. The distribution of neutral densities and the establishment of high neutral pressures in the divertor volume can be strongly influenced by divertor geometry. Such design issues nevertheless require a solid physics foundation on which to be based, particularly when accounting for the high cost of divertor modules in next step devices.

1.4 Issues for predicting divertor operation

The brief review above has indicated that detachment is at least a $2D$ problem. The process is of sufficient complexity that neither experiment nor theory have been able to fully characterize all aspects needed to fully understand the importance of all contributing phenomena. In recent years numerical codes (see Chapter 3), running on simulation grids produced from real experimental magnetic reconstructions have been increasingly used, together with experimental data to improve understanding of the complex interplays involved in the SOL and divertor. Validation of $2D$ SOL codes is especially important for the assessment of SOL and divertor performance, especially divertor detachment in ITER or future burning plasmas where power levels, heat and particle loads will be orders of magnitude larger than in current machines.

Under high recycling or detached conditions, the mean free path of neutrals in the divertor volume can become large, so that code packages generally consist of an iterative solution to the fluid equations describing the plasma background, combined with a Monte Carlo approach to the simulation of neutral trajectories on this background. For plasmas encountered in the tokamak SOL, a classical, fluid description of energy, particle and momentum transport along field lines is usually appropiate. Only at low plasma densities are kinetic corrections sometimes required to limit the transport of these three quantities. In contrast, the understanding of perpendicular transport mechanisms is currently comparatively very limited. Perpendicular transport rates at least 10 to a 100 times larger than classically expected values (at least for particle transport) are required if code and experiment are to agree. Not only is anomalous perpendicular transport likely a function of radial distance in the SOL, but there is increasingly strong evidence that there are significant poloidal variations.

Codes are thus often run repeatedly, each time modifying the assumptions regarding perpendicular transport, until reasonably good agreement with the experimental observations is obtained. Attempts have recently been made to automate this process [20]. Generally, however, such a repeated procedure is very CPU intensive. For ITER and

future reactors, where experimental data are by definition unavailable, predictive calculations therefore can only be made through extrapolation of current values for perpendicular transport found to be similar, to some extent, for most machines, at least at low densities.

At all but the lowest densities, perpendicular transport in regions radially remote from the separatrix (the far SOL) is dominated by anomalous *intermittent transport* [21] originating in the perpendicular propagation of 'blobs' of plasma [22] and the development of streamers. It is known that anomalous radial transport increases with upstream plasma density [23] and it is therefore to be expected that it might play a role in determining the onset and evolution of detachment.

1.5 Aim and contribution

Since fluxes of particles and heat truly relevant to next step devices (such as ITER) cannot be attained in current tokamaks, predictions of divertor detachment behaviour depend on the use of large codes, coupled with experimental tests on today's devices. Helping to improve understanding in this way is the principal objective of this thesis. It aims to use the experimental results from two very different tokamaks, TCV and JET, together with the sophisticated coupled fluid/Monte-Carlo interpretative code package B2.5/Eirene, to study the physics of divertor detachment. The thesis focuses on studying the importance of atomic and molecular physics for achieving detachment in two machines differing in size, divertor geometry and divertor plasma parameters. The detachment phenomenon is studied in both pure helium and deuterium plasmas for TCV and helium only for JET, thus exploiting the very different atomic physics processes at work in each case and the lack of plasma-material chemistry in helium.

Dedicated experiments have been run on both tokamaks and simulations performed to match as closely as possible the experimental data. The helium plasma simulations performed for JET represent the first ever attempt to apply the B2.5-Eirene code to plasmas with helium as main fuel species and have clearly been able to reproduce the

experimentally observed detachment.

Earlier, preliminary simulations of TCV diverted discharges were unable to achieve detachment in deuterium plasmas without artificially increasing recombination rates by a factor 5 [24]. This thesis demonstrates how detachment can be naturally obtained in TCV if the assumption of pure diffusive transport is relaxed and a more complex ansatz for perpendicular transport adopted. It also infers an important role for intrinsic carbon impurities released from the main chamber walls.

Fast pressure gauges of the *ASDEX* type [25, 26] have been installed on TCV, results from which demonstrate clearly very low neutral pressures and compression ratios in the TCV divertor - far lower than in more conventional detached divertors. At such low pressures detachment would not be expected to occur. In the framework of this thesis several volumetric atomic and molecular processes, such as the role of molecular assisted recombination through D_2^+ or hydrocarbons (in form of CD_4), have been included in the code runs to study their influence on the onset of detachment. In fact, these simulations constitute one of the first ever attempts at coupled fluid - neutral code runs of the tokamak SOL and divertor plasma including hydrocarbons.

1.6 Outline of the thesis

This chapter has provided a brief overview of the general features of divertor detachment, qualitatively identifying the key players provoking its onset. Chapter 2 reviews the basic physics concepts and basic theory required to understand the function of and results from large SOL simulation codes. Atomic and molecular physics important for the SOL and divertor is also introduced, along with elementary descriptions of the plasma-wall interaction processes of relevance to the code simulations.

In Chapter 3, the B2.5/EIRENE (SOLPS5.0) code package is briefly presented in anticipation of results of its application to both JET and TCV in Part II of the thesis. In the latter details of diagnostics, experiment and simulations performed for TCV are presented in Chapter 5, discussing detachment in both D and pure He plasmas. Chapter 6 describes

17

the experimentally observed detachment in pure He plasmas on JET and presents the results of dedicated SOLPS5 simulations. This chapter concludes with a comparison of TCV and JET He discharges, attempting to provide explanations, via the simulation results from both machines, for the observed differences. The possible consequences of drifts on the onset of detachment are discussed on the basis of experimental data only for the case of TCV. A brief summary of the principle results obtained during this thesis work, together with some of the general conclusions that can be drawn from it is provided in Chapter 7.

Chapter 2

SOL and divertor physics

2.1 Introducing quantities related to SOL analysis

Before discussing parallel and perpendicular transport and introducing different divertor regimes (sheath limited, conduction limited/high recycling, detached), it is appropiate first to briefly review some basic expressions, definitions and relations for the SOL and their connection to the main plasma.

2.1.1 Quantities related to the magnetic field $\vec{B}$

The total magnetic field can be approximated as the sum of the toroidal field B_Φ and the poloidal field B_Θ:

$$\vec{B} = \vec{B}_\Phi + \vec{B}_\Theta. \tag{2.1}$$

The poloidal field is approximately

$$B_\Theta \approx \frac{\mu_o I_p}{2\pi a}, \tag{2.2}$$

with I_p the plasma current and a the minor radius of the torus. The *safety factor*, defined as the number of toroidal transits for one complete poloidal rotation of a field line is given by

$$q = \frac{r B_\Phi}{R B_\Theta}, \tag{2.3}$$

in the large aspect ratio, cylindrical approximation with r the minor radius. The *local pitch angle*, Θ_{pitch}, is an important quantity since it determines to a large extent the deposited particle and energy fluxes on the divertor targets:

$$\Theta_{pitch} \approx \frac{B_\Theta}{B_\Phi} \approx \frac{B_\Theta}{B}. \tag{2.4}$$

Throughout this thesis, the *connection length*, L_c in a divertor configuration is defined as half the distance between the two targets, along a magnetic field line. In a symmetric divertor configuration with equal X-point to target poloidal depths, the *connection length* can be approximated as

$$L_c \approx \pi R q. \tag{2.5}$$

if $B_\Theta/B_\Phi \ll 1$ as is usually the case in conventional, large aspect ratio tokamaks. Magnetic field lines in the separatrix vicinity and therefore close to the X-point, where B_Θ is smaller, have longer connection length than those radially further out in the SOL.

Defining l to be the 'radial width' of a magnetic flux tube in the poloidal plane, the (magnetic) *flux expansion* can be expressed as

$$f \equiv \frac{l_t}{l_u} \equiv \frac{\lambda_t}{\lambda_u} \simeq \frac{(B_\Theta/B)_u}{(B_\Theta/B)_t}, \tag{2.6}$$

with t denoting *target* and u *upstream* and where λ is the plasma *scrape-off layer width* or decay length[1].

Using eq. 2.6 the SOL cross-sectional area, perpendicular to $\vec{B}$ is

$$A_\parallel \approx 4\pi R \lambda_u \left(B_\Theta/B\right)_u \approx 4\pi R \lambda_t \left(B_\Theta/B\right)_t \tag{2.7}$$

and is constant along the magnetic field. The volume of the SOL is then

$$V_{SOL} = L A_\parallel. \tag{2.8}$$

As an example, the TCV magnetic configurations generally studied in this thesis, have a ratio of $(B_\Theta/B_\Phi)_u \sim 0.2$ and $(B_\Theta/B_\Phi)_t \sim 0.035$ giving $f = 6$ at the outer target. For JET discharges simulated here, $(B_\Theta/B_\Phi)_u \approx 0.2$ and $(B_\Theta/B_\Phi)_t \approx 0.06 \sim 0.04$ at the

---

[1]an approximation for the decay length will be given in Section 2.5

outer and inner targets, so that $f = 3 \rightarrow 4.2$.

Another important SOL quantity is the surface area of the LCFS, which defines the surface over which power and particle fluxes from the core region cross into the SOL:

$$A_\perp = 2\pi R 2\pi a \kappa^{1/2} \approx 4\pi^2 R a \kappa, \qquad (2.9)$$

with $\kappa = b/a$ the plasma elongation, using a as the horizontal minor radius and b as the vertical minor radius of an elliptical plasma in the poloidal plane.

2.1.2   The plasma wetted area and comments on tile alignment

To a first approximation the incident angle of magnetic field lines on an ideally flat surface perpendicular to the separatrix in the poloidal plane on the target is Θ_{pitch}. To compute the heat and particle loads onto the surface the *plasma wetted area*, A_{wet}, must be known. This is the total area in contact with the plasma, a quantity which one generally attempts to maximise in designing divertor targets. By appropriately shaping a divertor target (see [27] for an example) and/or arranging for oblique field line attack angles by slanting the target, A_{wet} can be increased.

The targets are usually composed of several tiles of various sizes and are therefore not uniform, flat homogeneous surfaces. Even if attention is paid to correct tile shaping, field line impact angles on some parts of some tiles may be not ideal. Tile misalignment can lead to plasma flux impinging at steeper angles, thus locally increasing particle and power flux. These areas are sometimes referred to as leading edges and tend to erode more readily. In contrast, other regions of the same tiles or of neighboring tiles may be magnetically shadowed, thus receiving less than the average plasma particle and heat flux. These shadowed regions tend to be cooler and are often regions of net impurity redeposition. Current two dimensional SOL simulations never explicitly account for detailed divertor structures but may do so implicitly through the specification of an average value of impurity production yields.

2.1.3 Power and particle influx to the SOL

The power entering the SOL, P_{SOL}, is the difference between the heating power and the power radiated inside the LCFS, P_{core}^{rad},

$$P_{sol} = P_{heat} - P_{core}^{rad}. \tag{2.10}$$

The following expressions may be used to estimate P_{SOL} and the particle flow, Φ_{SOL} from the main or core plasma into the SOL

$$\Phi_{SOL} = \frac{\bar{n}_{main}V_{main}}{\tau_p} \; [s^{-1}] \tag{2.11}$$

$$P_{SOL} = \frac{3\bar{n}_{main}k\bar{T}_{main}V_{main}}{\tau_E} \; [W], \tag{2.12}$$

with V_{main} the core plasma volume, $\bar{n}_{main}$ and $\bar{T}_{main}$ the average core density and temperature and τ_p and τ_E the particle and energy confinement times. The above equations implicitly assume that τ_p and τ_E do not depend on processes in the SOL. The principal energy source is in the core of the plasma, while particle sources can be distributed along the SOL (gas puff, recycling) and in the confined plasma (pellet fuelling, NBI).

2.1.4 Relation of main plasma density to upstream separatrix density

When simulating the SOL with $2D$ codes the density is often prescribed up to a few cm inside the LCFS. Alternatively, the upstream separatrix density, n_u^{sep} is prescribed in the simulation. Even if n_u^{sep} is known from experiment, the absolute location of the measured profiles is always subject to some uncertainty and they are often shifted radially using simulations and approximate pressure balance along field lines at low densities as a guide. Stangeby [28] gives an empirical relationship between *line averaged density*, $\bar{n}_e$ and n_u^{sep}

$$n_u^{sep} = \bar{n}_e^{1.6}, \tag{2.13}$$

whilst measurements in L-mode plasmas often find that

$$n_u^{sep}/\bar{n}_e \approx 0.3, \tag{2.14}$$

is approximately satisfied. A linear regression based on experimental data from different machines has recently been given by Porter [29]

$$n_u^{sep} = 0.00236\bar{n}_e^{1.08}\kappa^{1.11}B_\Phi^{0.78}. \tag{2.15}$$

2.1.5 Global particle recycling

Plasma facing surfaces are saturated if $\Phi_{ion}^{tot} \leq \Phi_{neu}^{tot}$, with Φ_{ion}^{tot} the total impinging ion flux and Φ_{neu}^{tot} the total neutral flux released as a result of the ion impact. The processes of absorption into and adsorption onto a surface of ions and the subsequent release of atoms or molecules from the surface is called particle *recycling*. In some situations, $\Phi_{neu}^{tot} < \Phi_{ion}^{tot}$ and pumping occurs. This can be through active pumping, for example using cryogenic pumps, or due to pumping by the walls ('passive' pumping). A local recycling coefficient may be defined for plasma-facing surfaces, as in the code used in this thesis but, particularly in the context of experiment, a global *recycling coefficient*, R_{global}, is usually used to characterize the degree of recycling:

$$\Phi_{neu}^{tot} = R_{global}\Phi_{ion}^{tot}. \tag{2.16}$$

An estimate for R_{global} can be obtained from the measurable plasma density decay time

$$\tau_p^* = (\langle n_e \rangle V) \left/ \frac{d}{dt}(\langle n_e \rangle V) \right., \tag{2.17}$$

with $\langle n_e \rangle$ the volumetric averaged density and V the plasma volume. If τ_p is known or can be estimated, then

$$R_{global} = 1 - \frac{\tau_p}{\tau_p^*}, \tag{2.18}$$

giving an approximate estimate for R_{global} which can be interpreted as an average recycling coefficient for all surfaces. Those receiving a higher particle flux are more likely to be saturated than surfaces receiving fewer particles and in any practical situation the estimation of local particle recycling coefficients is virtually impossible. In many tokamaks, especially those with extensive graphite first wall components, $R_{global} \approx 0.9$ to 1 and they are therfore largely self-fueled through recycling if active pumping is negligable.

23

2.2 Introduction to and validity of the fluid approach

Basic SOL theory is developed under the assumption of toroidal symmetry and is performed at the simplest level in one-dimension, along a coordinate parallel to the magnetic field. The one-dimensional equations presented here assume a straight field line bounded by solid surfaces, a current-free plasma ($j_{\parallel} = 0$) and no neo-classical or drift effects. Much of the basic theory reviewed follows Stangeby's recent book on the plasma boundary of magnetic fusion devices and references therein [28]. Codes such as the B2.5 code used in this thesis solve equations in the poloidal cross-section, hence in 2-D. In Part II it will become clear that experimental measurements only provide data at few specific poloidal locations. Values for n_e, T_e and particle fluxes are usually available only upstream and at the divertor targets. Calibrated or uncalibrated radiation measurements are often only supplied as integrated values along a fan of viewing chords and, in some cases, such as the total radiation from bolometry or selected line radiation measurements, a 2-D reconstruction with some uncertainty is sometimes available.

To understand the different regimes of divertor operation it is generally sufficient to consider average values of the plasma without requiring details of $f(x, v)$, the *distribution function*. The SOL may therefore be described using a *fluid* approach as opposed to a *kinetic* treatment, which would in any case be intractable in any real geometry. Simple 1-D scenarios are, however, readily modeled kinetically, an approach which may become a requirement under certain circumstances [30]. Reference [31] discusses the strengths and weaknesses of using a kinetic approach compared to a fluid treatment. But is it really valid to adopt a fluid approach when modeling the SOL?

A fluid treatment is appropiate if the collisional mean-free-paths (mfp) of electron and ion self-collisions are small compared to characteristic lengths in the SOL, such as the magnetic connection length or parallel gradient lengths [32]. The self-collisional mfp's for electrons and ions at temperature T $[eV]$ are given by [28]

$$\lambda_{ee} \approx \lambda_{ii} \approx \frac{10^{16}T^2}{n_e}, \tag{2.19}$$

24

where $n_e[m^{-3}]$ is the electron density. Typical values for TCV and JET are shown in Table 2.2

. A further useful quantity when analyzing collisionalities and characteristic lengths is the *Knudsen number*, defined as the ratio of λ to the characteristic length L of the system analyzed:

$$K = \lambda/L_c. \tag{2.20}$$

The inverse of K is often used to qualitatively characterize different divertor oper-

	TCV low density	TCV high density	JET low density	JET high density
$T_e[eV]$	50	20	~ 100	~ 40
$n_e[10^{19}m^{-3}]$	1.0	2.5	0.5	2.0
$\lambda_{ee}[m]$	2.5	0.16	20	0.8
$L_c[m]$	21	21	60	60

Table 2.1: *SOL conditions at the separatrix for typical plasma densities encountered in this thesis*

ating regimes, by defining SOL collisionality parameters for ions and electrons, based on *upstream* plasma conditions [28, 33]. Thus, for deuterium plasmas,

$$\nu^*_{SOL,e} \equiv L_c/\lambda_{ee} \approx 10^{-16}n_u L_c/T_{eu}^2 \tag{2.21}$$

$$\nu^*_{SOL,i} \equiv L_c/\lambda_{ii} \approx 10^{-16}n_u L_c/T_{iu}^2, \tag{2.22}$$

with $\nu^*_{SOL} \equiv 10^{-16}n_u L_c/T_u^2$ for $T_i = T_e$. Ions and electrons, however, tend to be decoupled in the SOL such that $T_e \neq T_i$. The *temperature equilibration time* over which the ion and electron populations relax to equilibrium is

$$\tau_{eq} = \frac{3\pi(2\pi)^{1/2}\epsilon_0^2 m_i T_e^{3/2}}{n_e Z^2 e^4 m_e^{1/2} \ln \Lambda}. \tag{2.23}$$

For equipartition to occur, $\tau_{eq} < \tau_\parallel$, with the latter being the parallel loss time, an expression which will be defined in Section 2.5 (eqn. 2.67). At JET a value of $\nu^*_{SOL} \gg 85$ is found in the detached regime [33], while values of $\nu^*_{SOL,e} > 10$ are typical for intermediate

and $\nu_{SOL,e}^* > 50$ for high collisionality with a significant $\nabla_\parallel T$ [28].

In the *sheath limited* regime, densities are low and temperatures relatively high, so that the self-collisionality is low. Driven by the source upstream and the sink of particles at the targets, plasma flows, parallel to the magnetic field $\vec{B}$, with conduction playing a minor role (parallel temperature gradients are low) and convection transporting most of the energy flux. Chapter 10 of [28] provides a good comparison of the fluid and kinetic treatment of collision less plasmas, showing that surprisingly there is little difference in the results. Therefore, even at low collisionality in the sheath limited regime the fluid code remains applicable for SOL modeling.

The Braginskii equations [34], derived for high collisionality, are the basis of the fluid code used in this thesis. They constitute a set of velocity moment equations, which are closed in the direction parallel to $\vec{B}$ using approximate expressions for the conducted heat fluxes, $q_\parallel$. This problem of closure will be treated to some degree in Section 2.3. The heat flux, $q_\parallel = \chi_\parallel \nabla_\parallel T$, is a kinetic phenomenon arising when a parallel temperature gradient ($\nabla_\parallel T$) exists and the $f(x,v)$ becomes asymmetric. The parallel heat flux diffusivity, $\chi_\parallel$ (usually called the heat conduction coefficient), is inversely proportional to the collision frequency and strongly dependent on temperature ($\propto T^{5/2}$). For very high collisionality (a situation never really satisfied in the edge plasma), $q_\parallel \to 0$ and no temperature gradient can be sustained. Chapter 1 briefly introduced the *conduction limited* regime in which strong gradients in $T_\parallel$ arise and heat conduction becomes important. If at any point $\lambda \sim \nabla T_\parallel$, the fluid approach must be modified, but can be maintained through the introduction of kinetic corrections in the form of parallel *heat flux limits* (Section 2.3.1). Unfortunately, however, only comparison with experiment or with the results of specific kinetic simulations can determine the appropriate value for these heat flux limits.

With further increases in density λ_{ii}, λ_{ee} decrease to low values compared with any parallel gradient scale lengths (see Table 2.2). With some kinetic corrections at the onset of the conduction limited regime, the fluid approach is thus valid for SOL modeling, particularly when the focus lies with the study of the mechanisms leading to the onset of detachment.

2.3 Fluid conservation equations in 1D parallel to B

In most cases parallel transport along the magnetic field is stronger/faster than transport across it and much insight can therefore be gained by reducing the analysis to $1D$ parallel to $\vec{B}$. Nevertheless, as will be shown in Part II, cross-field transport can strongly influence the overall SOL properties. For the purpose of this brief review the perpendicular transport will be treated simply as providing sources and sinks for particles, momentum and energy in the SOL.

It is not the intention here to derive the plasma fluid conservation equations. A number of excellent treatments can be found in the literature on this now classical topic in plasma physics [28,34,35]. Plasma fluid equations are essentially *velocity moment equations* of different *order* derived from the *collisional Fokker-Planck kinetic vector equation* [28] (here in $1D$):

$$v_x \frac{\partial f_a}{\partial x} + \frac{eE}{m}\frac{\partial f_a}{\partial v_x} = \sum C_{ab} + S(x,\vec{v}). \tag{2.24}$$

with f_a the distribution function of species a, x the coordinate along $\vec{B}$, $\vec{v}$ the velocity (component in the x-direction, v_x), and C_{ab} the collisional operator between species a and b. The quantity S is a net source of particles if positive and a sink if negative and is a specified quantity, e.g. through a boundary condition where the field line intersects a surface as a consequence of volumetric plasma neutral interactions along x or, in the $1D$ formulation, due to cross field transport. Gyration effects are neglected compared to the treatment in [35], no $\vec{E} \times \vec{B}$, $\nabla\vec{B}$ and curvature drifts are included and $\vec{E}$ is assumed parallel to $\vec{B}$. The hierarchy of *velocity moment equations* is obtained by multiplication of the the kinetic equation (2.24) with the different moments $d\vec{v}$ (0th order), $mv_x d\vec{v}$ (1st order), $\frac{1}{2}m\vec{v}^2 d\vec{v}$ (2nd order) and then integrating over the entire velocity space in order to obtain average values, such as density and temperature. The fluid equation of order n is closed by involving the next higher ordered equation, $n+1$, for the kinetic distribution f_a. Truncation of the development of higher orders is performed by an approximation which

closes the equation of order n without calculating the next order. In principle the fluid conservation equations listed below are always valid, but it is the approximations applied in the process of truncating equations of order $> n$ that limits their regime of validity.

The *particle conservation equation* or *continuity equation* (1st order equation) is given by:

$$\nabla_x(nv) = S(x) \qquad (2.25)$$

with n the particle density and v the plasma fluid velocity. The plasma is considered to be quasi-neutral and thus

$$n_e = \sum_i Z_i n_i \,, \qquad (2.26)$$

with n_i and Z_i the density and charge of ion species i respectively. Equation 2.25 is valid for both electrons and ions and contains two unknowns, n and v.

The *momentum conservation equation* (2nd order equation) may be written:

$$\nabla_x(m_i n v^2 + p_{\parallel i} + p_e) = -m_i(v_i - v_n)\overline{\sigma v}_{in_{mom}} n_n n + m_i v_n S(x). \qquad (2.27)$$

Since the electrons are generally strongly self-collisional (collisionality $\nu \propto m_e^{-1/2}$), the parallel and perpendicular electron temperatures $T_{\parallel e}$, $T_{\perp e}$ and thus also the parallel, $p_{\parallel e}$ and perpendicular, $p_{\perp e}$, static electron pressures equilibrate faster than those of the ions and are thus assumed to be isotropic in the SOL. To obtain equation (2.27) the electron and ion momentum equations have been summed, thereby dropping all terms containing the electron mass m_e (since $m_e \ll m_i$, with m_i the ion mass). The remaining variables are the ion velocity, v_i, the neutral velocity, v_n, the momentum collision rate coefficient $\overline{\sigma v}_{in_{mom}}$, between ions and neutrals and the neutral density, n_n. The first term on the RHS of equation (2.27) is important when elastic collisions between neutrals and ions dominate - a crucial element in detachment -, whilst the second term shows that sources can accelerate the plasma flow but sinks will remove momentum from the flow.

The static pressure for electrons and ions is

$$p_{e,i} = n_{e\,i} k T_{e,i}, \qquad (2.28)$$

with $k = 1.38\,10^{-23}\,JK^{-1}$ the Boltzmann constant. Frequently, T is written in energy units so that $p = nT$, with T in $[eV]$. The second order momentum of the kinetic equation thus provides a second conservation equation, but now with an additional unknown variable, T.

Since the collision frequency for ions is lower than that for electrons, pressure asymmetry for ions is treated next[2]. The parallel ion pressure, $p_{\parallel i}$, is coupled to the perpendicular ion pressure, $p_{\perp i}$, through collisions. Since pressure is the product of density and temperature, the exchange of pressure in these two directions is connected to the exchange of heat. When collisionality is very weak only parallel pressure gradient forces are available for accelerating the plasma. If the collisionality is high, then the ion pressure will be isotropic. For intermediate collisionality, a parallel gradient in the perpendicular pressure, $-\nabla_x p_\perp$, can exert a force on the plasma and one defines the *parallel stress tensor*

$$\pi \equiv \frac{2}{3}(p_\parallel - p_\perp) \tag{2.29}$$

to describe the coupling of parallel and perpendicular pressures. Ignoring the electrons and a number of terms in the ion fluid equations it is possible to derive an approximate expression for π_i

$$\pi_i = -\eta_\parallel \nabla_x v, \tag{2.30}$$

where $\eta_\parallel$ is defined as the Braginskii parallel viscosity coefficient. Since the ratio of the *pressure anisotropy relaxation time* for electrons and ions scales with $\sqrt{m_e/m_i}$, it is normally assumed that p_i is less isotropic than p_e. If the relaxation time becomes too large due to low collisionality, then in fluid modeling a limit on π_i known as the *viscous stress limiter* must be introduced, based on kinetic corrections (see also Section 26.3 in [28]). A typical value for the limit is $\pi_i \approx -0.5 p_i$ and is fixed in the fluid codes when modeling the SOL.

Using the definition of π_i in eqn. (2.29) and assuming, as throughout this section, the absence of parallel currents ($j_\parallel = 0$) the momentum conservation equation can be

---

[2]in principle a similar treatment is also valid for electrons at low collision frequency

rewritten as

$$\nabla_x \left(m_i n v^2 + p_i + p_e + \pi_i \right) = -m_i(v_i - v_n)\overline{\sigma v}_{in_{mom}} n_n n + m_i v_n S(x). \qquad (2.31)$$

If π_i is small then the *total plasma pressure* is

$$p_{tot} = m_i n v^2 + p_i + p_e, \qquad (2.32)$$

with the first term on the RHS being the dynamic pressure. It is important to note that it is this total pressure which is reduced along the field line in the detached regime.

From the discussion of the difference in collisionality between ions and electrons and the resulting pressure anisotropy for the ions, it would be necessary to derive two energy equations for ions, one each for the parallel and perpendicular directions. In the subsequent sections only a single ion temperature will be used and no directional distinction made. The parallel and perpendicular energy conservation equations are summed to yield an *ion energy conservation* (3-rd order equation) which can be written as

$$\nabla_x \left[(\frac{5}{2}p_i + \frac{1}{2}m_i n v^2 + \pi_i)v + q_{\parallel i} \right] = envE + Q_{eq} + Q_{Ei}. \qquad (2.33)$$

A similar *electron energy conservation* equation may also be derived

$$\nabla_x \left[\frac{5}{2}p_e v + q_{\parallel e} \right] = -envE - Q_{eq} + Q_R + Q_{Ee}, \qquad (2.34)$$

where all terms including m_e have been dropped.

The terms on the RHS of eqns. 2.33, 2.34 are energy sources and sinks for the ion and electron species. When summing the electron and ion energy equations, terms related to the ambipolar electric field, E cancel out, if $v_i = v_e$, energy is simply transfered from electrons to the ions by the electric field and there is no net energy source or sink for the plasma. The variable Q_{eq} represents the equilibration term due to electron-ion collisions, whilst Q_R is the joule heating term resulting from friction between ions and electrons. Since $m_e \ll m_i$, Q_R appears as a heating source for electrons and can be neglected for the ions. The remaining two terms Q_{Ee} and Q_{Ei}, represent sources or sinks for the ions and electrons due to interaction with neutrals (e.g. radiation losses for the electron 'channel').

The heat flux $q_\parallel$ has been introduced as a new variable and it is the expression for the approximation of this new quantity, that is used to close the fluid equations. The total energy flux $q_{\parallel\,i,e}^\epsilon$ is defined as the sum of conducted and convected energy. To clearly distinguish the total energy flux from the heat flux, the heat flux will always be labeled $q_{e,i}$. Using the approximative expressions for the heat flux to be defined in Section 2.3.1, the set of equations can be closed to yield 4 equations for the 4 variables T_e, T_i, n and v.

2.3.1 Parallel heat flux and heat flux limits

From collisional considerations [36] the following expressions result for the parallel ion and electron conductive heat fluxes:

$$q_{\parallel i} \equiv \chi_{\parallel i} \nabla_x T_i = -\kappa_{0i} T_i^{5/2} \nabla_x T_i \qquad (2.35)$$

$$q_{\parallel e} \equiv \chi_{\parallel e} \nabla_x T_e = -\kappa_{0e} T_e^{5/2} \nabla_x T_e \qquad (2.36)$$

with the ion and electron heat conductivity coefficients:

$$\kappa_{0i} = \frac{1249}{Z_i^4 m_i^{1/2} \ln \Lambda} \approx 60 \qquad (2.37)$$

$$\kappa_{0e} = \frac{30692}{Z_i \ln \Lambda} \approx 2000 \qquad (2.38)$$

where the temperatures are given in $[eV]$, lengths in $[m]$, the Coulomb logarithm $\Lambda \approx 15$ [28], the mass in units of atomic mass $[amu]$, q in $[W/m^2]$ and the approximate numerical values have been calculated assuming a D plasma. If He^{2+} is the dominant ion species, κ_{0i} is 30 times smaller in a helium plasma.

The equivalent formulation for the expressions of q in eqns. 2.35 and 2.36 is that derived by Spitzer-Härm [28, 36]

$$q_{SH} \approx -2.9 \times 10^{-19} n_{e\,,i} v_{th} \lambda_{e,i} \nabla_x T_{e,i}, \qquad (2.39)$$

where

$$v_{th} = (k T_{e,i}/m_{e,i})^{1/2} \qquad (2.40)$$

31

is the thermal velocity of the plasma species. As collisionality decreases, $q_{SH} \to \infty$. This would not be a problem if the typical scale-lengths of $\nabla_x T$ were also free to evolve, but in the SOL with fixed sources and sinks, the scale-lengths are limited to the system size. The power entering the SOL is given and must be exhausted along the magnetic field lines. If the volumetric energy sinks, $Q_{Ei,e}$, do not increase with decreasing collisionality, then even at intermediate collisionality, kinetic analysis shows that the temperature gradient must steepen to allow heat conduction along the field line. The value of $\chi_\parallel$ is then lower than given by Spitzer-Härm and is limited to some fraction, α_{hfl}, of the free-streaming heat flux such that

$$q_{limit} = \alpha_{hfl} n v_{th} kT. \tag{2.41}$$

Section 2.4 will show that a 'natural' heat flux limit arises in the SOL at low collisionality due to the heat transmission capability of the sheath itself (sheath limited regime) [37]. The parallel conducted heat flux is conventionally expressed as

$$\frac{1}{q_\parallel} = \frac{1}{q_{limit}} + \frac{1}{q_{SH}}, \tag{2.42}$$

where the correct value to be assumed for the *ion* and *electron heat flux* limits is difficult to assess and must normally be derived by comparison with experimental data or kinetic simulations. Typically $\alpha_e \approx 0.2$, whilst $\alpha_i \approx 0.6 \sim 1.5$. An extensive analysis can be found in [28, 37] and references therein.

For any given temperature gradient, it is clear from eqns. 2.35 and 2.36 ($q_{\parallel e} \gg q_{\parallel i}$) that most of the conducted heat is transported by the electrons so that the ion heat flux can be easily neglected in the analysis. But when simulating the SOL, parallel temperature gradients are NOT prescribed a priori, only the power entering the SOL and the sinks are specified and the temperature gradient must establish itself 'naturally'. At low to moderate collisionality, the upstream T_i and T_e are decoupled, with $T_i \sim 2T_e$ at least, being typical. Since $\chi_{\parallel i} < \chi_{\parallel e}$, one expects $\nabla_x T_i > \nabla_x T_e$ and a stronger effect is observed on the parallel temperature profiles when applying an ion heat flux limit than an electron heat flux limit. This, as will be seen in the results presented in Part II, is also observed for simulations of TCV (figure 5.32) and JET.

2.4   The plasma-wall transition: *the sheath*

One of the locations in the SOL where fluid treatments fail is the interface, or *sheath* region, between the plasma and material walls. A kinetic treatment is thus required to provide boundary conditions used for a SOL fluid model. This essentially reduces to obtaining expressions for the sources and sinks of the particle, momentum and energy conservation equations. For the plasma temperatures concerned by this thesis, there is little fast particle reflection (see Section 2.7) and no charged particles will leave the material surface. It thus provides a net sink for all three quantities.

The SOL divides into a narrow region, of order a few 10's of μm, called the sheath, right in front of the material surface and the *pre-sheath*, extending in a divertor tokamak along magnetic field lines from the inner target to the outer target sheaths (figure 2.1) and will often be referred to as the plasma or SOL plasma. Electrons and ions have different
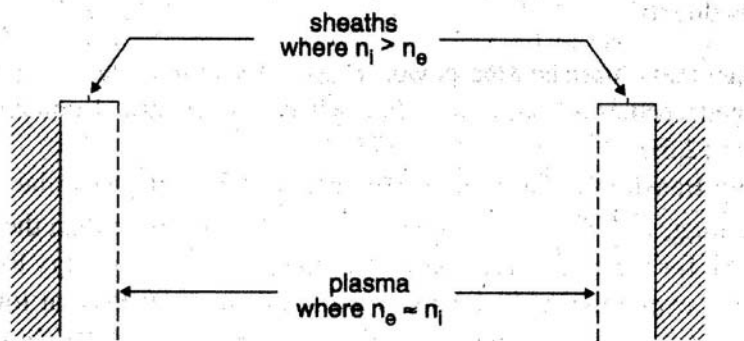

Figure 2.1: *Schematic view of the SOL with presheath (plasma) and sheath (from ref. [28]).*

masses and therefore different mobility. As a consequence, any material surface in contact with a plasma rapidly charges up negatively with reference to a plasma potential, $V = 0$, distant from the sheath. The resulting electric field repels electrons and accelerates ions onto the surface.

As shown in Fig. 2.2, in a magnetized plasma, such as the tokamak SOL, the sheath itself can be divided up into the approximately quasi-neutral *magnetic pre-sheath* (MPS),

also called the *Chodura sheath* and an *electrostatic* or *Debye sheath* (DS), where $n_e < n_i$ (and hence a net positive charge density). Electrons and ions gyrate around magnetic
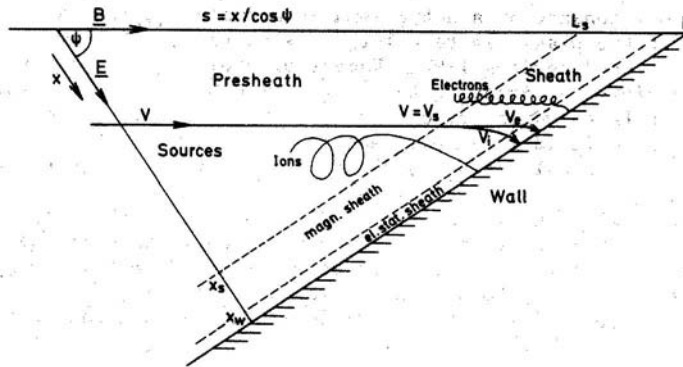

Figure 2.2: *Schematic view of the presheath and sheath in a scrape off layer with magnetic field $\vec{B}$ incident with oblique angle ϕ onto a surface (from ref. [38]).*

field lines during their motion along the magnetic field, with the ion Larmor radius being larger than that of the electrons by a factor $\sim \sqrt{m_i/m_e}$. The Chodura sheath has a width of the order of a few ion Larmor radii, $\rho_i = m_i v_\perp / eB \cong m_i c_s / eB$, with c_s the sound speed (see below, eqn. 2.46).

The size of Debye sheath is of the order of a *Debye length*

$$\lambda_{Debye} \equiv \left(5.53 \times 10^7 T_e / n_e\right)^{1/2} \; [m], \tag{2.43}$$

with $T_e \; [eV]$, $n_e \; [m^{-3}]$. Due to the net charge and small value of λ_{Debye}, a large electric field exists perpendicular to the surface in the DS. Ions and electrons are forced to move parallel to $\vec{E}$ when they cross from the MPS into the DS. The ion velocity at the entrance of the MPS is determined to first order by that required at the entrance to the DS (see below). A detailed derivation can be found in [28, 38]. Conditions at the MPS are determined mainly by those at the DS entrance, whatever the angle between the magnetic field and the surface normal.

The electric potential at the sheath entrance, V_{se}, (referred to the far field plasma at $V = 0$) also known as the pre-sheath potential, can be found by solving for Poisson's

equation in the DS and combining it with the momentum conservation fluid eqn. (2.27) for the ions in the pre-sheath, assuming no ion-neutral collisions

$$V_{se} \simeq -0.7 \frac{kT_e}{e}. \tag{2.44}$$

If the mfp for ion-neutral collisions, $\lambda_{in} \ll L_{in}$, with L_{in} the length of the zone in front of the divertor target in which typically most of the plasma neutral friction occurs, then

$$V_{se} \approx -\ln(L_{in}/\lambda_{in}) \frac{kT_e}{e}. \tag{2.45}$$

For TCV in the detached regime when friction is most important, $L_{in} \approx 1 - 10m$, while in the high recycling regime when T is often not below $5eV$, L_{in} is only approximately a few cm and λ_{in} ranges from a few mm at high T to several cm during detached conditions. The absolute value can be considerably larger than that obtained in eqn. 2.44. Further details of the different models used to derive V_{se} can be found in Chapters 1 and 10 of [28].

The electric field that arises due to the potential difference between the stagnation point ($V = 0$) and the sheath entrance in the pre-sheath (V_{se}), is responsible for accelerating the ions and thus for the plasma flow towards the surface, even if this field is tiny compared to the electric field in the sheath. The *Bohm-Chodura* criterion states that the velocity, v_{se}, at which the plasma enters the sheath must be at least as large as the ion sound speed:

$$v_{se} \geq c_s = (e(Z_i T_e + \gamma T_i)/m_i)^{1/2}, \tag{2.46}$$

with Z_i the ion charge, $\gamma = 1$ for isothermal flow, $\gamma = 5/3$ for adiabatic flow with isotropic pressure and $\gamma = 3$ for $1D$ adiabatic flow with no perpendicular heat conduction (see Chapters 2 and 10 in [28]). In the fluid code B2.5, c_s is usually assumed to be adiabatic. It is also possible to fix $v_{se} = c_s$ or to allow supersonic solutions at the sheath edge - the consequence of which has been tested when simulating TCV plasmas. When drift terms are activated in multi-fluid codes (sections 2.10, 3) the correct setting of boundary conditions at the targets is made difficult as gradient of drift velocities and currents [39–41] need to be accounted for, thus altering the original Bohm-Chodura condition. Introducing

the definiton of the flow Mach number

$$M = v/c_s, \tag{2.47}$$

with v the plasma flow velocity, the *Bohm-Chodura* criterion (eqn. 2.46) becomes $M_{se} \geq 1$. Using the ion fluid equations for continuity and momentum, an interesting relation for the Mach number is readily derived [28]

$$\frac{dM}{dx} = \frac{S}{nc_s}\frac{1 + M^2}{1 - M^2}, \tag{2.48}$$

demonstrating clearly that the fluid equations breakdown when $M \to 1$ and a singularity appears $(dM/dx \to \infty)$.

The electrons feel a retarding conservative electric field in the presheath and satisfy the Boltzmann relation throughout this region. Their density at the sheath entrance is

$$n_{se} = n_0 \exp(V_{se}/(T_e)), \tag{2.49}$$

with n_0 the electron density at $V = 0$. Using the above equation with $V_{se} = -0.7T_e$ gives

$$n_{se} = 0.5n_0 \tag{2.50}$$

and employing the *Bohm-Chodura* criterion (eqn. 2.46) provides a simple expression for the particle outflux to the targets:

$$\Gamma_{se} = n_{se}v_{se}. \tag{2.51}$$

The important boundary condition is the Bohm-Chodura criterion - particle and momentum fluxes 'adjust' such that this criterion is fullfilled at the sheath entrance.

The sheath acts as an energy filter for the electrons and only electrons with energy sufficient to overcome the potential barrier are lost. The total potential fall is the sum V_{se} and V_w, where V_w is the potential difference between the sheath edge and the surface. In the simplest case the plasma is assumed collisionless in the sheath (a very good approximation for the tokamak SOL) and that no secondary electrons are produced due to ion

impact, both of which would modify the value of V_w. For an unbiased (floating) surface, V_w is called the floating potential, V_{sf}. This is the case for the divertor targets of both JET and TCV. For a Maxwellian electron distribution [28],

$$\frac{V_{sf}}{T_e} = 0.5 \ln \left[\left(2\pi \frac{m_e}{m_i} \right) \left(1 + \frac{T_i}{T_e} \right) \right] \left(\frac{1}{(1 - \delta_e)^2} \right), \tag{2.52}$$

where δ_e is the coefficient of secondary electron emission. Under typical divertor conditions $V_w \sim 3T_e$. The net electron energy flux through the sheath is [28]

$$q_{se,e}^\epsilon = \gamma_e e T_e \Gamma_{se}, \tag{2.53}$$

where

$$\begin{aligned} \gamma_e &= 2 + |V_{sf}|/(eT_e) + |V_{pre-sheath}|/(eT_e) \\ &\approx 2 + 3 + 0.7 = 5.7 \end{aligned} \tag{2.54}$$

is the *electron sheath heat transmission factor*. The value of γ_e can be adjusted in fluid codes to best suit to the particular SOL plasma being modelled.

In contrast to electrons, the ions are accelerated in the pre-sheath and sheath electric fields and the velocity distribution function is strongly distorted at the wall. Kinetic calculations are therefore required to derive the value for the *ion sheath heat transmission coefficient*, γ_i, but a reasonable approxmation in many cases is to assume a drifting Maxwellian

$$q_{se,i}^\epsilon = \left(\frac{5}{2} kT + \frac{1}{2} m_i c_s^2 \right) \Gamma_{se}, \tag{2.55}$$

so that $\gamma_i = 3.5$ if $T_e = T_i$. Values of $\gamma_i \approx 2 - 3$ have been found using both kinetic analysis and simulations (see Section 5.3 for an example of values used for TCV). The total *sheath heat transmission factor* for electrons plus ions is thus

$$\gamma \simeq 7 - 9, \tag{2.56}$$

whilst the energy transferred by the sheath for $T_i = T_e$ is

$$q_{se}^\epsilon = \gamma kT_e \Gamma_{se} \tag{2.57}$$

and is an upper limit on the parallel SOL energy flux. The plasma density, temperatures and their gradients adjust such that the total energy flux is equal to that which can be transmitted by the sheath. This is strictly only the case in the sheath limited regime - in detached regimes, for example, volumetric losses play a siginifcant role in establishing these parameters.

The sheath electric field acts effectively to transfer energy from the electrons to the ions, accelerating the latter to the surfaces. In addition to their directed kinetic energy at the sheath edge, the ions gain a further $Z_i e V_w$ of energy in passing across the sheath. Since $V_w \sim 3T_e$, ions can reach surfaces with high energies under some conditions, often sufficient to overcome the threshold for physical sputtering (Section 2.6.1).

2.4.1 Total deposited power flux on surfaces

The sheath energy transmission coefficient introduced in Section 2.4 (eqn. 2.57) limits the energy flux that can be transmitted across the sheath by ions and electrons. The power that reaches the material surface is also, however, determined by the total particle flux including neutrals and charged particles. The total parallel power flux carried across the sheath also includes the flux of potential energy of ions and neutrals due to their degrees of ionisation and dissociation. On material surfaces, ions recombine with electrons to form neutral atoms, whilst atoms, if the surface is sufficiently saturated, recombine to form molecules. The potential energy from the recombination process is released as heat to the material and contributes to the deposited power. The total parallel power flux is

$$
q_\parallel^{total} = \left(\gamma_e kT_e + \gamma_i kT_i + e E_{pot}^{ion} + e E_{pot}^{diss} \right) \Gamma_{se} \tag{2.58}
$$

$$
\approx \left(7kT + e E_{pot}^{ion} + e E_{pot}^{diss} \right) \Gamma_{se} \, \text{with} \, T_e = T_i \, [eV], \tag{2.59}
$$

where E_{pot}^{ion} and E_{pot}^{diss} are respectively the ionisation and molecular dissociation potential energies of the species in question. For deuterium, with $E_{pot}^{ion} = 13.6eV$ and $E_{pot}^{diss} = 4.52eV$:

$$
q_\parallel^{total} = (7eT + e18.1eV)) \Gamma_{se}. \tag{2.60}
$$

The power deposited on the targets through ion-electron recombination and subsequent molecular formation on material surfaces becomes comparable to the depoisted heat flux when $T < 3eV$.

In a high density divertor such as that forseen in ITER, the power deposited onto material surfaces surrounding the divertor volume through neutral and photonic fluxes can be important. It appears that the values estimated thus far are not critical [10], but a proper estimation requires credible prediction from $2D$ codes.

2.5 Perpendicular transport and radial profiles in the SOL

2.5.1 Introduction

The physics of radial transport in the main SOL is a complex, far from completely understood phenomena. It has long been and remains an active field of both theoretical and experimental study. This section provides a brief, rather pragmatic introduction, discussing the essential components from the SOL modeler's viewpoint.

As stated at the beginning of Section 2.3, cross-field transport of particles, momentum and energy can be treated essentially as sources or sinks in $1D$ analysis of the SOL. When writing down the fluid conservation equations for $2D$ [34], it is likewise seen that all the terms describing perpendicular transport can be grouped on the RHS of the conservation equations so as to appear as sources or sinks for transport in the parallel direction to $\vec{B}$.

But what is the order of magnitude of the perpendicular transport and how does it affect the SOL, especially the performance of the divertor? Power entering the SOL from the core region (above the X-point) is transported along field lines to the divertor targets. A parameter of critical importance for future fusion reactors is the power deposition profile width on the targets, since this determines the peak and average power fluxes. In combination with fast parallel transport to the divertors, cross-field transport determines the shape of the radial profiles of density and temperature together with the distribution of charged particles, not just on the targets but also on the walls of the main chamber. This main chamber interaction can have an important influence on impurity production.

Cross-field radial transport in the fully ionized plasma of magnetic fusion devices cannot yet be calculated from first principles. The SOL radial particle flux is normally described by an equation of the form

$$\Gamma_\perp = -D_\perp \frac{dn}{dr} + v_\perp n, \tag{2.61}$$

where the first term on the RHS, is proportional to the density gradient, describes a diffusive process with with *diffusion coefficient*, $D_\perp \, [m^2 s^{-1}]$ and the second describes a

radial convective component, with *radial velocity*, $v_\perp$. When modeling the SOL, the two terms in the transport ansatz of eqn. 2.61 are simply intended as a prescription of the radial transport in terms of a flux, not necessarily revealing its underlying nature. In some cases, experimental measurements can be used to ascertain the relative importance of convective versus diffusive components, but quantitative estimates remain difficult. The radial and poloidal variations of $D_\perp$ and $v_\perp$ remain largely unknown and there is as yet no experimentally verified physical model upon which to base an assumption. It is useful to define an *effective diffusion coefficient*, $D_\perp^{eff}$ [42] such that

$$\Gamma_\perp = D_\perp^{eff}(r)\nabla_r n \tag{2.62}$$

which implicitly includes the convective and diffusive terms and can be measured under some circumstances [42]. An equivalent relation can be introduced using an effective perpendicular convective velocity $v_\perp^{eff}$ such that

$$\Gamma_\perp = nv_\perp^{eff}(r). \tag{2.63}$$

For many numerical simulations, however, $D_\perp$ is assumed spatially constant in the absence of any better alternative. In any particular simulation, the choice of values for $D_\perp$ and $v_\perp$ must be made, were possible, using experimental data as a guide, systematically comparing measured profiles with the plasma solution and making appropriate adjustments to the transport coefficients until agreement is found.

2.5.2 Diffusive cross field transport: $D_\perp$

A well known empirical result derived from experiments in non-toroidal plasmas is [43]

$$D_\perp^{Bohm} = 0.06T_e/B. \tag{2.64}$$

For TCV, assuming $T_e = 50eV$, $B = 1.5T$, one obtains $D_\perp^{Bohm} = 2m^2/s$. If radial diffusion were controlled solely by classical cross-field diffusion from electron-ion collisions, then [44]

$$D_\perp^{class} = 8\,10^{-4}T_e^{-3/2}n(kT_e + kT_i)/B^2, \tag{2.65}$$

$T[K]$, which, assuming that $T_i \approx 2T_e$ in the upstream SOL, yields $D_\perp^{class} = 10^{-3} m^2 s^{-1}$ for TCV. Experimental values for $D_\perp^{eff}$ are typically found to be in the range between $0.1 m^2/s$ and $10 m^2/s$ [28, 42].

The radial plasma density profile can be explained in terms of a simple radial particle balance equation (see e.g. [45]),

$$\frac{d\Gamma_\perp}{dr} = -\frac{n}{\tau_\parallel} + S_{iz}, \tag{2.66}$$

with $\tau_\parallel$ a parallel loss time and S_{iz} the ionization source in the SOL. Assuming convective parallel transport only and that $S_{iz} = 0$ in the SOL (corresponding to a low density, hot edge - sheath limited regime)

$$\tau_\parallel = \text{(particle content of SOL)} / \text{(loss rate to targets)}$$
$$\approx 2L_c n / 2(n_{se} c_s) = L_c n / (0.5 n c_s) = 2L_c/c_s. \tag{2.67}$$

Combining eqns. 2.61 and 2.66 with $S_{iz} = 0$ whilst assuming spatially constant $v_\perp$, $D_\perp$ and applying the ansatz of a radially decaying density

$$n(r) = n(0) \exp(-r/\lambda_n), \tag{2.68}$$

for solving the resulting differential equation, with λ_n the radial decay length, leads to the expression

$$\lambda_n^2 - v_\perp \tau_\parallel \lambda_n - D_\perp \tau_\parallel = 0. \tag{2.69}$$

Equation 2.69 has as a general solution

$$\lambda_n = \frac{v_\perp \tau_\perp}{2} \pm \sqrt{\left(\frac{v_\perp \tau_\perp}{2}\right)^2 + D_\perp \tau_\parallel}. \tag{2.70}$$

For purely diffusive radial transport eqn. 2.70 leads to the often employed and simple relation

$$\lambda_n = \sqrt{2L_c D_\perp / c_s}. \tag{2.71}$$

In this simplest situation a $D_\perp$ can be estimated from experimental data if the measured density profile is observed to decay exponentially. Such a procedure is not, however,

applicable in the high recycling or detached regimes which constitute the main interest of this thesis. Nevertheless, a number of simulations applied to a variety of tokamaks (e.g. DIII-D [46,47], JET [48], ASDEX-U [49,50] and other tokamaks [51]) have obtained reasonable qualitative agreement with experimental data.

Assuming purely convective transport results in the non trivial value of

$$\lambda_n = v_\perp \tau_\parallel. \tag{2.72}$$

Therefore the same λ_n may be obtained assuming either a purely diffusive or a purely convective radial transport. Furthermore, the ansatz of a spatially constant purely diffusive transport or a spatially constant purely convective radial transport with the same λ_n lead to identical values for $\Gamma_\perp$ if

$$v_\perp = \sqrt{\frac{D_\perp}{\tau_\parallel}}, \tag{2.73}$$

as

$$\Gamma_\perp^D = \frac{D_\perp}{\lambda_n} n(r) = \sqrt{\frac{D_\perp}{\tau_\parallel}} n(r) \tag{2.74}$$

and

$$\Gamma_\perp^v = v_\perp n(r). \tag{2.75}$$

2.5.3 Intermittent convective perpendicular transport: $v_\perp$

Experimental observations, particularly in Alcator C-Mod [42,52–54], have shown that cross-field particle transport can be characterized by $D_\perp^{eff}$ increasing substantially with radius in the SOL. It is also observed that $D_\perp^{eff}$ increases across the entire SOL with increasing plasma density with a simultaneous rise in the fluctuation levels of density, $\tilde{n}/n$ and poloidal electric field, $\tilde{E}_\theta$. The latter, in combination with the toroidal magnetic field, B_Φ, results in a fluctuating radial drift velocity, $\tilde{E}_\theta \times B_\Phi$, which, if in phase with $\tilde{n}$, causes a net, time-averaged outward radial particle flux

$$\Gamma_r^{fluct} = \frac{\langle \tilde{n} \tilde{E}_\Theta \rangle}{B_\Phi}. \tag{2.76}$$

This is an electrostatic fluctuation driven flux always found to be much stronger than that due to magnetic fluctuations in the SOL. It is thought that the turbulence is due to

micro instabilities [5, 44, 55], leading, for example, to *unstable drift waves* in the presence of radial pressure gradients. If the electrons could move freely parallel to the magnetic field, the Boltzmann relation would hold exactly, but in the SOL the sheath created by the plasma-wall contact at the end of each field line (see Section 2.4), restricts the motion of the electrons and can drive *drift waves* unstable [55].

Measurements over the past few years indicate that non-diffusive, intermittent convective transport perpendicular to $\vec{B}$ can be responsible for at least 50% of the cross-field particle transport [21]. Krasheninnikov first proposed a picture in which high pressure plasma *blobs*, formed perhaps through turbulence mechanisms, detach from the separatrix region and move radially outward in the SOL [22]. In $3D$ these structures are radially thin filaments extending along a field line. Such blobs have been observed with fast cameras and probes in the SOL. They are thought to be coherent propagating structures that travel radially at different velocities and with different sizes [56]. A charge dependent drift, induced by ∇B curvature drift or 'neutral wind' [57] in toroidal devices can polarize a blob through charge separation, figure 2.3. In the SOL, where the plasma is in contact
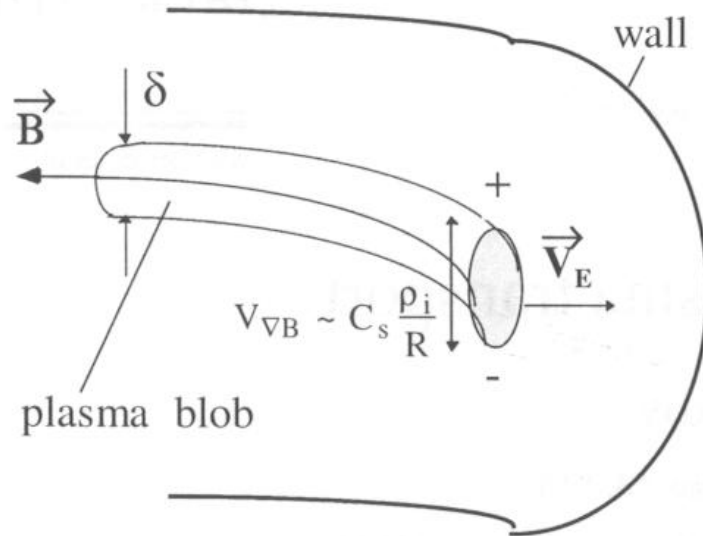

Figure 2.3: ∇B *plasma polarization and associated $\vec{E} \times \vec{B}$ drift result in outward motion of the plasma blob in the SOL [22].*

with divertor targets, the effective "sheath resistivity" [58] forms a poloidal electric field. The formation of E_Θ is more important further away from the X-point and therefore from

the separatrix where magnetic shear becomes less strong [22, 55]. The resulting $\vec{E} \times \vec{B_\Phi}$ drift moves the blob radially outward, as in the case of the smaller scale perturbations discussed earlier. Indeed a distinction between the two might seem purely academic since, similarly to blobs, the experimentally measured fluctuations are correlated over long distance in the parallel direction.

In a plasma fluid simulation the modeller can only be interested in the average effect of these blobs on the total radial flux. It has been shown that the blob transport paradigm can explain, at least qualitatively, the experimentally observed flat density profiles [56] that occur especially in the *far SOL*, the region extending into the SOL beyond the first λ_n. Neutral ionisation in the SOL can sustain the blob transport so that main chamber wall recycling of neutrals or even neutrals escaping from the divertor chamber might act to enhance such 'blobby' transport.

It would thus seem appropriate to assume the existence of a convective radial flux component, $\Gamma_\perp^{conv} = n v_\perp$, when simulating the SOL by assigning either a value for $v_\perp$ or for $\Gamma_\perp$, in which $v_\perp$ is calculated based on the local plasma density profile in the SOL. Such an approach has been attempted in this thesis for TCV simulations (see Part II). References [59–61] demonstrate that a good match with experimental data, especially spectroscopic, can be obtained if one invokes a convective radial particle outflux in $2D$ simulations of the divertor SOL. In these simulations it is assumed that $v_\perp$ increases with radius and, in many cases, that the radial transport inside the LCFS is essentially diffusive, consistent with experimental measurements showing that intermittent radial transport is small inside the LCFS. One may also note that drift waves due to fluctuations are more stable on closed field lines, leading to a smaller radial transport there.

There are indications that radial transport is of 'ballooning nature' being stronger on the LFS of a tokamak than the HFS. A higher $D_\perp^{eff}$ or $\Gamma_\perp^{conv}$ has thus sometimes been assumed in the outboard SOL when simulating SOL plasmas with $2D$ codes.

In a simple analytic model, Stangeby has assumed a case with no convective transport and radially increasing $D_\perp$ (see part C in [45]). If plasma is in contact with the main chamber walls, particle transport of this nature would tend to steepen the SOL density

profile owing to the presence an ionization source in the SOL due to recycling at the walls. A criterion for a radially constant density profile can also be derived assuming constant $D_\perp$ and radially increasing $v_\perp$ (see B in [45]). The experimentally observed flat radial density profiles with increasing upstream density in the far SOL are therefore a further indication that SOL particle transport deeper in the SOL and at high densities becomes increasingly convective.

Radial impurity transport is not necessarily the same as transport for the main plasma species and little is known about cross-field transport of impurity ions in the SOL. The radial convective transport of impurities can, depending on the charge state, even be in the inward direction (pinch). For now, only 'adhoc' assumptions can be made, in the hope that a match of simulation with experiment indicates that the choice was reasonable [61].

2.5.4   Main chamber recycling

Analysis of experimental profiles of n_e, T_e, S_{iz} can provide strong hints as to the nature of radial transport. The shape of the SOL profile is a result of the competition between parallel transport along field lines to the divertor targets and cross-field transport to the main chamber walls. Measurements in a number of tokamaks have observed the appearance of a 'shoulder' or a 'second-e-folding length' [42] in the radial density profile as density increases. Beyond this 'shoulder', the radial density profile flattens leading to a long decay length towards the main chamber walls.

Early studies [62] had already noted the presence of a radially extended region with constant density, called a *density plateau sublayer*, when ionization of recycled neutrals occurs in the SOL. An existence criterion for this sublayer may be written as [62]:

$$S_{iz} \approx \left(c_s n \right) / \left(2 L_c \right). \tag{2.77}$$

In tokamaks such as Alcator C-Mod it has been observed that even under relatively low density conditions cross-field SOL particle transport can dominate parallel transport in any given flux tube in order to balance the ionization of incoming neutrals [42]. The

machine is then said to be in a *main chamber recycling regime* (Fig. 2.4). Analysis with a simple model, beginning from eqn. 2.66 shows that if the neutral density at the separatrix in this regime reaches a critical value

$$n_0 = \Gamma_{0\perp}\sqrt{\frac{2\pi m_i}{kT_i}}, \tag{2.78}$$

the SOL ionization sources can be balanced by the radial outflux. In eqn. 2.78, $\Gamma_{0\perp}$ is the neutral influx into the SOL, which may be derived from neutral pressure measurements. If the ion outflux, $\langle \Gamma_\perp \rangle$ to the walls, averaged radially over several flux tubes, is balanced entirely by a neutral influx that originates at the main chamber, a critical value for the main chamber recycling regime may be obtained [42]:

$$\langle \Gamma_\perp \rangle_{crit} = \frac{c_s}{2L_c k_{ion}}\sqrt{\frac{kT_i}{2\pi m_i}}, \tag{2.79}$$

with k_{ion} the ionization rate coefficient (see Section 2.7). Divertor leakage, f_L, is defined as

$$\Phi_{leak} = f_L \Phi_{dt}, \tag{2.80}$$

with Φ_{leak} the neutral leakage flux, specifying what fraction of the flux reaching the target surfaces, Φ_{dt}, returns to the main chamber. For large f_L, the plasma flux to the wall can be enhanced by a factor of ≈ 2 compared to the case when $f_L = 0$ [45]. Main chamber recycling would indeed be established earlier in high recycling or detached regimes when parallel particle flow stagnates in the SOL. Two main reasons can be identified: a) it is experimentally observed that radial particle flux in the SOL increases with increasing density and b) that as plasma in the divertor volume cools down, the neutral mfp increases, augmenting the probability for f_L to increase. Stangeby has offered an alternative definition of the onset of *main chamber recycling* [45]. It occurs when the integrated flux to the main chamber walls, Φ_{mcw}, is larger than Φ_{dt}

$$\Phi_{mcw}/\Phi_{dt} > 1. \tag{2.81}$$

So far, main chamber recycling has only been experimentally proven to be present in $R = 1.5m$ (or smaller) class machines. It is currently not at all clear if it is important for
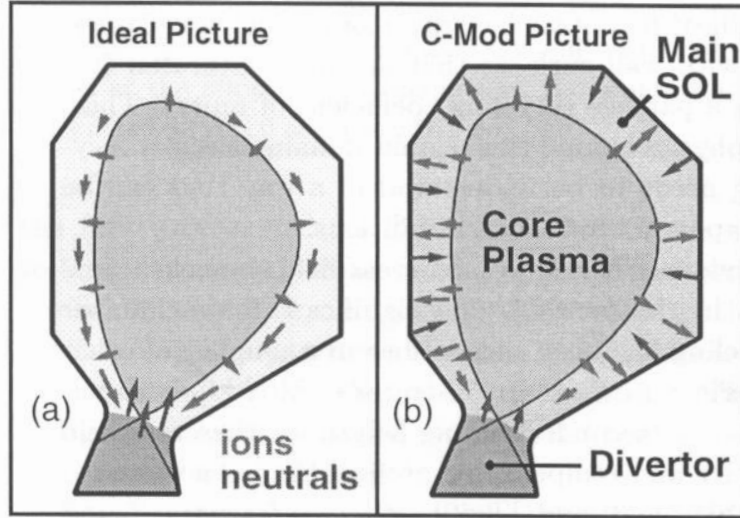
Figure 2.4: *Ideal divertor operation (a) with dominant parallel particle transport and (b) the situation observed in C-Mod, where main chamber recycling is important [42].*

JET or will be a factor in even larger devices (e.g. ITER). It is important to note that if the core plasma is not feuled by pellet or neutral beam injection, then particles must be supplied by gas puffing or wall recycling. Furthermore, if there is little or no pumping at the plasma edge, the core density is maintained only by recycling. The latter can occur at the wall or at the divertor targets. If main plasma refueling is mainly provided by wall recycling, then the wall-separatrix distance is unimportant and the main SOL is in a 'limiter configuration'. The Engelhardt model [28, 45] then applies, stating that

$$\Gamma_\perp \propto D_\perp^{eff} \bar{n}_u^2 \tag{2.82}$$

where $\bar{n}_u$ has been assumed proportional to $\bar{n}_e$. If $D_\perp^{eff}$ also increases with density, then the flux to the wall becomes very strong and the tokamak may transit from a divertor to a wall dominated recycling regime. This can have important consequences for impurity production and subsequent contamination of the main plasma in the case of carbon walls where chemical sputtering may be significant. The role of main chamber recycling in impurity production can be studied by changing to a main plasma species such as helium which is not chemically active with carbon, but which still exhibits similar radial transport behaviour.

2.5.5 Perpendicular energy flux

Whilst particle sources can be distributed along the entire SOL, especially at high up-stream densities (see Section 2.5.4), power enters the SOL *only* from the core. Upstream radial density profiles can be strongly influenced by the radial particle flux and it has been shown above that there are cases in which the main chamber particle flux can be stronger than the divertor particle flux. With the exception of cases in which a large amount of power is lost by radiation in the SOL itself, the picture is very different for power balance and therefore for the role of cross-field power transport. Perpendicular power and particle transport compete with parallel transport, but whilst parallel particle transport becomes small when the plasma fluid is nearly stagnant, the energy flux parallel to $\vec{B}$ can be still high due to heat conduction ($q_{cond} \propto T^{5/2}$, eqns. 2.35 and 2.36). The radial energy flux may be written,

$$q_\perp^\epsilon = q_\perp^{diff} + q_\perp^{elconv} + q_\perp^{ionconv} + q_\perp^{neutrconv} + q_\perp^{cx}, \tag{2.83}$$

in which radiation losses in the SOL above the X-point are neglected. Here

$$q_\perp^{diff} = -n \left(\chi_{\perp e} \nabla_\perp T_e + \chi_{\perp i} \nabla_\perp T_i \right) \tag{2.84}$$

is the *diffusive radial heat flux*, which, like particle diffusion, is found to be anomalous at least for electrons [63]. In the absence of any better assumptions, guided by theory or experiment, $\chi_{\perp i,e}$ are often assumed equal in simulations. Values for the electron and ion radial heat diffusion coefficients, $\chi_{\perp i,e}$ lie between 0.1 and 10 and are normally larger than $D_\perp$ by factors in the range of 2 to 5 [28]. In equation 2.83, $q_\perp^{elconv}$ is the *electron heat convection*

$$q_\perp^{elconv} = \frac{5}{2} T_e n v_\perp \tag{2.85}$$

and

$$q_\perp^{ionconv} = \frac{5}{2} T_i n v_\perp \tag{2.86}$$

is the *ion radial heat convection*. The *neutral heat convection* is given by

$$q_\perp^{neutrconv} = \frac{5}{2} T_0 n v_{0\perp}, \tag{2.87}$$

with T_0 the neutral temperature and $v_{0\perp}$ the average radial velocity of the neutral flux. Particularly at high plasma density the mfp for CX collisions is smaller than the ionization mfp and λ_n. Then in the SOL, $T_0 \approx T_i$, as a consequence of CX collisions with short mfp for the neutrals, and the perpendicular plasma outflux is balanced by a neutral influx,

$$nv_\perp = n_0 v_{0\perp}. \tag{2.88}$$

In the SOL convective region upstream these two fluxes would therefore be in approximate equilibrium, with no resulting net energy flux to the walls. A large perpendicular convective particle flux would thus not necessarily imply a strong net energy flux to the main chamber walls due to ion outflux. The *conducted neutral heat flux*

$$q_\perp^{cx} = -\kappa_{cx}\nabla_\perp T_i \tag{2.89}$$

is due mainly to CX collisions (random walk), with

$$\kappa_{cx} \approx n_0 \lambda_{cx}^2 \nu_{cx}, \tag{2.90}$$

where λ_{cx} is the neutral CX mfp and ν_{cx} the collisional frequency. This is an approximation, treating neutrals as a fluid, and is valid only if λ_{cx} is shorter than the temperature gradient length. It is used here only as an estimate. When simulating the neutral transport with a Monte-Carlo code that follows the trajectories of test neutrals in a plasma background, the heat transport from neutrals is automatically properly accounted for, if all the relevant reaction rate coefficients are included.

The complexity of energy transport makes it difficult to evaluate the dominant energy transport channel. By comparing experiment with simulations in which radial convective transport is assumed to increase with radius and in which $\chi_\perp$ is constant in space [42, 53, 54], it is found that at low density where diffusion dominates radial transport, cross-field power transport is mostly diffusive. Only after more than one density e-folding length (λ_n) does charge-exchange transport dominate. At high upstream densities, most of the power in the far SOL is transported by electron convection and CX collisions to the wall. If λ_n and λ_T are known and perpendicular power and particle

transport is assumed largely diffusive close to the separatrix, the cross-field power flux may be written

$$q_\perp^\epsilon = \sum_{e,i} \chi_{\perp_{e,i}} nkT_{e,i}/\lambda_{T_{e,i}} + \frac{5}{2} D_\perp n_e kT_e/\lambda_n. \tag{2.91}$$

In the separatrix vicinity, radial power transport is highest since the source of power is closest and less power has been lost in the parallel direction compared to regions further out. The temperatures of the SOL plasma are highest there too and due to the strong $\propto T^{5/2}$ dependence, parallel heat conduction (eqns. 2.35, 2.36), parallel heat transport generally dominantes radial heat transport. As a result it is found, e.g. for C-Mod [42], that only 20% to 25% of the power entering the SOL is transported to the wall, with the majority reaching the divertor volume. The divertor configuration can thus be non-ideal in terms of particle balance, leading to a high self-sustained wall flux in the SOL above the X-point, but appears to be ideal concerning power transport, where most of the power entering the SOL is carried in the parallel direction towards the divertor. Again this is related to the distributed nature of the particle source and the localised nature of the power source (i.e all from the core boundary).

2.5.6   Perpendicular transport of parallel momentum

With regard to pressure balance along flux tubes in the sheath and conduction limited regimes account must be taken of the magnitude and nature of perpendicular transport of parallel momentum. For further discussion and details of this rather complex issue, the interested reader is referred to [28]. In a simplified picture, in which diffusive cross-field transport is assumed diffusive, parallel momentum is transported across field lines by:

- perpendicular particle transport, in which particles carrying parallel momentum are momentum sources on a neighbouring field line and which may be written as $S_{mom, D_\perp} = mv_\parallel D_\perp n/\lambda_n^2$.

- *perpendicular shear stress* diffusing momentum $\propto \eta_\perp dv_\parallel/dr$ with $\eta_\perp \approx nmD_\perp$ being the *anomalous shear viscosity coefficient* [28,64] and giving a momentum source of

$$S_{mom,\eta_\perp} = v_\parallel \eta_\perp / \lambda_v^2,$$

with λ_v the e-folfing length for $v_\parallel$ It can be shown using simplifying assumptions on parallel particle transport that the ratio of the total momentum source (the sum of the above 2 terms) to total pressure is $\sim 25\%$. In the absence of ionization sources, recombination sinks or ion-neutral friction, it is thus usually assumed that total pressure is preserved along a field line.

2.6 Plasma-wall and neutral-wall interactions

When ions or neutrals strike a solid surface they may be

- absorbed and trapped by the surface they encounter

- reflected

- absorbed or adsorbed by the surface and released as a thermal particle with a velocity dependent on the surface temperature

- release surface material through chemical or physical sputtering and thus produce intrinsic impurities

- induce electron emission[3].

The first three process constitute the fuel recycling process and their net effect is represented by the parameter R_{global}. Backscattering is usually expressed in terms of particle and energy reflection coefficients R_N and R_E calculated using computer codes. Their values depend on the combination of projectile and target species and may be found in [65] and references therein. The TRIM database used by SOLPS5 is derived from these calculations [65, 66]. For the plasma species and wall materials concerned by this thesis, datasets are available for all projectile target combinations [65–67]. In general, implantation of projectiles into target materials increases with increasing impact energy, while reflection increases with increasing relative mass of the target material with respect to the projectile. Thermal re-emission usually occurs when the impact energy of the projectile is low ($< 10eV$). Indeed, for most plasma parameters considered in this thesis thermal re-emission of particles is the dominant recycling process. If surfaces are already saturated with deuterium (often the case for graphite walls), D^+ ions or D neutrals arriving there with low energies recombine with high probability and a D_2 molecule is re-emitted. This is by far the dominant release mechanism for recycled particles at divertor target plates in the high recycling and detached regimes when T_e is low.

---

[3]Electron emission is not discussed further here (see [28]).

Target/Projectile	D	He	C
Graphite, E_{th}	$30eV$	$29eV$	$42eV$

Table 2.2: *Threshold energy for physical sputtering for the projectile target combinations relevant to this thesis [28]*

2.6.1 Physical sputtering

Energetic ions or neutrals can transfer their momentum to the material surface and release target material if enough energy is transferred to overcome the surface binding energy E_B. For carbon, $E_B = 7.4eV$ [28]. An estimate of the threshold energy E_{th}, required to release a surface atom can be made assuming vertical impact of the projectile:

$$E_{th} = \frac{E_B}{\delta\left(1 - \delta\right)}, \tag{2.92}$$

with

$$\delta = \frac{4M_1 M_2}{\left(M_1 + M_2\right)^2} \tag{2.93}$$

where, M_1 and M_2 are the projectile and surface atom masses. The physical sputtering yield, namely the number of impurities released per incoming projectile, is usually calculated using the Roth-Bodansky formula [68]. It has been pointed out, however, that due to varying surface properties, such as roughness, experimental sputtering yield data can vary by up to a factor ~ 2 compared with the calculated values [28]. It should also be recalled that the sheath plasmas accelerates ions toward surfaces. As a result, even in low T_e plasmas physical sputtering can still be substantial (example: with $V_{sf} \sim 3.5eT_e$, He^{2+} ion energies at the wall exceed E_{th} of graphite for $T_e > 4.5eV$).

2.6.2 Chemical sputtering

Plasma-surface chemistry can also be responsible for significant impurity release: in the case of chemical affinity between projectile and surface. This is a particularly important mechanism in many modern tokamaks (such as TCV and JET) where graphite first wall

protection is used with hydrogenic plasma fuel. In this case, deuterium atoms can break inter-carbon bonds of the surface material to produce $C - H$ bonds that ultimately release hydrocarbons. For some time, there has been a substantial research effort directed towards quantifying the magnitude of the chemical yield for D on C in tokamaks. The most recent values for Y_{chem} may be found in [69] and references therein.

Reported yields usually lie between 1% and 5% but depend strongly on surface properties. For amorphous carbon layers resulting from re-deposition processes common in tokamak divertors, Y_{chem} might be as high as 10% [70]. The yield has been found to be dependent both on the impinging hydrogenic isotope [71] and on whether or not the projectile is an ion or a neutral, with ions resulting in higher yields [28]. In addition, Y_{chem} increases with surface temperature and is also dependent on the impinging flux, increasing with decreasing particle flux [68, 69, 72]. Chemical sputtering will be an important factor in the comparison between experiment and simulation for TCV to be presented in Chapter 5.

2.7 Volumetric atomic and molecular physics

2.7.1 Introduction

The low plasma temperatures in the high recycling and detached regimes mean that both atomic and molecular species may be present in abundance. Due to the multitude of reactions that atoms and molecules can undergo with the plasma their presence greatly increases the complexity of the SOL plasma.

2.7.2 Collision radiative model

In the density regime of the divertor plasmas considered in this thesis ($\approx 10^{19} m^{-3}$) multi-step excitation and de-excitation processes can be important. If excitations and de-excitations between different atomic or molecular levels are very fast processes compared with the timescales of interest in the numerical simulations, the population densities of excited molecular, atomic and ionic levels relax to a local population distribution. The time spans of interest in this work are those affecting the kinetic energy of a particle or the change of the type of species (e.g. ionization). In numerical simulations only representative samples of particle species are considered. In such a situation, while following the particle history of a test particle through a given background, each test particle represents a 'train' of excited particles. This means e.g. that if in any computational cell a certain particle density of test particles is obtained as a result of the simulation, these 'test' particles represent not only the ground state but also all excited particles by a fraction proportional to the population density of each level. Since each test particle represents for a series of real particles, including all excited states of that species, effective rates are sought which provide the rate of change to a different simulated species and which may themselves again be representative of a 'train' of particles.

If such rates are provided in the most simple situation by rate coefficients including only direct processes, then in the case of e.g. an ionization rate, the presence of excited atomic levels in the plasma has no effect and only processes from the ground state to

the ionized state are considered. Further complexity is added in the *corona model*, which takes into account intermediate excitation processes through collisions and spontaneous emission and is usually a good approximation for $n_e < 10^{18} m^{-3}$.

Over the past decades *collisional radiative models* (CRM) for atomic and molecular hydrogen have been continuously developed [73–76]. Such models account for

- excitation via electron impact,

- de-excitation via electron impact,

- de-excitation via spontaneous emission.

The resulting rate coefficients, $< \sigma v_{rel} > (n_e, T_e)$, with σ the cross-section and v_{rel} the relative velocities of the interacting species, can be strongly dependent on n_e for $T_e < 10eV$. Knowing the the velocity v of the test particle, the mean free path is readily calculated

$$\lambda = \frac{v}{< \sigma v_{rel} > n_e}. \tag{2.94}$$

### 2.7.3 Volumetric atomic and molecular processes

An overview of relevant volumetric processes for atomic and molecular species in a hydrogen (thus also deuterium) and helium edge plasma conditions is given in [77–81]. The most relevant inter-species volumetric processes can be categorized as follows:

- Electron impact ionization:
  $A + e \rightarrow A^+ + 2e,$

- Charge exchange (including a "truely" elastic component in case of symmetric reactions: $A = B$):
  $A + B^+ \rightarrow A^+ + B,$

- Three body recombination (or electron impact recombination EIR):
  $A^+ + e + e \rightarrow A + e,$

- Radiative (and di-electric, in case of He^+) recombination:

  $A^+ + e \rightarrow A + h\nu$,
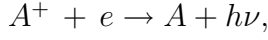
- Dissociation of molecules:

  $B + e \rightarrow C + D$, where B, C and D can also be ionized species.
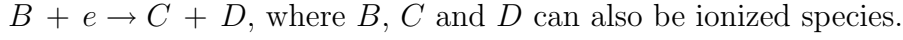
Molecular assisted recombination (MAR) via positive molecular ions B^+, is then, for example a combination of a charge exchange reaction followed by a dissociation process that does not result in ionization of the products:

$A^+ + B + e \rightarrow A + B^+ + e \rightarrow A + C + D$, where C and D must be neutral for recombination to occur. Such a process competes with these resulting in charged species C^+ and/or D^+, in which case molecular assisted dissociation (MAD, one charged product) or molecular assisted ionization (MAI, two charged products) would occur. Details of specific volumetric reactions used in the SOLPS5.0 simulations for this thesis will given in part II (see e.g. Tables 5.1 (p.142) and 5.3 (p.157)).

During detachment, processes leading to plasma recombination are of interest. In order to evaluate the contribution of these processes, the recombination time τ_{rec}, already mentioned earlier in this Chapter, is important:

$$\tau_{rec} = \frac{1}{\nu} = \left(<\sigma v_{rel}> n_e \right)^{-1}, \tag{2.95}$$

with ν the recombination frequency.

In addition, the databases, where possible, include information about the effective net energy loss (or gain) rate coefficients resulting from radiation losses during the excitation and de-excitation processes of each ionization event. The total cooling of the plasma, P_{cool} for each ionization event is then composed of the thermal energy transformed into potential energy (e.g. $13.6eV$ for H) and P_{rad}. For three body recombination net energy transfer to the electrons is also possible if the kinetic energy transferred to an electron is larger than the sum of radiation losses (in the course of deexcitation processes) and energy removal from the background electrons (since one electron has been effectively removed).

2.8 Simple 'Two-Point Model', conduction limited heat flux and collisionality

In what follows the discussion will be limited to divertor SOL's. As density increases upstream, a point is reached at which the SOL transits from the sheath limited to the conduction limited regime. The main particle source moves from the core plasma to an area in front of the targets due to increased recycling, power transport via convection decreases and conduction determines the parallel energy transport over much of the SOL. In order to construct a set of simple analytic relationships linking the upstream and target parameters in this regime, it is usually assumed that:

1. Ion-neutral friction is negligible along the SOL.

2. Radiation losses along the SOL are negligible compared to P_{SOL}.

3. All neutrals recycling from the targets are immediately ionized in front of the targets on the same flux tube as the original impinging ions.

4. The only parallel plasma flow is that between the ionization zone and the target (eqn. 2.48), $v = 0$ upstream and $v = c_s$ at the target sheath entrance.

5. No cross-field particle and momentum transport.

6. Surfaces are the only particle sinks, no volumetric recombination.

It is then possible to restrict the analysis to a single, 'independent' flux tube. Momentum and energy along each flux tube are conserved giving

$$p_t^{tot} = n_t(2kT_t + mc_s^2) = 2n_ukT_u = p_u^{tot}; \; T_e = T_i, \tag{2.96}$$

. with p_t^{tot}, p_u^{tot} being the total pressure at the target and upstream respectively.

A zero-dimensional modell of the SOL based on the $1D$ conservation equations and using the above simplifications constitutes what has become known as 'Two-Point' model [82]. This model describes plasma parameters not as a function of parallel distance along

the SOL but simply provides a connection between upstream and target. If, for example, n_u and $q_\parallel$ are supplied as control parameters, the model yields three equations for three unknowns , T_t, n_t, T_u. Since $v_\parallel = 0$ along most of the SOL in the conduction limited regime, power is purely conducted. Assuming ion heat conduction to be small compared with its electron counterpart, integrating equation 2.36 from 0 to L_c and making use of eqns. 2.57 and 2.96 leads to the following equations of the Two-Point-Model [28]

$$2n_t T_t = n_u T_u \tag{2.97}$$

$$T_u^{7/2} = T_t^{7/2} + \frac{7}{2}\frac{q_\parallel L_c}{\kappa_{0e}} \tag{2.98}$$

$$q_\parallel = \gamma n_t k T_t c_s. \tag{2.99}$$

These equations can be readily solved, invoking simplifying assumptions [28] to provide expressions for the physical quantities of interest

$$T_u \simeq \left(\frac{7}{2}\frac{q_\parallel L_c}{\kappa_{0e}}\right)^{2/7} \text{with} \, T\,[eV]\,, T_u^{7/2} \gg T_t^{7/2} \tag{2.100}$$

$$T_t \propto q_\parallel^{10/7} L_c^{-4/7} n_u^{-2} \tag{2.101}$$

$$n_t \propto n_u^3 q_\parallel^{-8/7} L_c^{6/7} \tag{2.102}$$

$$\Gamma_t \propto n_u^2 q_\parallel^{-3/7} L_c^{4/7} \tag{2.103}$$

One of the assumptions used in deriving the equations is that all the power enters the SOL at the upstream location whilst in reality, of course, the power enters the SOL everywhere along the LCFS. Adopting the ansatz of uniform power flux crossing the entire separatrix decreases the temperature exponent in eqn. 2.98 to 7/4 and results in T_u being 20% lower.

Several consequences of the above equations are of note:

- T_t increases faster than $q_\parallel$.

- T_t decreases only weakly with increasing connection length.

- T_t decreases strongly with upstream density n_u.

- Γ_t increases with decreasing $q_\parallel$.

- T_u is a very robust quantity.

With increasing n_u (and hence main plasma density), T_t decreases, collisionality increases and strong parallel temperature gradients arise in order to exhaust (conduct) P_{SOL}. The heat flux is now limited by the heat that can be conducted along the SOL (hence the term *conduction limited regime*), but the total heat flux reaching the divertor targets has not been reduced. Since the particle flux onto the targets increases with n_u^2 (eqn. 2.103), recycling increases strongly and the SOL particle balance is self-sustained by the target particle source (*high recycling regime*). In this case, T_t can reach very low levels ($\sim$ few eV), such that physical sputtering (see Section 2.6.1) at the targets can be significantly reduced or even eliminated. This is due both to the low ion temperatures in this regime and the fact that the sheath potential (which accelerates the ions) is a strong function of T_e (eqn. 2.52). If $T_i \neq T_i$ a condition for strong parallel T gradients to exist may be written in terms of SOL collisionality (eqns. 2.21, 2.22) [28]:

$$\nu_{SOL,e}^* \geq 25 \, \text{and} \, \nu_{SOL,i}^* \geq 2, \tag{2.104}$$

while for $T_e = T_i$

$$\nu_{SOL}^* \geq 50. \tag{2.105}$$

It can also be further shown [33] that for the plasma to be in the conduction limited regime, ν_{SOL}^* should fall within the following approximae range:

$$10 \geq \nu_{SOL}^* \leq 85. \tag{2.106}$$

2.8.1 Corrections to the Two-Point Model using loss factors

A divertor SOL in the conduction limited regime is characterized by high recycling and, in a tokamak with carbon targets, significant impurity production through chemical sputtering (Section 2.6.2). When the recycled neutrals and impurities are ionized in the SOL, the energy balance can be strongly affected. If sufficiently abundant, neutrals can also result in large momentum losses through elastic and inelastic ion-neutral collisions. In

order to account for these volumetric losses, the Two-Point Model can be extended by introducing corrections in the form of *loss factors*, f.

For volumetric charge-exchange and radiation losses:

$$q_{rad} + q_{CX} \equiv f_{power} q_\parallel, \tag{2.107}$$

so that power loss in the SOL increases with increasing f_{power}. Momentum losses can be expressed in terms of the total static target and upstream pressures, $p_{t,u}$ and a momentum loss factor, f_{mom},

$$p_t \equiv f_{mom} \frac{1}{2} p_u, \tag{2.108}$$

so that pressure loss *increases* with *decreasing* f_{mom}. As will be seen shortly, temperature gradients are reduced if some power is convected instead of being conducted along the SOL. This is expressed in terms of the *conduction factor*

$$q_{\parallel\, cond} \equiv f_{cond} q_\parallel^\epsilon, \tag{2.109}$$

where the conducted fraction *increases* with *increasing* f_{cond}. These correction factors lead to the following relations [28], which will be of use in Section 2.9 when discussing the conditions for achievement of detachment:

$$T_t \quad \propto \quad \frac{(1 - f_{power})^2}{f_{mom}^2 f_{cond}^{4/7}} \tag{2.110}$$

$$T_u / T_t \quad \propto \quad \frac{f_{cond}^{6/7} f_{mom}^2}{(1 - f_{power})^2} \tag{2.111}$$

$$n_t \quad \propto \quad \frac{f_{mom}^3 f_{cond}^{6/7}}{(1 - f_{power})^2} \tag{2.112}$$

$$\Gamma_t \quad \propto \quad \frac{f_{mom}^2 f_{cond}^{4/7}}{1 - f_{power}} \tag{2.113}$$

These equations demonstrate that the interdependency of the various quantities of interest (T_u, T_t, n_t etc.) becomes very complex when volumetric processes are even qualitatively accounted for. Whilst the inclusion of the energy loss due to hydrogenic recycling (assuming that neutrals are re-ionized in the same flux tube as that of the impinging ions) can still be treated analytically (see Section 5.5 in ref. [28]), and hence provide insight

into the stability of solutions (e.g. of n_t) for the SOL, the inclusion of impurities or, in a Helium plasma, of two main ion species He^+ and He^{2+} is beyond any simple analysis.

In the case of carbon targets, intrinsic impurity production provides a clear example. As n_u increases, T_t decreases, physical sputtering becomes less likely and f_{power} decreases, decreasing Γ_t but again increasing T_t. With increasing Γ_t, however, chemical sputtering increases (since $\Gamma_{chem}^{sput} \propto \Gamma_t \propto n_u^2$) again increasing f_{power}. This complexity is enhanced by the inclusion of neutral recycling, its effect on f_{mom}, where the neutrals are ionized and how this again affects f_{cond}. The volumetric loss process is inherently two or even three dimensional and can only realistically be treated numerically, using basic analytic theory as a guide.

2.8.2 Comments on the high recycling divertor and main chamber recycling

In the absence of drifts ideally the flux upstream is zero in the conduction limited regime. In reality some flux is measured at the entrance to the divertor, such that $\Gamma_{\parallel u} \neq 0$, with the particle flux entering being lower than that reaching the divertor targets. The ratio $\Gamma_t / \Gamma_{\parallel u}$ is often also wrongly called *flux amplification*. But this ratio has no effect on Γ_t since this is given through the conservation equations and occurs naturally, independent of Γ_u [45]. In contrast, the mechanism by which an 'increased' flux may arise at the target plates must be distinguished from the increase of flux toward the walls leading to the *main chamber recycling regime*. This is a result of radial transport mechanisms and is not related, for example, to pressure balance but mainly to particle flux balance resulting from an equilibrium of volumetric particle sources, ion flux and neutral recycling not driven by pressure balance (transport across flux tubes).

In the idealized picture discussed thus far, the SOL particle balance is provided purely by recycling neutrals in an ionization zone in front of the targets. Main chamber recycling is an experimentally observed phenomenon (at least for small scale machines $R \leq 1.5m$) and results in a particle source for the upstream plasma. Stangeby [45] has described a

simple model in which high recycling at the target plates and main chamber recycling are decoupled particle circuits. The particle flux onto the targets is fully balanced and accounted for by neutrals recycling there and the radial outflow to the walls in the main chamber is balanced by a neutral influx from the walls such that the particle circuits close consistently.

2.9 Divertor detachment

2.9.1 Introduction

Whilst the upstream parameters n_u and T_u are ideally determined largely by particle and energy fluxes into the SOL from the confined region, equations 2.110 to 2.113 show that the target parameters can be strongly influenced by the value of the loss factors f_{mom}, f_{power} and f_{cond}. In the conduction limited regime, the total power deposited on the target, including the flux of potential energy transported by the charge carriers, can be reduced to $\sim 75\%$ of P_{SOL}. But the particle flux remains rather high ($\propto n_u^2$). In order to reduce Γ_t (and thus the total power flux onto the target), but still maintain high neutral pressures (which will permit the exhaust of He ash in a reactor), the divertor must be operated in the *detached regime.*

Although complete understanding of the detachment phenomena has not yet been achieved, it is believed that the main mechanisms for its onset are known [11, 28, 83]. Quantitative understanding of the detached state awaits clarification of the role of numerous processes such as $\vec{E} \times \vec{B}$ and diamagnetic drifts or a number of atomic and molecular physics aspects. Part of the reason for the incomplete picture is the complexity and sensitivity of the determining factors that lead to a reduction of Γ_t. They are in some cases strongly nonlinear phenomena and can vary in their relative importance from one experiment to another. Evaluation of the relative contribution is often hindered by incomplete or even minimal diagnostic coverage and thus the lack of constraints for numerical modeling of the main SOL and divertor volumes. A quantitative understanding of divertor detachment can only really be obtained through the use of numerical codes including all the relevant physics in combination with sophisticated experimental diagnostics.

In principle, detachment at any point on the target means that no particle or energy flux reaches that point. It may be characterized by two aspects:

1. Reduction of total plasma pressure along a magnetic flux tube

2. Decrease (disappearance) of the ion particle flux.

Detachment usually begins when n_u is increased beyond values encountered for the high recycling regime. At JET, for example, it is often found that [33]

$$\nu_{SOL}^* > 85, \tag{2.114}$$

for it to occur. Under these conditions, temperature gradients along the SOL are still rather strong and $T_i \approx T_e$ in the divertor volume. In experiment the onset of detachment often occurs at positions along the target where L_c and thus ν_{SOL}^* is highest. Since L_c is largest near the separatrix, detachment almost always occurs first in this region. Detachment can also be produced by injection of seed impurities, even for relatively low n_u. The ITER divertor is designed to operate in the 'partially' detached state in which the strike point location (highest L_c) where the highest parallel power flux is carried is detached, but in which a significant part of the main SOL remains attached [9]. Such an operating condition is judged desirable from experience in current experiments which often show that complete detachment is accompanied by strong radiation instability at the X-point (MARFE) and subsequent plasma disruption in L-mode or transition to L-mode for H-mode plasmas.

2.9.2   Reduction of measured particle flux

The most readily measurable signature of divertor detachment, is the reduction of target flux. To quantify detachment the notion of degree of detachment (DOD) has been introduced [11, 28]

$$DOD \equiv \Gamma_t^{calc}/\Gamma_t^{meas} \equiv \frac{C\bar{n}_e^2}{\Gamma_t}, \tag{2.115}$$

with C a constant, Γ_t^{meas}, the measured target flux and Γ_t^{calc} that estimated from the Two-Point model. Equation 2.115 assumes that $n_u \propto \bar{n}_e$ (Section 2.1.4). Experimentally, the transition to detachment is often observed by a 'roll over' of $\Gamma_t(\bar{n}_e)$, with an increase of Γ_t during high recycling and then a fast reduction as $\bar{n}_e$ increases further. This behavior was first documented on ASDEX in 1983 [84]. Indicative DOD values as criteria for partial and total detachment (on JET) are summarized in Table 2.3 [11]. The extent to which,

Detachment state	DOD^{peak}	$DOD^{integral}$
Partial detachment	> 2	< 10
Total detachment	> 2	> 10

Table 2.3: *Criteria for characterization of detachment on JET* [11]

for example, the ITER divertor can be operated in the partially detached state represents an important control problem which cannot be easily addressed by experiments in current machines, so that the momentum loss factor is an important factor in determining Γ_t and will dominate provided f_{cond} is very small. The influence of f_{power} is discussed later. The ion fluid momentum can be reduced (and hence detachment approached) by two principal processes:

1. Elastic and inelastic charge-exchange collisions, provided the neutrals escape the flux tube without being re-ionized (at least not in the same flux tube),

2. Particle removal by ion-electron recombination.

Both processes are inefficient if the temperature in the divertor is above a certain threshold. To first order, this threshold can be estimated as $T_e \sim 5eV$ since for higher plasma temperature in front of the target electron impact ionization of neutrals is high and they cannot escape the divertor volume, taking with them the ion energy.

2.9.2.1 Charge-exchange momentum removal

For CX reactions to remove momentum the mfp, λ_{CX}, must be longer than the characteristic SOL width in the divertor. In a so called *gas target* divertor [28,85], the larger the number, N of CX collisions each neutral can undergo before escaping the divertor volume or being re-ionized, the more momentum is removed, decreasing Γ_t. For net momentum removal to occur, it is important that prior to a collision the neutral was not traveling in the same direction as the ion and that after a collision it can either deposit the collected momentum on a material surface or transfer it to other neutrals which ultimately reach

the walls. Momentum removal depends strongly on the degree of divertor volume 'closure' and on the temperature and density profiles in the divertor. In general, CX processes become strong plasma momentum sinks when $T \approx 2eV$ over a sufficiently large volume.

Assuming that plasma is 'lost' to the target at a rate Γ_{se}, the average *dwell time* of a plasma ion in the divertor is [85]

$$\tau_{dwell} = \frac{\bar{n}_i L_{cushion}}{\Gamma_{se}}, . \tag{2.116}$$

and is an approximation for the time that an ion resides in the region of length $L_{cushion}$ between the ionization front and the target plate, assuming an average ion density, $\bar{n}_i$ along $L_{cushion}$ and a flux equal to Γ_{se} at the sheath entrance (see Section 2.4). In providing an estimate of τ_{dwell}, eqn. 2.116 implicitly assumes that the velocity across the divertor is equal to the velocity at the sheath entrance. Plasma entering the divertor volume can be accelerated to high parallel flow velocities by parallel gradients of static electron and ion pressures and through volumetric ionization sources (eqns. 2.48 and 2.31). Charge-exchange processes increase τ_{dwell} in analogy to a 'plug in a drain', 'slowing' down the plasma flow that has been previously accelerated in the ionization zone. It appears to be difficult, however, to explain the large experimentally observed reductions in Γ_t only by invoking "truely" elastic and inelastic charge exchange losses of the type $X^+ + X \rightarrow X + X^+$ [86].

2.9.2.2   Volumetric plasma recombination

The second mechanism leading to a reduction of Γ_t is net ion removal through volumetric recombination processes of which two types may be broadly distinguished: *Electron ion recombination* (EIR) and *molecular assisted recombination* (MAR). Both are described in more detail in Sections 2.7 and Part II of this thesis.

For volumetric recombination to occur $\tau_{rec} > \tau_{dwell}$. Elastic and inelastic CX events not only therefore reduce f_{mom} directly, but also increase the probability for EIR and MAR, providing a further indirect reduction of f_{mom}. Although EIR has been identified as a major contributor to the detachment process [87], MAR has not been clearly shown

to play an important role in the onset of divertor detachment, at least in tokamaks [88]. It has been observed to occur, however, in divertor plasma simulators [89]. A number of authors (e.q. Krasheninnikov [19,86,90], Pigarov [77] or Janev [78,79]) have nevertheless suggested an important potential role for MAR in divertor detachment. Concerning recombination processes and assuming that $\tau_{rec} > \tau_{dwell}$ in each case, it useful to summarize the conditions under which each occurs (for D plasmas):

- EIR can be important if $T_e < 1.5eV$ if n_e and τ_{dwell} are sufficiently large,

- MAR via D_2^+ can be important if n_{D_2} is high and $T \approx 2eV$

- MAR via C_xD_y can be important for up to $T_e < 8eV$, especially if $x > 2$.

2.9.2.3 Signature for volumetric recombination

An increase in the ratio of emission of line radiation from highly excited atomic levels relative to low excitation states (for example in the case of the deuterium Balmer lines D_γ/D_α) has been identified as a clear indication for the presence of recombination processes [91]. It can be used as method for calculating the recombination rate in the divertor volume [92]. Using Deuterium as a main plasma species, a number of tokamak experiments have observed a strong correlation in the increase of D_γ/D_α with decreasing Γ_t (e.q. JET [91], ASDEX-U [93], C-MOD [94] and DIII-D [95]).

2.9.3   Divertor geometry and neutral pressure

Since neutrals are necessary for the dissipation of plasma momentum to the walls, high neutral densities are beneficial for detachment to occur. A closed divertor structure as shown in figure 1.4 (Section 2) is therefore of advantage for the early onset of detachment. If the divertor throat is deep enough, the volumetric conductance for neutrals can be small enough by itself to prevent neutrals from escaping the divertor volume. The presence of plasma can, through CX collisions, further decrease the probability of neutral escape. This is also known as plasma *plugging*.

As more momentum is transferred from the plasma to the neutrals, the neutral pressure in the divertor volume increases [96]. The compression ratio, defined as

$$p_{compr} = p_n^{div}/p_n^u, \tag{2.117}$$

with p_n^{div} the neutral pressure in the divertor and p_n^u the neutral pressure upstream close to the main chamber wall, is often used as a measure of the degree of neutral plugging. At the onset of detachment, values of p_{compr} in the range $\sim 50 - 100$ have been observed in a number of divertor tokamaks [26, 96]. Both the positioning of target surfaces and the magnetic geometry inside the divertor volume influence the overall distribution of neutrals and thus the general divertor performance [14, 97].

2.9.3.1 Volumetric power removal

Equation 2.113 shows that an increase of f_{power} increases Γ_t. Pure removal of power cannot therefore decrease Γ_t. Volumetric momentum removal and power exhaust are two competing processes, the extent to which f_{mom} plays a role itself depends strongly on f_{power} further upstream.

In D plasmas divertor detachment begins when the plasma temperature in the divertor volume has decreased to values below 5eV. In machines containing carbon surfaces, it is usually found that strong $CIII$ and CIV line emission occurs close to the X-point, implying $T_e \sim 10 - 15eV$ in this region. The largest amount of volumetric power exhaust is therefore generally provided by impurity radiation, which in present day tokamaks is due to the use of carbon first wall materials [98, 99]. In machines with substantial ion target fluxes, line radiation from recycling deuterium in the region between the ionization front and the target plates can also be a large contributor to volumetric power removal.

If the power entering the divertor is too low for re-ionization of recycling neutrals to occur, then it is possible for the target particle flux to decrease suddenly, especially if the neutrals are re-ionized inside the confined region and not in the main chamber SOL. In such a situation, however, the power and particle flux into the SOL are also modified, changing the upstream conditions such that pressure may already fall upstream. This

power detachment as it is sometimes called, is of no practical relevance for a burning plasma. Since the divertor has by definition become transparent and ceases to fulfill its role as an area of high neutral pressure where the pumping can occur and the plasma-material interaction be localized.

2.10 Influence of Drifts on the SOL plasma

In 2-D SOL plasma codes, it is usually assumed that power uniformly crosses the poloidal boundary at which the power flux is set. Even if this were the case, in both experiment and simulations, power and particle influxes from the core region into the SOL are asymmetric. One obvious reason for such asymmetry originates from the toroidal geometry which provides for a higher surface area on the LFS compared with the HFS. A second, lesser effect relates to the compression of flux surfaces on the LFS due to the Shafranov shift [5] which would favour enhanced cross-field transport there if the latter were proportional to radial gradients. Finally, the tendency for enhanced (ballooning like) transport (Section 2.5.3) on the LFS deposits more particles and energy there. All of these effects are expected to enhance the transfer of power and particles into the LFS SOL, leading to asymmetric power deposition favouring the outer divertor.

In recent years, an increasing number of measurements on several tokamaks [100–105] have revealed the existence of strong particle flows with high velocities up to $M \sim 0.5$ at some locations in the main SOL. It is also usually observed that the upstream parallel Mach number, $M_{\parallel u}$, decreases with rising density. In most cases, these SOL flows change direction upon reversal of B_Φ. The asymmetries usually observed between the inner and outer divertor plasmas in SNL discharges are also modified by field reversal [103]. It is thought that one of the main driving mechanisms both for SOL flows and divertor asymmeteries are (neo-) classical drifts.

Edge codes are being increasingly used with drift terms activated to simulate SOL flows. In general, experimentally observed tendencies can be reproduced, but in the majority of cases, the observed magnitude of the parallel particle flows is usually far higher than simulations can predict [101, 105]. Some of the causes of divertor asymmetries (for example the difference of power flux into the divertors due to geometrical effects mentioned above), are accounted for in $2D$ SOL fluid codes.

It is not yet clear if the major SOL fluid codes (EDGE2D, SOLPS5, UEDGE) have all the drift related terms properly implemented, nor have full code-code benchmarks yet

been performed with drifts included. Ongoing code comparison studies at JET (EDGE2D-SOLPS5) have highlighted important differences, for example, in how drift terms are implemented in the core regions. In addition, if drift terms are included in simulations, these often become numerically very unstable, with the result that it is far from being a 'standard' application to activate them in code edge plasma modeling. Nevertheless, progress is being made [105,106] and there is an increasing effort toward code benchmarking. This is particularly important for ITER divertor simulations, which have still not been attempted with drift terms activated.

The emphasis in this thesis has been on the investigation of the effects of atomic and molecular processes and cross-field transport on detachment. Some attempts have been made to study the influence of drifts in the code but have met with little success due to numerical instability. Only at the time of writing has some progress begun to be made elsewhere by expert SOLPS5 users [106]. In what follows, some aspects of drifts and their possible influence on detachment will be outlined for later use in discussing results from TCV in Part II. This discussion does not distinguish between the origin of each drift with respect to the guiding center or fluid picture. For a much more complete description of drifts and their effects on the SOL and divertor plasma, an extensive literature source exists (see [28, 107–109] and references therein).

2.10.1 Definitions

The velocity due to $\vec{E} \times \vec{B}$ drifts is

$$\vec{v}_{E \times B} = \frac{\vec{E} \times \vec{B}}{B^2} \tag{2.118}$$

and is charge independent. The ∇B velocity (guiding center drift) is defined as

$$v_{\nabla B} = \frac{v_\perp^{gyro} m}{2eB^3} \vec{B} \times \nabla B, \tag{2.119}$$

with $v_\perp^{gyro}$ the gyro-velocity (positive charge for ions, negative for electrons). In the poloidal plane, if B_Φ ($\propto 1/R$) is in the clockwise direction (viewed from the top of the torus) then ∇B is inward (right to left) and $v_{\nabla B}^{ion}$ is downward. This is known commonly

as the 'forward' or normal field direction and is the standard field direction for most tokamaks. For anticlockwise B_Φ, all the above directions also reverse and this is known as the 'reversed' field direction. This is the standard operating mode in TCV, in contrast to most tokamaks.

The ohmic current $I = I_\Phi = I_\Omega$ is a consequence of the applied electric field, E_Ω induced by the current transformer of the solenoid. The toroidal component of E_Ω causes an ion drift toward the inner target for forward field and toward the outer target for reversed field, independent of the relative directions of $\vec{B}_\Phi$ and $\vec{I}_\Omega$. Reversing $\vec{B}$ without simultaneously reversing $\vec{I}_\Omega$ switches the magnetic helicity so that protection tiles or diagnostics (e.g. Langmuir probes) will not function if they are not designed for symmetric operation.

In the following sections a D plasma is assumed with singly charged ions. For He, all terms including the particle charge must be modified appropriately to account for doubly charged helium ions.

2.10.2   Poloidal $\vec{E} \times \vec{B}$ drifts: $\vec{E}_r \times \vec{B}$

Poloidal $\vec{E} \times \vec{B}$ drifts are driven by radial electric fields, themselves a consequence of the presence of radial temperature gradients caused by parallel losses on open field lines due to the presence of the sheath (Section 2.4). With $V_{plasma} = 0$ at the wall, $V_{plasma}(r) \approx 3kT_e(r)/e$ and $E_r \equiv -\delta V/\delta r$, the SOL radial electric field is

$$E_r \approx \frac{3kT_e}{e\lambda_{T_e}}. \tag{2.120}$$

The electric field results in a drift velocity, the major component of which is in the poloidal direction, see Fig. 2.5(a). The effect on pressure asymmetries due to this drift can be substantial and may have a direct effect on target parameters. In reversed field the direction of the drift is from outside to inside in the SOL and from inside to the outside in the private flux region. Once a steady state has been obtained at the two targets (with closed particle circuits) and an asymmetry established, the pressure differences in the target vicinity are balanced by a return flow, observable along the main SOL.
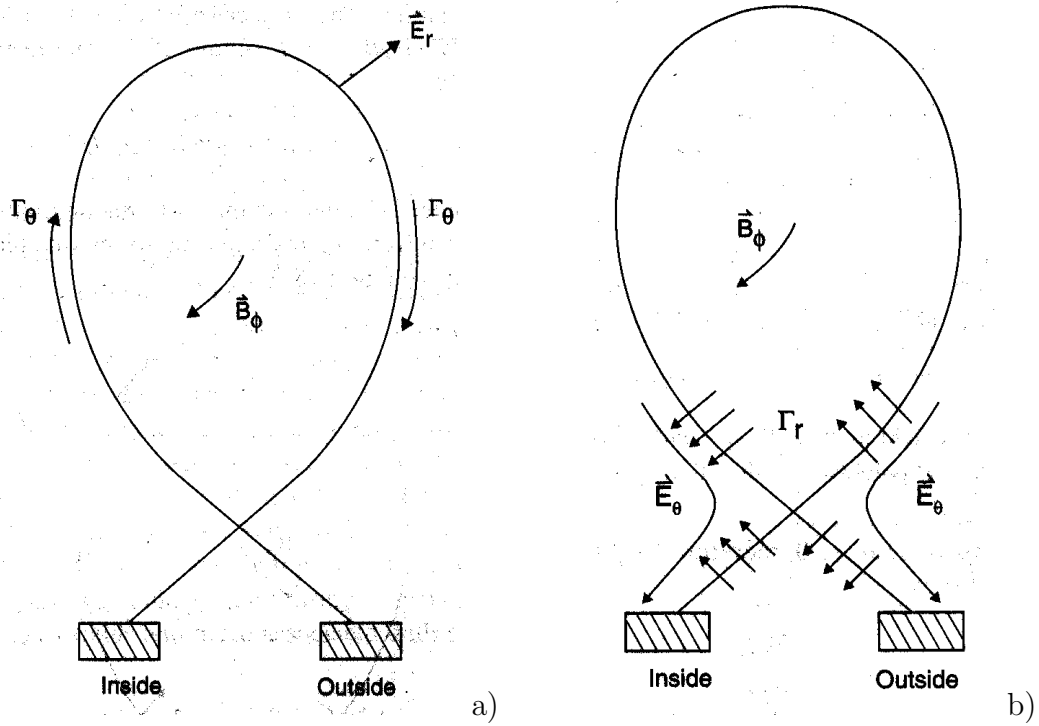
Figure 2.5: *Direction of fluxes in forward field due to drifts: (a) poloidal flux as a result of the $\vec{E}_r \times \vec{B}$ drift, (b) radial flux as a result of the $\vec{E}_\theta \times \vec{B}$ drift (from [28]).*

2.10.3 Radial $\vec{E} \times \vec{B}$ drifts: $\vec{E}_\theta \times \vec{B}$

Parallel field temperature gradients necessarily result in poloidal temperature gradients and thus a poloidal electric field

$$E_\theta = -\frac{1}{e}\nabla_\theta T \qquad (2.121)$$

which can be estimated knowing $\nabla_\Theta T$, usually strongest around the X-point (an example for TCV can be found in Fig. 5.56). This poloidal electric field drives a radial velocity, the direction of which is shown in Fig. 2.5(b) for forward field. The direction reverses in reversed field. Strong $\vec{E}_\theta \times \vec{B}$ fluxes have been measured in the PFR of DIII-D [100]. This radial drift leads to an increased pressure in the outer SOL and drives a parallel 'return' flow along $\vec{B}$ from the outer SOL along the top of the machine to the inner SOL. Assuming that re-ionization of neutrals occurs close to the divertor targets and that there is no strong interaction of the drift circuit with the recycling flux circuit, this drift flux

closes before the target plates are reached.

2.10.4 Diamagnetic drifts

Diamagnetic drifts (replacing guiding center ∇B-drifts in the fluid picture) are a result of pressure gradients. Because the ∇p force is charge independent, the drift itself is charge dependent

$$v_{\nabla p} = \frac{\vec{B} \times \nabla p}{enB^2}.$$
(2.122)

These drifts are largely divergence free, forming approximately closed circuits in the divertor and not driving fluxes onto target surfaces. The diamagnetic drifts close through the magnetic pre-sheath along both targets, not influencing the Bohm-Chodura criterion. Due to their charge dependence, these drifts produce currents $j = e(\Gamma^i - \Gamma^e)$. Diamagnetic radial and poloidal currents close inside the plasma and do not reach the target surfaces.

2.10.5 Pfirsch-Schlüter flows

The non-divergence free components (due to $B_\Phi \propto 1/R$) of both the diamagnetic and the poloidal $\vec{E}_r \times \vec{B}$ drifts contribute to the velocity of the ion Pfirsch-Schlüter flow, which reverses its direction with magnetic field reversal [110]

$$v_\parallel^{PS} = 2q \cos\theta \left(\vec{E}_r - \frac{\nabla_r p}{en} \right) \times \frac{\vec{B}}{B^2},$$
(2.123)

where the angle θ is measured from the outer midplane. The velocity is zero at the top and the bottom of the machine and highest at the inner and outer midplane. For reversed field, the flow resulting from this velocity is from the inside to the outside, clockwise in the poloidal plane. The PS flows are weaker inside the LCFS since E_r and $-\nabla p$ are in the opposite direction, but reinforce in the SOL where they are in the same direction.

2.10.6 The influence of drifts on particle and power fluxes

The distribution of particle flows driven by drifts and other mechanisms is known to be much more complex than that of the power flows. Whilst power sources are located only

in the core plasma, particle sources are distributed throughout the SOL, in the divertors and even to some extent inside the core plasma. Unlike particles, power is also very different in that it does not recycle at surfaces. Recent EDGE2D code simulations have successfully reproduced the in/out power asymmetries observed in the JET divertor for forward and reversed field [111, 112]. These asymmetries have also been found to scale as expected on the basis of $\vec{E} \times \vec{B}$ flows [103, 111]. In contrast, neither the measured SOL particle flows nor the particle recycling asymmetries can be successfully matched by the simulations.

In order to compare and estimate the magnitude of the parallel particle flows and fluxes in the sheath-limited and conduction-limited regimes, Table 2.4 summarizes (using estimates from [28, 108, 109]) the parallel, $\Gamma_\parallel$ and radial, Γ_r fluxes and the total flow, Φ_θ, per unit toroidal length at the midplane.

In the sheath-limited regime the poloidal drift is expected to dominate particle flow in the SOL, whilst in the conduction-limited regime, the poloidal drift is likely to be more important. Both the poloidal drift and the PS flux depend strongly on radial gradient lengths. With increasing density, radial pressure profiles are observed to flatten in the SOL and these drift fluxes are reduced. Only numerical simulations will ultimately be able to provide a complete picture of drift flows and their consequences for the divertor.

In the context of this thesis and particularly in the light of the discussion of TCV detachment in Section 5.2.2, the most important issue is how the drifts might influence divertor asymmetries and hence the onset of detachment. Unfortunately, the situation is far from clear, both in theory and experiment [109]. It is, however, recognized that in medium to high density conditions and particularly in the relatively low power L-mode discharges discussed in this work, the radial $\vec{E} \times \vec{B}$ is in the right direction to explain a number but not all experimental observations. These are conditions in which parallel temperature gradients develop most readily leading, as shown in Section 2.10.3, to a net radial flux. For TCV, where reversed field is the standard operating direction, the radial drift will bring more plasma particles to the outer divertor. This increased supply of particles will promote a higher level of local recycling, increasing energy losses

	$\vec{E}_r \times \vec{B}$	$\vec{E}_\theta \times \vec{B}$	Pfirsch-Schlüter
SL Γ_r	/	$(B/B_\theta)nkT_e/(2eLB)$	$n\left[\left(\vec{E}_r - \frac{\nabla_r p}{en}\right) \times \frac{\vec{B}}{B^2}\right]$
SL $\Gamma_\parallel^{mid}$	return: $n\frac{E_r}{B_\theta}$	neglected since $\Phi_\theta > \Phi_r$	$\sim 2q\frac{nkT}{e\lambda_{SOL}B}$
SL $\Phi\,[m^{-1}toroidal]$	$\Phi_\theta \approx -\frac{3nkT_e}{eB}$	$\Phi_r \approx \frac{nkT_e}{2eB}$	/
CL Γ_r	/	$(B/B_\theta)nk\nabla_\theta(T_{eu})/(eB)$	$n\left[\left(\vec{E}_r - \frac{\nabla_r p}{en}\right) \times \frac{\vec{B}}{B^2}\right]$
CL $\Gamma_\parallel^{mid}$	return: $n\frac{E_r}{B_\theta}$	$nv_\parallel = -\frac{nkT}{eB_\theta\lambda_{SOL}}$	$\sim 2q\frac{nkT}{e\lambda_{SOL}B}$
CL $\Phi\,[m^{-1}toroidal]$	$\Phi_\theta \approx -\frac{n_{eu}kT_{eu}^{sep}}{eB}$ with $n_{eu} \approx 0.5n_u$	$\Phi_r \approx \frac{nkT_{eu}^{sep}}{eB}$ with $n \approx \bar{n}_{LCFS} \gg n_u$	/

Table 2.4: *Particle fluxes: Summary of the related expressions for the radial drift flux Γ_r, the parallel (return) flux $\Gamma_\parallel$ and the total flow per unit toroidal length Φ, where r denotes the radial flow due to $\vec{E}_r \times \vec{B}$ and θ the poloidal flow due to $\vec{E}_\theta \times \vec{B}$. SL and CL denote respectively the sheath limited regime with $\nabla_\parallel T \approx 0$ and the conduction limited regime with $T_{eu} \gg T_t$. The table gives approximate values for these quantities, using λ_{SOL} as a typical SOL width. Outward radial velocities are positive. Parallel velocities are positive from the inner target to the outer target over the top of the machine. The quantities given are for reversed field (ion ∇B drift 'up') and change sign in forward field. To compare the magnitude of flows compare absolute values of Φ independent of the index.*

and in a deuterium plasma, the production of and hence radiation from impurities. This positive feedback mechanism might be expected to provoke an earlier onset of detachment compared with forward field for which the radial drift reverses direction, driving particle fluxes preferentially to the inner divertor. Ultimately, it is only through self-consistent code runs including all the relevant physics (drifts, geometry, plasma-material interaction, neutral dynamics) that the full impact of drifts on divertor asymmetries can be examined in combination with experiment. In the absence of such simulations, Section 5.2.2 will argue on the basis of experimental data alone that although drifts undoubtedly play a role, they are not the determining factor causing anomalous detachment in TCV.

Chapter 3

Numerical tools

Two-dimensional edge plasma modeling has been for many years a standard tool for interpretative and predictive studies of the tokamak SOL [113]. Nevertheless, the numerical codes are not simple in their use and can be tremendously CPU intensive. Often, the lack of user-friendly interfaces originates in the complexity of the physics involved in the SOL and the multitude of 'knobs' at the user's disposal. The high CPU intensity is mainly due to the use of Monte Carlo codes for simulating the behavior of neutrals or even photons [114] in the SOL and divertor.

Basically three packages exist, based on the $2D$ plasma 'fluid' codes, UEDGE [115], EDGE2D [116] and B2 [117]. Each solves a modified, multi-fluid version of the $2D$ Braginskii equations [34] and their newer versions also allow the activation of current and drift related terms. To model the neutral species, some codes such as UEDGE or B2.5 include a fluid model, in which the neutrals are treated in a simplified fluid approximation, neglecting molecular effects [118].

For a full treatment of neutral-plasma interactions and of the divertor geometry, especially when the geometrical and physical scale lengths are comparable to the average mean-free-paths, each of these codes has been coupled to Monte-Carlo codes that simulate the neutral species with varying degrees of sophistication. These coupled codes are UEDGE-DEGAS2 [119], UEDGE-EIRENE [120], EDGE2D-NIMBUS [121], B2 and B2.5- EIRENE [107, 122], with DEGAS [123], NIMBUS [124, 125] and EIRENE [65, 126]

being the Monte-Carlo neutral codes. In each of the latter a representative set of neutral particle histories is simulated in a plasma background which may be either provided by a fluid code or specified by the user.

For completeness it should also be mentioned that sophisticated $2D$ modeling exists in the form of the 'Onion-Skin-Method' (OSM) [28, 127]. In OSM the boundary conditions are given by radial profiles (e.g. target profiles) covering the entire radial range of the computational domain. The solution along $\vec{B}$ is then performed solving the $1D$ fluid equations with perpendicular transport introduced as source and sink terms. Compared with the $2D$ type of code used for this thesis, the clear advantage of this method is that no a priori knowledge of cross-field transport is required. Indeed the effective values of $\chi_\perp$ and $D_\perp^{eff}$ can be extracted from the OSM solution. As a consequence, computational times, even when coupled to a Monte-Carlo code, are hugely reduced. Due to the prescription of radial profiles, OSM is an 'interpretative' code, whilst $2D$ fluid codes are implicitly also 'predictive', though with the serious drawback of requiring values of the anomalous cross field diffusion coefficients as input.

3.1   SOLPS5.0

For the numerical simulations of the TCV and JET SOLs described in Part II of this thesis, the code package SOLPS5.0 (**S**crape **O**ff **L**ayer **P**lasma **S**imulator) has been used. Earlier simulations by A. Loarte for TCV [16] had been performed using SOLPS4.0.

The code package consists of [128]

- *DG*, a graphical interface for the input, used for the establishment of new configurations and originally developed for SOLPS4.0.

- *Carre*, a grid generating code [129].

- *B2.5*, a computational fluid code for the plasma, solving the modified multi-fluid Braginskii equations [130–132], including a fluid treatment for neutrals [118].

- *EIRENE*, (versions '96' and '99', often referred to as 'EIRENE-old' and 'EIRENE-new' respectively).

- an interface, coupling B2.5 and EIRENE.

- *b2plot*, a diagnostic routine for the visualisation of code results.

The following sections describe in more detail some aspects of the SOLPS5.0 package, following chronologically the codes employed when beginning a simulation for a new configuration. A SOLPS manual is available on the Internet [133]. The most extensive description and introduction to B2 can be found in the PhD thesis of M. Baelmans [107].

3.1.1 DG

In order to limit the extent of the grid that is generated for the case of interest and to be able to define the locations of the targets, a poloidal cross-section of the experimental geometry is required. Two-dimensional poloidal cross-sections of the main plasma-facing components of a variety of tokamaks to which SOLPS has been applied may be found in the database of the SOLPS code itself. If this is not available it can be generated using *DG*, beginning from a technical drawing file (e.g. in HPLG format, a special technical printing format for technical drawings). If EIRENE is also being used (stand-alone or coupled), *DG* can provide a basic EIRENE input file containing the geometry as given by this technical drawing.

The poloidal flux surfaces required to generate a $2D$ simulation grid with *Carre* can be obtained through the EFIT [134] (for JET) or LIUQE (for TCV) [135] magnetic reconstruction codes and uploaded into *DG*. The user then defines the type of divertor geometry present (e.g. SNL) and the grid spatial resolution. It is important to note that when using *DG* and *Carre* magnetic flux surfaces are by default permitted to intersect wall surfaces only at targets. It is therefore standard from a practical point of view not to include intersections of magnetic surfaces with main chamber walls, even though this is possible in principle, if the grid cell boundaries are manually defined in B2 and EIRENE.
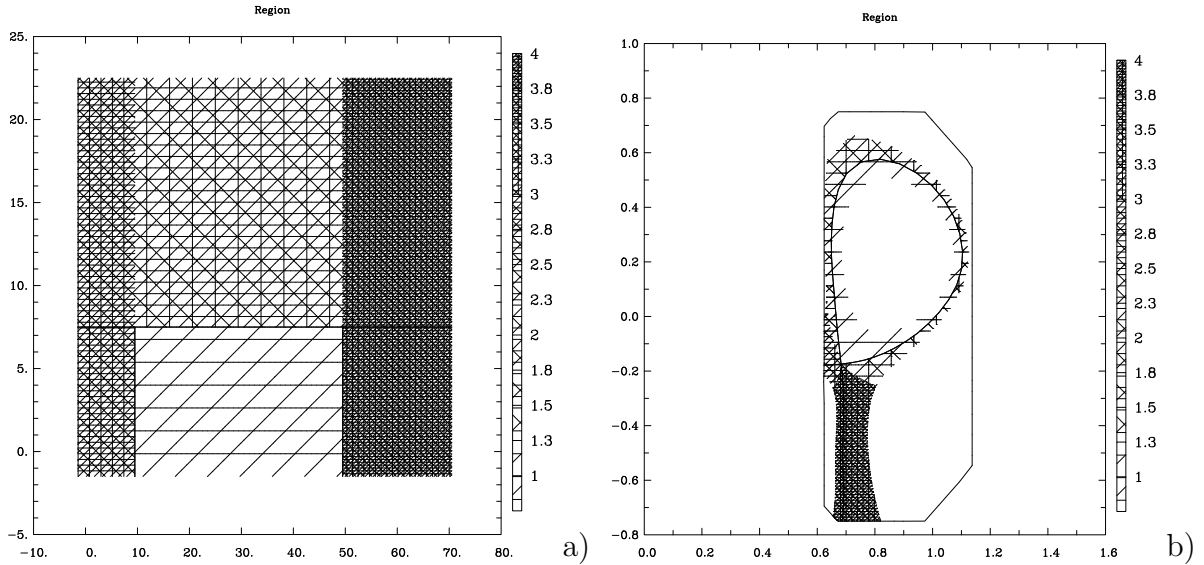
Figure 3.1: *Regions (hashed areas) in the (a) 'computational' (the axes indicate cell numbers) and (b) 'physical' (axes in [m]) domains of a typical SNL grid used for the simulations. The domains are shwon here for the case of TCV discharge #24532 at t = 1.0s. The associated grid can be seen in figure 5.26.*

3.1.2 Carre

This program uses output files created by *DG* to generate the curvilinear, quasi-orthogonal grid used by B2.5 and EIRENE which aligns strictly with the magnetic field, minimizing numerical diffusion. Numerical calculations inside B2.5 are performed on a topologically rectangular mesh, often referred to as the *computational domain* (see Fig. 3.1). Transformation between the physical geometry and this mesh is provided through metric coefficients that are included in the output of Carre. The grid resolution should be higher when strong gradients in plasma parameters are expected to exist, but can be relatively coarse in regions of small or negligible gradients. Grids usually therefore have higher spatial resolution in the poloidal direction close to the targets and around the X-point, whilst the highest spatial resolution is requested around the separatrix in the perpendicular direction. A future, new version of SOLPS, SOLPS6.0, includes a grid refinement method that adapts the mesh according to normalized gradients of plasma parameters [136].

3.1.3 B2.5

A rewritten version of the B2 code, B2.5, has been readily available since 2000 - 2001 and is being increasingly used. It is completely written in FORTRAN 90, using dynamic memory allocation. The original B2 code, which is at the core of the SOLPS4.0 code package (used for simulation of the ITER divertor), was originally written by B. Braams [117]. It solves the current-free Braginskii equations [34] for a multi-species plasma in which an arbitrary number of ionic species at various concentrations may be included. All ion species are assigned the same T_i. The original B2 code did not account for drifts and a first attempt was made by Baelmans to include them, together with a first coupling of the B2 code to EIRENE [107].

At each iteration, corresponding to a single time step, volumetric and surface source terms are computed, solving for momentum conservation, continuity, energy conservation and finally again for the continuity equation. The above procedure is repeated for a number of internal iterations (usually 10) to relax the equation solutions before proceeding to the next time step (external iteration step). The process is repeated until convergence is reached. The latter is monitored by analyzing the residuals of each equation. Steady state is achieved if, independently of the time step chosen, no 'major' variation of plasma parameters is observed. This must include steady state of the densities, temperatures, energy and particle fluxes at various locations in addition to the total particle and energy content of the plasma. Whilst B2 required time steps $< 10^{-5}s$, B2.5 can now be run with time steps of up to $10^{-3}s$, depending on the plasma regime. This has greatly accelerated simulations, particularly when using B2.5 without coupling to EIRENE. If the internal iterations converge sufficiently, each time step provides a solution in 'real time' corresponding to the numerical time step chosen.

The B2.5 code includes the treatment of currents and drifts, being able to handle the effects of electric fields in both the SOL and in the confined region. It solves an extended and modified set of equations that now also includes the current continuity equation and the equation for charge conservation. Details of the equations included in the current

B2.5 code can be found in [130, 131]. For the purposes of numerical stability, divergence free terms in the particle and current balance equations are canceled analytically. Radial and parallel currents are included and there is some discussion on the proper implementation of the ion-electron heat exchange term in the presence of anomalous particle fluxes [130, 131, 137]. The work presented in this thesis has been performed using the B2.5 code, including the minor effect of Joule heating through currents, but without the addition of drift related terms ($\vec{E} \times \vec{B}$ or diamagnetic).

A fluid approximation for the neutral species is included in B2.5. When coupled to EIRENE the neutral source terms of the B2.5 fluid model are rescaled by 10^{-10}. Only atomic neutral species are present in the fluid model and the neutral temperature is set equal to T_i. The neutral model includes a 'first-flight' approximation that better accounts for the distribution of neutrals away from material surfaces. For a more detailed description see [118] and references therein. The main advantages of a fluid model for neutrals, applicable if their ionization mfp is less than typical gradient lengths for neutral and plasma parameters, are the faster convergence and ease of monitoring (due to the lack of 'Monte-Carlo' noise). A drawback is the influence of the neutrals on the T_i profiles, which depends sensitively on neutral flux limits, neutral thermal diffusivity, neutral conductive heat flux limits and boundary conditions at the edges of the grid nearest to the main chamber walls. A rough guide to the most appropriate settings using fluid neutrals has been derived by comparison with simulations in which B2.5 was coupled to EIRENE [118].

3.1.3.1   Using B2.5

Only time independent, steady state plasma solutions have been sought in the work of this thesis - the full time dependent capability has not been used. The fluid code B2.5 can be run stand alone or coupled with EIRENE. Once a computational grid has been established, proper boundary conditions must be specified. Beginning simulations under low recycling, attached plasma conditions is recommended. A scan of different input parameters is usually undertaken, including variations in n_u, P_{SOL}, $D_\perp$, $\chi_\perp$ until the closest match to experimental data is obtained - if these are available. Depending on the plasma

conditions being simulated, a new simulation may require ~ 1000 iterations before reaching an acceptable converged steady state.

The 'positive direction' of flows in B2.5 is from the inner target to the outer target ('east' to 'west') and from the core plasma perpendicular to the magnetic flux surfaces outward ('south' to 'north'), see Fig. 3.1(a) for orientation. Simulation grids usually extend a few cm inside the LCFS (at the outer midplane) and the innermost grid boundary is often also referred to as the 'core' or 'south' boundary, where, due to the structure of the computational grid, part of the 'south' boundary also forms the grid boundaries of the PFR. The furthermost extension of the grid toward the main chamber walls comprises the so-called 'north' grid boundary of the grid, see also figure 5.26.

Boundary conditions must be specified for the energy, continuity, potential and momentum equations. They are specified in terms of fluxes or derivatives of the fluxes themselves, so that while the user handles 'physical' quantities, the imposed boundary conditions are translated by the code as sources and sinks of particles, momentum and energy for which the code will relax the plasma solution until convergence is reached. In recent years it has become possible to run B2.5 using feedback schemes on e.g. simulated gas puffs, adapting their strength such that requested midplane separatrix densities or core densities can be controlled.

3.1.4 EIRENE

The EIRENE code solves time dependent or stationary, linear transport equations for test particles in a $3D$ volume of arbitrary complexity by the means of Monte-Carlo methods and was originally developed for studying the tokamak plasma edge [126]. An EIRENE manual is available on-line [65]. Test particle trajectories are followed through a prescribed background[1]. Linearity means that self-collisions between particles of the test species are excluded, though they can be accounted for through the BGK-approximation [138, 139].

---

[1]in this thesis a plasma supplied by B2.5

Recently begun simulations by Kukushkin using SOLPS for the SOL are using this option to account for the high neutral densities encountered in the ITER divertor [140]. In this thesis self-collisions of neutrals are not included.

The EIRENE code is based on the Monte-Carlo principle. Early attempts to simulate particle histories on given backgrounds date back to 1950-1960 and were developed for neutron transport calculations [141, 142]. In plasma physics, the principle is used for the computation of statistical expectation values of complex processes between test particles and the plasma.

The basic Monte-Carlo principle may be described as follows: a sample of $\mathcal{N}$ particles of the test species is launched from a particle source with strength $\mathcal{Q}$, each having a certain direction and velocity, which themselves might follow a prescribed distribution. All events of type $\mathcal{A}$ that may be encountered on a trajectory have a probability $P(\mathcal{A}) = N_{\mathcal{A}}\sigma_{eff}(\mathcal{A})/\Sigma_t$ with $\sigma_{eff}(\mathcal{A})$ the effective cross-section, $\Sigma_t = \sum_{\mathcal{B}} N_{\mathcal{B}}\sigma_{\mathcal{B}}$ the total cross-section for all possible events $\mathcal{B}$, with $\mathcal{A} \in \mathcal{B}$. Using random numbers, $\mathcal{R}$, generated equally in the interval $[0\,1]$, the length, l, of the simulated trajectory may be written

$$l = -\lambda \ln \mathcal{R}, \qquad (3.1)$$

with λ the mfp of the test particle. Formally, the Monte-Carlo method is used to integrate the particle transport equation statistically using discrete Markov-chains [65, 141, 142]. Each test particle is followed along its trajectory until it is either absorbed at a material surface or ionized and becomes a species of the plasma background. A number, N, of histories are created, from which averaged values may be derived such as the density, $n = t\mathcal{Q}/(V\mathcal{N})$, with t the time the test particle has spent in a given cell of volume V. The uncertainty in the statistical average is thus $\propto 1/\sqrt{\mathcal{N}}$. Rate coefficients for volumetric processes are passed to EIRENE through databases (such as e.g. AMJUEL [65], HYDHEL [81], METHAN [65, 143]) giving coefficients of 8th order polynomials.

The EIRENE code is written in FORTRAN (77 and 90). It can be used 'stand-alone' or coupled to other codes as in SOLPS5.0. The vessel geometry, grid and the atomic and molecular data to be used are specified through a formatted input file. Two versions of

EIRENE are included in the SOLPS5.0 package. Version '96 has been the most commonly used to date for coupled calculations, but does not, in contrast to Version '99, include friction between molecules and ions or the possibility for multiple molecular species. Both versions have been employed during this thesis. Still newer versions, including photon transport and dynamically allocated memory are available but have not yet been coupled to B2.5. Coupled versions of EIRENE are parallelized in connection with EMC3 (3D plasma edge simulation), but not SOLPS.

3.1.5 Coupled simulations

Once EIRENE has completed the simulation of a set of neutral particle histories on a plasma background provided by B2.5, sources and sink terms for particles, momentum and energy are transferred to B2.5. The latter then relaxes the solution through several internal iterations and provides EIRENE with a new plasma background together with values, for example, of the particle flux at the grid boundaries from which surface and volumetric neutral sources are coupled in EIRENE. This iteration scheme is then repeated until satisfactory convergence is obtained. Ideas have been proposed, but not yet implemented, for the combination of a kinetic description of neutrals in regions of long mfp with a fluid model in regions of short mfp [130, 144].

3.2 Hardware architecture for the simulations

The code package SOLPS5.0 has been provided by IPP Garching through D. Coster. The code is updated remotely, but each user may modify the local copy of the source. The simulations for JET presented in this thesis have been performed using the code installed on the **J**ET **A**nalysis **C**luster (JAC), which is accessible remotely and consists of a growing number of PCs with the Linux operating system. Users run the code from their own directories, in which each retains a personal compiled version of the code.

Simulations for TCV have been performed on a small dedicated cluster of 4 Linux based, 2.4GHz Pentium IV computers. The cluster is managed by the freely available

OPENMOSIX clustering software [145]. With the present capacity, up to 8 coupled simulations can be undertaken simultaneously.

Results from simulations executed on the JAC and at CRPP can be stored in a centralized MDS database located on a server at IPP Garching [146]. Each simulation is stored under a different run number and accessed in the same way as tokamak experimental data. Experimental data from TCV have from the beginning been archived under the MDS+ storage system. Access through MDS to JET data has also recently been implemented. The availability of simulation results through MDS has significantly eased comparison with experimental data.

On the available architecture (JET and CRPP) each iteration in the coupled simulations, performed during this thesis, is allocated CPU time in the range $\sim 50s$ to over $100s$, of which only $\sim 7s$ is required by B2.5. The rest is used by EIRENE and will depend on the number of atomic and molecular species included. With at least ~ 1000 coupled iterations per converged simulation, each run uses over 24 hours of CPU time. This increases if feed-back schemes on some plasma parameters are used. When the importance of volumetric plasma sinks increases (as in detachment) the numerical time step is reduced from $10^{-3} - 10^{-4}s$ to values as low as $10^{-6}s$ in order to reach convergence in steady state, thus further increasing the required number of iterations.

Part II

Simulating divertor detachment in TCV and JET

Chapter 4

Introduction: Part II

The SOLPS5.0 code package has been used during this thesis to investigate the physics of divertor detachment on both the TCV [147] and JET tokamaks. Though both are very different in size and divertor geometry, an attempt has been made to draw conclusions on the nature of the detachment process in each by comparing code simulations with experiment through the use of two distinct plasma species: deuterium and helium. The following two chapters describe the result of this exercise with strong emphasis on TCV.

A change of the main ion species has a considerable impact on the performance of the divertor and thus on the onset of detachment. If the magnetic and divertor geometry (parallel-field connection lengths, degree of neutral baffling, etc.) are maintained, the choice of gas fueling species modifies the volumetric losses in the divertor and the SOL. These power losses (especially impurity and main plasma species line radiation) are determined by the choice of the gas and governed by the interaction with the material of the first wall and divertor targets. By exchanging helium for deuterium in a machine containing significant quantities of graphite, whilst retaining the important geometrical parameters, the effect on the character of detachment of a significant change in both the principal atomic physics processes and the nature of the carbon impurity source can be studied.

In both JET and TCV comparative campaigns of pure He and D plasmas have been executed, in each case with experimental time dedicated to detachment study in ohmic

(TCV) or L-mode (JET) plasmas, thus providing a 'simple' background for the modeling effort. This study follows earlier work by Loarte [148] who first applied the SOLPS4 code to the simulation of DIII-D results on the effect of He operation on divertor detachment. Note that all JET data presented in this thesis have been obtained in the MARK II GB
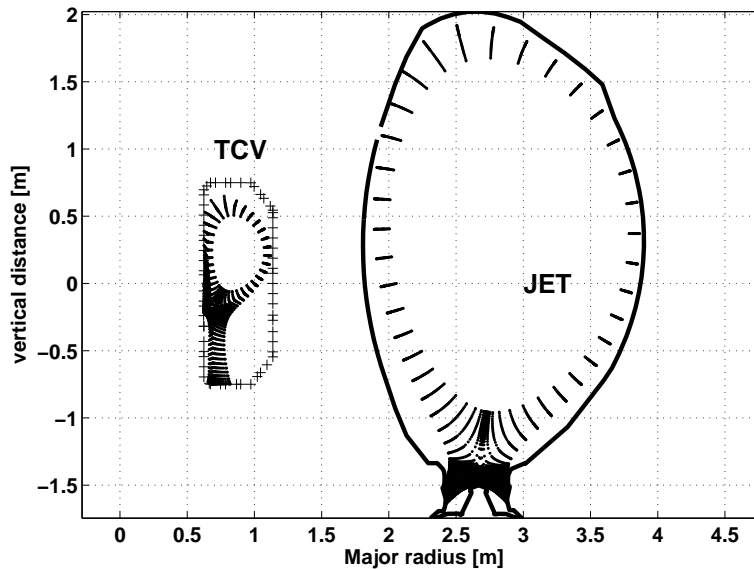
Figure 4.1: *Comparison of size and shape of TCV and JET together with the coverage of the grids used in the simulations. The contour of the JET vacuum vessel used in the simulations differs slightly from the real design at the baffles and in the top left corner of the first wall for a better coverage of the SOL by the grid.*

(Gas Box) divertor configuration (see Fig. 4.1 and 6.6).

The JET and TCV tokamaks differ greatly in size and divertor configuration geometry. Figure 4.1 illustrates the vessel contour and size of the two tokamaks including the extent of coverage of the typical SOLPS5 simulation grids. Although each operates with fully carbon divertor targets, the magnetic geometry of single null divertor configurations is very different. While TCV has an open divertor with no baffling structures, the JET MarkIIGB divertor (the design of interest to this thesis) is closed, with a septum dividing the inner and outer divertor volumes. At JET the inner and outer divertor strike points are positioned on vertical targets. In contrast, TCV diverted plasmas usually run with both strike points on the central column (vertical target) or with the outer strike

94

point on the vessel floor (this is the standard configuration simulated here). Whilst for JET the X-point to the strike point connection lengths for the inner and outer divertors are approximately equal (X-point to inner $14m$ and to outer $12m$), with a total outer midplane to target connection length of $\sim 50m$ (at $I_p = 2.5MA$, $B_T = 2.4T$), TCV is characterized by a highly asymmetric divertor. The short X-point to inner target poloidal depth (corresponding to only $\sim 2.5m$ parallel to the total field) contrasts with the much longer X-point to outer target distance of $\sim 57cm$, which is associated with an outer midplane to target connection of $\sim 21m - 25m$ (at $I_p = 340kA$, $B_T = 1.4T$), 70% of which appears between the X-point and the target. In addition, the vertical position of the inner strike point is similar to that of the X-point on TCV, while at JET both strike points are located below the X-point, in a much more conventional divertor geometry. Whilst the JET pulse length and high power operation at high density requires divertor cryo-pumping for density control, TCV has no active pump and relies on wall pumping alone over the short available pulse length.

With TCV (Tokamak à Configuration Variable), tokamak plasmas of very different shapes and magnetic configurations can be obtained. The present thesis focuses only on a single magnetic equilibrium. Using ECRH a total additional heating power of $4.5MW$ could theoretically be reached. However, for the density ramp discharges, required to study detachment, only ohmic heating can be used since the cut-off density for the present ECRH system is far too low for effective heating at high $\bar{n}_e$. The heating power for detachment studies on TCV has therefore been limited to $400kW - 600kW$. In contrast, the total power employed during dedicated L-mode detachment campaigns at JET included ohmic heating (with $I_p = 2.5MA$) and a total power from NBI of up to $5MW$, resulting in $P_{SOL} \approx 5MW$. Nevertheless, the power flux crossing the LCFS $q_\perp$ is comparable in both machines under these conditions. The LCFS area for TCV standard divertor configurations is $\sim 10m^2$, but is $\sim 100m^2$ for JET, giving $q_\perp \approx 50kW/m^2$ in both cases.

Chapter 5

Divertor detachment in TCV

5.1 Introduction

Since the low field side main chamber wall of TCV has been equipped with graphite tiles, divertor detachment at the outer divertor target has been reproducibly observed in deuterium fueled, ohmic heated density ramp experiments with the $\vec{B} \times \nabla B$ ion drift directed upward (the standard B_Φ direction on TCV) [16]. Without the use of seed impurities, detachment in deuterium had *never* been observed at any reasonable plasma current prior to the increased first wall graphite coverage [149]. Detachment at the inner target is almost never obtained. Figure 5.1 shows the interior of TCV before and after the installation of graphite tiles on the low field side main chamber walls.

The measured outer target ion fluxes and densities are much lower than those found in detaching plasmas on larger tokamaks, or those with higher toroidal magnetic field and/or strong divertor baffling [16, 24]. Moreover, experimentally observed detachment and even the high recycling behavior at the outer target is found to behave 'anomalously' with respect to changes in upstream density, as with increasing n_u the peak particle flux to the target does not at first strongly increase, then roll over and decrease, but instead steadily decreases. Early modeling attempts were performed with the SOLPS4.0 (B2-EIRENE) code package [50], but could not reproduce the observed loss of outer target

current during high recycling or detached regimes without recourse to artificial means, such as increasing the rate coefficient for 3-body and radiative recombination by a factor of 5 [24].

The first part of this Chapter summarizes the essential experimental data obtained during density ramp detachment discharges. This will provide the basis for comparison with the simulations in Section 5.3. Specific experiments have been performed to study detachment in D and He under matched conditions and in forward and reversed field discharges.

Section 5.3 describes the simulation attempts to reproduce the observed anomalous outer target detachment. Sensitivity studies have been performed on various boundary conditions and parameters, including the effect of heat flux limits. Though attempted, converged solutions have unfortunately not been found thus far when drift terms are activated.

In addition to possible effects of drifts, alternative possible candidate mechanisms can be invoked to explain the TCV detachment anomaly. Each has been investigated here, with the influence of deuterium and hydrocarbon molecules, hitherto only rarely included in SOLPS5 tokamak simulations. The effects of adopting atomic and molecular data provided by a collisional radiative model and the further refinement including molecules distinguished by their vibrational levels (henceforth also named *vibrationally resolved molecules* VRM) have also been investigated [150]. Possible geometrical effects when changing from a cylindrical to a toroidal approximation of the torus inside EIRENE have also been analyzed. None of these additions have been found to reproduce the observed detachment when using spatially constant transport coefficients $D_\perp$ and $\chi_\perp$.

Inspired by UEDGE simulations for DIII-D [59–61] and C-MOD [54] and solicited by recent experimental observations on perpendicular intermittent transport on TCV, radially dependent perpendicular convective transport has been introduced into the simulations on the low field side, while maintaining spatially constant diffusive perpendicular transport coefficients. This leads to considerable improvement when comparing with experiment, especially in the detached regime. When varying the chemical sputtering yield

on the main chamber walls, significant target detachment can be obtained. The effect is stronger still when $CD4$ molecules are introduced.

a)

b)
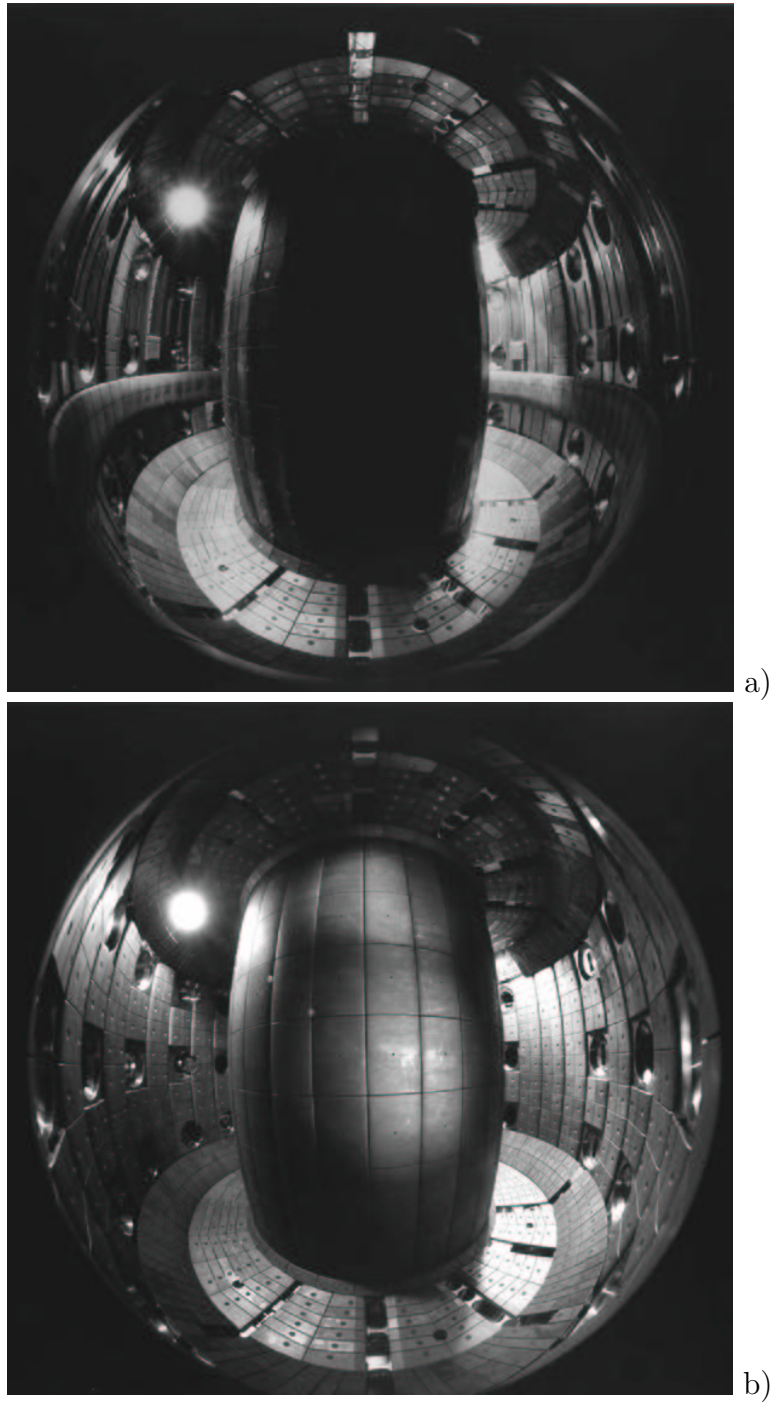
Figure 5.1: *Photographs of the TCV interior (a) prior (1994) and (b) after (1998) increasing the LFS main chamber walls graphite coverage. The additional graphite armor installed in 1998 increased the total surface coverage by carbon from $\sim 65\%$ to $\sim 90\%$.*

5.2 Experiment

5.2.1 Diagnostics

Simulations can only be effectively constrained if sufficient experimental data is available. Unfortunately, the SOL is often the region in which measurements are hard to make, especially with regard to good spatial coverage. The SOL is a radially narrow region, requiring good spatial resolution, and is often characterized by strong poloidal variations in plasma parameters and particle sources etc. Often, therefore, the extent to which edge code modeling can be constrained is limited.

On TCV, as elsewhere, the main experimental data are provided by fixed and reciprocating Langmuir probes (RCP) together with an edge Thomson scattering (TS) system, which has been on loan from RFX for a short period during the time interval of this thesis. Upstream profiles are provided by the edge TS system and the RCP, whilst the fixed Langmuir probes provide data at the inner and outer targets. Fast pressure gauges of the ASDEX type have been installed on TCV as part of this thesis work and provide measurements of the neutral pressure at the outer midplane[1] and below the outer target. This data may be used to compute the neutral compression ratio (eqn. 2.9.3).

Additional diagnostics include foil bolometers and AXUV cameras for measuring the total radiation and its poloidal distribution, a CCD camera measuring the distribution of light emission in the divertor region, spectrometers with vertical and horizontal chords, a photo diode measuring D_α and some impurity line emissions. Unfortunately, the majority of these spectroscopic diagnostics are uncalibrated and in most cases insufficient chords are available for complete tomographic inversion of the radiation distribution.

---

[1]more precisely at the vertical position $z = 0$, whilst the midplane in the configurations simulated here is at $z = +23cm$ (see Fig. 5.2).

5.2.1.1 Fixed and fast reciprocating Langmuir probes

The distribution of the fixed Langmuir probes inside the TCV vessel is shown in figure 5.2, together with the typical magnetic configuration used for TCV detachment studies. Photographs of the Langmuir probes in the central column tiles and in the vessel floor
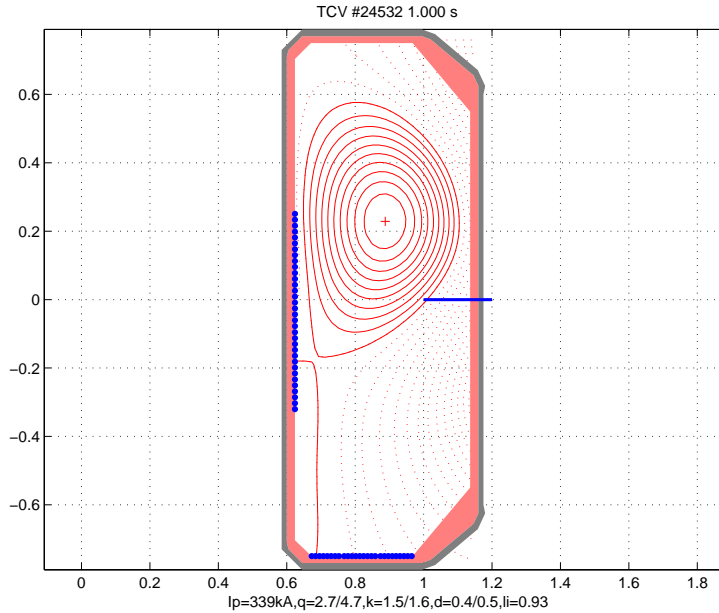
Figure 5.2: *Reconstructed magnetic equilibrium of discharge #24532 at 1s together with the locations of the fixed Langmuir probes (•) and fast reciprocating probe (−).*

may be found in Fig. 5.3. The divertor Langmuir probe diagnostic (LP) consists of 34 single probes located in the central column tiles and 26 in the vessel floor. The probe spacing is $17.2\,mm$ along the inner and $11.4\,mm$ along the outer target. They are graphite, cylindrical probes of $4.0mm$ diameter with a spherical tip protruding $1.0mm$ above the tile surface at the outer target and flush mounted and embedded in the divertor tiles at the inner target. Selected probes can be acquired at a frequency of $50kHz$, whilst the majority are usually acquired at $10kHz$. The probe voltage is normally swept at $100Hz$ using a programmable waveform designed to provide the maximum number of data points in the region of the probe characteristic from which T_e is derived.

Each probe measures the ion saturation current i_{SAT} from which, knowing the projected probe surface area, $A_\perp$ (itself dependent on the probe geometry and the magnetic
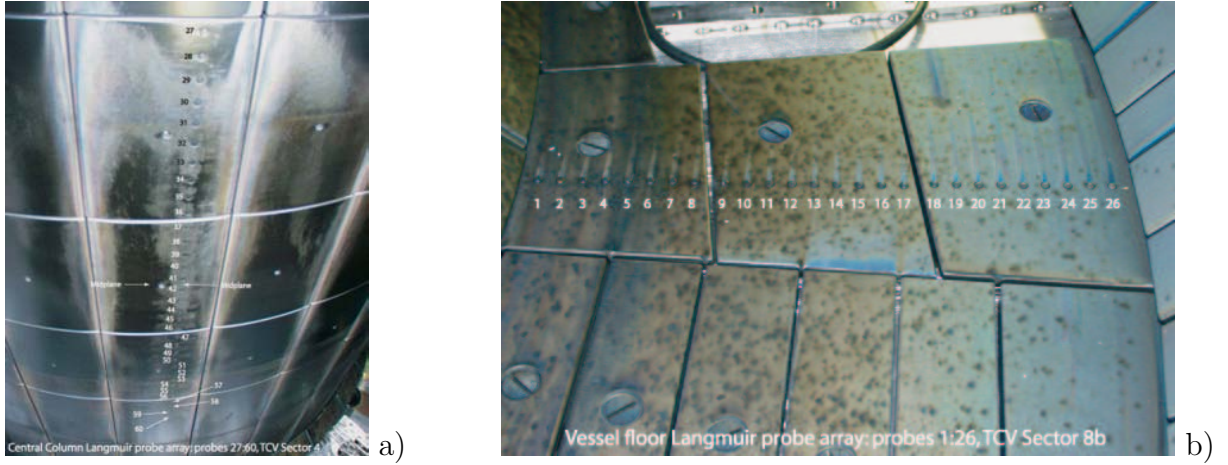
Figure 5.3: *Photographs of the fixed Langmuir probes in (a) the central column and (b) the vessel floor tiles.*

field line impact angle) the *ion saturation current density*, $j_{SAT} = i_{SAT}/A_\perp$. The effective probe area can, in some tokamaks, be modified by plasma erosion, but this is not a significant problem in TCV where reductions in $A_\perp$ due to extremely shallow field line impact angles, for example in cases of high flux expansion can be more problematic. Some probes, especially at the TCV outer target, can be shadowed by neighboring tiles causing virtual 'current holes' in the radial profiles of j_{SAT}.

Electron temperatures are derived applying standard fitting procedures to the equation describing the probe sheath current-voltage characteristic:

$$I_{pr}(V) = i_{SAT}\left[1 - \exp\left(-\left(V - V_f\right)/kT_e\right)\right], \tag{5.1}$$

where V_f is the probe floating potential when the applied voltage, $V = 0$. For low j_{SAT} and T_e (typical of detached plasmas) the ratio of ion to electron saturation current can approach unity and diverges in many cases from exponential behavior, leading essentially to a failed analysis (see, for example, experimental values of T_e in figure 5.35) [151]. In addition, it is frequently observed that tokamak divertor target probes under high recycling or detached conditions yield T_e values higher than those measured by alternative methods [152]. It is not currently understood how to resolve the discrepancy between the very low T_e ($\sim 1\,eV$) associated with recombining detached plasmas and values $\geq 5\,eV$

measured by Langmuir probes (see [151] and references therein).

The local electron density is derived knowing j_{SAT} and T_e via

$$j_{SAT} = e n_e c_s \qquad (5.2)$$

using an isothermal assumption ($\gamma = 1$ in eqn. 2.46) and $T_i = T_e$ for c_s (assumed to be valid especially at high collisionality), while the Mach number at the target is set to $M = 1$. The atomic mass of the main fueling species is used as ion mass. In the evaluation of n_e, $Z = 1$ is assumed when calculating c_s, thereby neglecting in helium plasmas, a possible high fraction of He^{2+} in the target ion flux. The ratio of He^+/He^{2+} is, however, not known experimentally. The inferred error amounts to at most 15%, if the entire ion flux consists of He^{2+} and reduces with increasing He^+ fraction. It should also be noted that eqn. 5.2 does not contain the usual multiplying factor for the derivation of far field density from a local measurement (as is required when computing n_e from RCP data). This is because the target tile in which the probe is embedded itself defines the plasma flow to the target.

There are clearly a number of interpretative difficulties in deriving n_e and T_e from the probe characteristic, particularly under high recycling conditions. Values are thus to be treated with some caution. A more robust quality is j_{SAT}, both in absolute magnitude and as a direct indicator of detachment. A review of electrical probes as diagnostics for the tokamak edge has been given by Matthews [153] and contains detailed discussion of the above mentioned problems.

Inspection of results from a series of discharges with approximately constant, medium line averaged density ($\sim 7 \times 10^{19} m^{-3}$) yields statistical errors on j_{SAT} and n_e of $\sim 7\%$ and $\sim 15\%$ for T_e. This provides a lower limit for the measurement accuracy, since no error propagation from fitting procedures or systematic errors have been applied when processing data. An estimate of the true inherent error in deriving n_e, T_e from the probe characteristics using standard sheath theory is difficult but probably does not exceed $\sim 20\%$ in non-detached conditions.

The 5-pin, fast reciprocating Langmuir probe system is located on the vacuum vessel midplane and is thus situated approximately $20cm$ below the magnetic axis of standard diverted discharges on TCV (figure 5.2). A basic description of the system, originally on loan from UCSD but now fully incorporated into the TCV diagnostic set, may be found in [154]. During a typical discharge the probe reciprocates twice into the plasma. In each case the probe passes through the *wall shadow*, where field lines connect to the main chamber walls, then through the SOL, with field lines connecting the two targets. In some cases plasma a few mm inside the LCFS may also be sampled but invariably leads to strong perturbations of the discharge.

Using the same assumptions, as for the fixed target probes, upstream profiles of T_e and n_e may be computed from RCP data. It is, however, less likely that $T_i = T_e$ in the upstream region, thus introducing an overestimation for n_e ($\sim 20\%$ if $T_i = 2T_e$). In addition, according to Stangeby [155] and Hutchinson [64], the presence of parallel flows in the probe pre-sheath requires further corrections in the calculation of n_e depending on the value of $M_\parallel$. Although strong flow has recently been measured in the TCV edge, no correction is included in n_e profiles presented here. In fact, the exact correction required is not well known. One proposal is to treat the Langmuir probe pin essentially as receiving flux from one side only (in a strongly flowing plasma) and to compute the density from $j_{SAT} = 0.36e\exp(M)n_e c_s A_\perp$, where the factor $0.36\exp(M)$ is derived from Hutchinson's fluid theory [156] and replaces the factor 0.5 in the standard isothermal fluid theory (eqn. 2.50). With $A_\perp$ being reduced by a factor of 2, the end result for n_e (in the extreme case $M = 1$) does not differ considerably. Again, as for the fixed probes, data for absolute values of n_e should be used with caution.

In addition to the 'DC' values for n_e and T_e, the probe may also be used, and is in fact designed for, the measurement of edge turbulence. Details may be found in a recent article [23]. Measurements of the turbulent driven radial flux in the far SOL made with this probe will be referred to later in connection with the use of a convective transport description in SOLPS5.0 (Section 5.3.4).

5.2.1.2 Thomson scattering

The TCV tokamak is equipped with a main Thomson scattering system optimized for the plasma parameters encountered in the confined region of the plasma, where T_e is in the range $50\,eV - 20keV$. During the most recent experimental campaigns an additional Thomson scattering system, capable of measuring n_e and T_e at the edge of the core plasma and just outside the LCFS has been available, providing the opportunity to compare density and temperature profiles measured with the RCP with a second, non-perturbing diagnostic. Figure 5.4 illustrates the laser and viewing chords of the entire Thomson scattering system, including the top three bundles of viewing chords (for a total of 9 channels) which constitute the edge Thomson system.

The spatial resolution of the edge system is $10mm$, compared with $\leq 35mm$ for
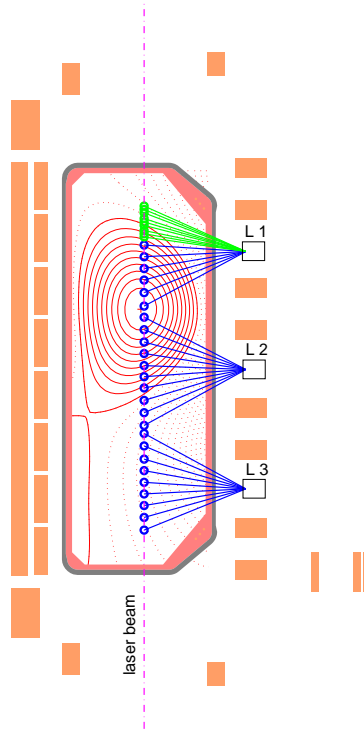
Figure 5.4: *The TCV Thomson scattering system viewing chords superimposed on the standard divertor configuration. The edge system benefits from the higher flux expansion at the top of this equilibrium to provide midplane mapped profiles with good spatial resolution.*

106

the core system. The filters are such as to allow temperature measurements in the range between $5\,eV - 1\,keV$ for densities down to $5 \times 10^{18} m^{-3}$. The accuracy for T_e is on average 15% and for n_e $15\% - 25\%$ for the data presented in this thesis. Both edge and main system share the main probing beam, generated by 3 Q-switched Nd:YAG lasers operating at $20Hz$ repetition frequency.

A divertor TS system has been designed [157] and implemented using main system laser beam relayed into the outer divertor region. Unfortunately, the diagnostic has not yet provided any useful data owing largely to inadequate filters, which must be located very close to the laser wavelength for measurements of low T_e. Apart from target probe data, no information on T_e and n_e in the divertor volume is therefore available on TCV.

5.2.1.3   ASDEX type fast pressure gauges

In the course of this thesis TCV has been equipped with two ASDEX fast pressure gauges. For the majority of discharges studied, one gauge was located on the vessel midplane via a lateral port such that the gauge head is recast a few cm from the LFS wall radius (referred to as the midplane gauge). This gauge has recently been relocated to a second lateral port at $z = -0.51\,m$ so that a few measurements of the neutral gas pressure in the wide open outer divertor fan far away from the separatrix have been obtained and are awaiting analysis. A second gauge is located behind a small hole ($\varnothing=4\,cm$) in the floor tiles of the outer divertor target at a major radius of $R = 0.74m$ (referred to as the divertor gauge), providing essentially 'local' measurements of the divertor neutral pressure.

Photographs of the gauges prior to installation on the tokamak are shown in Fig. 5.5, where the metallic gauge head cover containing a small orifice on one side and enclosing the delicate main electrodes can be clearly seen. The integral components are sketched schematically in Fig. 5.6. The gauge is aligned such that it is as much as possible parallel to $\vec{B}$, but in practice correct functioning is still possible if the field direction varies by as much as $\pm25°$.

Each gauge consists of 4 electrodes fixed on a ceramic base plate:
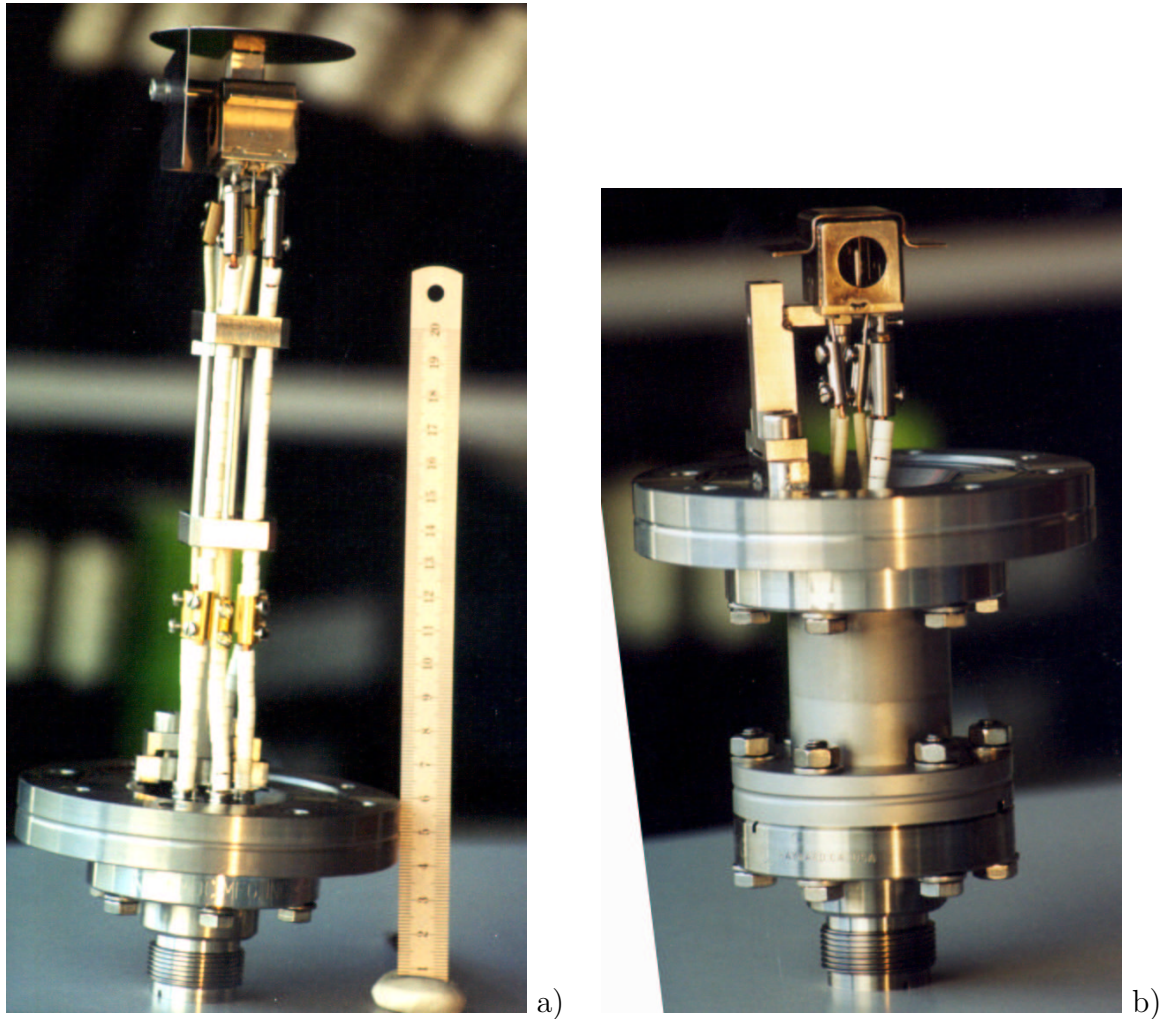
Figure 5.5: *Photographs of (a) the midplane gauge and (b) the divertor gauge prior to installation in the tokamak*

- a thoriated tungsten wire filament $0.6\,mm$ in diameter, serving as the electron source through thermal emission and heated by a DC current of $12\,A$ to $20\,A$ depending on external conditions. The filament potential is maintained at $50\,V$.

- a control grid consisting of a stainless steel plate with a horizontal slit parallel to the filament whose potential is varied between $25V$ and $105V$ at a frequency of several kHz (chopping the emission current).

- an acceleration grid held at $250\,V$ and consisting of vertical slits and bars in an
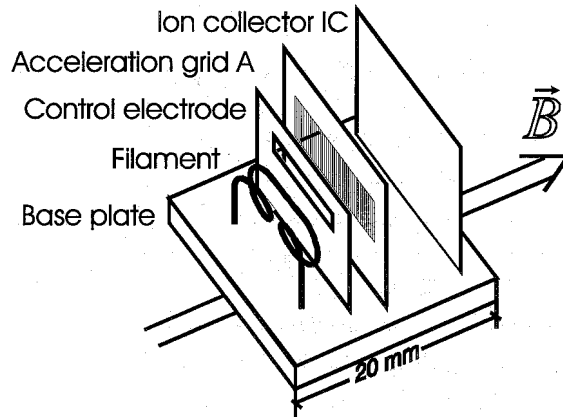
Figure 5.6: *Schematic of an ASDEX type gauge, showing the linear arrangement of the 4 electrodes* (from [158]).

aperture of the same dimensions as the control grid slit.

- a metal plate held at filament potential and serving as an ion collector.

In a strong magnetic field, the escape probability for electrons leaving the filament is $\sim 35\%$. The latter constitute the measured emission current, e_c (measured at the acceleration grid) and will freely oscillate in the electric potential between the filament and the collector plate until they collide with other particles or are collected by the acceleration grid. In the absence of a magnetic field, electrons would not be guided and would be lost at a higher rate. The confining field increases the probability of neutral ionization by allowing the emitted electrons to spend more time within the ionization volume. The measured ion collector current, *ic*, is proportional to the neutral density in the gauge.

The gauge conductance is deliberately limited such that neutrals entering the gauge volume are thermalized due to multiple collisions with the walls, adopting an average velocity $\langle v_{in} \rangle$, determined by gauge parameters (such as the temperature). In flux equilibrium, the particle flux density hitting the gauge entrance is measured

$$\Gamma_{ext} = \Gamma_{int} = n_{in}\langle v_{in} \rangle / 4 = c n_{in}, \tag{5.3}$$

109

with c being a proportionality constant that can be determined through calibration. The measurement time resolution, which is essentially determined by the electronics and the orifice in the gauge head, is $2ms - 4ms$. Gauge calibration is performed with thermal gas in the presence of the tokamak magnetic fields. The pressure, p_{neutr}, can then be derived from measurements of ec and ic, for $ic < ec$, via

$$p_{neutr} = S \frac{ic}{ec - ic} \tag{5.4}$$

with $1/S$ the gauge sensitivity depending on the magnitude of B and on the neutral pressure [158]. During operation an electronic system feeds back on the filament current such that ec is maintained approximately constant. This avoids oscillations in the filament current whilst preserving gauge head lifetime. A more detailed description of these ASDEX type gauges may be found in a number of papers [96, 137, 158–160].

Figure 5.7 shows the sensitivity of the divertor gauge in deuterium for different magnetic fields, typical of TCV operation, and for a variety of neutral pressures. The results are derived from measurements performed on TCV using gas injection and toroidal fields only. Clearly, S varies only slightly with B_Φ in this range but depends strongly on the neutral pressure. In experiments with the standard divertor configuration, it is usually found that for $\bar{n}_e < 4 \times 10^{19} m^{-3}$ the collector current noise level is too high to permit calculation of p_{neutr}.

5.2.1.4 Optical diagnostics

A system of conventional foil bolometer cameras provides a measurement of the total radiated power and, through tomographic reconstruction, its poloidal distribution. An important shortcoming of foil bolometers with regard to divertor modeling is their sensitivity not just to photons but also to neutral particles. Since tomographic inversion techniques assume, a priori, that the plasma is transparent to the escaping radiation, reconstructed distributions become increasingly unreliable at high plasma densities when the neutral density increases in localized regions (divertor).

At the time of writing, construction and installation of a new AXUV fast bolometry
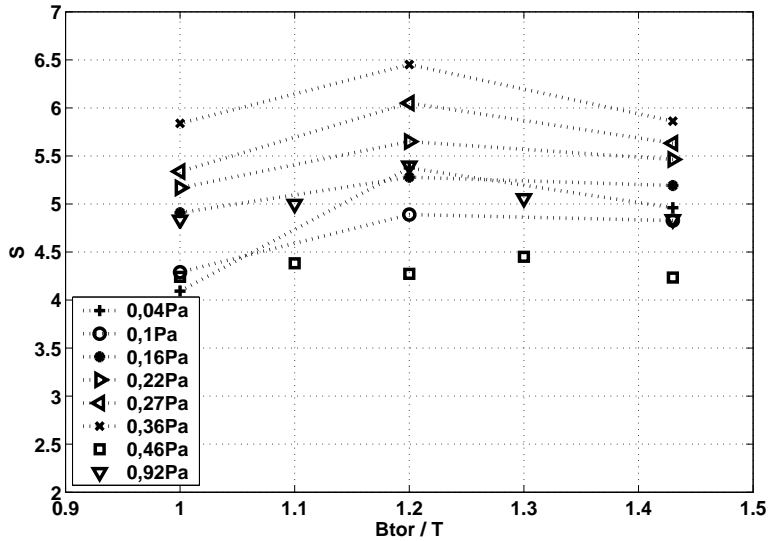
Figure 5.7: *The inverse sensitivity S of equation 5.4 as a function of B_Φ and neutral pressure in D for the divertor gauge, (the midplane gauge behaves in a similar fashion).*

system has just been completed. This unique new system was designed with the help of SOLPS5.0 simulations of recycling light emission intensities [161]. Prior to this, two prototype AXUV cameras have been in operation at TCV, but the limited poloidal coverage restricts their use for reconstructions of poloidal radiation distributions. These cameras have the advantage of being insensitive to neutrals - they are semiconductor devices sensitive only to photons.

In addition to total radiation cameras, a set of vertical and horizontal spectrometers is available and has been used to determine the the concentration of D during pure He discharges. A system of tangentially viewing CCD cameras equipped with different interferometric filters of specific bandwidth has also recently been installed for the observation of the spatial distribution of line radiation in the divertor volume from D_α, D_β, D_γ or $CIII$ emission. Tomographic inversion of the raw data provides a full $2-D$ distribution of the divertor emission and is in principle ideal for code comparison [24]. It is unfortunate, however, that there has been insufficient effort available both to fully exploit this system and perform the full calibration necessary for full code-experiment comparison to be possible. This is especially important during detachment when the low values of

divertor T_e yield hydrogenic line emission which varies extremely strongly even for small variables in T_e.

5.2.2　Detachment

Compared with previously reported measurements and modeling of TCV detachment [16, 24, 162], improved experiments have been performed during this thesis using the new and upgraded diagnostics described above. The review of these experiments which follows begins with a comparison of standard ohmic density ramp discharges with $I_p = 340kA$, $B_\Phi = 1.43T$ and D and He as main plasma species. In both cases, discharges are run in reversed field. These are the discharges for which numerical simulations are presented in Section 5.3 and constitute the principal focus of the TCV SOLPS5.0 modeling work. The consequence of reduced heating power in reversed field is then explored comparing measurements as I_p is reduced to $260kA$. Only at these low currents can comparison be made with forward field matched discharges. This is a consequence of the lower L-H transition threshold with favorable ion $B \times \nabla B$ drift which leads to discharges with $I_p > 280kA$ in forward field transiting to an (often ELM-free) H-mode at any reasonable density. Detachment physics is impossible to study in a controlled and reproducible manner under such conditions.

Standard vacuum vessel conditioning is performed 2-3 times a year, including vessel bake-out at ~ 250℃ and boronisation by plasma chemical vapor deposition (PCVD) in a $10\% \, B_2D_2$, $90\% \, He$ gas mixture, putting down a reasonably homogeneous boron layer of $\approx 10nm$ thickness on the in vessel surfaces. In between D tokamak discharges helium glow discharge is used to establish similar short term surface properties before each plasma shot [163].

Although variations do occur (depending on the proximity of discharge execution to vessel boronisation or high power ECRH campaigns), ohmic density ramp discharges are generally extremely reproducible on TCV. In what follows data from different discharges will often therefore be used in combination, particularly since not all diagnostics are available for every pulse.

5.2.2.1 Comparison of density ramp discharges at $I_p = 340kA$ with D or He as main gas fueling species and reversed field

The magnetic configuration of these discharges is shown in figure 5.2 and is identical for discharges in D and He. It has $\kappa \sim 1.65$ and $\delta \sim 0.35$ and is therefore reasonably close to the forseen baseline ITER plasma shape, even if the divertor geometry is of course radically different to that of conventional tokamaks. In TCV plasmas of this type the complete diverted equilibrium is formed at $\approx 0.4s$ and the duration of the fully diverted phase is $\sim 0.8s - 1s$. In TCV, the continuous vacuum vessel means that a significant fraction of the breakdown voltage is lost through driving current in the vessel walls. Since higher breakdown voltages are required in pure He than in D, unassisted ohmic breakdown has not been possible in He and a small D prefill is required. During the most recent campaigns, breakdown has been obtained without a D prefill using ECRH assistance. The neutral D flux, monitored by a neutral particle analyzer (NPA) is observed to fall to very low values for $t < 0.25s$ into the discharge, indicating that the walls quickly pump the D prefill. The changeover from D to He is rapid on TCV, where after ~ 6 identical discharges, the ratio, $He/(He + D)$ rises to more than 80%. This is monitored using the HeI line at $728nm$ and D_α at $652nm$, taking into account the Jonson-Hinnov factor ^{2} (S/XB). At high densities ratios higher than 90% are obtained [164].

Figures 5.8 and 5.9 compile a selection of plasma and divertor signals from a pair of matched D and He discharges. In deuterium the density limit is typically reached at $\sim 50 - 55\%$ of the Greenwald density limit $(n_G = I_p/(\pi a^2))$ [165, 166] for these types of discharges. In pure He, the limit is $\sim 15\%$ higher. In D the density limit is reached at $\sim 80\%$ of P_{ohm} (see also figure 5.17) while in He $P_{RAD} \sim 0.5 P_{ohm}$, see figure 5.10. It is interesting to observe that this behavior is inverted compared with observations made at JET, where $P_{RAD} \sim P_{IN}$ in He at the density limit and with the radiation fraction reaching about $0.6 - 0.65$ in L-mode D discharges [167, 168].

The values for Z_{eff} in Figs. 5.8 and 5.9, computed using X-ray measurements, are

---

^2S is the ionization rate coefficient, X the excitation rate coefficient from electron collisions, B the photon emission coefficient
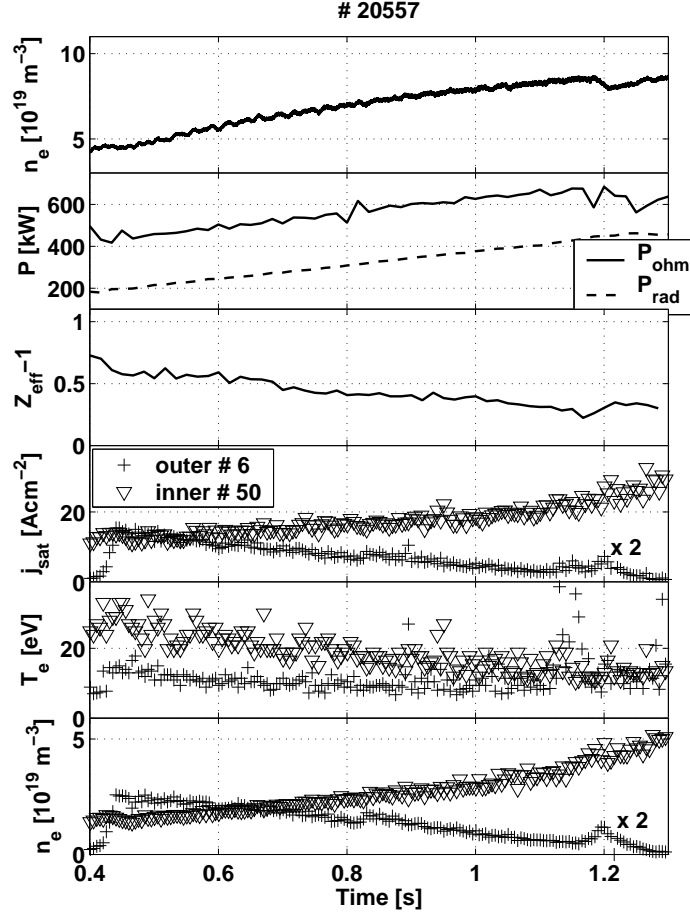
Figure 5.8: *Composite illustrating experimental data from a typical ohmic density ramp discharge in D (#20557).*

corrected for the charge of the main ion species (assuming He^{2+} as the main ion species in pure helium). In both cases the measured $Z_{eff} - Z$, where Z is the main ion charge, decreases with increasing density, approaching zero in D and negative values in He. This implies that He^+ ions play an important role at high density, but seems improbable given that even at the highest $\bar{n}_e$, He^+ would not be expected inside the LCFS since T_e in the confined plasma is high enough to fully ionize the helium[3].

Figures 5.8 and 5.9 include data from two probes located near the inner and outer strike point regions. While at the outer target (probe #6), j_{SAT} decreases strongly from

---

[3]Even at the highest densities ($n_e^{sep} \sim 3 \times 10^{19} m^{-3}$), SOLPS5.0, simulations yield $n(He^+)/n(He^{2+}) < 5\%$ inside the LCFS
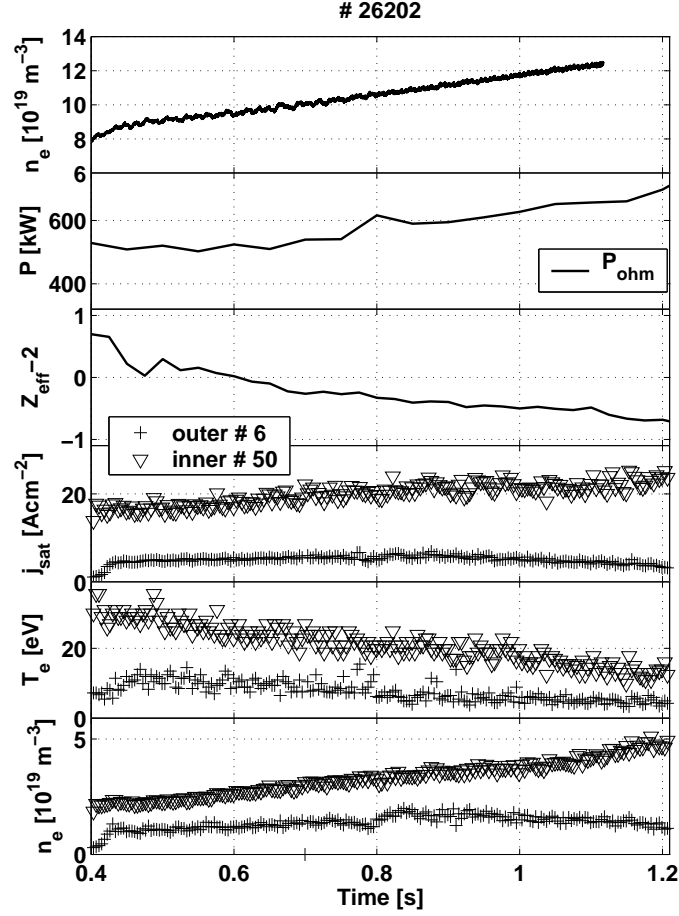
Figure 5.9: *Composite illustrating experimental data from a typical ohmic density ramp discharges in He (#26202). The total radiated power is available for a different shot with different density ramp, see figure 5.10.*

the peak value early on in the density ramp in D, it remains rather constant followed by a slow decrease in He. This is the signature of the outer divertor detachment in deuterium that has been previously reported for TCV [16, 24, 162]. With increasing density, the ion flux to the inner target increases steadily, without any evident sign of detachment in either He or D. For both He and D, T_e decreases with increasing $\bar{n}_e$ at both targets. Despite the fact that the strike point current has disappeared at high density at the outer target, the measured T_e never falls below $\sim 5eV$. Photodiode measurements of D_α emission, figure 5.11, across the lower part of the outer divertor in deuterium show a strong increase when $\bar{n}_e \sim 7 - 8.0 \times 10^{19}m^{-3}$, indicating that strong recombination processes
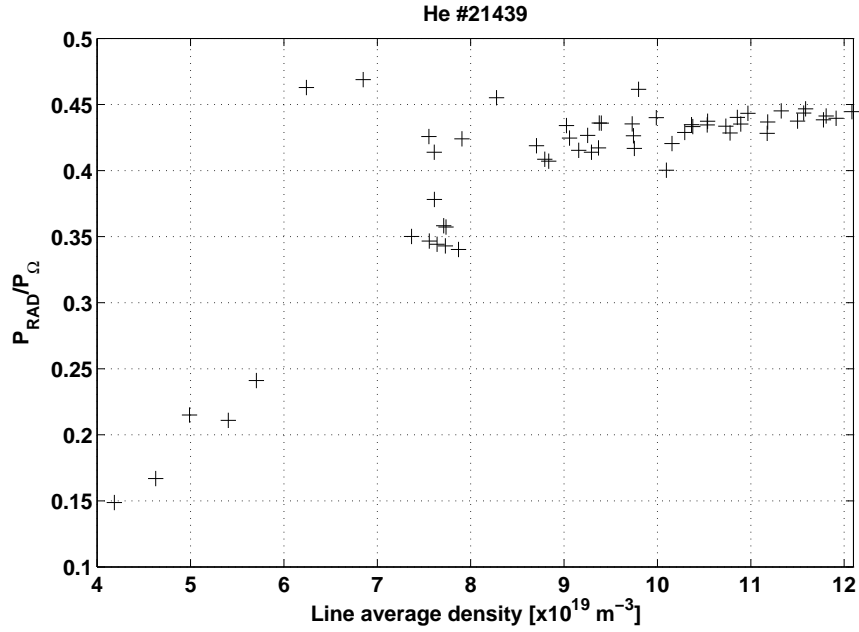
Figure 5.10: *Fraction of total radiated power for a density ramp discharge in He (#21439)*

are occuring. With decreasing ion flux and decreasing T_e, if emission were purely from
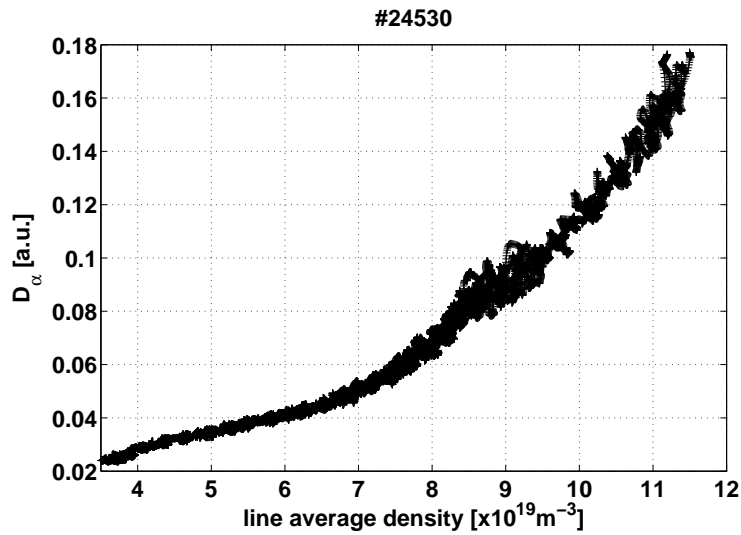
Figure 5.11: D_α *emission across the lower part of the outer divertor for discharge #24530*

excitation processes, a strong decrease in D_α emission would be expected for $T_e < 5eV$. An increase in D_α would, however, be expected if the excited emitting atomic level is populated as a result of recombination processes [91]. In deuterium n_e clearly decreases

117

at the outer target, whilst it remains relatively constant in He. In both cases, there is no sign of a density reduction at the inner target at any time. The simulataneous reduction of n_e, j_{SAT} and T_e and the increase in D_α emission are a clear sign that effective particle removal and not only momentum removal is occuring in deuterium.

From the conditions observed at both targets the decrease in Z_{eff} can be qualitatively understood as has been shown in the case of JET [167]. In He plasmas, if the concentration of D can be assumed negligible, intrinsic impurities such as C can be produced only through physical sputtering (by ions or neutrals). A reduction of T_e toward and below the threshold for physical sputtering then leads to a decrease and ultimately to an arrest of intrinsic impurity production with a subsequent reduction in Z_{eff}. In D the situation is more complex since intrinsic C impurities can be produced through both physical and chemical sputtering and by ions and neutrals. A reduction of the target ion flux does not necessarily reduce the total particle flux on any surface since momentum transfer from ions can increase the neutral fluxes to the walls. A less marked reduction in Z_{eff} might therefore be expected in deuterium. Although the absolute magnitude of the Z_{eff} for He in figure 5.9 may be questioned, it does appear that Z_{eff} decreases less with increasing $\bar{n}_e$ in D than in He.

Figure 5.12 compiles measurements of the midplane and outer target neutral pressures assuming thermalized neutrals at room temperature (as was the case during gauge calibration). The neutral pressure at both locations rises with density as expected, but in contrast to observations made on other tokamaks, the compression ratio *decreases* from the beginning of the discharge to values around 5 at the highest densities. In larger tokamaks or small machines such as Alcator C-Mod operating at high density, the compression ratio is found to increase from values similar to those of TCV at low densities to values during high recycling that are at least one order of magnitude higher than anything observed on TCV in such regimes, followed by a steady decrease to ratios that remain nearly a factor ~ 10 larger than those reported here for medium/high $\bar{n}_e$ [96]. A rise of neutral pressure can result from two phenomena: a) the ion flux has increased, thus the recycling increases and therefore as a consequence the neutral pressure or b) because
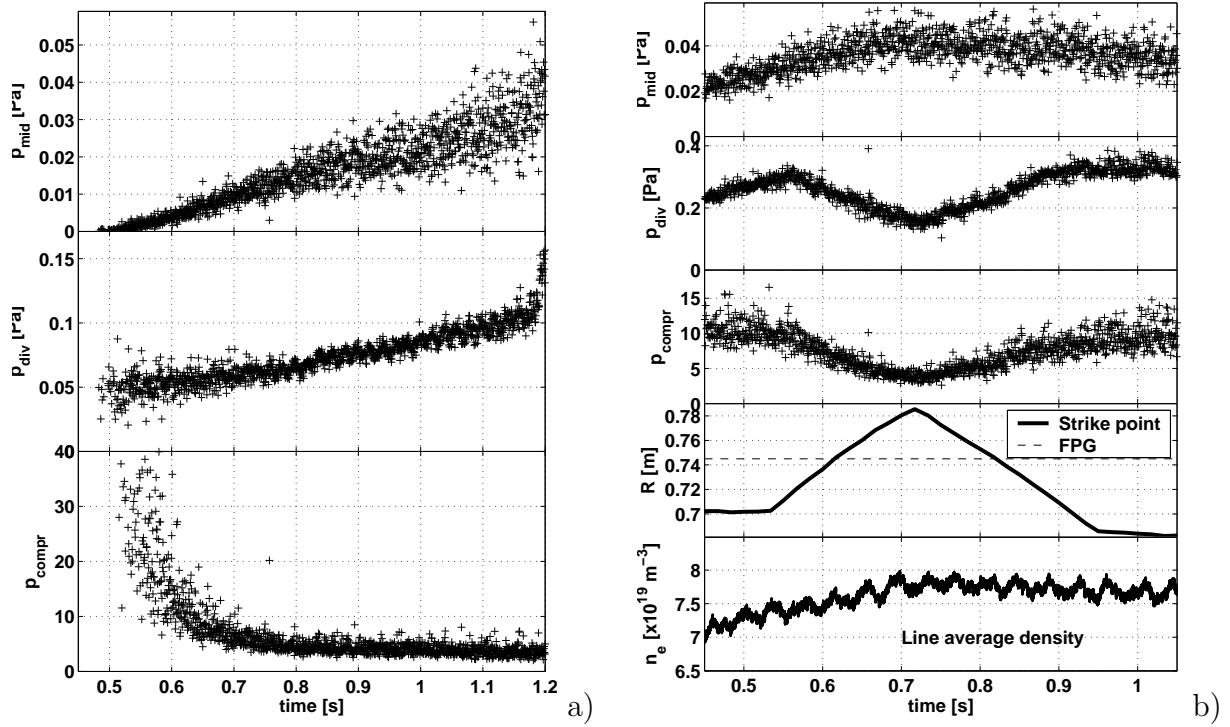
Figure 5.12: *a) Composite of midplane and divertor neutral pressures, together with the resulting compression ratio for the D discharge #20557 shown in figure 5.8 a. b) Pressure and compression ratio measurements for a medium to high $\bar{n}_e$ discharge during a sweep of the outer strike point position (#20585). Note that the sweep was performed at larger flux expansion ($f_{exp} \sim 10$).*

ions have transferred momentum through CX reactions to neutrals and the ion flux is decreasing. Since p_{div} increases with decreasing j_{SAT}, the neutrals transport the excess ion momentum to the walls and process (b) should thus be invoked for the divertor, as is also expected to occur during detachment (see Section 2.9). At the midplane the situation is less clear since the first wall ion flux is not measured. Horizontal D_α chords at the same vertical location as the RCP measure an increase of emissivity with rising density and assuming that volumetric recombination is unlikely to occur upstream ($T_e \gg 1 - 2eV$, see e.g. Fig. 5.13), the increase of emissivity there is a signature of increasing recycling at the main chamber walls and therefore of an increasing ion flux, which is reflected in an increase of neutral pressure. The compression ratio decreases, implying that the TCV

divertor is either becoming more transparent for neutrals, thus allowing them to escape from the target regions upstream, or that the perpendicular particle flux to the main chamber walls is increasing faster than the increase of momentum transfer in the divertor or a combination of the two.

During both D and He discharges, although the vertical position of the inner strike point remains constant throughout the discharge the outer strike point is observed to move slowly inwards. Typically, if the outer strike point is located at $R = 0.74m$ when the divertor is formed, it will have moved inwards to $R = 0.7m$ by the end of the divertor phase. This is due to uncompensated ohmic field components and could in principle be rectified but would require significant modifications to discharge preparation.

A decrease of p_{div} could therefore also be associated with a movement of the strike point since the pressure at the gauge will vary according to the profile of j_{SAT}. Figure 5.12 (b) shows the pressures and compression ratios during a deliberate strike point sweep at fixed $\bar{n}_e$ in the range $7 - 8 \times 10^{19} m^{-3}$ (but higher flux expansion than in #20557). This density is $\sim 75\%$ of the density limit in this type of discharge. Figure 5.12b clearly shows that the pressure at the gauge drops, reducing the compression ratio when the gauge is located in the PFR (i.e. for $R > 0.74m$). But for R in the range $0.70 \rightarrow 0.74m$, the variation in compression ratio is not large, likely due to the relatively broad target profiles at these densities (see Fig. 5.15b or 5.21b). Since for all discharges in which detachment has been studied the gauge is positioned well inside the divertor SOL, it may be concluded that the low compression ratios observed at high densities are not an artifact of strike point position drifts.

In what follows, all upstream and target profiles have been mapped to the outer midplane are shown in terms of distance from the separatrix if not explicitly stated otherwise. Before comparing the target profiles for He and D discharges, figure 5.13 illustrates example upstream n_e, T_e and electron pressure p_e profiles from the RCP and edge TS systems at low and high $\bar{n}_e$. The profiles, at least measured by Thomson scattering, are very similar for both discharges, especially in view of the experimental error bars estimated in Section

5.2.1.2. Such similarity in edge profiles for matched conditions in D and He has also been
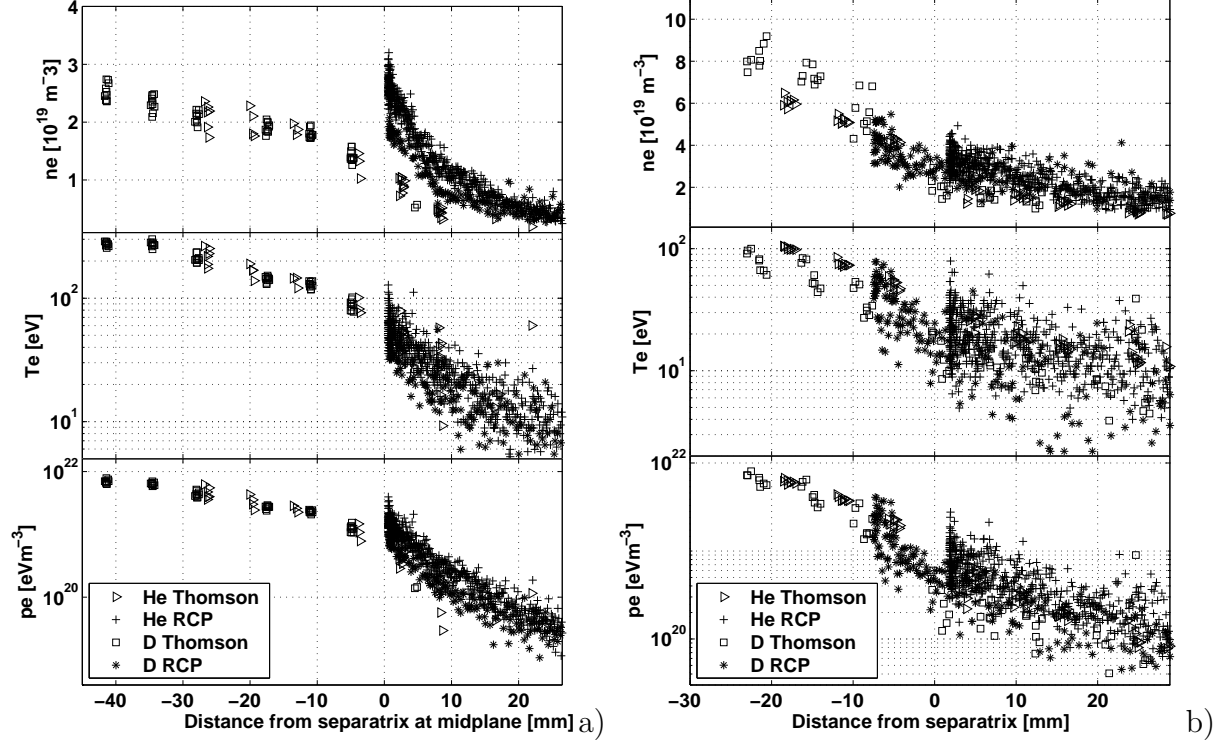
Figure 5.13: *Comparison of upstream midplane profiles of He and D discharges for similar $\bar{n}_e$, with a) a low density case at $\bar{n}_e \approx 3.5 \times 10^{19} m^{-3}$ (He #26212, D #26979) and b) at $\bar{n}_e \approx 10^{20} m^{-3}$ ($\sim 10\%$ higher in He. He #26222, D #24532)*

seen at JET [167]. It is interesting to note that especially at low densities, during which Mach flows with high Mach numbers ($M_\parallel \approx 0.4$ close to the separatrix) are also measured on TCV [104], the RCP measures higher densities than those measured by edge Thomson, whilst at high densities agreement improves. At high densities, fluid flows in the SOL are observed to be smaller ($M_\parallel < 0.2$), as expected qualitatively on the basis of classical drift theory (Section 2.10). As described in Section 5.2.1.1, errors in the derivation of n_e from Langmuir probes are likely to occur when $T_i \neq T_e$ and at high values of $M_\parallel$, for which these data are not corrected. The edge TS n_e and T_e profiles are also consistent with those from the main TS system, as shown in the high density example of Figure 5.14 where the data are from both systems are combined[4]. Despite the scatter in the

---

[4]the same is also observed at low $\bar{n}_e$
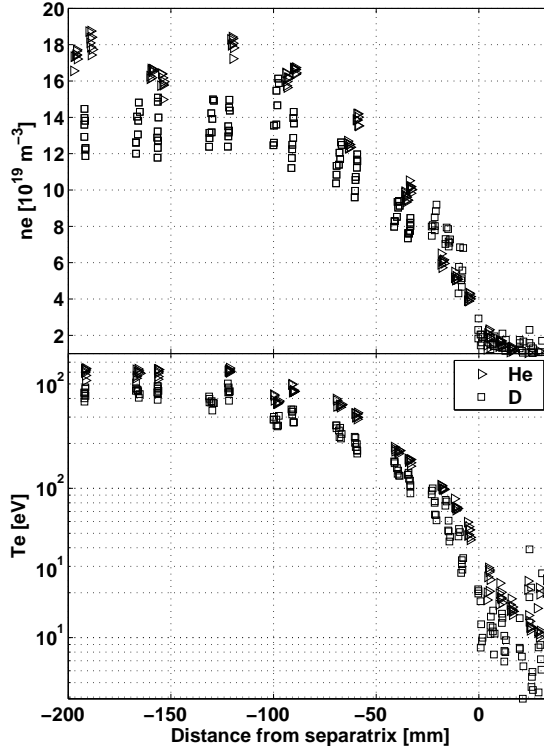
Figure 5.14: *Upstream n_e and T_e profiles for He (#26222) and D (#24532) as in figure 5.13b, now completing edge TS data with that from the main Thomson system at $\bar{n}_e \approx 10^{20} m^{-3}$ ($\bar{n}_e \sim 10\%$ higher in He).*

RCP data, T_e profiles from the two systems (RCP and TS) agree extremely well at both densities, making it unlikely that radial shifts need to be applied to account for imprecise knowledge of diagnostic spatial positions. The density profiles show a distinct tendency to flatten in the far SOL with increasing $\bar{n}_e$. Such trends are seen regularly elsewhere and have been associated with the main chamber recycling regime [42] (see also Section 2.5.4).

Figure 5.15 compares outer target profiles for low and high $\bar{n}_e$ for the matched He and D discharges of figures 5.8 and 5.9. Apart from a slightly higher target ion flux in D, the two discharges differ only slightly in terms of upstream and target profiles at low $\bar{n}_e$. The picture is very different at high upstream densities. Figure 5.15(b) clearly shows very strong detachment in the deuterium plasma with the peak ion flux reduced by a factor ~ 7. Since in both cases the slow strike point drift referred to earlier occurs, the large
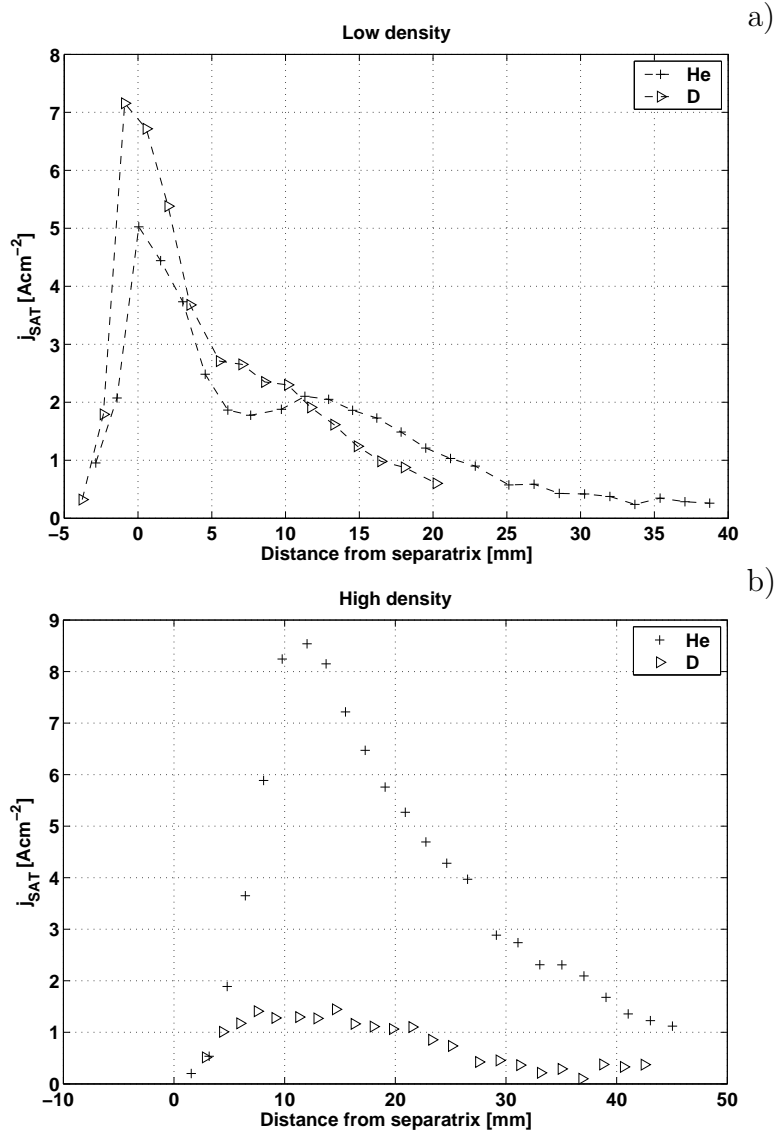
Figure 5.15: *Comparison of outer target j_{SAT} profiles mapped to the midplane for He and D at (a) low and (b) high $\bar{n}_e$ for identical discharges as in figure 5.13 (data averaged over $t = 0.1s$).*

reduction in j_{SAT} seen in D cannot be ascribed to this movement. In He the peak target flux increases by $\sim 60\%$ from low to high $\bar{n}_e$ and there is no apparent sign of detachment. The peak values of j_{SAT} for He and D differ by a factor of ~ 8 for identical upstream conditions at high density.

The apparent movement of the profile peak position with respect to the separatrix in

passing from low into high $\bar{n}_e$ is not completely understood. Shifts in the peak of $\sim 5mm$ (midplane) are typically observed in diverted discharges of this type, even if the density is constant throughout the discharge (at low or high density). As mentioned earlier, the strike point typically moves inward by $\sim 40mm$ at the targets due to uncompensated ohmic fields. Some of the shift may be accounted for by differences between the reonstruction accuracy throughout the strike point movement (as the strike point moves towards or away from in-vessel Mirnov coils). Further shifts can occur at higher density due to transport effects in the divertor and can be seen in the code simulations to be shown later. But these are insufficient to account for the full $10mm$ midplane shift seen in Fig. 5.15.

Returning to the issue of detachment, Figure 5.16 compares the integrated currents measured across the outer target during D and He fueled density ramps and calculates the DOD (see Section 2.9) from this integral current and also from j_{SAT} near the strike point at the beginning of the divertor phase. The integral current (Fig. 5.16a) demonstrates
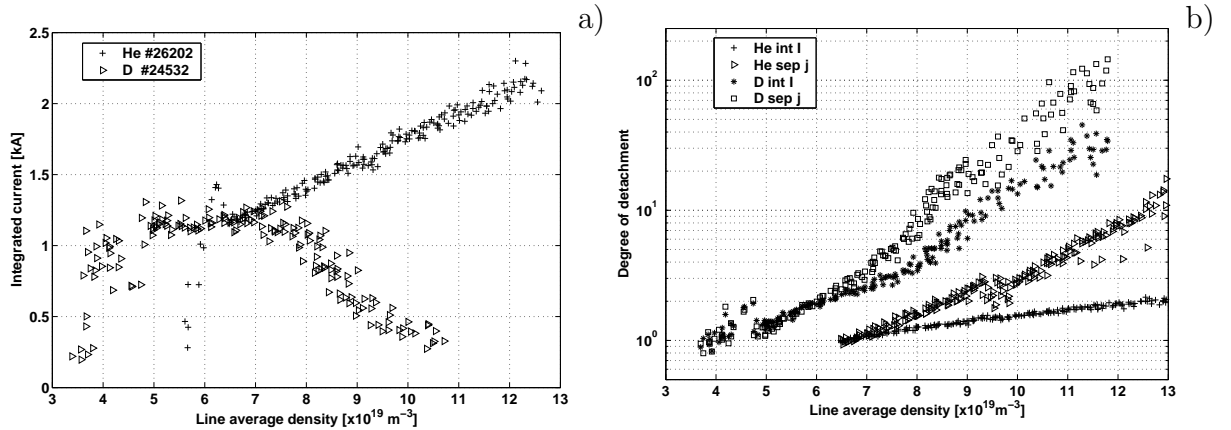
Figure 5.16: *Comparison of He (#26202) and D (#24532) density ramp discharges for the density ramp dependence of (a) the integral target current and (b) the DOD from j_{SAT} close to strike point position (probe #5, + He, * D) and integral current ($\triangleright$ He, $\square$ D).*

once again the striking difference between He and D with regard to the detachment behaviour. The decrease at $\bar{n}_e > 7 - 8.0 \times 10^{19}m^{-3}$ in deuterium usually coincides with a steep increase of the D_α emission from the divertor volume (see figure 5.11). These latter

observations for D-fueled discharges have been extensively reported for different outer divertor flux expansions and varying heating power (plasma current) [16, 24, 162].

According to Table 2.3 the DOD values in Figure 5.16(b) indicate that the He discharge at most reaches partial detachment for the integral current at the end of the density ramp. It appears, however, that detachment is reached close to the strike point in He (at least close to probe #5 for which the local DOD is shown here). In fact this is only because the profile peak has moved away from the nominal separatrix position (Fig. 5.15) as described earlier. It may therefore be concluded that detachment does not occur at the outer strike point in He plasmas at $340kA$. Similar conclusions also apply to the inner target as discussed previously. In contrast, the integral and peak DOD values for deuterium in Fig. 5.16b clearly show that almost complete detachment occurs (at least according to the criteria of Table 2.3) for the same upstream conditions as in He.

For the upstream conditions and heating power reported thus far, the outer target in He thus remains in the sheath-limited to conduction-limited regime throughout the density ramp. The integral j_{SAT} is only approximately linearly dependent on upstream density and parallel temperature gradients arise with target temperatures at most a factor 5 lower than upstream T_e (compare also figures 5.13, 5.41 and 5.42).

In deuterium, the outer target is in the conduction-limited, high recycling regime already in the initial phase of the density ramp and begins detaching early on at $\bar{n}_e \sim 6.5 \times 10^{19} m^{-3}$, with an even stronger signature for $\bar{n}_e \approx 7.5 - 8.5 \times 10^{19} m^{-3}$. The inner target remains attached at all densities.

The deuterium density ramp discharge #17823 has been exhaustively studied in earlier papers describing TCV detachment [16, 24]. It is one of the few discharges in the standard divertor configuration at $340kA$ for which good reconstructions of the poloidal distribution of the total radiation are available. Figure 5.17 compiles fractional radiated powers from different regions together with P_{SOL} and where it should be noted that P_{ohm} increases throughout the discharge (Fig. 5.8). At the onset of detachment at $(\bar{n}_e \sim 6 \times 10^{19} m^{-3})$, more than 50% of the total input power is being radiated, of which the largest fraction is
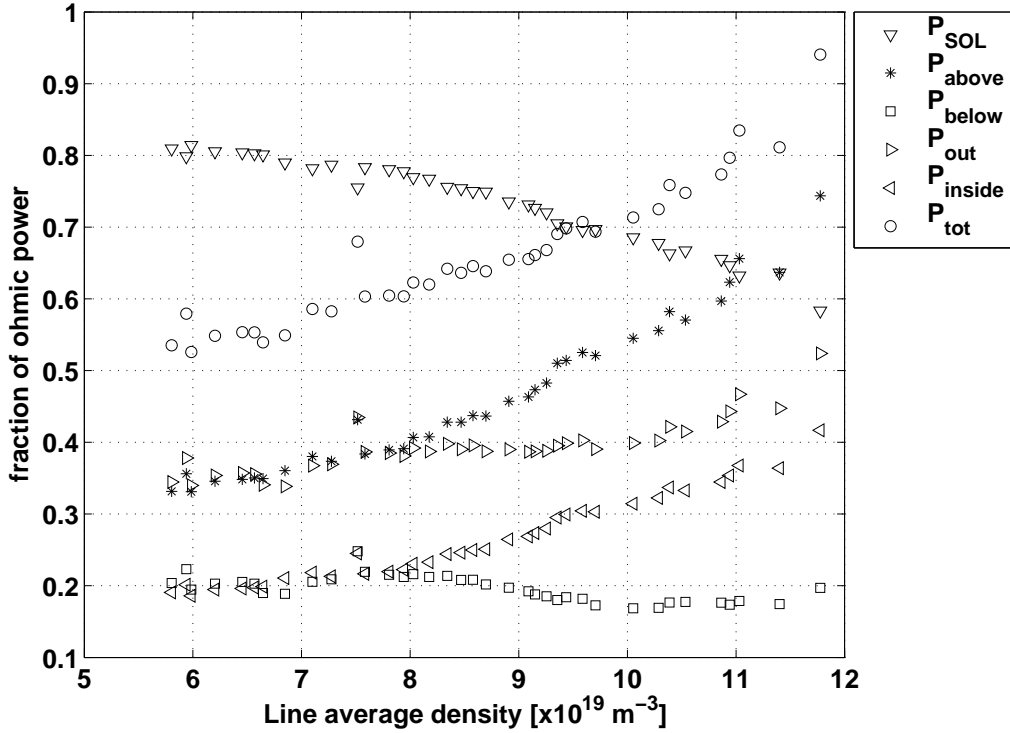
Figure 5.17: *Radiated power fractions (wrt P_{ohm}) and P_{SOL}/P_{ohm} from tomographic reconstruction of the D discharge #17823. The fraction of total power radiated (P_{tot}) is shown together with that radiated above (P_{above}) and below (P_{below}) the X-point, inside (P_{inside}) and outside ($P_{outside}$) the separatrix.*

above the X-point outside the separatrix (although caution should be exercised given that resolution in the reconstruction is restricted in the separatrix vicinity). As $\bar{n}_e$ increases, the fraction of radiation above the X-point increases whilst more power is radiated from inside the LCFS. At the highest densities, more than 60% of the heating power is radiated above the X-point and thus cannot reach the divertor volume. Recalling that the inner target is at about the same vertical position as the X-point (Fig. 5.2), part of P_{above} includes power radiated from the volume of the inner divertor. Throughout the discharge the fraction of radiation from below the X-point, which essentially includes the entire outer divertor volume, remains approximately constant. Closer inspection of the data in Fig. 5.17 reveals that at the highest $\bar{n}_e$, only $\sim 1/3$ of P_{SOL} reaches the divertor volumes.

Although the accuracy of the bolometric reconstruction may be questioned for the rea-

sons given in Section 5.2.1.4, it can be concluded that for $340kA$ density ramp discharges, $P_{SOL} \approx 440kW$ and remains relatively constant throughout the density ramp, whilst at the same time the divertor volumes might only be receiving $\sim 150kW$ of conducted power after the onset of detachment. One may also ask how a relatively large fraction of power might be radiated above the X-point, especially outside the separatrix. The implication is that the main chamber walls and not just the divertor targets can be an important impurity source.

Unfortunately, technical problems with the bolometry diagnostic have prevented detailed reconstructions of the poloidal distribution in the He discharges. It is hoped that the new AXUV system with much improved spatial resolution might provide better reconstructions in the future.

An important quantity in the simulations presented later will be the level of recycling to associate to the wall surfaces. Estimates of R_{global}, Section 2.1.5, can be obtained directly from the temporal behaviour of plasma density in a machine like TCV with no active pumping. Using equation 2.18 and assuming $\tau_p \sim \tau_e$ (where the electron confinement time is estimated from [169]) it is generally found that $R_{global} > 0.95$ in standard deuterium discharges. Figure 5.18 compiles time traces of various quantities used to derive R_{global} assuming two different values of τ_p, representing the approximate maximum and minimum values found for τ_e in ohmic plasmas. In He, $R_{global} > 0.98$ is generally found.

Figure 5.19 provides support for the estimate of $R_{global} \neq 1$ in figure 5.18 since $\bar{n}_e$ is observed to decrease slowly in the low density case (#26979), even in the presence of a residual gas puff. An estimate of the magnitude of this wall pumping can be made by comparing target ion fluxes with gas input. Referring again to discharge #26979 in Fig. 5.19 and assuming constant $\bar{n}_e$ between $0.5s$ and $1.2s$, the integral target flux is $\sim 1kA$ or $6.2 \times 10^{21} D^+ s^{-1}$ (see Fig. 5.16 at low $\bar{n}_e$).

The gas puff is the only net particle source for the entire system and in the same period $\sim 0.25 \times 10^{21}$ D_2 molecules (and thus 5×10^{20} D atoms) are added to the system. Assuming no volumetric losses, similar integral ion fluxes to the inner and outer targets
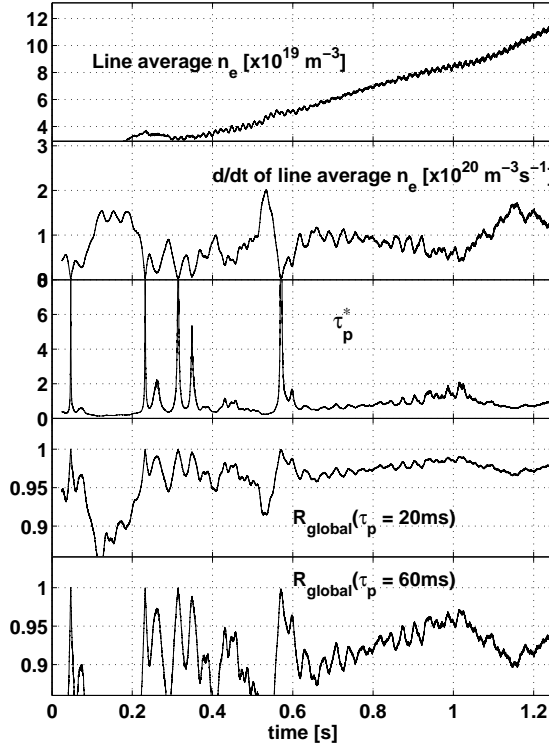
Figure 5.18: *Composite for D discharge #24532 with τ_p^* calculated according to eqn. 2.17 (but using $\bar{n}_e$ instead of $< n_e >$) and the global recycling coefficient (eqn. 2.18) derived assuming particle confinement times of $\tau_p = 20ms$ and $60ms$, where $\tau_p \sim \tau_e$ is assumed in the absence of any knowledge of τ_p and where τ_e for TCV is extracted from [169]).*

and negligible main chamber wall fluxes, the ratio of puffed particles to total ion flux is $\approx 4\%$, implying $R_{global} \approx 0.96$, and in rough agreement with the values presented in figure 5.18.

5.2.2.2 Comparing deuterium discharges at $340kA$ and $260kA$

In forward field, ohmic L-modes in the diverted configurations discussed here are only possible if $I_p < 260kA$. Above this value ELM-free H-modes are obtained, making comparisons in quiescent conditions impossible between the two field directions. Before comparing low I_p, D plasmas in forward and reversed field, it is thus instructive to compare otherwise identical pulses at $260kA$ with those at $340kA$ which have been discussed at
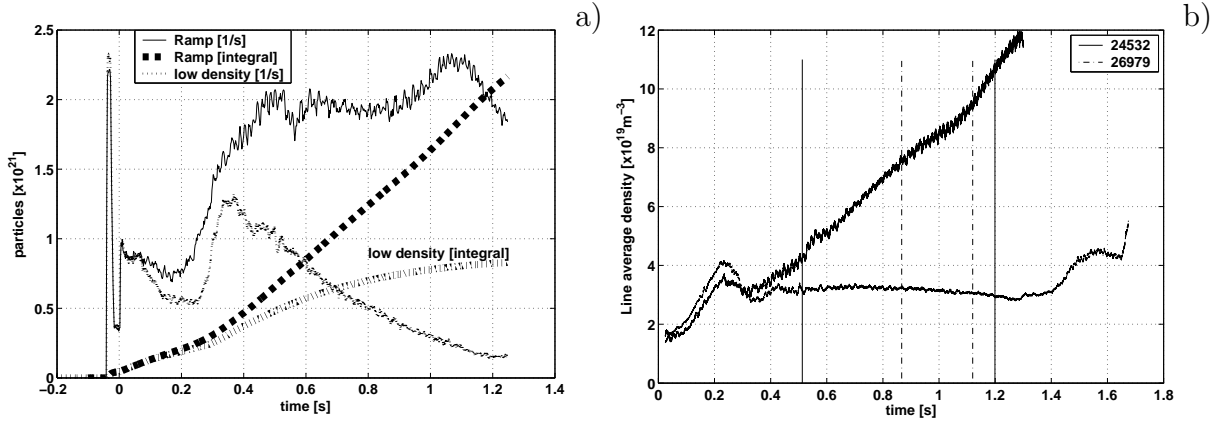
Figure 5.19: *Particles puffed into a D discharge during a density ramp (#24532) and during a low density discharge (#26979, $\bar{n}_e \approx 3.5 \times 10^{19} m^{-3}$), (a) the measured particle flux per second and the total number of particles (assuming $T = 300K$ when converting to mbar l), (b) $\bar{n}_e$ for the two discharges - the vertical lines indicate the times at which RCP measurements are made (for later use).*

length above.

As expected, the maximum density reached during discharges with $I_p = 260kA$ was $\sim 60\%$ of that for $I_p = 340kA$ ($\sim 6.5 \times 10^{19}$ vs. $\sim 1.1 \times 10^{20} m^{-3}$). Figure 5.20 compares the upstream profiles at fixed $\bar{n}_e \approx 6.5 \times 10^{19} m^{-3}$ for the two plasma currents. The similar upstream density profiles reflect the fixed $\bar{n}_e$ of the comparison but the lower P_{ohm} means that less power crosses the separatrix and the T_e profile is lower at lower I_p. In the context of the 2-point model (Section 2.8), $T_u \propto P_{SOL}$ if T_t is low and the magnetic geometry unchanged.

Figure 5.21 compares the ion fluxes at the outer target at low and high densities for these two plasma currents. At low $\bar{n}_e$ and thus low upstream density, the j_{SAT} profiles are very similar. Assuming that λ_q does not change as I_p decreases, the SOL parallel power flux is dependent only on P_{SOL}. The target ion flux is weakly inversely dependent on $q_\parallel$ so that a $\sim 30\%$ higher Γ_t ($\propto q_\parallel^{-3/7}$ eqn. 2.103) might be expected at lower power. In addition, $\Gamma_t \propto L^{4/7}$ and so reducing I_p increases q_{95}, leading to a further enhancment expected in Γ_t compared with higher I_p. This is not observed, indicating possibly that at lower P_{SOL} detachment begins even earlier in the density ramp. At higher density (Fig.
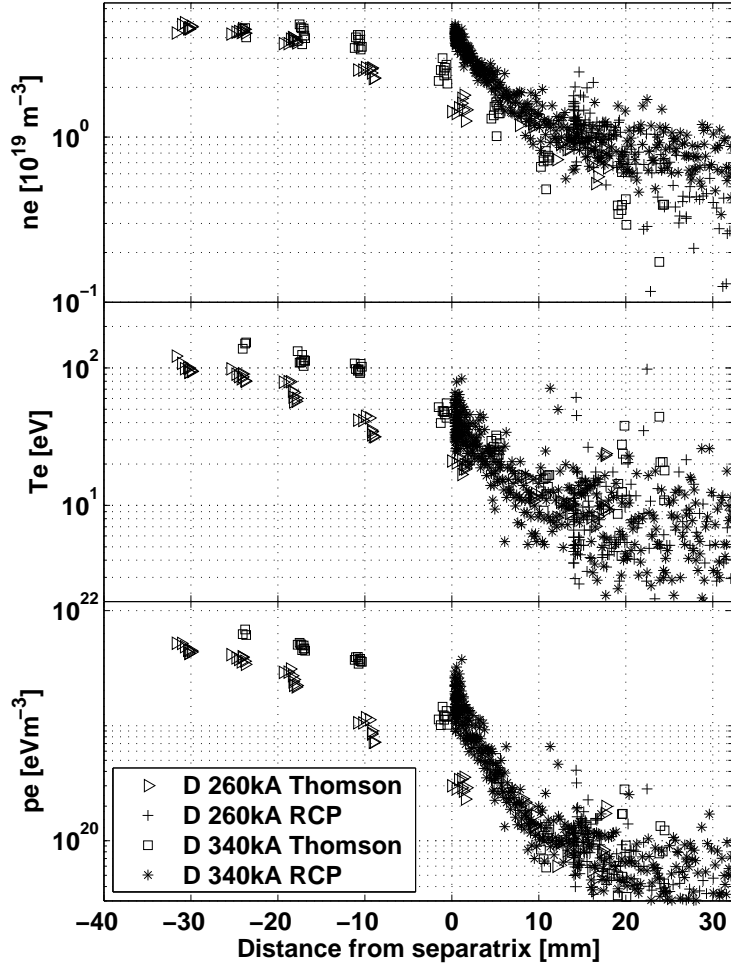
Figure 5.20: *Upstream midplane profiles for D discharges with 260kA (#24452) and 340kA (#26066) at identical $\bar{n}_e \approx 6.5 \times 10^{19} m^{-3}$ (corresponding to the highest $\bar{n}_e$ reached at 260kA)*

5.21b), but still only medium density for the 340kA discharge, the peak value of j_{SAT} has decreased and thus detachment begins earlier compared to higher current. This can also be seen in Fig. 5.23 where the $\bar{n}_e$ dependence of the integral currents at 260kA and 340kA are compared.

Thus, even though the 2-point model (without corrections) would predict higher fluxes at low input power for fixed n_u when reducing I_p, lower target fluxes are measured.
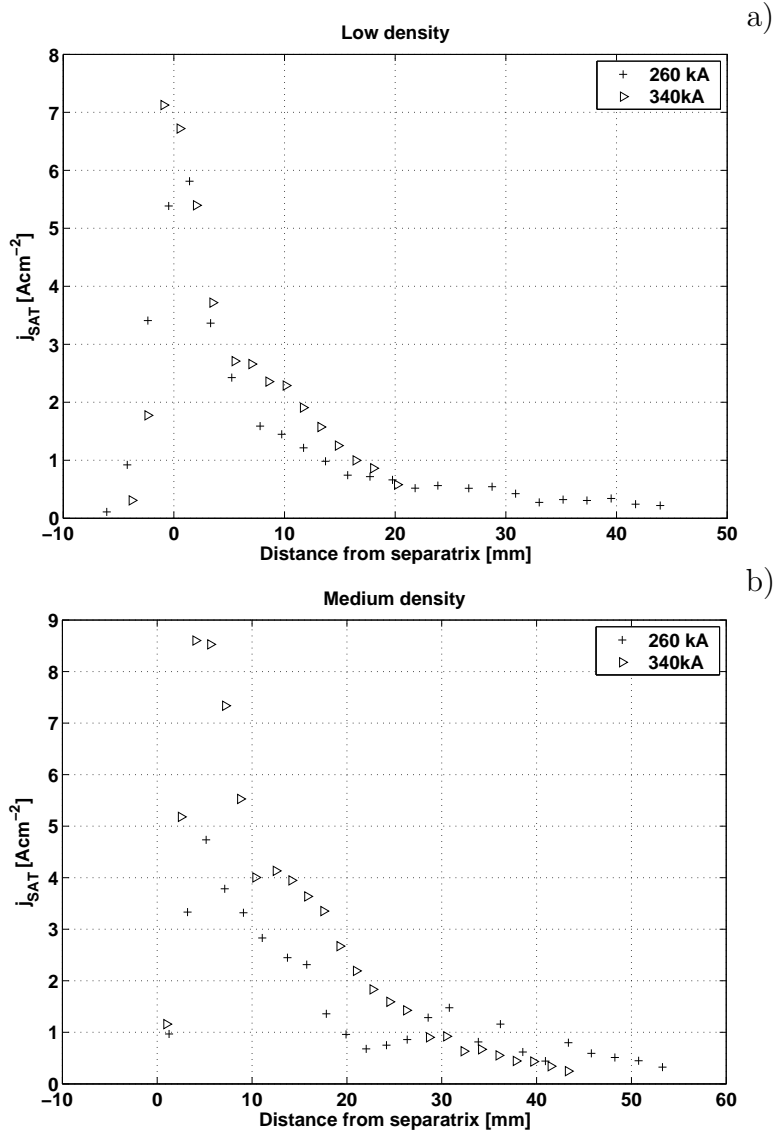
Figure 5.21: *Comparing outer target j_{SAT} profiles mapped to outer midplane in D discharges with $260kA$ (#24458) and $340kA$ (#26979) (a) $\bar{n}_e \approx 3.5 \times 10^{19}m^{-3}$ and (b) $\bar{n}_e \approx 6.5 \times 10^{19}m^{-3}$. Note that this latter is only a medium density for $I_p = 340kA$ and close to the maximum density reached at $260kA$.*

5.2.2.3 Comparing D fueled discharges at $260kA$ in reversed and forward field

One way in which the possible influence of drifts on the detachment threshold can be studied is by comparing identical discharges in forward and reversed field. For reasons alluded to earlier and associated with the L-H transition threshold for favorable $\vec{B} \times \nabla B$

direction, this has been performed at $I_p = 260kA$ in the standard divertor configuration. Both I_p and B_T must be reversed to maintain constant magnetic helicity. This is both for diagnostic purposes (fixed Langmuir probes and RCP) and to avoid machine conditioning issues.

Good pairs of matched forward and reversed field density ramp and constant $\bar{n}_e$ discharges have been obtained. The density limit appears to be very similar. Figure 5.22 compiles upstream profiles of n_e, T_e and p_e for identical low and high $\bar{n}_e$ at 260kA. Within
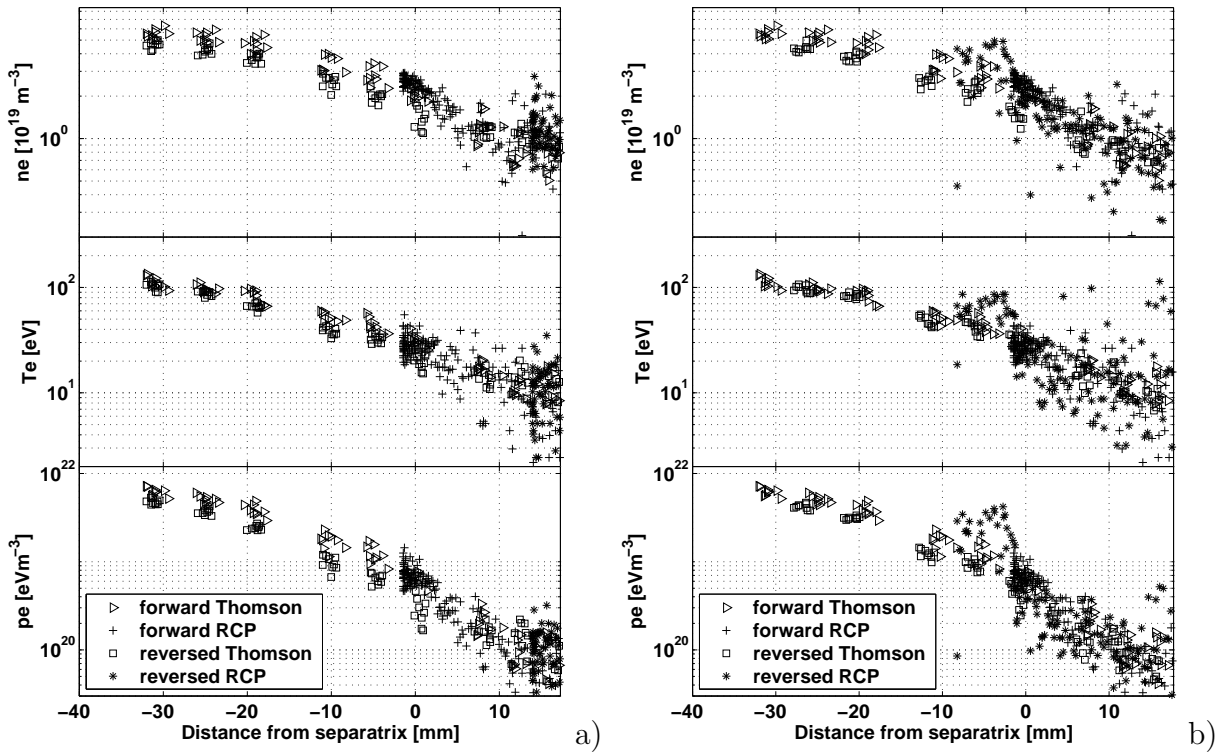
Figure 5.22: *Upstream midplane mapped profiles from deuterium density ramp discharges in forward (#24396) and reversed (#24422,#24459) field at 260kA for (a) low density, $\bar{n}_e \approx 3.5 \times 10^{19} m^{-3}$ and (b) medium to high density, $\bar{n}_e \approx 6 \times 10^{19} m^{-3}$.*

experimental scatter, field direction affects neither the magnitude nor the shape of the upstream profiles. The integral outer target currents for forward and reversed field, including, for illustration, the data from #24532 at 340kA in reversed field, are compared in figure 5.23 as a function of $\bar{n}_e$. A clear difference can only be seen for intermediate $\bar{n}_e$ when comparing discharges at $I_p = 260kA$. Whilst in reversed field the integrated
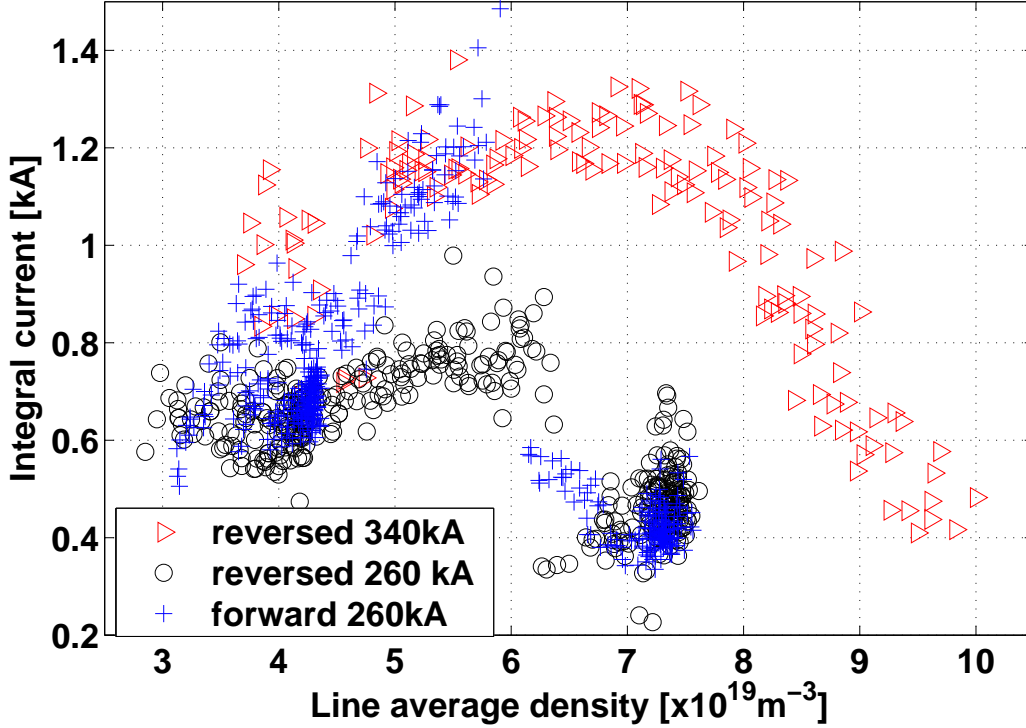
Figure 5.23: *Density dependence of the integral current at the outer target for deuterium density ramp discharges at 260kA in forward field (#24395, #26797, #26814) and at 260kA (#24459, #26953, #26814) and 340kA (#24532) in reversed field.*

current first increases weakly and begins to decrease at $\bar{n}_e \sim 6 \times 10^{19} m^{-3}$, in forward field the integral current rises at a similar rate as the reversed field discharge at $I_p = 340kA$, but then collapses to values similar to those for the $I_p = 260kA$ discharges in reversed field for $\bar{n}_e > 6 \times 10^{19} m^{-3}$.

Figures 5.24 and 5.25 compare the n_e, T_e and j_{SAT} profiles in forward and reversed field at the inner and outer targets. In general, the differences in the profiles between forward and reversed are more pronounced at the inner compared with the outer target at all densities. In addition, it appears that at lower I_p in reversed field (cf. the standard case at 340kA), detachment also occurs at the inner target at the highest density. This is also true in forward field at low current but to a somewhat lower degree. With regard to T_e, the major differences appear at the outer target where the reversed field temperatures are systematically higher than in forward field at all densities through most of the SOL. At

133
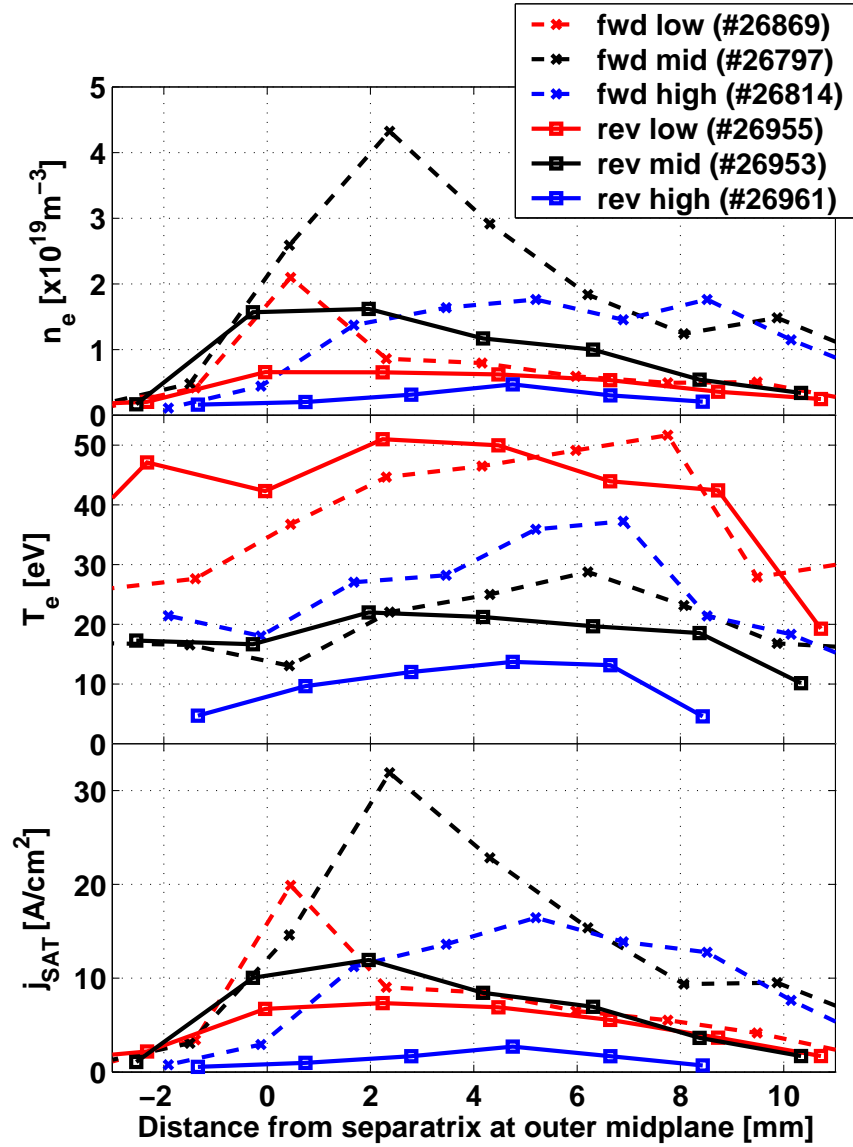
Figure 5.24: *Comparing midplane mapped inner target profiles in forward and reversed field at $I_p = 260kA$ for 3 different upstream densities; low density: $\bar{n}_e \approx 2 \times 10^{19}m^{-3}$, medium density: $\bar{n}_e \approx 4 \times 10^{19}m^{-3}$, high density: $\bar{n}_e \approx 7.3 \times 10^{19}m^{-3}$. The profiles have been averaged over $\Delta t = 0.1s$ around $t = 1.0s$ in each discharge.*

the inner target, forward and reversed field yield similar T_e profiles except at the highest density. In terms of particle flux, the inner target (Fig. 5.24) generally recieves a higher flux in forward field than in reversed field. At the outer (Fig. 5.25) the only significant difference between the two field directions appears at medium upstream density, where it
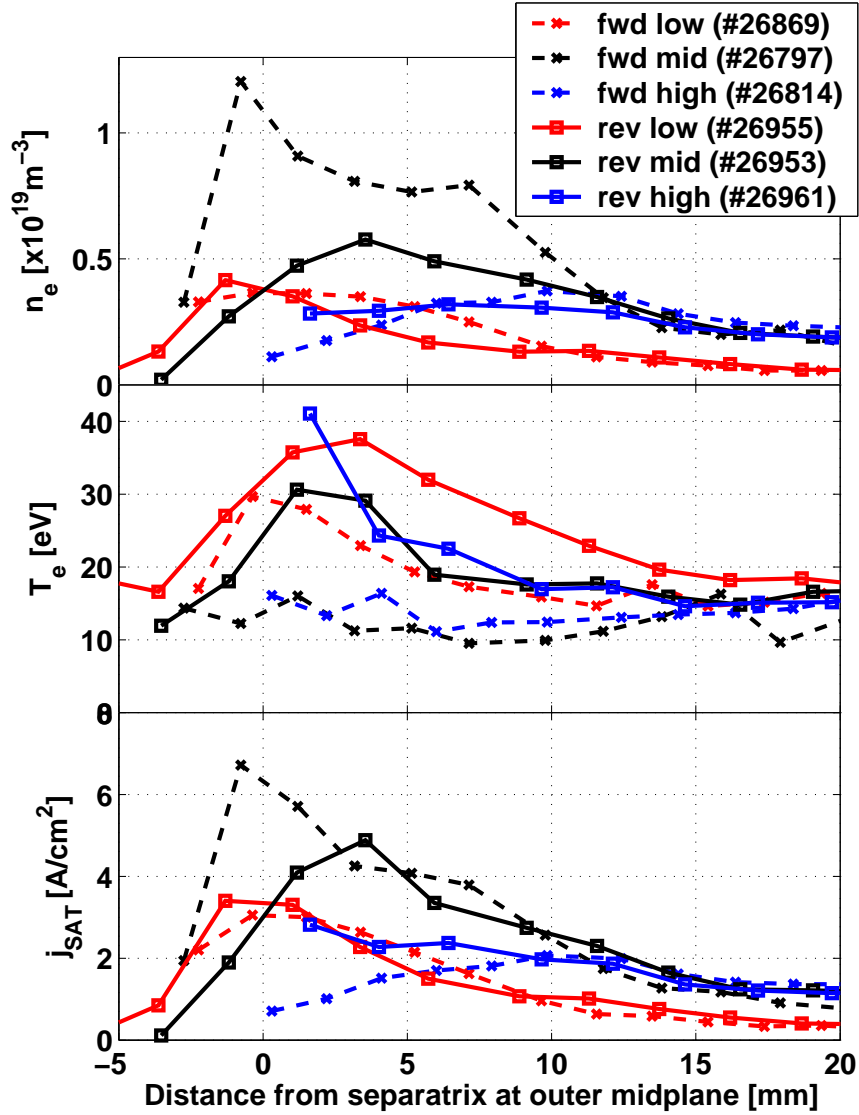
Figure 5.25: *Comparing midplane mapped outer target profiles in forward and reversed field at $I_p = 260kA$ for 3 different upstream densities; low density: $\bar{n}_e \approx 2 \times 10^{19}m^{-3}$, medium density: $\bar{n}_e \approx 4 \times 10^{19}m^{-3}$, high density: $\bar{n}_e \approx 7.3 \times 10^{19}m^{-3}$. The profiles have been averaged over $\Delta t = 0.1s$ around $t = 1.0s$ in each discharge.*

seems clear that detachment in the strike point vicinity is beginning in reversed field but has not yet begun in forward field.

Leaving aside for the moment the issue of differences in target T_e between the two field directions, the observed target flux response to field reversal and upstream density

is consistent with the presence of a radial $\vec{E} \times \vec{B}$ drift (Section 2.10.3) which would be expected to move particles from the HFS to the LFS for reversed B_Φ. This $\vec{E}_\Theta \times \vec{B}$ drift arises only in the presence of strong poloidal gradients in T_i and T_e, a condition manifestly satisfied in TCV even at relatively low density (at least according to the simulations to be presented later - see for example Fig. 5.32). Under these conditions, the influence of the poloidal $\vec{E}_r \times \vec{B}$ drift is expected to be negligible in comparison (Table 2.4). As mentioned in Section 2.10.6, this increased supply of particles will augment the local density, mostly in the vicinity of the divertor throat (the unconventional TCV divertor geometry excludes any significant convective movement of particles from the inner divertor into the more extended outer divertor leg). This accumulation will locally depress the temperature (since pressure must be conserved), likely promoting energy loss due to increased local radiation (from carbon impurities). As a consequence, less energy is available to the outer divertor and the onset of detachment may occur earlier in reversed field for much the same reasons (power starvation by increased upstream radiation) that will be invoked later in this chapter to explain the anomalous detachment itself.

In this simple picture therefore, the effect of drifts is to promote a slightly earlier onset of detachment in reversed field (as seen in the j_{SAT} profiles at medium density in Fig. 5.25). Enhanced upstream radiation losses might also explain why the reversed field integral currents in Fig. 5.23 are lower than in forward field at all but the lowest densities. Radial $\vec{E} \times \vec{B}$ drifts do not, however, appear to be consistent with the outer target T_e variation with field direction. On the basis of both poloidal and radial $\vec{E} \times \vec{B}$ drifts, the outer target might be expected to be hotter in forward field. Instead, the opposite is observed. No explanation is offered here save to say that simulations later in this chapter will demonstrate that probe measured electron temperatures are to be treated with extreme cautions except at the lowest densities. What is also interesting is the observation that there is little asymmetry in any of the parameters between field directions at the outer target for the lowest density. It seems to be relatively clear, however, that the observed outer target detachment occurs for both field directions for similar upstream densities at fixed I_p. Ultimately, it may be that the unconventional TCV divertor geometry itself

dominates over any drift effect in these simple ohmic plasmas. Further investigation requires detailed radiation balance in the divertor and main SOL, together with code runs including drifts. The latter has not, unfortunately, been possible during this thesis.

5.3 Simulation

5.3.1 Introduction

The principal aim of the SOLPS5.0 simulations is to understand the driving mechanism for the observed outer target detachment in TCV ohmic plasmas. It will become quickly evident that with the 'standard' set of assumptions usually adopted in these code simulations, detachment cannot be obtained at all with the code. This was the essential conclusion reached in early attempts [16, 24] to understand the phenomena, as has been pointed out at the beginning of this chapter. The approach has been to systematically introduce more sophisticated options, particularly with reference to atomic and molecular physics, inspired by the observation that detachment appears to occur in TCV at values of plasma parameters in the divertor which are far from those in other tokamaks at which 'classical' detachment is seen to occur. The modeling efforts have also included the first ever SOL simulations in TCV pure He plasmas.

In the course of this 'stepwise' approach the reader will hopefully be convinced that it is fundamentally an issue of the assumed nature of perpendicular transport in the main SOL which is the main driver of the reversed field anomalous detachment. Once this is established, there is indeed room for the more exotic atomic and molecular physics to play an important role. As Section 5.2.2.3 has demonstrated, magnetic field direction does influence the onset but not the occurrence of detachment as a whole. Unfortunately, the significant difficulties experienced in obtaining converged solutions in coupled runs with drift terms activated have meant that their effects have not been studied here numerically. Nevertheless, although they almost certainly do play a role in triggering the 'earlier' onset of detachment, they are likely not the principal driver.

Henceforth, the code simulations focus on a single, intermediate outer target flux expansion case with magnetic equilibrium common to all the experimental data shown thus far. The grid used is shown in Fig. 5.26. It has been generated from the reconstructed equilibrium of discharge #24532 at $1.0s$ and extends $3cm$ inside and $1.8cm$ outside the midplane separatrix. It has 72 poloidal cells (numbered ix), including the guard cells at
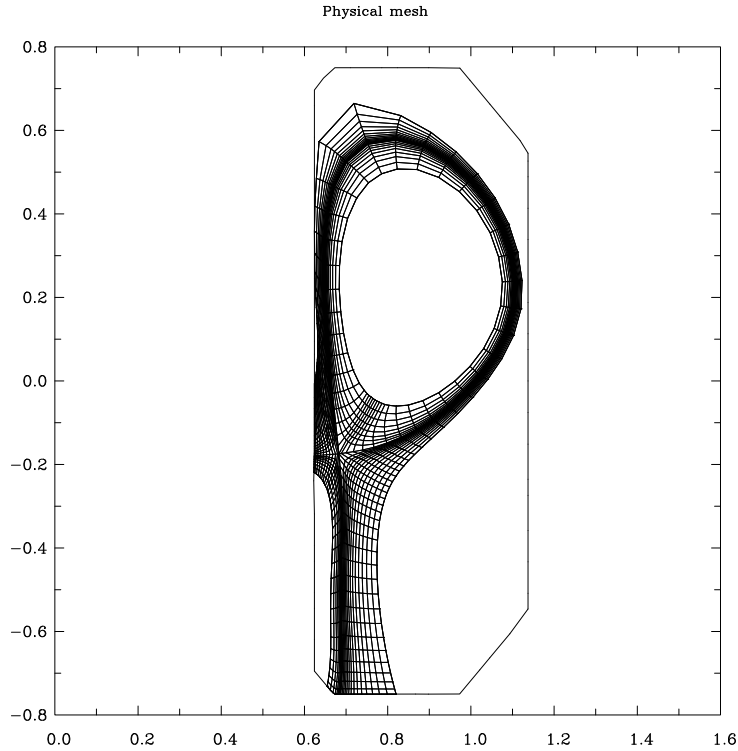
Figure 5.26: *Grid used for the majority of TCV simulations, generated from the magnetic equilibrium of discharge #24532 at 1s (axis units [m]).*

the inner and outer target and 24 radial cells (numbered *iy*) including the guard cells at the inner and outer grid boundaries, with the separatrix being located between cell numbers 9 and 10. The first 11 poloidal cells cover the inner divertor, 40 cells cover the main SOL and the last 21 the outer divertor. The ion species included in the fluid code for the simulations of deuterium plasmas are D^+ and all charge states of C, while for the He plasmas both He^+ and He^{2+} ions are included.

Unless otherwise stated, the following default assumptions have been adopted in all simulations presented:

- B2.5 coupled to EIRENE '99 is used for D plasma simulations, whilst EIRENE '96 is used for He plasmas (this is a purely 'historical' choice and is a result of the fact that simulations of JET pure He plasmas had been performed prior to the TCV work (see Chapter 6.3)[5].

---

[5]From a physical point it does not matter much which version of EIRENE is used for simulating pure

139

- The power crossing the separatrix is fixed at $P_{SOL} = 440kW$, corresponding to discharges with $I_p \approx 340kA$ and is assumed to be equally shared between electrons and ions. For most cases P_{SOL} is fixed at $iy = 8$ or $iy = 0$. The radial distance from the core boundary at which P_{SOL} is fixed turns out to be important only at high separatrix densities and high impurity content (and radiation) inside the LCFS as this then affects the power crossing the LCFS. The power crossing the core boundary, P_{core}, adapts to match P_{SOL}. Computational rings inside the iy chosen as the boundary for P_{SOL} should be excluded from interpretation, in particular at high upstream densities.

- The density is prescribed at the outer midplane separatrix (n_e^{sep}). A feedback mechanism is used on a gas puff, described as a point source inside EIRENE of D_2 for D plasmas and He for pure He plasmas. This increases the input particle flux if the computed density at the separatrix is below the required density and reduces it otherwise.

- For D plasmas a particle recycling coefficient of $R = 0.98$ is used on all surfaces, including the targets, based on the approximate values from experimental findings reported earlier (see Fig. 5.18 and related discussion). For He plasmas $R = 1$ is assumed at the targets and $R = 0.98$ on the main chamber walls. The actual value of the local recycling coefficient at any particular surface cannot be determined experimentally and it is likely that the value at the targets is closer to unity. Using a value below unity, however, facilitates convergence of the code since the evolving simulations can respond more quickly to densities exceeding the prescribed value at the separatrix given that ion target fluxes are in most cases higher than main chamber wall neutral fluxes.

- The core boundary is fully absorbing for neutrals. The total ion outflux from the core is equal to the neutral influx into the core and is redistributed equally over the entire inner core boundary.

He plasmas since molecular effects play no role (see also Section 3.1.4)

- Heat transmission coefficients with values $\gamma_e = 5.1$ and $\gamma_i = 3.5$ (a reasonable assumption when $T_e = T_i$, see Section 2.4) are assumed at both targets. In principle $\gamma_e + \gamma_i$ could be somewhere between 6.5 and 9 (see also figure 5.30).

- $M \geq 1$ at both targets.

- A decay length of $3cm$, as is often assumed in edge codes, is fixed at the north boundary for all ion densities (main ions plus C), T_i and T_e.

- The parallel velocities at the north and south boundaries are assumed to be zero. This is an adhoc assumption and no sensitivity study has been performed on this boundary condition.

- Electron and ion heat flux limits are fixed at $\alpha_e = 0.3$ and $\alpha_i = 10$ respectively. The latter effectively corresponds to prescribing no heat flux limit on the ions. The viscous stress limiter is set to 0.5.

- Physical sputtering is implemented according to the Roth-Bodansky formula [68].

- Chemical sputtering from D^+ and D impact is set to be 3.5% on all surfaces.

- Ion sputtering (physical and chemical) occurs only at the divertor targets. No ion sputtering is therefore assumed at the north boundary, corresponding to an absence of impurity release at the main chamber walls. The significance of this assumption will become evident later.

- Carbon impurities in all ionization states are assumed to be deposited on material surfaces with a sticking coefficient of unity.

Neutrals, first ionization and recombination processes resulting in neutrals are treated by EIRENE, in which the reactions listed in Table 5.1 are included in nearly all the simulations presented here. Data from a collisional radiative model (CRM) (as presented, for example, in [170]) are used to replace the previously employed direct ionization and recombination rates.

The production of H^- via instantaneous dissociation of H_2^- is neglected. The mean-free-path for its production through dissociation of H_2 via vibrational excitation is of the order of $12cm$ (AMJUEL, H.2 2.2.17) whilst its recombination through CX reactions with background ions (AMJUEL, H.4 7.2.3a) is of the order of $4mm$. It can therefore be assumed that the low quantities of particles produced are nearly instantaneously removed from the plasma and should not therefore play an important role in the overall dynamics. Due to the low percentage of C^+ ions compared to D^+ ions present in the plasma, volumetric recombination of C^+ is not included in the set of reactions.

Reaction	Type and number	Database
$H + e \rightarrow H^+ + 2e$	H.4 2.1.5	AMJUEL
$H + H^+ \rightarrow H^+ + H$	H.1, H.3 3.1.8	HYDHEL
$H_2 + e \rightarrow H + H + e$	H.4 2.2.5	AMJUEL
$H_2 + e \rightarrow H_2^+ + 2e$	H.4 2.2.9	AMJUEL
$H_2 + e \rightarrow H + H^+ + 2e$	H.4 2.2.10	AMJUEL
$H^+ + H_2 \rightarrow H^+ + H_2$	H.1, H.3 0.3	AMJUEL
$H^+ + H_2 \rightarrow H + H_2^+$	H.2 3.2.3	AMJUEL
$H_2^+ + e \rightarrow H + H^+ + e$	H.4 2.2.12	AMJUEL
$H_2^+ + e \rightarrow 2H^+ + e$	H.4 2.2.11	AMJUEL
$H_2^+ + e \rightarrow 2H + e$	H.4 2.2.14	AMJUEL
$H^+ + \text{electrons(s)} \rightarrow H + h\nu$ or electrons	H.4 2.2.12	AMJUEL
$C + e \rightarrow C^+ + 2e$	H.4 2.6A0	AMJUEL
$H^+ + C \rightarrow C^+ + H$	H.3 2.2.14	METHAN

Table 5.1: *List of reactions common to all simulations. The reaction rates are given for H plasmas [65] but should also be valid for deuterium plasmas too, [171]). The second column defines the type of reaction and its identification number, whilst the third column the name of the database (see also [65])*

As for experimental data all radial upstream and target profiles shown in the following sections are mapped to the outer midplane and presented in terms of distance from the separatrix if not explicitly stated otherwise. All simulated target profiles for n_e that are compared to experimental data include the actual value from the code (denoted with symbols $*-$) and the predicted density assuming $T_i = T_e$ (denoted with symbols $\triangleright-$), as is assumed when computing n_e from Langmuir probe measurements (denoted with '.') of j_{SAT} and T_e.

5.3.2 Spatially constant diffusion coefficient

The first simulations of these types of TCV discharges were performed using the SOLPS4.0 code with spatially constant fixed transport coefficients. Section 2.5 has emphasized that there is no a priori knowledge of which values should be chosen for $D_\perp$ and $\chi_\perp$. Radially and poloidally fixed transport coefficients certainly can provide reasonable matches with experiment, especially at low upstream densities, even if this is likely to be an overly simplified description of the radial transport.

In practice, experimental upstream and target profiles are matched as well as possible at the lowest densities and the resulting transport coefficients used for higher $\bar{n}_e$ simulations, assuming that volumetric processes, which play an increasing role with increasing $\bar{n}_e$, do not change the assumed nature of radial transport.

The comparison of SOLPS5.0 simulation results with experimental data is therefore performed by beginning at low $\bar{n}_e$. In this situation, with an attached plasma and negligible volumetric sinks for particles and power in the SOL, there is no reason, other than possible effects from the neglected drift terms, why results from simulations should not agree with measured data within experimental error bars. Beginning with D plasmas, once the best possible agreement with experiment is obtained, the separatrix density is progressively raised and the influence of a number of simulation parameters investigated, including the introduction of molecular effects. A similar exercise is then performed for a pure He plasma with respect to the effect of separatrix density alone since molecular

effects are absent.

5.3.2.1 Deuterium discharges

Figure 5.27a compares upstream profiles calculated by the code for two simulations with slightly different prescribed n_e^{sep} ($1.0 \times 10^{19} m^{-3}$ for #8524 and $1.5 \times 10^{19} m^{-3}$ for #8523). Regarding upstream profiles, agreement is rather good for both n_e and T_e at the lowest of
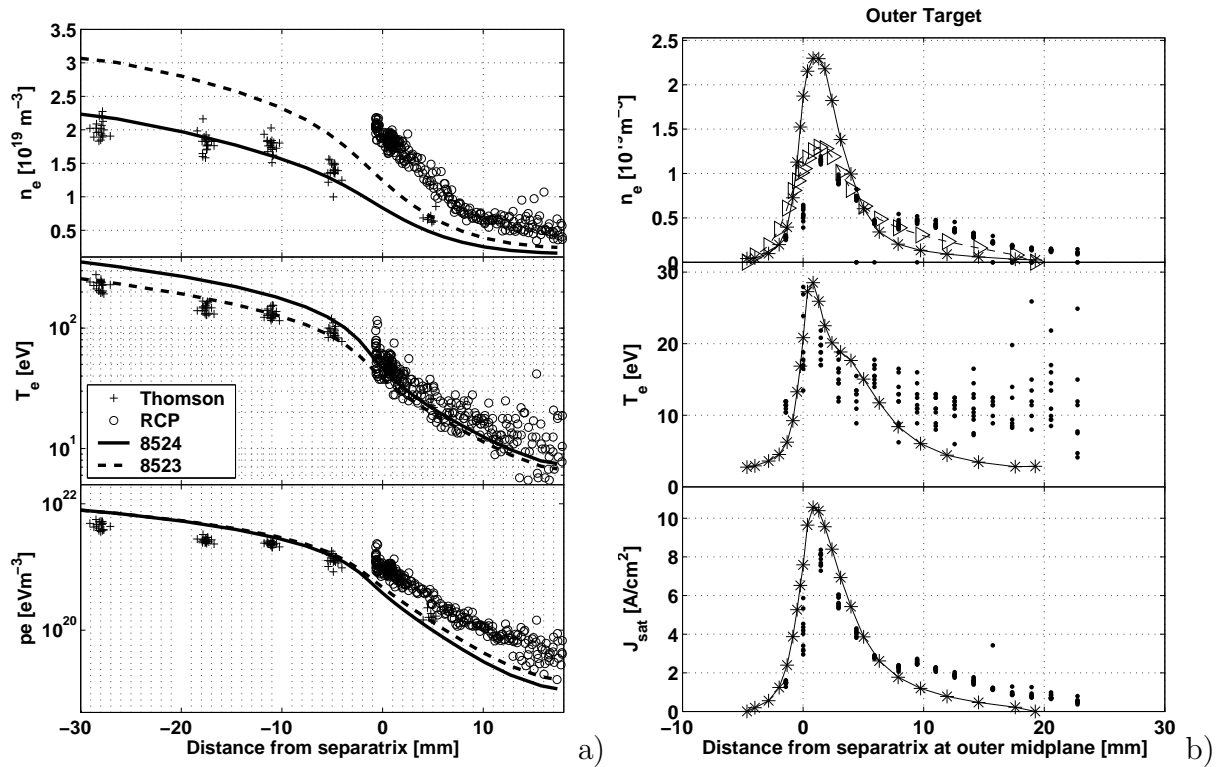
Figure 5.27: *a) Upstream experimental profiles from identical TCV discharges #26979 and #26980 together with two simulations #8524 and #8523 at different upstream densities. b) Comparison of fixed Langmuir probe measurements (.) for #26979, taken between $t = 1.06s$ and $t = 1.12s$ (corresponding to the time interval over which the RCP measured the profiles in a)), with simulation #8524 ($*-$). Assuming $T_e = T_i$, the code predicts the density profile $\triangleright-$ from the simulated j_{SAT}.*

the two values of n_e^{sep} (case #8524), with the caveat, as discussed in Section 5.2.1.1 that, the RCP density data may require correction due to the possible influence of SOL flows.

Both simulations have been performed with spatially constant transport coefficients with values: $D_\perp = 0.2m^2s^{-1}$ and $\chi_\perp = 1.0m^2s^{-1}$. Unless otherwise stated, these values are appropriate to all subsequent simulation results. One may also note that both code and experiment indicate that quite significant parallel temperature gradients exist already at these (lowest accessible) experimental upstream densities. A true sheath limited regime has therefore not been achieved. Figure 5.27b compares simulation results with outer target fixed Langmuir probe data. For j_{SAT} and T_e the agreement is good, whilst for target n_e, SOLPS5.0 overestimates the experimental value by about a factor 2. If, however, the code predicted ion flux density[6] and T_e are used to recompute a target density in exactly the same way as is performed when processing the fixed probe data (i.e. assuming $T_i = T_e$, Section 5.2.1.1), excellent agreement is recovered between experimental and simulated densities.

How can this be understood? Assuming $T_i = T_e$, the Langmuir probe measures a lower n_e than that predicted by the simulations. Since the experimental and simulated j_{SAT} and T_e are in agreement, T_i must in fact be lower than T_e in reality. Indeed at low densities the code predicts a value for T_i in the strike point region which is nearly a factor 2 lower than T_e (Fig. 5.28). To see how this situation arises, consider that electrons transfer energy to the sheath electric field, which is then removed from the plasma in the form of ion kinetic energy as the latter are accelerated across the sheath. In the absence of inter-ion collisions, T_i cannot change since the ion velocity is directed toward the wall and no energy is lost during sheath acceleration. The loss of electron energy due to the sheath can be compensated in the pre-sheath through ion-electron collisions. For the target parameters in figure 5.28 the temperature equipartition time (eqn. 2.23) is $\sim 1.0 \times 10^{-4}s$. The ion fluid moves at a velocity[7] of $\sim 1.4 - 2.0 \times 10^4 ms^{-1}$ between the entrance of the outer divertor throat and the target, corresponding to $M_\parallel \sim 0.2 - 0.5$ and a dwell time of the ion fluid (eqn 2.116) in the outer divertor of $\tau_{dwell} \sim 7 \times 10^{-4}s$. This is sufficiently long for energy to be transferred from ions to electrons along the outer

---

[6]Note that SOLPS5 computes fluxes across cell surfaces and n_e and T_e at cell centres.
[7]see as an example a (high density) conduction limited attached case (#8006) in figure 5.58
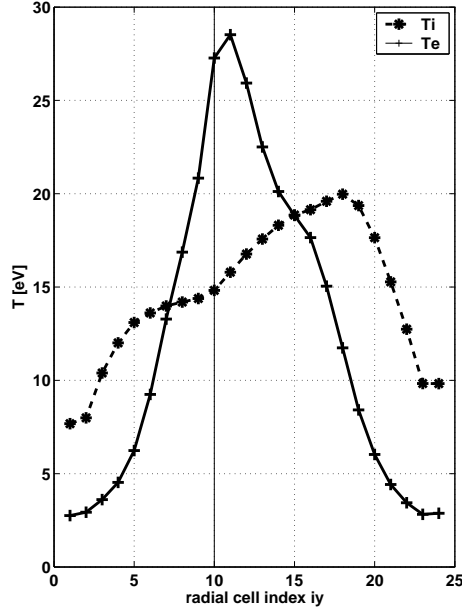
Figure 5.28: *Outer target profiles (here as function of radial cell index) of T_e and T_i for simulation #8524. The vertical line denotes the separatrix position.*

divertor such that the ions supply energy to the electrons, which is subsequently lost in the sheath. This can at least partially explain why $T_i \approx T_e$ might be expected at the outer target in TCV, even for low $\nu^*_{SOL} \sim 10 - 15$ upstream. For $T_i < T_e$ to occur the ion energy lost across the sheath itself needs to be larger than what could now be transferred from electrons to ions in the divertor volume and/or transported parallel to $\vec{B}$ through the ion channel from regions upstream, as no further net energy transfer from ions to the electrons is possible [8].

Figure 5.29 illustrates the sensitivity of upstream and outer target profiles to a very limited scan of spatially constant transport coefficients for the low density case of Fig. 5.29. The largest variation is observed on the target T_e profiles - upstream T_e profiles are rather resilient ('stiff') to moderate variations in the perpendicular transport coefficients. Similar sensitivity studies have been performed to investigate the effects of varying

---

[8]see also figure 5.32 in the context of flux limits which shows some typical poloidal profiles for T_e and T_i at low upstream density
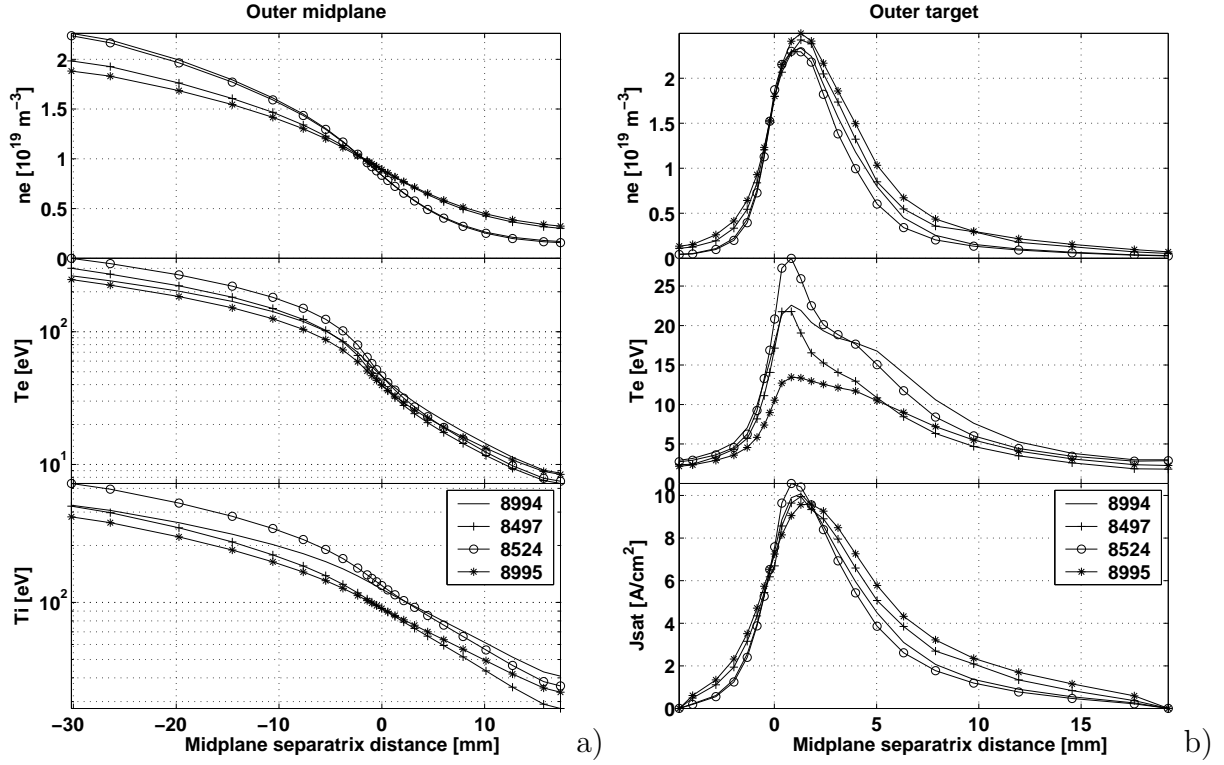
Figure 5.29: *Simulated (a) upstream and (b) outer target profiles for varying $\chi_\perp$ and $D_\perp$ at fixed $n_e^{sep} = 1.0 \times 10^{19} m^{-3}$ mapped to the outer midplane. #8994: $D_\perp = 0.2 m^2 s^{-1}$, $\chi_\perp = 1.5 m^2 s^{-1}$; #8497: $D_\perp = 0.5 m^2 s^{-1}$, $\chi_\perp = 1.0 m^2 s^{-1}$; #8524: $D_\perp = 0.2 m^2 s^{-1}$, $\chi_\perp = 1.0 m^2 s^{-1}$; #8995: $D_\perp = 0.5 m^2 s^{-1}$, $\chi_\perp = 1.5 m^2 s^{-1}$. Note that $D_\perp = 0.2 m^2 s^{-1}$, $\chi_\perp = 1.0 m^2 s^{-1}$ is the standard pair chosen for most simulations.*

power sharing among electrons and ions and of separate modifications to each of $\chi_{\perp i}$ and $\chi_{\perp e}$ at fixed $D_\perp$. Variations in power sharing up to 30% have no significant effect on target or upstream profiles. The same is true for changes in $\chi_\perp$ at fixed $D_\perp$. Relatively strong effects can be seen on the upstream T_i profiles with changes in $\chi_{\perp i}$, but this does not influence the target profiles. Measurements of T_i with sufficient resolution in the separatrix / SOL region are not yet available on TCV and so no experimental comparison is possible.

One of the other fixed parameters in the simulations is the total sheath heat transmission coefficient, for which a value of $\gamma = 8.6$ is used throughout. As shown in Section 2.4, this coefficient is itself dependent on the plasma parameters in front of the target.

Figure 5.30 illustrates the influence of a variation in γ on the target profiles for the $n_e^{sep} = 1.0 \times 10^{19} m^{-3}$, low density reference case. The choice of low density at which to
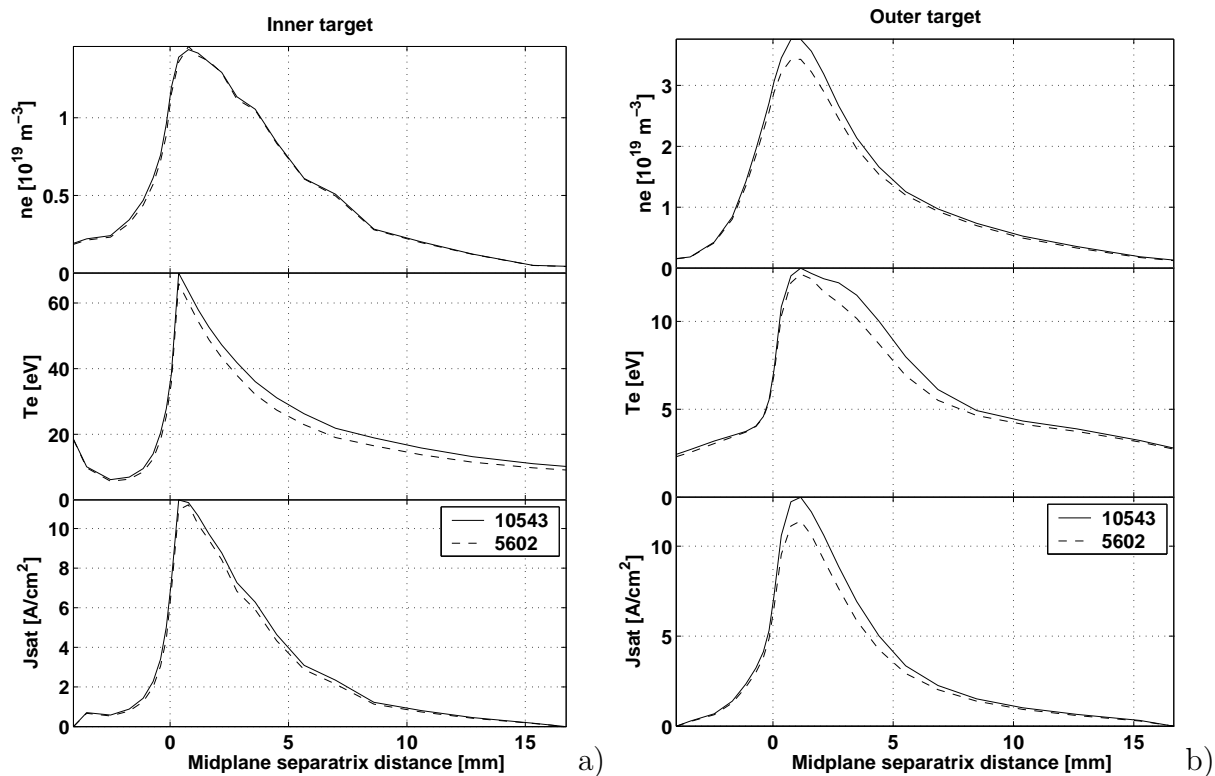
Figure 5.30: *Comparing the effect of choosing different heat transmission coefficients at the targets (a) inner target, (b) outer target for $n_e^{sep} = 1.0 \times 10^{19} m^{-3}$. Upstream profiles of T_e, T_i and n_e (not shown) are identical. For case #10543, $\gamma_e = 4$ and $\gamma_i = 2.5$ whilst for case #5602 $\gamma_e = 5.1$, $\gamma_i = 3.5$ are the standard values.*

make this comparison is appropriate in view of the sheath limited condition under which variations of γ are likely to affect the solution. A decrease of γ from 8.6 to 6.5 has little effect on the solution. The latter value represents a lower limit on γ on the basis of theory and kinetic simulations [28] (see also Section 2.4). Since even at this low separatrix density, parallel temperature gradients are developed (seen both in simulations and experiment) it is perhaps of little surprise that the target profiles are relatively insensitive to variations in γ.

Given that even this low density case is already apparently approaching conduction limited conditions (despite the low ν_{SOL}^*, typical for intermediate collisionality [28]), it is important to check the influence of heat flux limits, α_{hfl}, on the simulation profiles. Section 2.3.1 has pointed out that there is some uncertainty in the most appropriate choice of the heat flux limits α_{hfl}. Figure 5.31 compiles the upstream and outer target profiles for a selection of values for α_{hfl}. The limit is set for electrons and ions separately. Setting
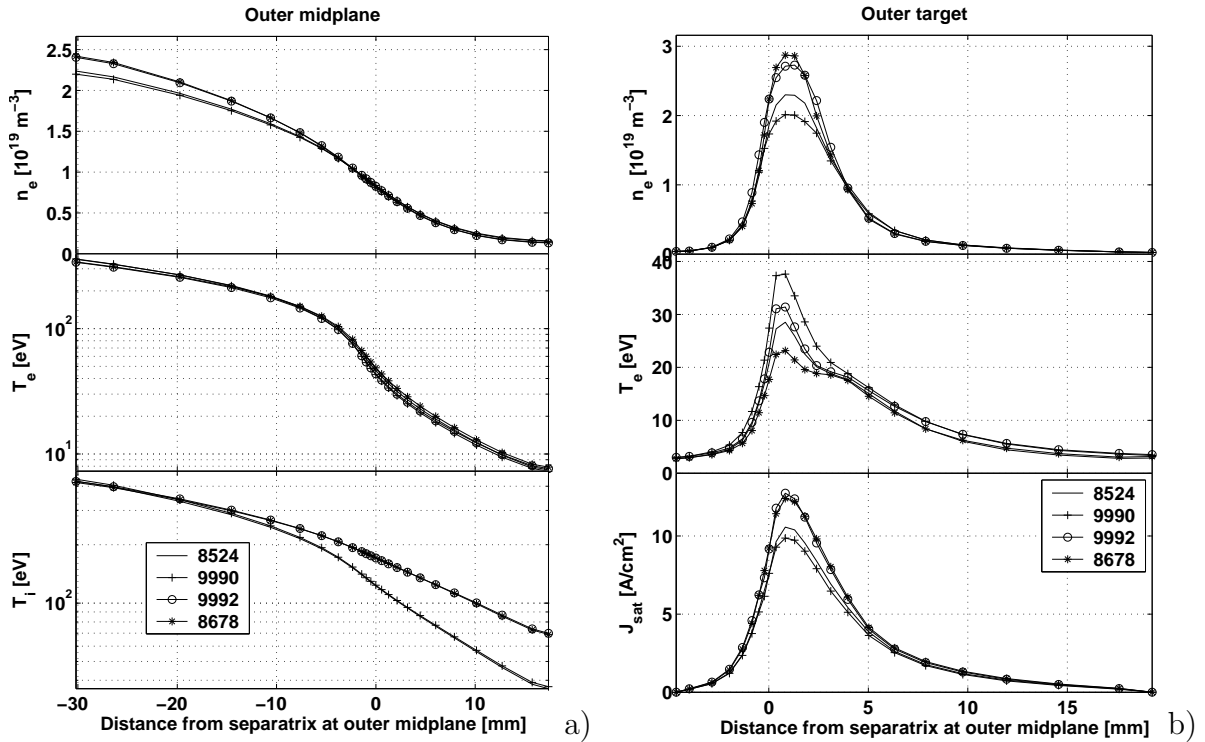
Figure 5.31: *The effect on upstream and outer target profiles of variations in conduction heat flux limits. Simulation cases correspond to: #8524: $\alpha_{hfl}^{elec} = 0.3$, $\alpha_{hfl}^{ion} = 10$; #9990: $\alpha_{hfl}^{elec} = 10$, $\alpha_{hfl}^{ion} = 10$; #9992: $\alpha_{hfl}^{elec} = 10$, $\alpha_{hfl}^{ion} = 0.3$; #8678: $\alpha_{hfl}^{elec} = 0.3$, $\alpha_{hfl}^{ion} = 0.3$;*

$\alpha_{hfl} = 10$ is interpreted as being equivalent to not imposing any conductive heat flux limit, whilst $\alpha_{hfl} = 0.3$ does constitute a strong limit. The results divide essentially into two groups with, $\alpha_{hfl}^{ion} = 0.3$ and $\alpha_{hfl}^{ion} = 10$, almost independently of the electron heat flux limit, α_{hfl}^{elec}. This result confirms the conclusions drawn in [37] and demonstrates the invariance of the upstream T_e profile to the choice of α_{hfl}. In general, only the upstream T_i is affected, with the target parameter variation being within experimental uncertainty.

Figure 5.32 compares the poloidal temperature profiles plotted as a function of grid
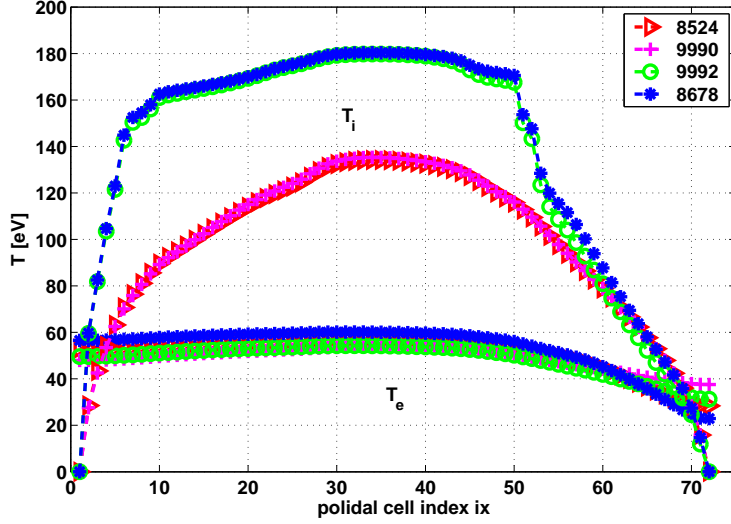
Figure 5.32: *Parallel temperature profile dependance on α_{hfl} along the first poloidal ring of the grid outside the separatrix for the simulations shown in figure 5.31. Note that the inner main SOL extends from $ix = 11$ to $ix = 50$.*

cell index, where the main SOL extends from $ix = 10$ to $ix = 50$ and the data are from the first radial ring of grid cells outside the separatrix (iy=11). The T_e profile is essentially unafected by the choice of α_{hfl}. In contrast, the effect on T_i is strong with the heat flux limit ($\alpha_{hfl} = 0.3$) acting like a parallel transport barrier for the ion heat flux. In addition, figure 5.32 shows how for given α_{hfl}, $\nabla T_{ix} \approx 0$ along the main SOL. The strongest effect of imposing an ion heat flux limit is to generate a strong gradient in T_i to both divertors under the X-point. Apparently, in TCV strong temperature gradients must establish in order to exhaust the power entering upstream.

Since at these high target temperatures, all neutrals recycling at the walls are ionized in the first grid cells in front of the targets, there are no volumetric ion sources further upstream and n_e is approximately constant along most of the SOL[9]. The gradient in T_i below the X-point then explains the relatively high[10] flow velocities for $M_{\parallel}$ mentioned

---

[9]see also case #8006 for high density in figure 5.55; even there the parallel n_e profile is flat along the SOL

[10]in the simple model of the SOL the plasma is assumed in the conduction limited regime to be stagnant up to the targets, where it is then accelerated to the Bohm velocity

earlier in connection with Fig. 5.28 since the gradient in static ion pressure accelerates the plasma long before the sheath entrance.

Having established good agreement between code (case #8524) and experiment at the lowest achievable experimental density, and the relative invariance of the numerical results to various code parameters, the density may now be raised and detachment sought in the code. Before doing so, it is interesting to note that the low density simulations match well both inner and outer target data (a comparison with inner target data at $\bar{n}_e \geq 1.5 \times 10^{19} m^{-3}$ is shown in Fig. 5.33 below) without drift terms activated. This is precisely the regime in which the drifts themselves might be expected to play a stronger role. Experiments certainly suggest [172] that this is true in the main SOL in TCV[11]. Fig. 5.23 indicates, however, that at least in so far as the integral ion flux is concerned, there is little difference between forward and reversed field.

Figures 5.33 and 5.34 compare experimental and simulated upstream and inner target profiles at intermediate ($n_e^{sep} = 1.5 \times 10^{19} m^{-3}$) and high upstream ($n_e^{sep} = 2.5 \times 10^{19} m^{-3}$) densities. With spatially fixed transport coefficients, relatively good agreement is achieved upstream for the intermediate density case. At high density, however, for the low density baseline assumption of $D_\perp = 0.2 m^2 s^{-1}$, the simulated upstream density profile deviates considerably from experiment, especially inside the LCFS. An increase to $D_\perp = 0.5 m^2 s^{-1}$ does improve the situation somewhat in the SOL but results in a similar discrepancy in the confined region. For comparison at the target the simulation with $D_\perp = 0.5 m^2 s^{-1}$ has been selected since it provides better agreement in the SOL at higher upstream densities than the $D_\perp = 0.2 m^2 s^{-1}$ case. Agreement at the inner target is generally good for the lower density case and reproduces the magnitude, but not the profile width of j_{SAT} at higher density. The experimental target T_e profile is not matched at higher n_e^{sep}. This is perhaps not surpriseing since it is known (Section 5.2.1.1) that Langmuir probes often yield high values of T_e in low temperature, high density conditions.

The situation is completely different at the outer target. This is illustrated graph-

---

[11]drift flows at the LFS with $M_\parallel \sim 0.5$ near the separatrix at low densities reverse direction when B_Φ is reversed
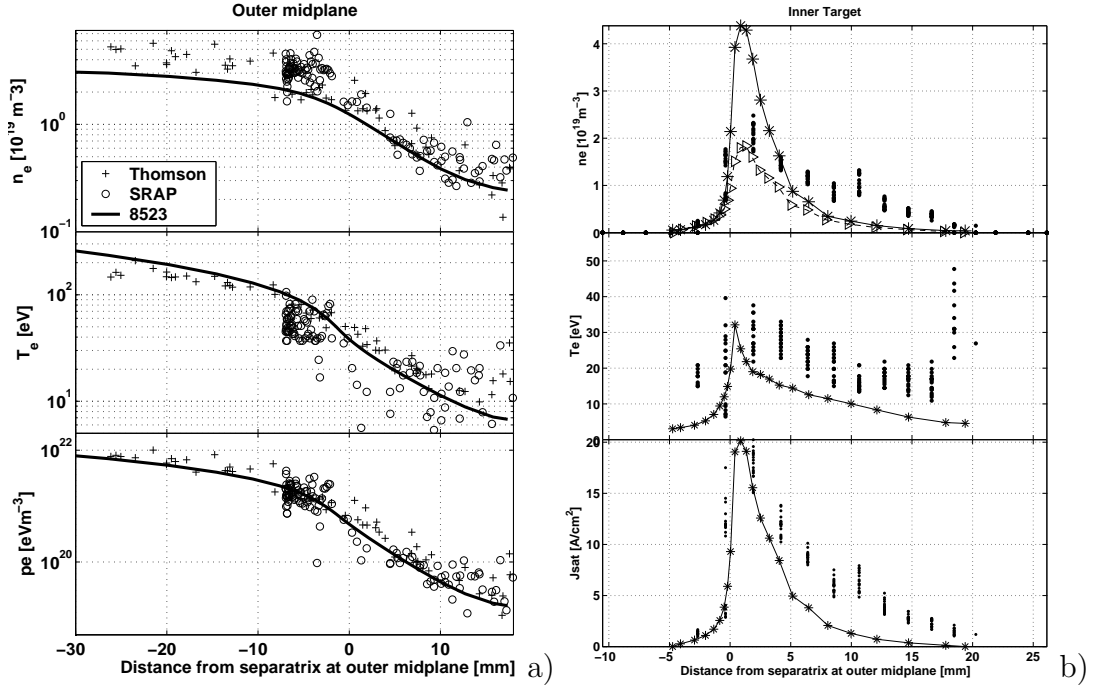
Figure 5.33: *Comparison of simulated (#8523) and experimental (#24532) profiles (a) upstream and (b) at the inner target for intermediate density, $n_e^{sep} = 1.5 \times 10^{19} m^{-3}$.*

ically in Fig. 5.35 where results from the same simulations as in figures 5.33 and 5.34 are compared with experiment. Even at a density only 1.5 times higher than for simulation #8524 (the low density reference case), considerable deviation from experiment is observed. At the highest densities, the code predicts a complete outer target temperature collapse and high target density, but still insufficient momentum removal or recombination for detachment to begin. This is precisely the result found in the earlier SOLPS4.0 simulations [24], where detachment was provoked by artificially increasing the 3-body recombination rate. Note also that, as for the inner target, there are strong deviations between the simulated and experimental target T_e at high density. At the highest density, there is a factor 7 discrepancy between code and j_{SAT}. Resolving this discrepancy is one aim of this thesis.

A further unknown quantity requiring specification in the simulations is the chemical sputtering yield, Y_{chem}. The discussion in Section 2.9 highlighted the importance
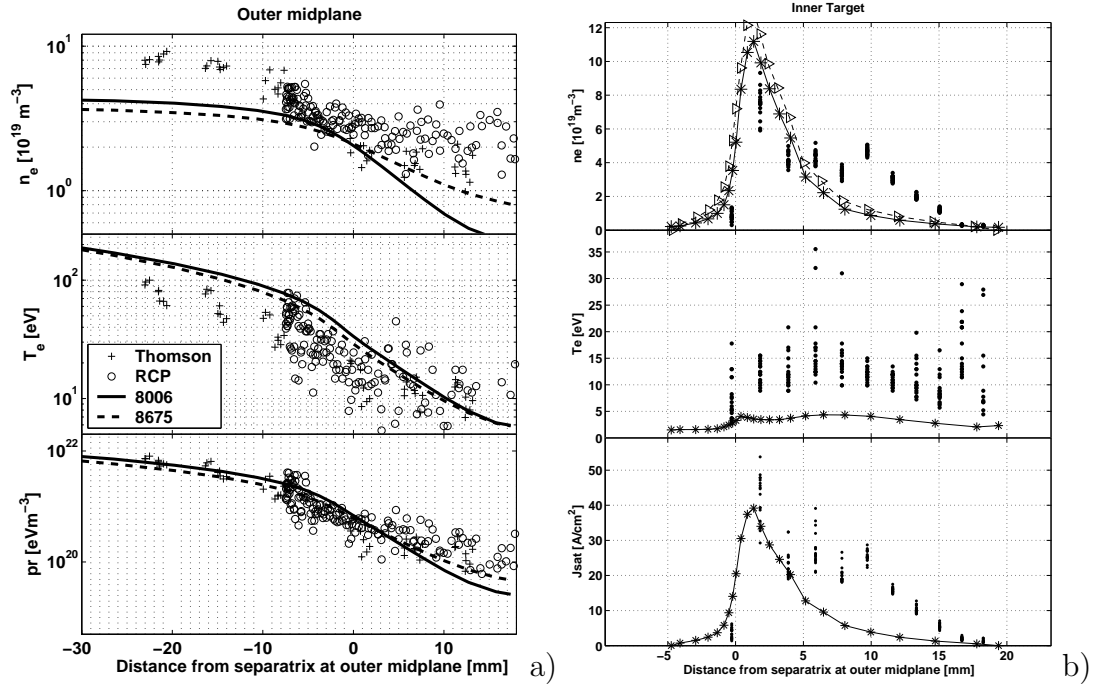
Figure 5.34: *Comparison of simulated (#8675, $D_\perp = 0.5m^2s^{-1}$, #8006, $D_\perp = 0.2m^2s^{-1}$) and experimental (#24532) profiles (a) upstream and (b) at the inner target for high density, $n_e^{sep} = 2.5 \times 10^{19}m^{-3}$. The comparison in (b) with the inner target data is from simulation #8675. Note again that $(\triangleright-)$ denotes computation of n_e from the simulated j_{SAT} assuming $T_i = T_e$.*

of volumetric radiation from impurities in decreasing the divertor plasma temperature such that the processes necessary for detachment can occur. Figure 5.36 investigates the sensitivity of the target solutions to impurity density by comparing simulations at fixed $n_e^{sep} = 2.5 \times 10^{19}m^{-3}$ but with varying Y_{chem}.

Increasing Y_{chem} from 0% to 10% changes the inner target results by at most 20% indicating that that volumetric losses are not determining the behaviour at the inner target. In contrast, at the outer target, parameters can be very much affected by the choice of Y_{chem}. For fixed $D_\perp$, progressive increases in Y_{chem} reduce T_e but increase n_e. Only at values of $Y_{chem} = 10\%$ is any reduction of n_e and hence j_{SAT} noted. Such values are not considered realistic for the target plate surfaces (Section 2.6.2 and [69]). It thus appears

153
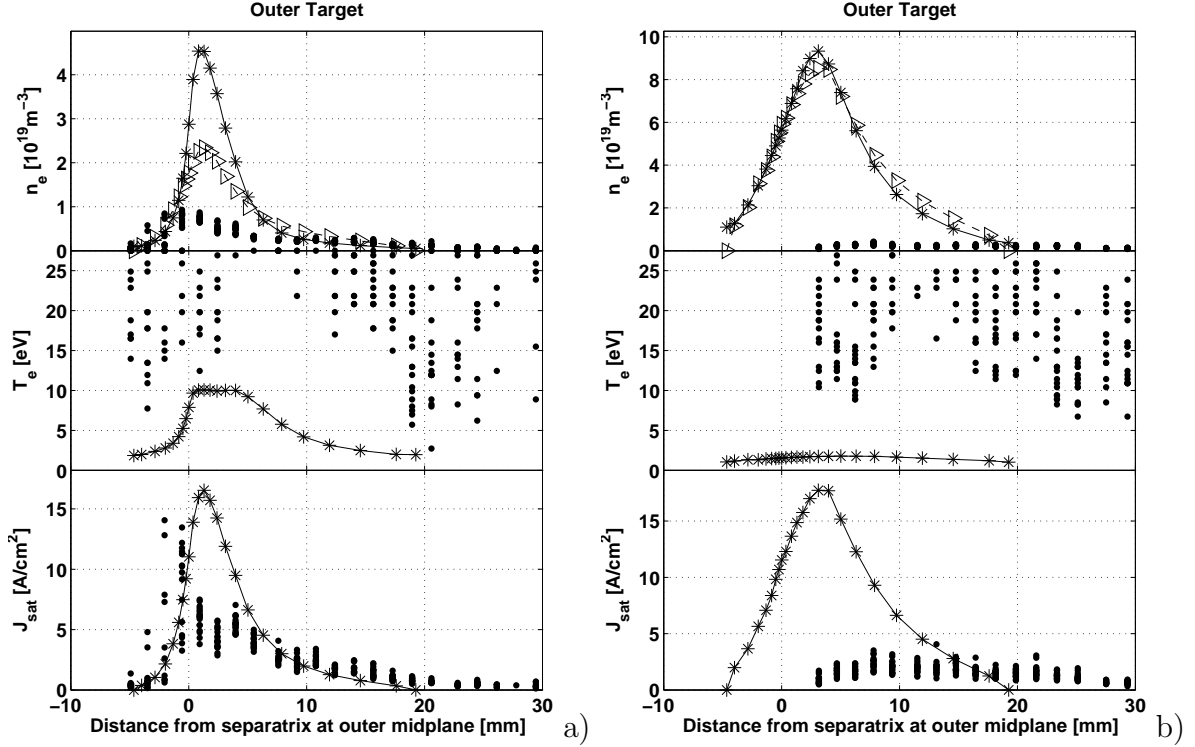
Figure 5.35: *Comparison of experimental (#24532) and simulated profiles at the outer target for the same conditions of discharge and simulation as in figures 5.33 and 5.34;a) lower density #8523, $n_e^{sep} = 1.5 \times 10^{19} m^{-3}$, b) higher density #8675, $n_e^{sep} = 2.5 \times 10^{19} m^{-3}$*

that even unrealistically high chemical yields are insufficient to produce any significant detachment for spatially constant perpendicular transport.

The code simulations indicate strongly that at high densities, measured target temperatures are probably over estimated. Even if the code does predict rather low T_e at the outer target at high n_e^{sep}, the divertor volume over which this low T_e persists is too small for the recombination to occur (the ion dwell time in the region is too short) - see Fig. 5.56 for an example of the simulated parallel T_e profiles. One is therefore led to seek alternative mechanisms by which recombination might occur. The results of this investigation are summarized below and have been recently published in ref. [150].
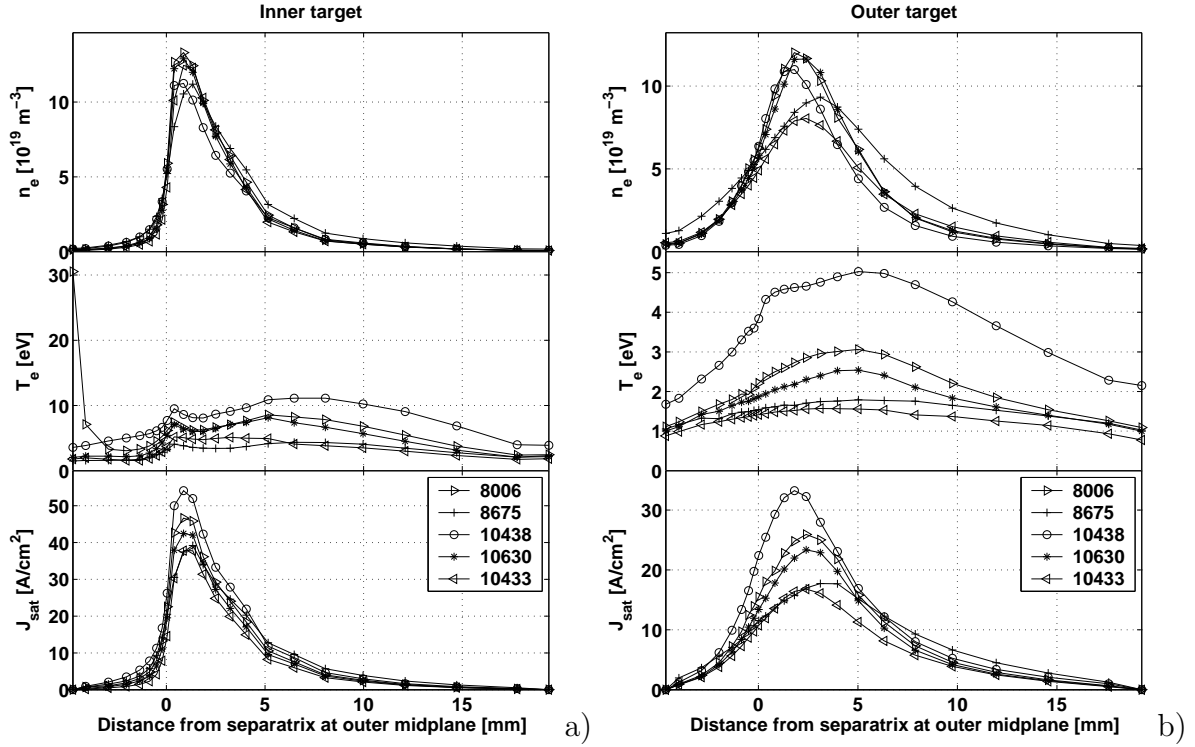
Figure 5.36: *Influence of Y_{chem} on inner and outer target profiles for fixed $n_e^{sep} = 2.5 \times 10^{19} m^{-3}$. $D_\perp = 0.5 m^2 s^{-1}$: #8675: $Y_{chem} = 3.5\%$; $D_\perp = 0.2 m^2 s^{-1}$: #8006: $Y_{chem} = 3.5\%$, #10438: $Y_{chem} = 0\%$, #10630: $Y_{chem} = 5\%$, #10433: $Y_{chem} = 10\%$. The chemical yield is fixed at the given values on all surfaces.*

Since the experimentally measured electron densities are rather low in front of the outer divertor and because the half-width of the target profiles is at most only about $3-4cm$ just before detachment occurs, the mean-free-path for molecules can be larger than the radial extent of the plasma in the divertor volume. In the collision-radiative model, the vibrational population of molecules leaving the wall surfaces is assumed to promptly attain thermal equilibrium with the plasma electron distribution. If the mfp for molecular dissociation is comparable to the width of the plasma itself, as is the case for TCV, it is unlikely to be sufficiently short for the validity of the CRM assumption to be guaranteed. In such cases, the vibrational population may be dominated by wall effects

and each vibrational level must be treated as an individual species. A similar treatment has been performed in [88] for detached hydrogen plasmas in the ASDEX-Upgrade tokamak, simulated with the B2-EIRENE (SOLPS4.0) code. The principal finding was that by including a detailed treatment of each vibrational level, be it by simulating them as individual species or by implict inclusion into the calculation for the reaction rates in the CRM, previously detached plasmas re-attach so that the upstream density must be increased by a factor $1.5 - 2$ in order to recover the detached solution. Nevertheless, it has been found that molecular assisted recombination (Section 2.7) can play a role in achieving divertor detachment in linear divertor simulators. As a consequence of the large outer divertor volume in TCV it cannot be excluded a priori that volumetric molecular effects could influence the detachment process.

Three volumetric processes for molecules involving ion conversion compete (see Table 5.2) and self-consistent simulations are required in order to resolve the dominant reaction path. Since no vibrationally resolved reaction rates are currently available for D_2, data

Molecular assisted recombination	MAR	$D_2(v) + D^+ \rightarrow D_2^+ + D$	$D_2^+ + e \rightarrow D + D$
Molecular assisted dissociation	MAD	$D_2(v) + D^+ \rightarrow D_2^+ + D$	$D_2^+ + e \rightarrow D + D^+ + e$
Molecular assisted ionization	MAI	$D_2(v) + D^+ \rightarrow D_2^+ + D$	$D_2^+ + e \rightarrow D^+ + D^+ + 2e$

Table 5.2: *Principal competing processes involving molecules and positivly charged molecular ions, generally MAI is the least important of them; v is the vibrational level*

for H_2 molecules have been employed here. Contrary to electronic states of atoms and molecules, which essentially depend only on the species nuclear charge, the energy of vibrational levels depends on the mass of the nuclei composing the molecule [173]. To first order, the energy of vibrational excitation levels of diatomic molecules scales as $\sqrt{1/m}$. In an adhoc approach to including this mass dependence, the energy gap between vibrational levels has been adjusted to account for the fact that the gap between one level and the next in H_2 does not correspond to a vibrational level in D_2. The vibrational levels dealt with in the simulations are thus to be taken as 'effective' levels but not as real vibrational levels for D_2. For example, the vibrational level $v = 4$ in the simulations would then

correspond to $v = 6$ for D_2 molecules. The charge-exchange reaction (ion conversion) $D_2(v) + D^+ \rightarrow D_2^+ + D$ that results in D_2^+ is resonant for the effective quantum number $v = 4$, which for both species corresponds to $\Delta E_{vib} \sim 2eV$. Simulations made for TCV include volumetric processes for vibrational species in the electronic ground state as shown in Table 5.3 for effective vibrational quantum numbers $v = 0 - 7$ and replace the effective (averaged over s vibrational distribution) inelastic reactions involving D_2 in Table 5.1. With vibrational species treated individually in EIRENE, the vibrational

Reaction	Type
$D_2(v = m) + e \rightarrow D_2(v = n)\,(m < n) + e$	H.2
$D_2(v = m) + e \rightarrow D_2(v = n)\,(m > n) + e$	H.2
$D_2(v = l) + e \rightarrow D + D + e$	H.2
$D_2(v = l) + D^+ \rightarrow D_2^+ + D$	H.2

Table 5.3: *Summary of inelastic volumetric processes for vibrationally excited molecules*

quantum number with which a moleucle departs from the surfaces must be defined. The largest possible production of D_2^+ occurs if large quantities of D_2 in $v = 4$ are present in the plasma. When using the CRM, thermal particle release of deuterium from surfaces is in the form of D_2. If the plasma-facing components are sufficiently saturated with deuterium, then D^+ and D atoms arriving there will 'see' deuterium adsorbed on the surface. As a consequence, recombination occurs before the impinging particle is adsorbed by the surface itself. If only one of the two recombining species is adsorbed on the surface, more molecular recombination energy is available for transformation into vibrational excitation energy. This is because less energy is required during particle release to overcome the surface potential binding the adsorbed species to the material surface than if both atoms were adsorbed at the surface prior to recombination. Molecules created in this way leave the surface in a vibrationally excited state. This process is known as the Elay-Rideal mechanism [174]. Measurements performed in ASDEX Upgrade and in industrial plasmas show the presence of vibrationally excited molecules, likely due to surface release due

to the Elay-Rideal mechanism [175–177]. The use of these excited states as a powerful diagnostic for measurements of T_e in the divertor volume has also been proposed and demonstrated [178, 179].

In the simulations presented here it is assumed that molecular recombination on material surfaces results in molecules with $v = 4$. It is further assumed that any molecules leaving material surfaces do so with $v = 4$. This latter condition can be contested since it could equally be assumed that molecules interacting with a wall deposit an energy equivalent of $\Delta v = 1$ there. Simulations performed for TCV show that the results are insensitive to the choice of molecule-wall interaction, as it was also the case in the ASDEX-U simulations [88].

Since the assumption that vibrational populations should be included is founded on the basis that the molecular mfp can become comparable to the distance between the vacuum vessel walls at or near the onset of detachment, it is natural to assume that the molecular trajectories should also be affected by the walls themselves. The standard cylindrical approximation of the tokamak in EIRENE[12] has therefore been replaced by a toroidal geometry in which 50 cyclinders connected end to end produce a polygonal approximation of the torus. Neutrals that interact with the plasma through elastic collisions may thus acquire a preferred velocity component in the toroidal direction. This may be particularly important in regions of strong plasma flow such as in the outer divertor volume where the neutral fluid will be affected by the torus curvature. A previously infinite straight trajectory in a cylinder in the toroidal direction now acquires a radial component. This could enhance momentum removal from the plasma. But it could also lead to a radial outward shift of the recycled neutrals, reducing neutral densities at smaller radii and hence the probability for momentum removal. As an example, a few sample neutral trajectories (50) leaving the outer divertor target using the toroidal approximation are shown in Fig. 5.37 projected onto the poloidal plane. The (few) curved trajectories in this representation are a result of including the toroidal approximation. This should be

---

[12]recall that EIRENE computes trajectories for particle histories in 3-D

compared with the trajectories shown in figure 5.38 where another 50 sample trajectories leave the outer target, but now computed using the cylindrical approximation. Atoms are affected only to a minor degree by the curvature as a consequence of their shorter ionization mfp in the outer divertor plasma of these simulations. Unfortunately, the
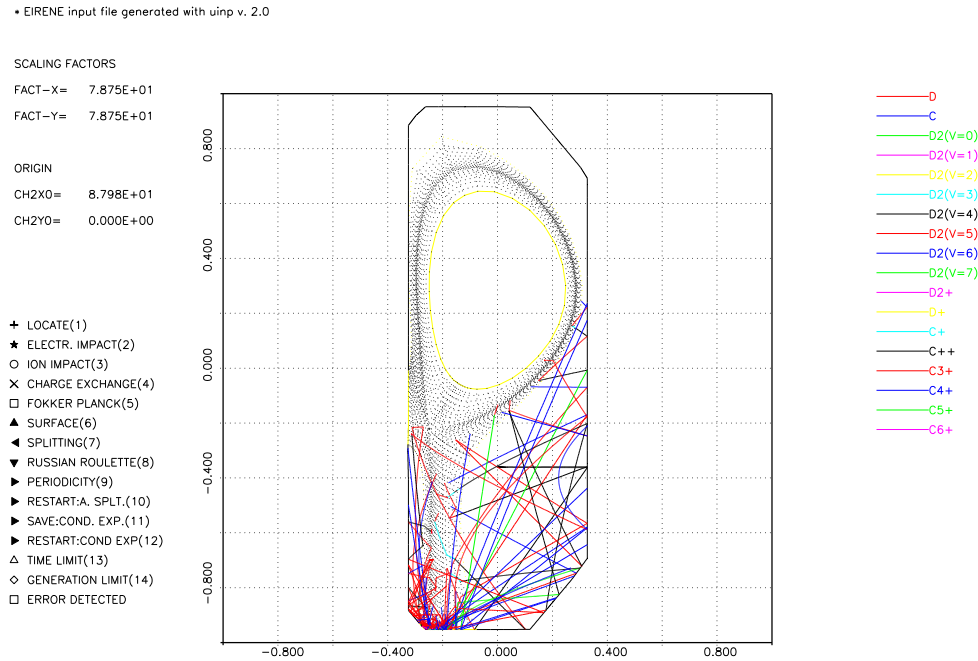

Figure 5.37: *Poloidal projection of* 50 *particle trajectories launched from the outer target (simulation* #6309*: VRM) using EIRENE with the polygonal approximation of the torus*

inclusion of toroidal geometry fails to produce any significant further reduction in the simulated target fluxes at high density [150].

An alternative MAR process is the catalytic mechanism proposed by Janev [79] provided by hydrocarbon impurities $(C_x D_y)$, known to be present in tokamak divertor plasmas when graphite is present [180, 181]. Experimental studies of the hydrocarbon enhanced MAR process have only very recently been reported from divertor simulators and other laboratory plasmas [182, 183]. Likewise, databases of collisional cross-sections for hydrocarbons have recently become available but although updated versions of re-

SCALING FACTORS

FACT−X= 7.875E+01

FACT−Y= 7.875E+01

ORIGIN

CH2X0= 8.798E+01

CH2Y0= 0.000E+00

+ LOCATE(1)
★ ELECTR. IMPACT(2)
O ION IMPACT(3)
✕ CHARGE EXCHANGE(4)
☐ FOKKER PLANCK(5)
▲ SURFACE(6)
◄ SPLITTING(7)
▼ RUSSIAN ROULETTE(8)
► PERIODICITY(9)
► RESTART:A. SPLT.(10)
► SAVE:COND. EXP.(11)
► RESTART:COND EXP(12)
△ TIME LIMIT(13)
◇ GENERATION LIMIT(14)
☐ ERROR DETECTED

D
C
D2
D2+
D+
C+
C++
C3+
C4+
C5+
C6+

0.800

0.400

0.000

−0.400

−0.800

−0.800 −0.400 0.000 0.400 0.800
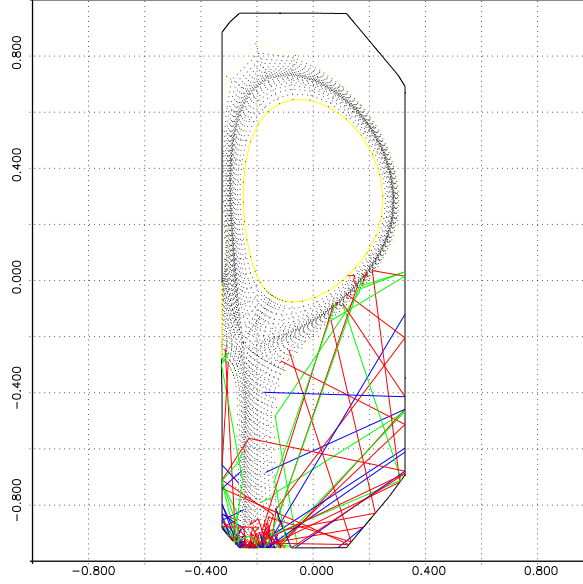
Figure 5.38: *Poloidal projection of* 50 *particle trajectories launched from the outer target (simulation #8006: CRM) using EIRENE with the cylindrical approximation of the torus*

action rate coefficients exist, they have not yet been translated into a form useable by codes [184–186]. It has been proposed by Janev that the higher hydrocarbons ($x > 1$) might lead to significant increases in volumetric recombination losses through MAR processes. Up to one order of magnitude larger rate coefficients for recombination compared to MAR via ion conversion to D_2^+ can be expected[13]. Of particular importance is the observation that hydrocarbon MAR processes might operate efficiently in the temperature range $T_e = 2eV - 8eV$ commonly found in divertors of several tokamaks, including TCV, especially at the onset of detachment.

The mechansim proposed is as follows

$$D^+ + C_x D_y \rightarrow D + C_x D_y^+ \tag{5.5}$$

$$e + C_x D_y^+ \rightarrow \sum_{k,l} C_{x-k} D_{y-l} + D \tag{5.6}$$

---
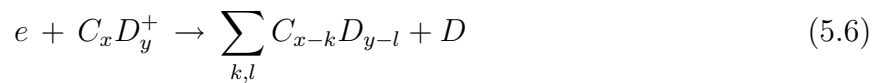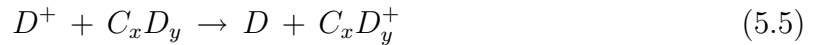
[13]depending on plasma conditions in the divertor volume
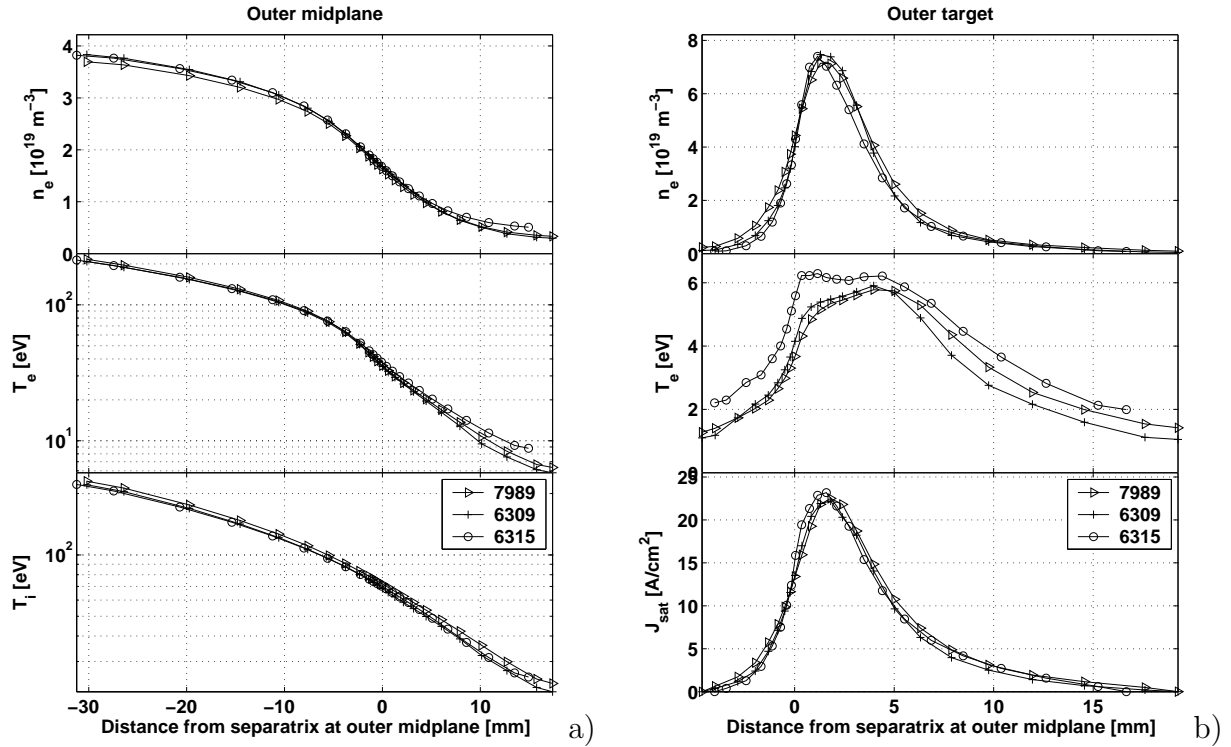
Figure 5.39: *Comparing simulated upstream and target profiles at $n_e^{sep} = 2 \times 10^{19} m^{-3}$ when a range of atomic and molecular physics are included in EIRENE. Simulations shown use #7989: CRM; #6309: VRM (vibrationally resolved moleucles); #6315: CRM and CD_4*

consisting of a CX reaction followed by dissociative recombination. Currently only the database for Methane is available in a format that can be used by EIRENE (METHAN in the EIRENE code [65, 143]). In order to simulate the effect of hydrocarbons, the reactions listed in Table 5.4 have been included into the reaction deck for EIRENE, while maintaining the CRM for simulating deuterium. No attemt has been made to include hydrocarbons and VRM simultaneously since the large number of species would be prohibitive with respect to CPU time. The assumption that atomic carbon and its charge states do not recycle at the walls is retained and extended to the $C_x D_y$ species. Hydrocarbon ions are recycled as neutral molecules with identical values for x and y as the impinging ion[14]. This is again a simple adhoc assumption.

---

[14]this property is not important for the present simulations since in the configuration used here, these

Reaction	type
$CH_y + e \rightarrow CH_y^+ + 2e$	H.1
$CH_y + e \rightarrow CH_{y-1}^+ + H + 2e$	H.1
$CH_y + e \rightarrow CH_{y-1} + H + e$	H.1
$CH_y + H^+ \rightarrow CH_y^+ + H$	H.1, H.3
$CH_y^+ + e \rightarrow CH_{y-1} + H^+ + e$	H.1
$CH_y^+ + e \rightarrow CH_{y-1}^+ + H + e$	H.1
$CH_y^+ + e \rightarrow CH_{y-1} + H$	H.1
$CH_y^+ + e \rightarrow CH_{y-2} + 2H$	H.1

Table 5.4: *Summary of volumetric processes included in EIRENE for simulating hydro-carbons in TCV plasmas. It is assumed that the rate coefficients are the same for CD_4 as for CH_4.*

In normal simulations without including hydrocarbons, the chemical erosion process is approximated by the simple release of carbon atoms from the surface. In reality, chemical erosion proceeds first by the release of hydrocarbons [68,187]. The C atoms that eventually appear in the plasma are the final products of what might be a complex chain of reactions. The relative proportions of the different hydrocarbons produced through chemical erosion are not well known. Laboratory experiments though show that low energy hydrogen neutrals produce CH_3 radicals rather than CH_4 which could subsequently lead to the preferential formation of higher C_2D_y hydrocarbons with a yield twice that for methane (see [187] and references therein). At low impact energies, the production of higher hydrocarbons increases [188–190]. It is also found that Y_{chem} is usually by a factor 2 larger for impacts of D and D^+ on carbon than for H and H^+ [68,188,191].

When hydrocarbons are included in the simulations, CD_4 rather than C is assumed to be produced by chemical sputtering. Physical sputtering continues to yield C atoms as before. Since each methane molecule leaving the surface includes 4 D atoms which can be released to the plasma through the dissociative chain from CD_4, retaining a recycling

ions are not followed by EIRENE but undergo further reactions at the location of their creation

coefficent of $R = 0.98$ (the fixed value used in all simulations without CD_4) would result in a net particle source for the plasma from the surfaces. In order to maintain approximate particle balance compared with previous results, the recycling coefficient must compensate the excess of D. The new value is computed to be approximately $R = R_{original} - 4 \times Y_{chem}$, yielding $R = 0.85$ for $Y_{chem} = 0.035$.

The inclusion of CD_4 into the simulations leads to a considerable increase in the required CPU time. More particle species are simulated so that the computational time must be increased in order to reduce numerical noise. In addition, the use of feedback on n_e^{sep} using the external gas puff means that the initial changeover to a simulation including hydrocarbons produces strong surface sources which the code needs time to compensate in order to recover a converged solution.

Figure 5.39 compares the results from simulations at a fixed $n_e^{sep} = 2 \times 10^{19} m^{-3}$ using CRM, VRM including the toroidal approximation and CD_4. Evidently, whilst nearly identical upstream profiles are maintained, none of these processes provides any reduction in outer target j_{SAT}. A slight difference was seen in [150] for VRM (CD_4 had not yet been included), but $v_{se} = c_s$ and not $v_{se} \geq c_s$ (Bohm-Chodura) had been set as target boundary condition. In any case the difference was at most 20% and not the required factor of $5 - 7$.

According to these simulations therefore, it would appear that MAR (either from VRM or CD_4) plays no role in the detachment process in TCV. Similarly, no evidence for chemical ion sources due to MAD and subsequent ionization of neutrals has been seen, in contrast to the findings in [88]. The observation that CD_4 does not enhance detachment does not exclude hydrocarbons from playing a role in the detachment process. Higher hydrocarbons, more likely to be formed during the chemical erosion process, are much more efficient in the MAR process [79] and could not be included in these simulations.

5.3.2.2   He fueled discharges

In order to see to what extent atomic and molecular physics and possibly improperly simulated impurity sources play a role in the onset of detachment, simulations of the

He fueled discharges have been performed using SOLPS5.0. In addition to the set of
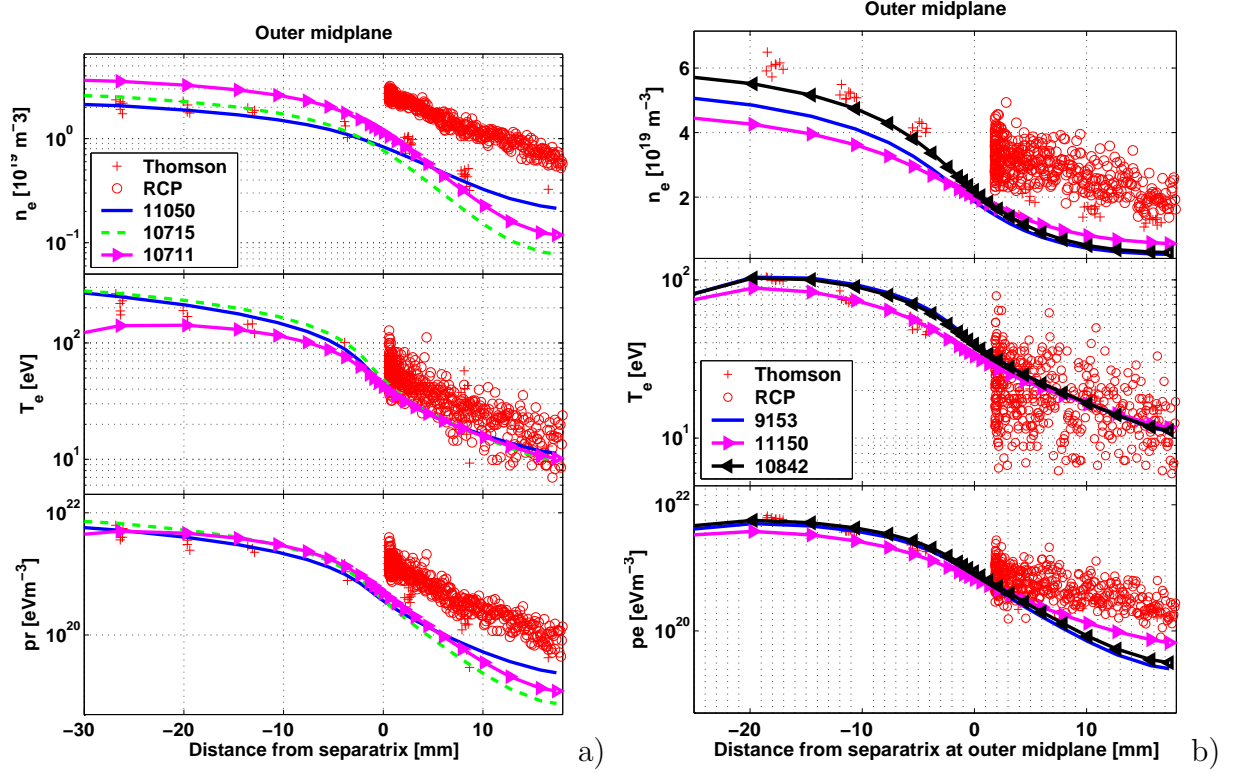

Figure 5.40: *Simulated and experimental upstream profiles for pure He discharges at (a) low (#26212) and (b) high (#26222) density. Simulations shown are #10715 at $n_e^{sep} = 1 \times 10^{19} m^{-3}$, #11050 at $n_e^{sep} = 1 \times 10^{19} m^{-3}$ using $D_\perp = 0.5 m^2 s^{-1}$, #10711 at $n_e^{sep} = 1.5 \times 10^{19} m^{-3}$, #9153 at $n_e^{sep} = 2.5 \times 10^{19} m^{-3}$, #11150 at $n_e^{sep} = 2.5 \times 10^{19} m^{-3}$ with $D_\perp = 0.5 m^2 s^{-1}$, #10842 at $n_e^{sep} = 3.0 \times 10^{19} m^{-3}$*

reactions in Table 5.1, the *He* simulations include the reactions given in Table 5.5 and are based on data incorporated into AMJUEL from a CRM by Fujimoto for helium [192]. The possible presence of metastable neutral Helium[15] is not investigated here. The fluid species in B2.5 now also include He^+ and He^{2+}. It should be noted that the CX reaction $He^+ + He \rightarrow He + He^+$ has a rate coefficient that is nearly a factor of 10 lower than the equivalent reaction for D for typical values of T_i in a divertor plasma (see also

---

[15] $He(1|1S)$, $He(2|1S)$, $He(2|3S)$

Reaction	Type and number	Database
$He + e \rightarrow He^+ + 2e$	H.4 2.3.9a	AMJUEL
$H + He^+ \rightarrow He^+ + H$	H.1 0.2	HYDHEL
$He^+ + He \rightarrow He + He^+$	H.3 5.3.1	HYDHEL
$He^{2+} + He \rightarrow He + He^{2+}$	H.3 6.3.1	HYDHEL
$He^+ + \text{electrons(s)} \rightarrow He + h\nu \text{ or electrons}$	H.4 2.3.13a	AMJUEL

Table 5.5: *List of additional reactions used for simulations in He. As in Table 5.1 rates for H remain valid in D.*

Fig. 6.12). Since this is the only sink for momentum, the momentum loss rate in He is expected to be lower than in D. This may then lead to τ_{dwell} being insufficiently long for volumetric recombination to be effective, as has been demonstrated for JET [193, 194], see also Chapter 6. As for the D simulations, gas puff fueling is used for the He cases with the usual feedback mechanism being applied to reach the prescribed n_e^{sep}.

Figure 5.40 compares the experimental and simulated upstream profiles at low and high density. Whilst generally reasonable agreement is found inside the LCFS, the differences in the SOL are notable, especially for n_e. At low density, it appears that the best match in He is obtained with $D_\perp = 0.5m^2s^{-1}$ (cf. $0.2m^2s^{-1}$ in D). Figures 5.41 and 5.42 compare the simulated and experimental target profiles. For both low and high n_e^{sep} the agreement in absolute magnitude is reasonable at the inner target and excellent at both targets for T_e. The main difference at the inner target is the larger experimental profile width, a discrepancy which rises with density. At the outer target, the experimental j_{SAT} is $\sim 30\%$ higher than in the simulations, leading to a discrepancy in the simulated target density. This is a natural consequence of the poor upstream match in n_e. At low n_e^{sep}, the outer target j_{SAT} (and hence n_e) profile becomes non-monotonic in the SOL, a trend which is also seen in D (see Fig. 5.27) and which becomes very marked at the very lowest densities achieved in D (not presented here). This 'hole' in the experimental profile is not understood.
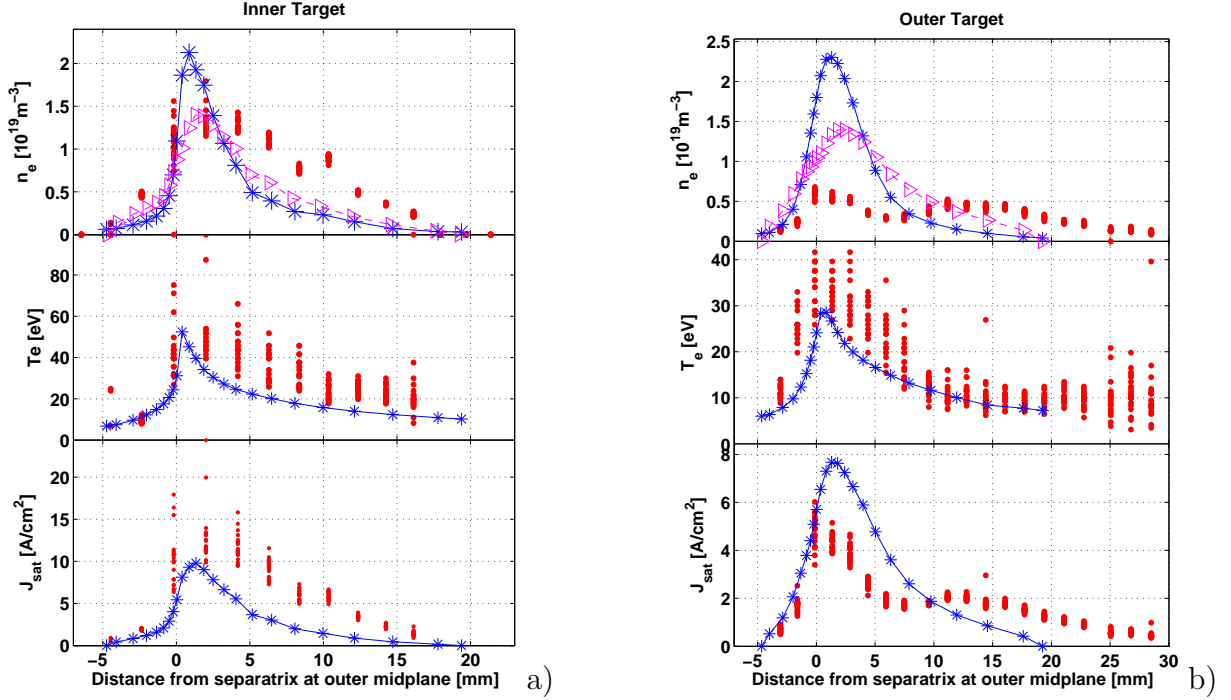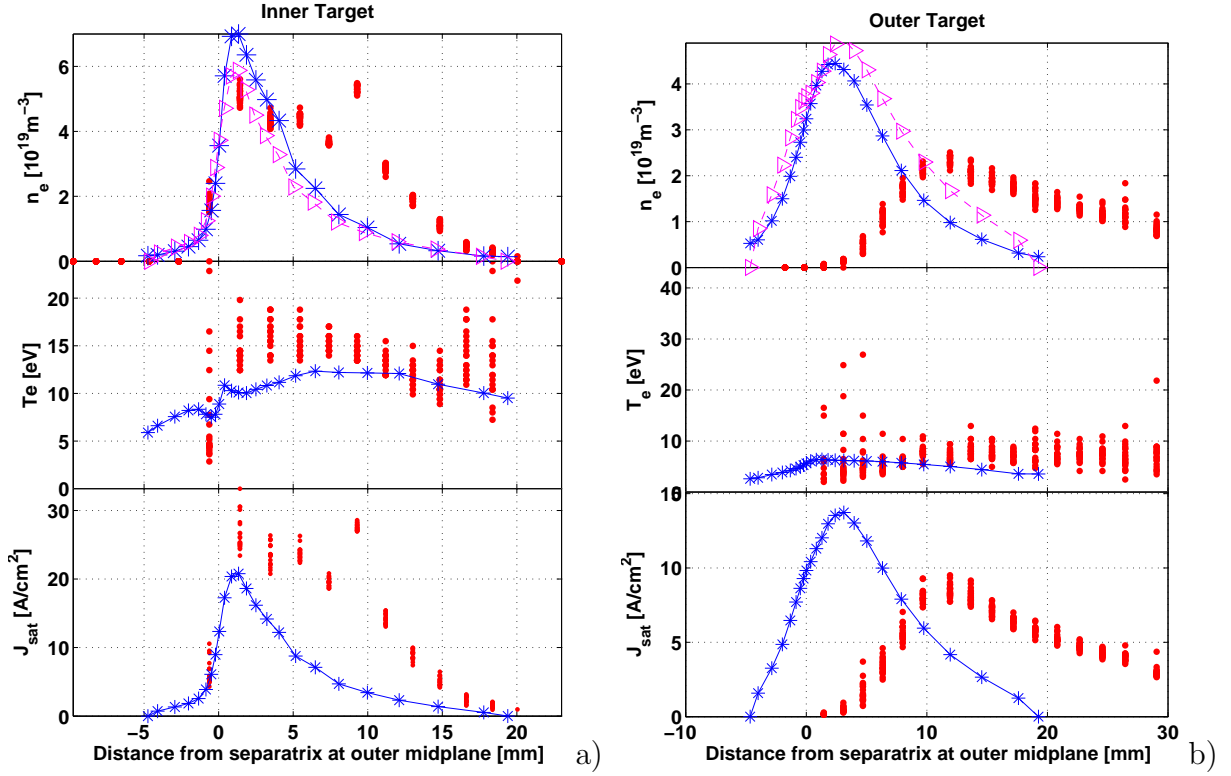
Figure 5.41: *Simulated and experimental midplane mapped profiles at the (a) inner and (b) outer targets for low upstream densities in He. The simulation case is #11050 at $n_e^{sep} = 1 \times 10^{19} m^{-3}$ with $D_\perp = 0.5 m^2 s^{-1}$. The experimental discharge is #26212, as in figure 5.40. Note that again $(\triangleright -)$ denotes computation of n_e from the simulated j_{SAT} assuming $T_i = T_e$.*

At high n_e^{sep} simulated j_{SAT} and n_e profiles diverge markedly from experiment, whilst T_e remains in good absolute agreement. As in D at high density (see Fig. 5.35), the experimental profile in He appears to shift by $\sim 10mm$ outward, only a part of which ($\sim 50\%$) might possibly be attributed to reconstruction errors. This displacement is not reproduced by the code, although the simulation results are far closer to experiment in absolute magnitude than at high density in D where detachment almost completely removes the target flux in experiment. One general reason for some of the discrepencies in the He simulations might be related to changes in P_{SOL}, especially at high densities where in the colder divertor plasma, He neutrals may more readily penetrate the core plasma due to their long mfp (cf. D neutrals) providing stronger volumetric power loss

166

Figure 5.42: *Simulated and experimental midplane mapped profiles at the (a) inner and (b) outer targets for high upstream densities in He. The simulation case is #11150 at $n_e^{sep} = 2.5 \times 10^{19} m^{-3}$ with $D_\perp = 0.5 m^2 s^{-1}$. The experimental discharge is #26222 as in figure 5.40.*

to the plasma through ionization inside the separatrix.

5.3.3 Concluding remarks on spatially constant transport coefficients

For both D and He plasmas $D_\perp$ must be increased in the SOL as $\bar{n}_e$ increases to provide any reasonable match with upstream profiles. Good agreement between simulations with spatially constant perpendicular transport coefficients and experiment in reversed field is found at the inner target for any density and both plasma species. The discrepancy at high n_e^{sep} between model and experiment at the outer target is very much smaller in He than

in D. The inclusion of toroidal geometry, together with additional volumetric processes such as VRM and CD_4 makes little or no difference to the simulated target parameters. This is a strong indication that the D simulations are missing an essential piece of physics which is of less importance in He. One such candidate, other than volumetric reactions, is the plasma-wall interaction, or more precisely, the amount of impurity production. At low temperatures, physical sputtering plays no role in He, whilst for D, chemical sputtering occurs at any energy. Interestingly, though, varying Y_{chem} in the simulations did not result in considerable differences.

From experiment it is known that the radiated fraction of the heating power is larger in D than in He. In the D simulations (#8675), a total volumetric power loss of $\sim 160kW$ is obtained at high $\bar{n}_e$, compared to $P_{SOL} = 440kW$, less than in experiment. Volumetric power loss in the He simulation at high n_e^{sep} (#9153) is $\sim 235kW$, 53% of P_{SOL}), and if it is assumed that in experiment most radiation originates from the region covered by the computational grid it may be concluded that this is then likely to be close to the experimental value ($\sim 55\%$ of P_{ohm}).

The missing link appears to be a combination of incorrectly modelled radial transport, (since upstream profiles agree less well with experiment at high densities), and possibly a missing source of impurities in deuterium plasmas. This missing source, if it exists, is likely to originate at the main chamber walls, since the variations in Y_{chem} attempted in the code (Fig. 5.36) are essentially operating only at the targets for as long as the target flux dominates over that leaving the main SOL due to perpendicular transport.

5.3.4 Applying convective radial transport

5.3.4.1 Experimental evidence for intermittent radial particle transport in the TCV SOL

Radial intermittent or 'bursty' transport has been recently observed in the TCV SOL using the RCP probe system on the LFS [23] in plasmas of identical magnetic configuration to that of Fig. 5.2 and in similar plasma conditions to those of interest here. The average radial intermittent particle flux is derived using equation 2.5.3 from measurements of plasma fluctuations, which the RCP is especially configured to make. It has been found that the density fluctuations and those in the turbulent driven flux have statistical properties that are universal across a wide range of discharge conditions and across the entire radial width of the SOL. One consequence of this [23] is that the average fluctuating particle flux, $\langle \Gamma \rangle$ at the plasma-wall interface scales solely with the local mean density $\langle n \rangle$, as is shown in Fig. 5.43. It is also shown in [23] that in L-mode discharges
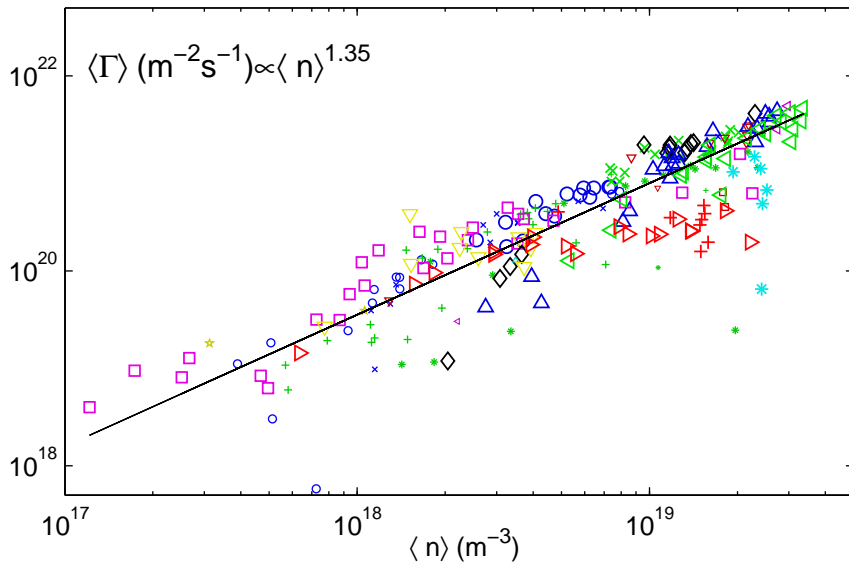
Figure 5.43: *Variation of $\langle \Gamma \rangle$ with local mean density $\langle n \rangle$. Data points shown are taken across a multitude of discharges in He, D L- and H mode plasmas, with forward and reversed B_Φ (taken from [23]).*

such as those considered here, the probability distribution function (pdf) of $\tilde{n}$ close to

or inside the separatrix is Gaussian, whilst in the far SOL density fluctuations become intermittent with a pdf strongly skewed toward positive events. Although some recent experiments have been performed at TCV to investigate the variation, if any, of $\langle \Gamma \rangle$ with poloidal position for relatively small displacements about the midplane, the analysis is not yet available.

5.3.4.2   Implementation of intermittent transport in SOLPS5.0

Based on the observation of turbulent transport in the TCV SOL, in particular the strong dependence on plasma density, it would appear natural that a purely diffusive description must be inadequate at high density. It is thus reasonable to invoke a convective component, through $v_\perp$ (eqn. 2.61 and Section 2.5.3), representing the intermittent nature of the observed turbulent flux. In the absence of a more quantitative theoretical foundation, this convective component is assumed to operate only on the LFS of the SOL, thus linking radial transport to a ballooning-like process, occurring preferentially in the regions of unfavorable magnetic curvature [5]. However, the reader should be aware, from the brief discussion and example given in section 2.5.2 (in particular eqns. 2.70 and 2.73) that concerning the result of the code the only important quantitiy is the total radial particle flux and that choosing a radially dependent $v_\perp$, $D_\perp$ or a combination of the two for describing this $\Gamma_\perp$ is equivalent.

To implement such a transport description, in particular concerning the spatial extent over which it is applied, requires a few modifications within B2.5. The resulting version of the code now allows the user to specify the poloidal and radial extent over which the convection is active. It is also possible to impose convection inside the LCFS to be some fraction, α, of the convective flux in the SOL. In the simulations presented below, convective transport is limited to poloidal cells $ix = [31\,48]$, corresponding to the region between the top right hand corner of the grid and the X-point. Perpendicular transport is assumed to be purely diffusive inside the LCFS ($\alpha = 0$) and spatially constant perpendicular diffusion coefficients are imposed as in Section 5.3.2, covering the entire grid. A further, ad hoc assumption is made that convective transport applies only to the main

ion species. In pure He, the main ions are assumed to be He^{2+} since the purely diffusive simulations show that the ion density of He^+ and the respective ion fluxes into and inside the SOL are approximately one order of magnitude lower than for He^{2+}. Radial impurity transport remains purely diffusive everywhere in the computational domain.

In principle, since convective transport is described by $\Gamma_\perp^{conv} = nv_\perp$, either a velocity or a flux could be prescribed in the code. In contrast to diffusive transport, which is proportional to a density gradient, convective transport contains no a priori information on $\nabla_r n$. Introducing convective transport into simulations could therefore yield density profiles with radially increasing density in the SOL, a behavior which is never observed in experiment (although flat density profiles are of course possible and are regularly observed at high density). In the modified version of the code, the user is therefore invited to define the maximum permissible value of $\Gamma_{\perp max}^{conv}$. In order to comply with the rest of B2.5, $v_\perp$ is then calculated from the imposed flux. Depending on the local density and radial density gradient at the beginning of each iteration, the following conditions apply:

- if $\nabla_r n < 0$ then $\Gamma_\perp^{conv} = \Gamma_{\perp max}^{conv}$ and $v_\perp = \Gamma_{\perp max}^{conv}/n_e$ with n_e taken locally.

- if $\nabla_r n \geq 0$ then $\Gamma_\perp^{conv} = 0$.

- $v_\perp \geq 0$, no convective inward flux

The first two conditions link the degree of convective flux with the local density gradient and allow $v_\perp$ to react to any increase in density at the grid edge due to ionization sources from recycling neutrals. Depending on the chosen value for $\Gamma_{\perp max}^{conv}$, this ansatz can lead to a very oscillatory behavior of $v_\perp$ and thus $\Gamma_{\perp max}^{conv}$, thereby introducing a source of numerical noise into the simulations. To limit the latter and facilitate convergence, a parameter, α_{flux}, has been introduced which increases or decreases $v_\perp$ according to the weightings: $v_\perp^{new} = (v_\perp - v_\perp^{old}) * \alpha_{flux} + v_\perp^{old}$ (increase) and $v_\perp^{new} = v_\perp^{old} - 0.5\alpha_{flux} * v_\perp^{old}$ (decrease).

Values of $\Gamma_{\perp max}^{conv}$ for the simulations are between $5 \times 10^{20} m^{-2}s^{-1}$ and $3 \times 10^{22} m^{-2}s^{-1}$. The higher $\Gamma_{\perp max}^{conv}$, the higher the possible noise and the larger the number of iterations

required before reaching convergence. Figure 5.44 illustrates the time evolution of the integral perpendicular D^+ flux across the LCFS, its mean value and the integral D^+ flux to the outer divertor target plate for a typical converged simulation. Transport across
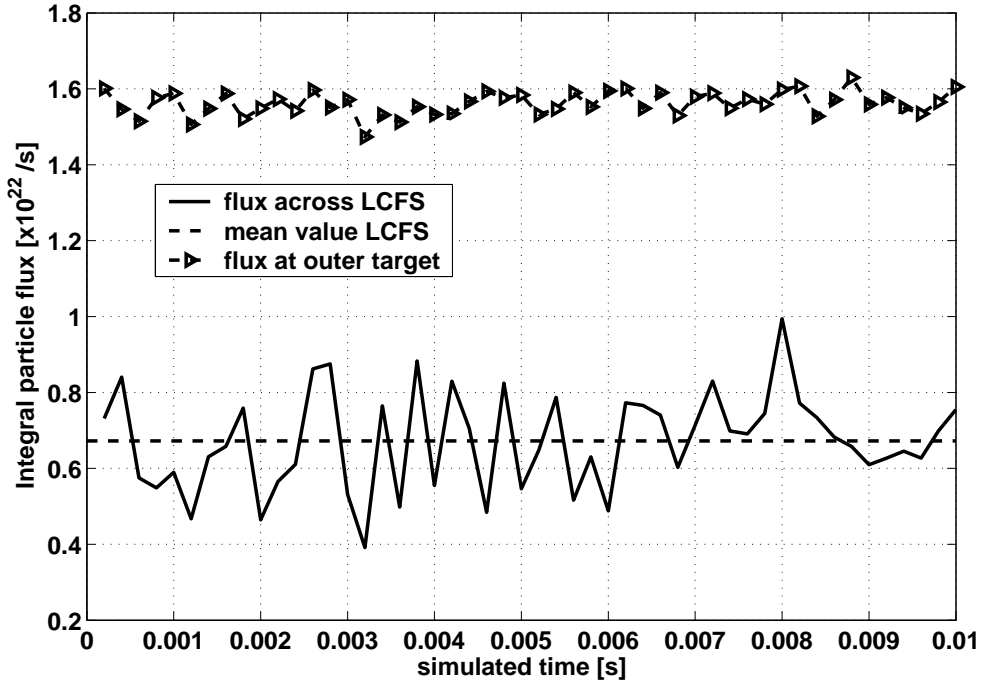

Figure 5.44: *Time dependent simulated integral ion fluxes across the LCFS and to the outer divertor for simulation #10452, using* $\Gamma^{conv}_{\perp\,max} = 2 \times 10^{22} m^{-2} s^{-1}$ *and* $\alpha_{flux} = 0.1$.

the LCFS in this example is purely diffusive and the oscillations seen are a result of the convective transport in the SOL. Since transport is diffusive inside the separatrix and the transport coefficients there are constant in time and space, the radial profile of the density gradient in the main plasma adapts itself continuously in order to fuel the SOL such that no positive density gradients can develop between the separatrix and the north boundary.

As a consequence of the convective ansatz, there are now two feedback mechanisms acting in the simulations. The first is the feedback on the gas puff which acts so as to obtain the prescribed n_e^{sep} and, secondly, feedback on $v_\perp$ which also affects n_e^{sep}. The inclusion of convection therefore increases substantially the time required for convergence.

Depending on starting conditions this increase is not less than a factor of 2.

Here and in what follows, the denomination NB or LCFS will be used to label integral fluxes, Φ, crossing the North Boundary and the separatrix respectively. It should also be noted that the coefficients for perpendicular heat convection, $\chi_{\perp i,e}$ remain unchanged in these runs. Heat will of course be convected cross-field with the particles (eqns. 2.85, 2.86). This Ansatz thus further increases the CPU time required for reaching convergence.

5.3.4.3   Comparison of upstream and target profiles at high upstream density

Section 5.3.2 has demonstrated how simulations provide a satisfactory match to experiment both upstream and at the targets for low n_e^{sep} (Fig. 5.27). In these cases, a convective component is not required in the model of radial transport and it can be readily shown that including even a small such component leads to strong departures from agreement at low density. This is not the case at high n_e^{sep}, where the data (Fig. 5.29) clearly show a broad SOL density profile, which cannot be matched by pure diffusion with constant $D_\perp$ alone. Convection is now added to study the effect at the highest n_e^{sep}. Table 5.6 summarizes the basic characteristics of the different simulations shown in the following figures. In this table, various options regarding atomic physics and chemical sputtering for the D code runs are noted. In particular, $MCW : 10$ denotes that a chemical yield of 10% is applied to all main chamber wall surfaces, whilst the 'standard' yield of $Y_{chem} = 3.5\%$ is assumed at the divertor targets as has been the case throughout. The abbreviations CRM and CD_4 respectively denote the use of the collisional radiative model and hydrocarbon molecules as described in Section 5.3.2. For all simulations presented in Table 5.6, $\chi_\perp = 1.0 m^2 s^{-1}$.

Figures 5.45 and 5.46 compare simulated and experimental upstream profiles for high n_e^{sep} in pure He and D plasmas. In the case of He, it is clearly impossible on the basis of comparison with experiment to choose between a simulation with $n_e^{sep} = 2.5 \times 10^{19} m^{-3}$ and spatially constant $D_\perp$ (cases #9153 , #11150) or a simulation with $n_e^{sep} = 2.0 \times 10^{19} m^{-3}$ and smaller convective transport (cases #11052, #11054). It seems relatively clear, however, that a large value of $\Gamma_{\perp max}^{conv}$ in He produces large deviations from experiment, es-

Simulation	Chemistry	Y_{chem} [%]	$D_\perp$ $[m^2 s^{-1}]$	$\Gamma^{conv}_{\perp\,max}$ $[10^{21} m^{-2} s^{-1}]$
#8006	CRM, $n_e^{sep} = 2.5 \times 10^{19} m^{-3}$	3.5	0.2	0
#8675	CRM, $n_e^{sep} = 2.5 \times 10^{19} m^{-3}$	3.5	0.5	0
#10452	CRM, $n_e^{sep} = 2.5 \times 10^{19} m^{-3}$	3.5	0.2	20
#9532	CRM, $n_e^{sep} = 2.5 \times 10^{19} m^{-3}$	MCW:10, Targets:3.5	0.2	20
#10100	CD_4 $n_e^{sep} = 2.5 \times 10^{19} m^{-3}$	3.5	0.2	20
#10841	CD_4 $n_e^{sep} = 2.5 \times 10^{19} m^{-3}$	MCW:10, Targets:3.5	0.2	20
#9153	He, $n_e^{sep} = 2.5 \times 10^{19} m^{-3}$	/	0.2	0
#11150	He, $n_e^{sep} = 2.5 \times 10^{19} m^{-3}$	/	0.5	0
#10968	He, $n_e^{sep} = 2.5 \times 10^{19} m^{-3}$	/	0.2	10
#11054	He, $n_e^{sep} = 2.0 \times 10^{19} m^{-3}$	/	0.2	5
#11052	He, $n_e^{sep} = 2.5 \times 10^{19} m^{-3}$	/	0.5	5

Table 5.6: *List of simulations shown in the various figures of this section. Note that code runs #8675, #8006 are pure diffusive cases presented in Section 5.3.2 and are included here for comparison. MCW=Main Chamber Walls.*

pecially inside the LCFS. In contrast, large values of $\Gamma^{conv}_{\perp\,max}$ in D yield better agreement between simulations and experiment upstream. Figures 5.47, 5.48, 5.49 and 5.50,
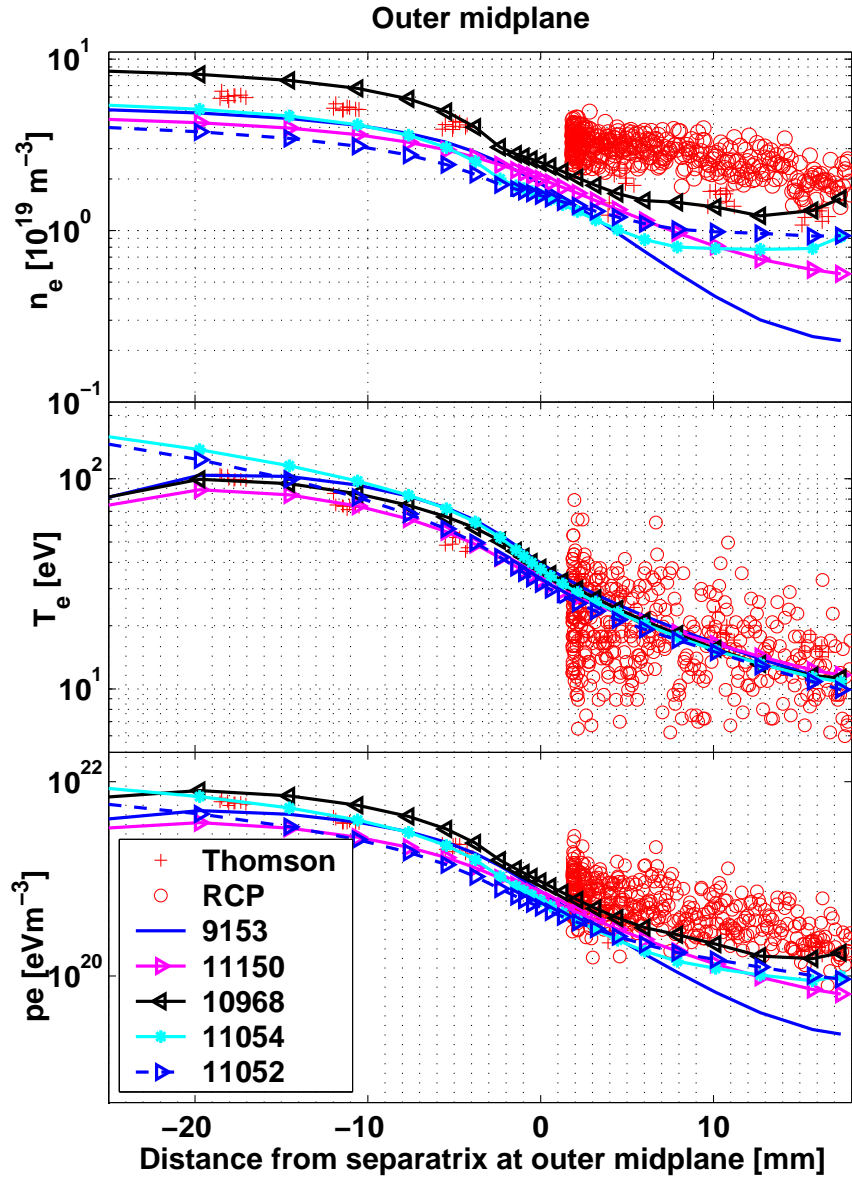
Figure 5.45: *Simulated upstream profiles with profiles from experiment for He (#26222)*
(see Table 5.6 for description of simulation parameters).

compare the results of the different simulations in He and D for the inner and outer target profiles. In He, increasing diffusive radial transport and/or reducing n_e^{sep} leads to broader target flux profiles - this is in the right direction to explain some (but not all) of the discrepancy between code and experiment at high n_e^{sep}, for which best match was
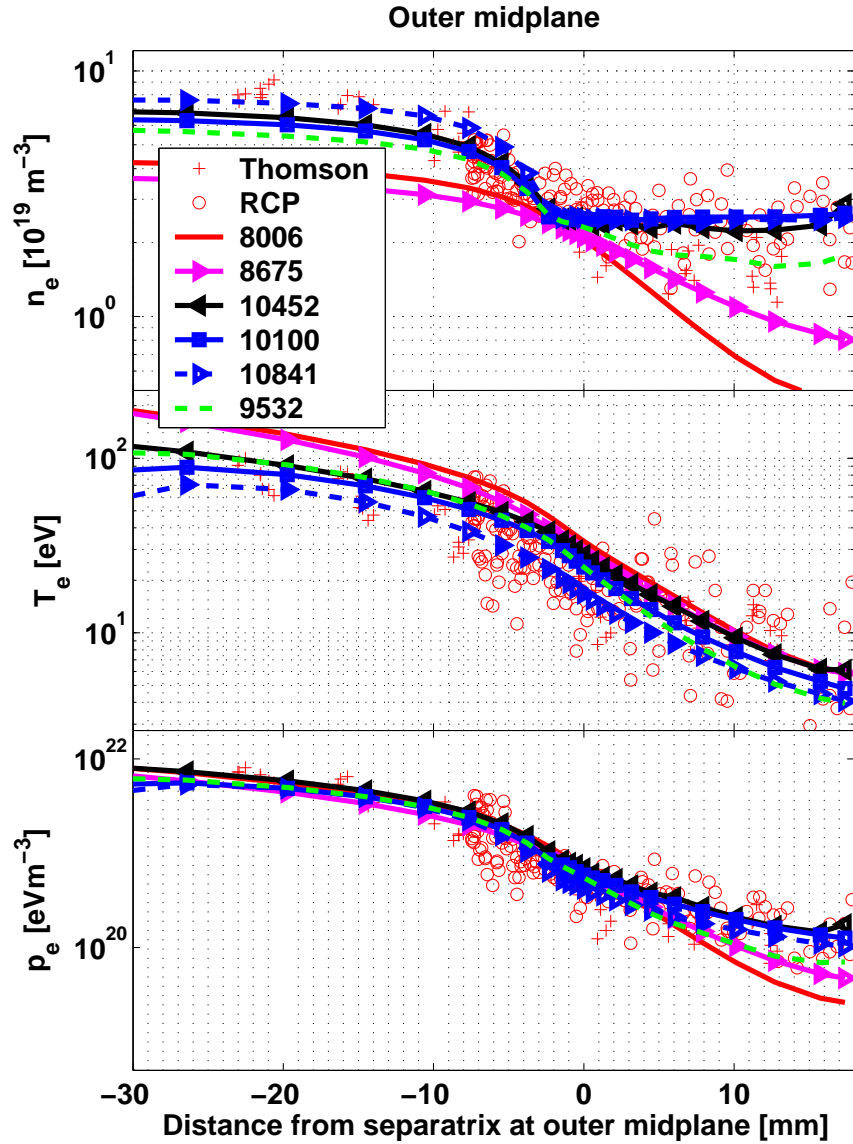
Figure 5.46: *Simulated upstream profiles with profiles from experiment for D (#24532) (see Table 5.6 for description of simulation parameters).*

with case #11150 for diffusive transport alone (Fig. 5.42). It is difficult to decide which combination of radial transport and n_e^{sep} best matches both upstream and target profiles.

In the D simulations strong convective transport in the SOL increases the inner and outer target peak and integral particle fluxes. This is opposite to the detachment behavior being sought. A key result is that an increase in the SOL radial transport, together
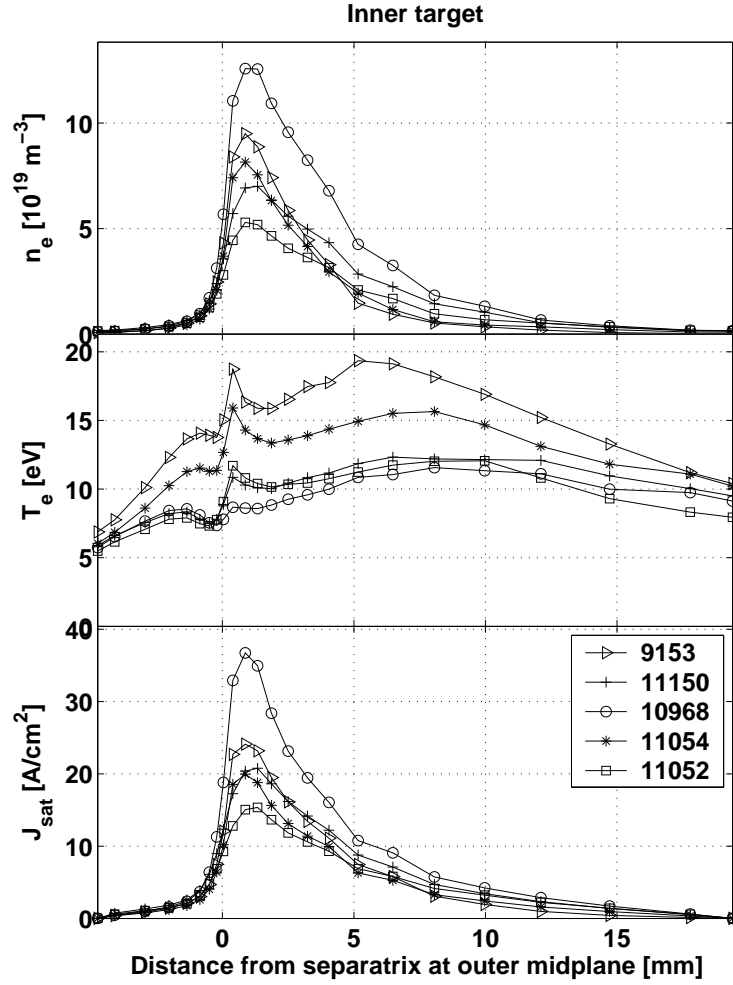
Figure 5.47: *Simulated inner target profiles for He (see Table 5.6 for description of simulation parameters)*

with an elevated main chamber wall chemical sputtering yield, Y_{chem}^{mcw} and the inclusion of CD_4 *does* lead to a considerable reduction in the outer target integral flux (compare cases #8006, #9532, #10841, #10100). Simulation case #10841 achieves the lowest outer target j_{SAT}, but also reduces the inner target flux by 25% in comparison with the purely diffusive case. In, neither case can the code match the inner target profile width, which remains high in experiment (see also Fig. 5.51). It should be noted, however, that for all cases with increased radial particle transport there is also a strong collapse in the inner target T_e. This may be an indication of an excess in the simulated radiation occurring

177
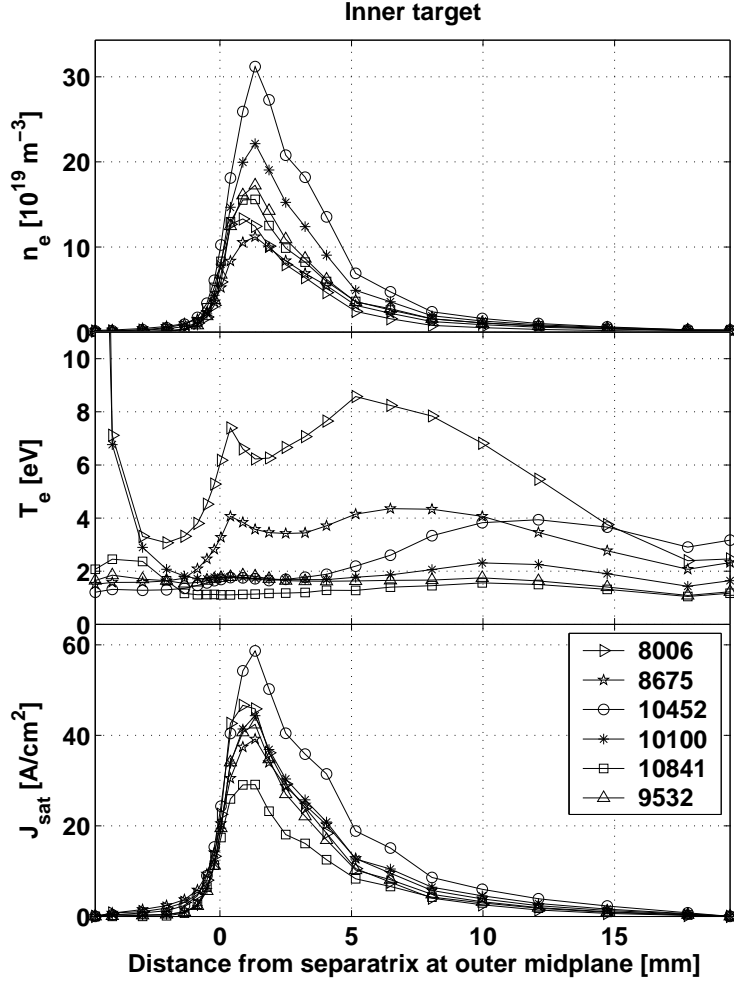
Figure 5.48: *Comparing simulated inner target profiles for D (see Table 5.6 for description of simulation parameters)*

above the X-point in the HFS SOL - this point will be revisited later.

In the context of simulation attempts thus far, it is of interest to note from Fig. 5.50 that for cases #9532, #10100 and #10841 the outer strike point j_{SAT} can be reduced considerably (up to a factor ~ 5) compared to the purely diffusive case #8006. Case #10100 (CD_4 without increased Y_{chem}^{mcw}) decreases the outer target j_{SAT} to a peak value very similar to that of #9532 (CRM, $Y_{chem}^{mcw} = 10\%$) but even further at the strike point. Figure 5.51 compares the simulated case yielding the lowest j_{SAT}(#10841) with experimental profiles at the inner and outer targets at high n_e^{sep}. At the outer target the simulated T_e
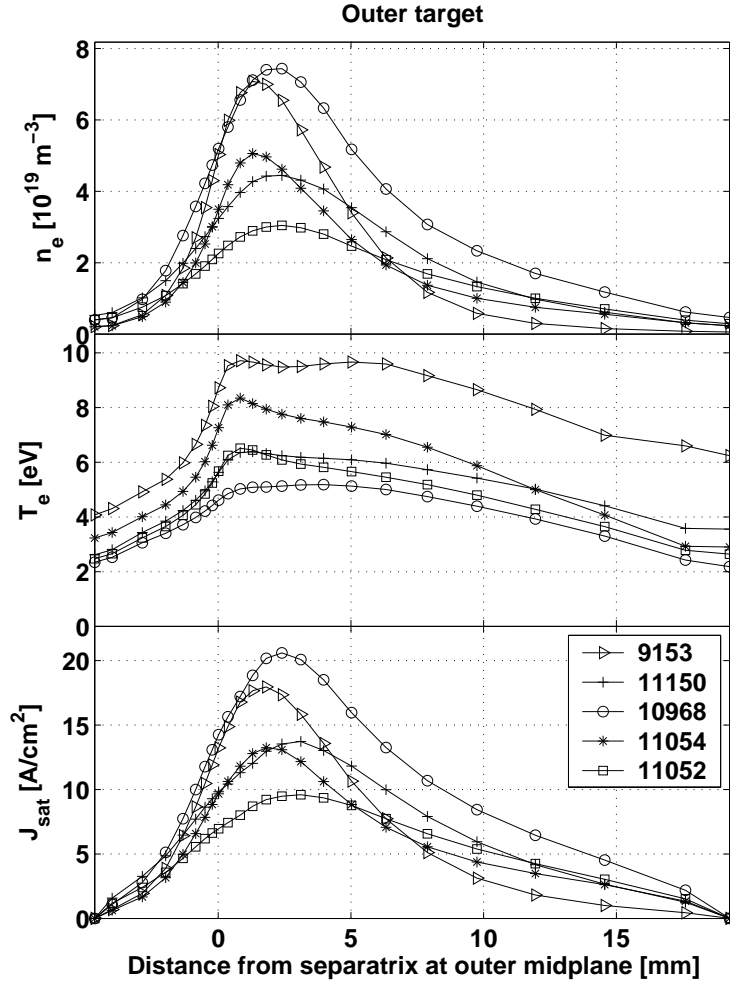
Figure 5.49: *Simulated outer target profiles for He (see Table 5.6 for description of simulation parameters)*

is considerably lower than the experimentally inferred values. This can be understood by recalling the remarks of Section 5.2.1.1 on Langmuir probe measurements at low T_e. If the measured T_e is higher than the real value in front of the targets, the derived values of n_e may be considerably lower than expected. The comparison must therefore focus on the particle flux (j_{SAT}) which is a straightforward experimental measurement provided the probe geometry and field line angles are well known. That this must be the case is demonstrated clearly by the agreement between code and experiment under low density, attached conditions (see Fig. 5.27). Although the simulated peak j_{SAT} value of case

179
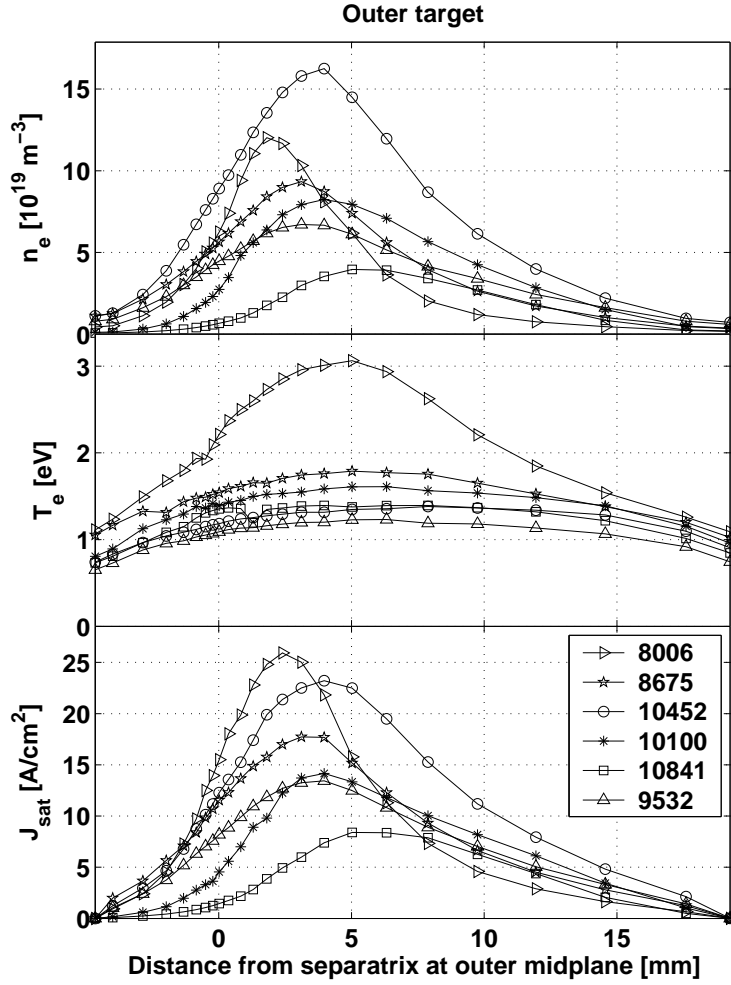
Figure 5.50: *Simulated outer target profiles for D (see Table 5.6 for description of simulation parameters)*

#10841 is still a factor ~ 4 higher than in experiment, it is nevertheless reduced by more than a factor of 3 compared with the pure diffusive case and a little less than a factor of 2 compared with the convective cases #9532 and #10100. Most importantly, and worth reiterating, Fig. 5.51 demonstrates that case #10841 (and to a lesser, but still significant extent, cases #9532 and #10100) reduces the strike point ion flux to values likely not far from experiment. Figures 5.50 and 5.51 thus imply that for cases #9532, #10100 and #10841, contrary to the pure diffusive case #8006, detachment occurs in the strike point region, leaving the far SOL more attached. This is the first time that such behaviour has
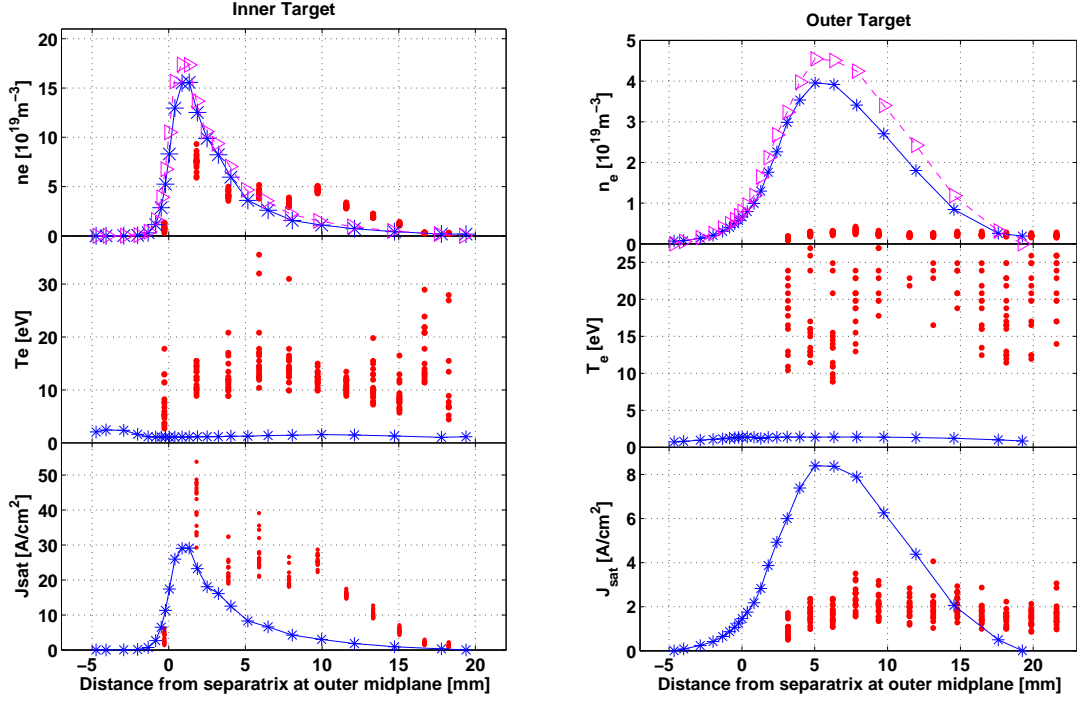
Figure 5.51: *Comparing simulated (#10841) and experimental (#24532) inner (a) and outer (b) target profiles for D at high $\bar{n}_e \sim 1.1 \times 10^{20} m^{-3}$.*

been seen in these TCV simulations. The rest of this section explores the details of this important result.

5.3.4.4 Comparison of detached and attached parallel profiles

In order to further understand the differences and similarities of the detached and attached cases, comparison of parallel to $\vec{B}$ profiles is a useful point of departure. The comparsion concentrates on cases #8006, #10100, #10841 and #9532, demonstrating the mechanism by which detachment itself occurs in the latter 3 simulations. In each case, parallel profiles are extracted from the second radial grid cell ($iy = 11$) on the SOL side of the separatrix, corresponding to a distance $\sim 2mm$ from the separatrix when mapped to the outer midplane and therefore to a flux tube close to the strike point where the strongest detachment is observed. The parallel distance is given as the total distance

along the field line from the inner to the outer target.

Figure 5.52 compares the parallel profiles of the D^+ particle flux and Fig. 5.53 the sum of the dynamic and static pressures. Case #8006 demonstrates behaviour typical of high recycling, with the flux increasing in front of the divertor plates and the pressure remaining approximately constant along the field line. In the three other cases, clear detachment is observed at the outer target. The parallel particle flux and pressure are
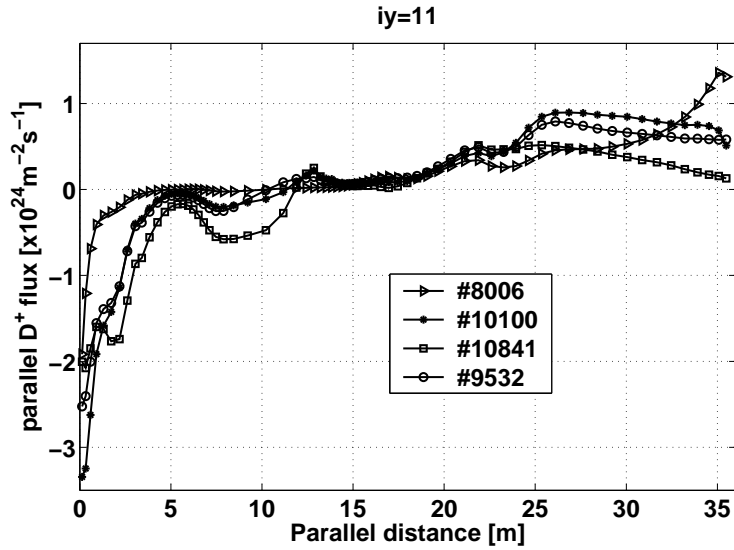
Figure 5.52: *Parallel particle flux profiles (iy = 11) of selected simulated simulations (D) (see Table 5.6 for description of simulation parameters).*

reduced, with the latter by a factor of 4 to 5 compared to its value at the entry of the outer divertor volume (at $\sim 22m$). The decrease of these two parameters is one of the principal characteristics of divertor detachment (see Section 2.9). In contrast, Fig. 5.54 shows clearly that in all simulations the plasma is more attached in the far SOL compared to the strike point location[16] - the pressure remains rather constant throughout most of the divertor volume, decreasing only slightly in front of the outer divertor target by a similar degree in all cases shown here.

Figure 5.55 demonstrates that case #8006 exhibits another typical feature of the high

---

[16]some detachment is though visible since for cases #10841 and #9532 in particular, the pressure is reduced by a factor of ~ 2
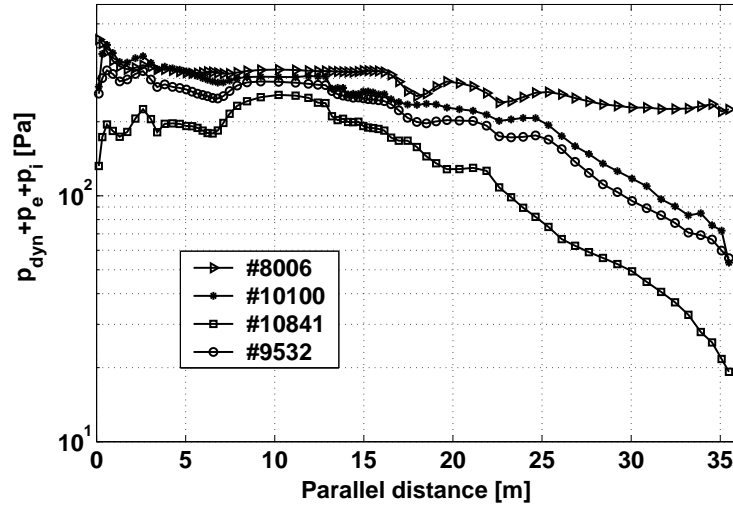
Figure 5.53: *Parallel profiles (iy = 11) for total plasma pressure ($p_{dyn}+p_e+p_i$) for selected simulations (D) (see Table 5.6 for description of simulation parameters).*
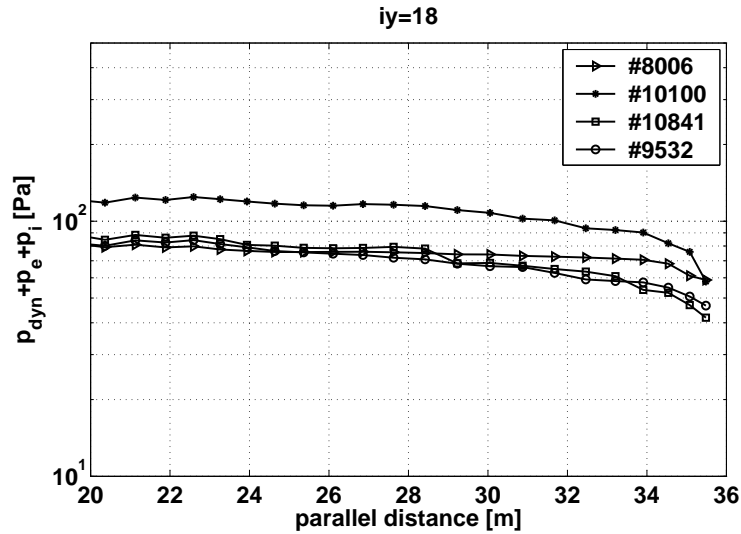

Figure 5.54: *Total pressure parallel profiles ($p_{dyn} + p_e + p_i$) along at least 15m of connection length for selected simulations (D) in the far SOL of the outer divertor, (iy = 18), corresponding to $\sim$ 6mm distance (see for reference e.g. Fig. 5.50) from the separatrix mapped to the outer midplane (see Table 5.6 for description of simulation parameters).*

recycling regime; a rapid density increase in front of the target plates. In comparison, for the 3 convective cases, n_e decreases as the target plate is approached, even though this

183

occurs only over the last metre in front of the target. Although detachment is therefore occuring, (since pressure and particle flux are decreased) in these two cases, it is not accompanied by a strong net reduction of n_e along the outer target. Such behaviour is, however, clearly observed for case #10841. In fact, only in this case is the outer divertor volume a net volumetric particle sink for the plasma, with less particles being ionized than removed. In each of the other three cases, the divertor volume continues to be a net particle source for the SOL plasma. It should nevertheless also be noted that volumetric particle sources and sinks can, in principle simply balance such that the divertor volume need not necessarily be a net particle sink. Case #10841 shows an interesting increase in n_e in the main SOL, in the region $\sim 10m$ from the inner target, which is associated with a strong decrease in T_e at the same location (Fig. 5.56). This appears to be the result of strong volumetric impurity radiation at the top of the machine in which the region of large flux expansion (see Figures 5.26 and 5.63) provides an extended volume where the temperature is well suited for carbon radiation.

To significantly reduce particle fluxes, volumetric three-body and radiative recom-
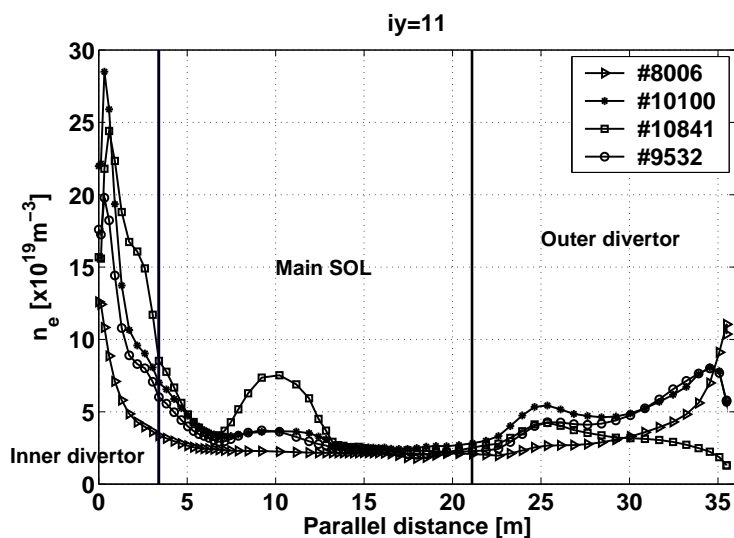
Figure 5.55: *Parallel n_e profiles for selected simulations (D), (iy = 11). See Table 5.6 for description of simulation parameters.*

bination requires high densities ($> 10^{20}m^{-3}$), and low temperatures ($< 2eV$) in a 'suffi-

ciently' large volume. In the case of MAR, the process can be active in regions where T_e is up to $8eV$ (as, for example, the case of hydrocarbon MAR). Figure 5.56 shows the parallel T_e profiles for the four cases considered thus far and Fig. 5.57 both the T_e and T_i profiles for code runs #8006 and #10100. As expected, due to the high collisionality in the main
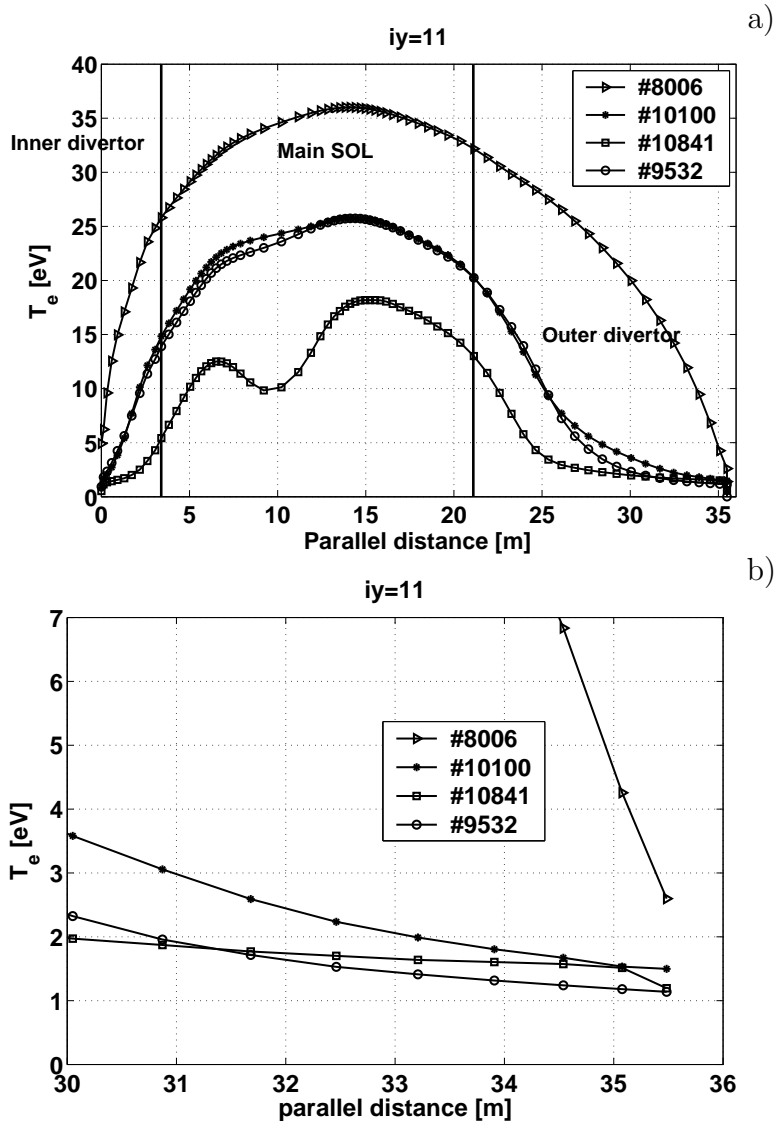

Figure 5.56: *Parallel T_e profiles for selected simulations (D) along (a) the entire SOL and (b) a short region in front of the outer divertor target (b), (iy = 11). See Table 5.6 for description of simulation parameters.*

SOL ($\nu_e^* \sim 80$, using approximate values of $T_e = 25eV$, $n_e = 2.5 \times 10^{19}m^{-3}$), T_i and T_e
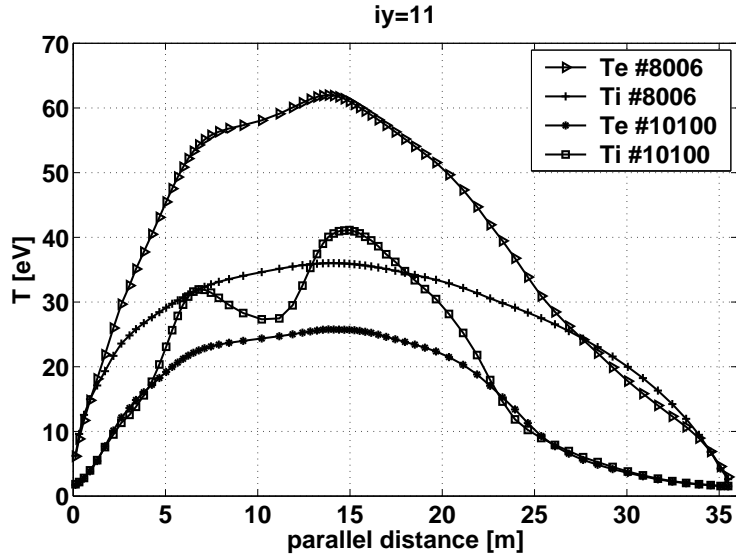
Figure 5.57: *Comparison of simulated parallel T_i and T_e profiles for selected simulations (D). See Table 5.6 for description of simulation parameters.*
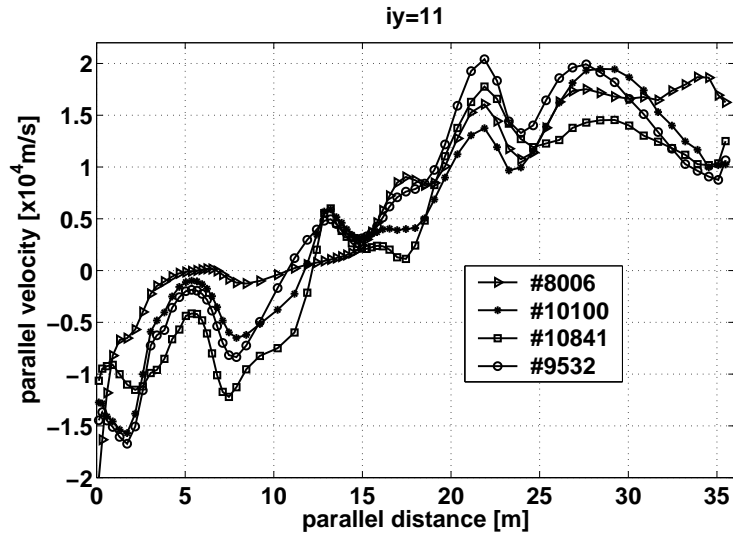
Figure 5.58: *Comparison of simulated parallel D^+ fluid velocity profiles (iy = 11). See Table 5.6 for description of simulation parameters.*

are equilibrated in large parts of the divertor volume, especially for the detached cases, of which #10100 serves as an example. The rate coefficients for three-body and radiative recombination (EIR, Section 2.7) increase rapidly below $T_e = 2eV$. For an electron

density of $\sim 10^{19} m^{-3}$, they increase by approximately a factor of 2 when T_e is reduced from $2eV$ to $1eV$ and climb even more steeply for lower temperatures. Even though T_e collapses in the detached cases compared to #8006, in none of the three cases does it fall much below $2eV$. The simulation results are very sensitive to T_e in the region in front of the divertor targets. The combined effects of a strong temperature sensitivity of the EIR coefficients at low T_e and the gas puff feedback mechanism used to regulate n_e^{sep} can lead to considerable numerical, time dependent oscillatory behaviour of n_e^{sep} itself, energy fluxes and target fluxes. This has been frequently observed when running some of these TCV cases (such as when Y_{chem} is increased beyond the nominal 10% used in cases #9532 and #10841).

Even in case #10841 for which both the particle flux and n_e are reduced along the outer divertor leg, the neutral flux resulting from EIR is only approximately 8% of the neutral particle flux from the outer divertor. It cannot therefore be concluded that strong volumetric recombination is causing the ion flux reduction in any of the three detaching cases compared to the diffusive case #8006. It does, however, play a role in explaining the reduced particle flux in #10841 compared with #9532 and #10100, since the case #10841 has a slightly lower T_e, promoting a slightly higher level of EIR.

Further support for the attribution of little importance to EIR in any of the 3 detached cases may be derived from the estimation of τ_{dwell} and τ_{rec} using the parallel plasma fluid velocity shown in Fig. 5.58. In all cases the parallel velocity is between $1 - 2 \times 10^4 m s^{-1}$ in the outer divertor. The region in which $T_e \leq 2eV$ begins about $10m$ before the outer divertor target in case #10841 and at most $5m$ in cases #9532 and #10100. The average value for the dwell time in this region is therefore $\sim \tau_{dwell} = 3 - 7 \times 10^{-4}s$, which, assuming an average value of $n_e \sim 3 \times 10^{19} m^{-3}$ and using the rate coefficient for EIR at $2eV$ (reaction H.4 2.1.8 AMJUEL), gives $\tau_{rec} \approx 0.1s$. This results in a ratio of $\tau_{rec}/\tau_{dwell} \sim 1\%$ and is an estimate for the magnitude of the volumetric sink through EIR (which was about 8% for #10841), showing that EIR is in any case small compared to the recycling flux from the outer target and does not remove a significant number of particles. These low numbers should not be taken to imply that EIR is not an important mechanism in

driving the degree of observed outer divertor detachment. Even the most highly detached simulation presented here (#10841) achieves ion flux reductions a factor ~ 2 too low for the integrated flux and a factor ~ 4 too low for the peak flux in comparison with experiment. There is thus considerable scope for EIR to be playing an important role in the real experimental situation.

The oscillations in the parallel ion velocity close to the entrances of the inner (at $\sim 5m$ from the inner target plate) and outer divertor throats ($\sim 22m$) are likely a result of a 'nozzle' effect, due to the expansion and compression of field lines in regions of strong poloidal curvature for the discharges simulated here (see e.q. Fig. 5.26). The plasma fluid is accelerated due to the resulting parallel pressure gradients.

Before adressing further the reason for the parallel particle flux reduction it is worth discussing briefly an additional result of these simulations. Observations on ASDEX-U [195], JT-60U [102] and B2-EIRENE simulations for JT-60U [196] have shown that high Mach flows occur in the divertor volume during detachment and the occurence of an X-point MARFE. Figure 5.59 demonstrates that similar results are obtained in the TCV simulations. In each of the cases with detached solutions at the outer target, $M_\parallel \geq 1$
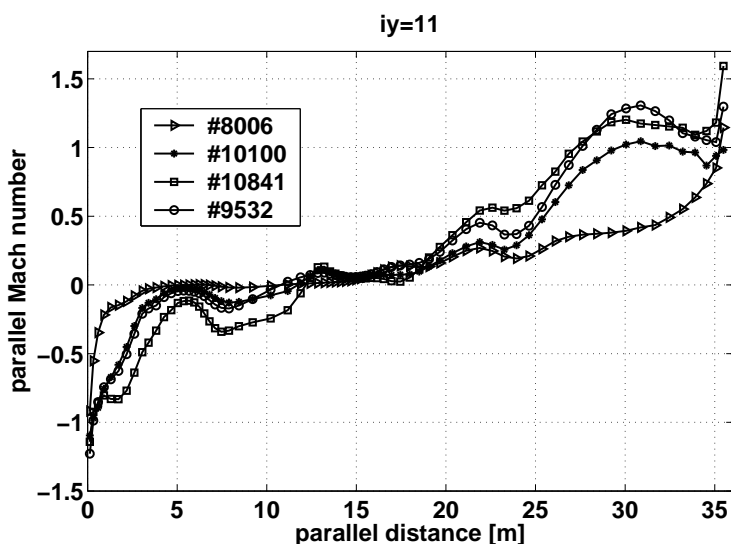

Figure 5.59: *Comparison of simulated (D) parallel Mach profiles (iy = 11). See Table 5.6 for description of simulation parameters.*

already $5 - 7m$ before the target plate and begins to increase rapidly near the entrance to the outer divertor throat at $\sim 20m$. In contrast, in the attached case (#8006), $M_\parallel$ increases only to ~ 0.4 in the divertor volume, followed by an increase to $M_\parallel \sim 1$ at the target. In all simulations, $M_\parallel < 0.2$ in the main SOL close to the separatrix. Along the LFS of the main SOL ($\sim 12m - 20m$) the flow velocities are apparently rather independent of the divertor being detached or attached and, it should be recalled, are obtained without drift terms activated in the code. They are thus due entirely to the presence of the divertors.

Figure 5.58 shows that the parallel D^+ fluid velocity is deccelerated by up to a factor 2 in the outer divertor, beginning at $\sim 30m$ for all three detached solutions. This is not the case for the purely diffusive case. In all detached cases, $\Gamma_\parallel$ is at least slightly reduced, even if for cases #9532 and #10100, the simultaneous increase of n_e partially compensates the reduction of $v_\parallel$ ($\Gamma_\parallel \propto n_i v_\parallel$). But Figure 5.53 demonstrates quite clearly that p_{tot} is decreased substantially in all detached conditions. One is thus led to ask why the total pressure is decreasing in the detached solutions and not in #8006. Since momentum removal through EIR has been excluded (since the particle sink is small), the answer must lie in momentum transfer to neutrals. Two explanations may be invoked.

Firstly, in the detached solutions T_e is reduced to values below $5eV$ in the divertor region. The temperature of D atoms is between $5eV$ and $3eV$ in the parallel field region between $30m$ and the target plate, decreasing towards the target. This neutral temperature is a consequence of Frank-Condon energies[17] from the dissociation of D_2, but also from CD_x^{l+} ($l = 0, 1, 1 \leq x \leq 4$), and CX processes with ions, which are hotter upstream than closer to the target (Fig. 5.57). The ionization mfp for atoms at these temperatures (thermal velocity, $v_{th} \sim 2 \times 10^4 ms^{-1}$) in a plasma of $n_e \sim 5 \times 10^{19} m^{-3}$, $T_e \sim 2 - 5eV$ is $\lambda \approx 12m - 0.2m$. Since the radial divertor width is $\leq 10cm$, atoms may thus escape the divertor volume with high probability. Even though the molecular density falls rapidly in front of the target plates, it is then only a factor ~ 2 lower than the atomic density up to a distance of $\sim 5m$ in front of the target, before a further rapid decrease. Molecules may

---

[17]providing atoms with a kinetic energy between $0.3eV$ and $5eV$

therefore also contribute to the momentum removal.

Secondly, as a consequence of the low temperature the atomic density is an order of magnitude larger than in the purely diffusive case #8006 (Fig. 5.60). The higher atomic
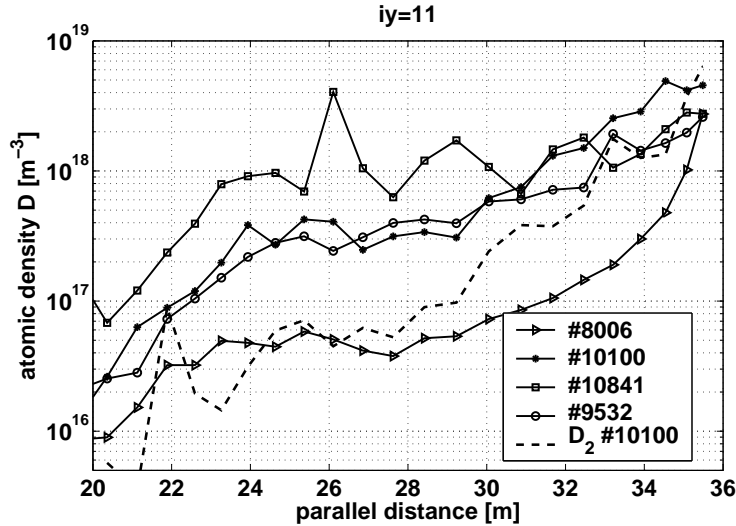

Figure 5.60: *Comparison of D-atom simulated densities in the outer divertor fan along the field line at iy = 11 together with one example D_2 density from #10100, (see Table 5.6 for description of simulation parameters).*

density, together with a lesser contribution from molecules provides for an increased number of elastic CX reactions in the detached solutions and therefore increased momentum removal. In combination with the moderate plasma density and reasonably low temperature (so that more neutrals carrying the ion momentum may escape the divertor volume before ionization occurs), this neutral density is sufficient to yield a significant degree of detachment, especially in the strike point region.

5.3.4.5 Simulated neutral pressure

The increased outer divertor transparancy as T_e decreases can be observed in Fig. 5.61, where the neutral outflux onto material wall surfaces computed by EIRENE is compared for the purely diffusive case (#8006) and the convective case #10452 in which the target ion fluxes are similar but for which n_e and T_e differ strongly (Fig. 5.50). In both cases
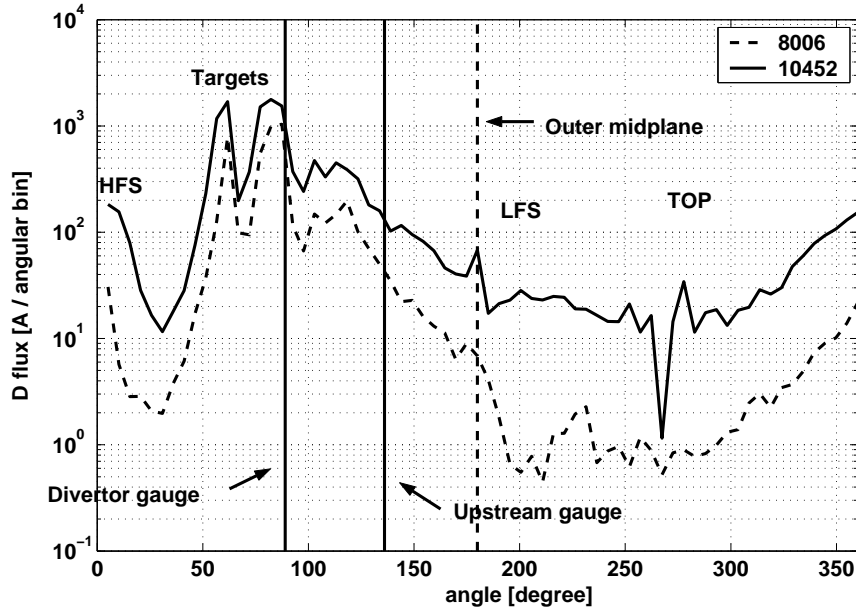
Figure 5.61: *Angular distribution of the D neutral flux onto the vessel walls as simulated by EIRENE for the purely diffusive case and a detached solution. The flux is given in Amperes per bin, with each bin corresponding to constant angular interval in the counter-clockwise direction beginning at the inner midplane centered on the magnetic axis (total of 70 bins). The locations of the ASDEX fast pressure gauges are indicated for reference.*

there is a large neutral flux in the angular range between 100° and 180°, corresponding to neutrals impinging on the LFS main chamber walls along the entire poloidal extent of the long outer divertor fan. As a consequence of the convective radial transport imposed in case #10452, the outer midplane neutral outflux is approximately a factor 10 larger than for #8006. This increases the far SOL density (Fig. 5.46), which in turn enhances the neutral influx due to ion recycling at the grid boundary and leads naturally to an increased probability for neutrals to escape the computational grid via CX processes.

An additional important test of the simulations is their ability to reproduce the divertor and upstream pressures measured by the fast ASDEX type gauges described in Section 5.2.1.3. Using the simulated values for the temperature and densities of the neutral atoms and molecules in the outermost cells of the computational grid, a neutral density in the fast pressure gauge enclosure can be estimated. Such calculations require some assumption

concerning the pressure regime of the neutral particles. The divertor gauge is located in a small CF63 port under the divertor floor behind a $40mm$ orifice in the protection tiles. The highest pressures there do not exceed $\sim 0.4Pa$ and the neutral mfp is expected to be larger than or comparable to the hole diameter. The midplane gauge is housed within a much larger lateral port and faces regions with much lower pressure (Fig. 5.12). In both cases, neutrals should thus be in the molecular flow regime with high Knudsen numbers, or at most, in the initial range of the transition to viscous flow. The atomic neutral density, n_{in}, inside the gauge head may then be computed following the arguments in [96]

$$n_{in} = \frac{n_{out}}{\sqrt{2}} \sqrt{\frac{T_{atom}^{plasma}}{T_{wall}}}, \tag{5.7}$$

where the gauge head and surrounding enclosure are assumed to be at room temperature $(300K)$ and n_{out} is the atom density estimated from the code simulations. The same calculation applies also for molecules but without the factor $\sqrt{2}$ in eqn. 5.7. Knowing n_{in} and with the assumption of a room temperature enclosure, the total neutral pressure follows trivially (combining atomic and molecular contributions). Table 5.7 compares experimental and simulated midplane and divertor pressures for $n_e^{sep} = 2.5 \times 10^{19} m^{-3}$ for a selection of the code runs in Table 5.6. Whilst there is some variation for the upstream simulated neutral pressure, it is a general observation that the simulated values are consideribly lower than the experimental values if only diffusive transport is assumed at high density. In the divertor region, simulated pressures are higher, but both diffusive and convective transport assumptions provide values comparable to experiment, though convective transport does yield the highest pressures.

The low variation in neutral pressure between simulations #8006 and #10841 despite the large difference in peak ion flux, implies for both cases that the opacity of the divertor fan is insufficient to prevent neutral escape. The measured neutral pressure, especially in the divertor, is in any case a consequence of the detailed balance between this divertor transparency and the momentum transfers from the plasma to the neutrals. For more detached cases than those achieved in the simulations, it is possible that momentum removal is increased in the outer divertor, at first increasing the neutral pressure. Such a

Simulation/ Experiment	Type	p_n^u [Pa]	p_n^{div} [Pa]	p_{compr}
#8006	Purely diffusive, $D_\perp$ constant	$\sim 0.006 - 0.01$	~ 0.1	~ 10
#10452	convective	~ 0.04	~ 0.35	~ 10
#10841	convective, CD_4, $Y_{chem}^{MCW} = 10\%$	0.02	0.15	~ 13
#9532	convective, $Y_{chem}^{MCW} = 10\%$	~ 0.02	~ 0.15	~ 8
#20557, #20558	Experiment	$\sim 0.03 - 0.04$	$\sim 0.1 - 0.15$	< 4

Table 5.7: *Comparison of simulated and experimental neutral pressures for some of the simulations (D) presented in this section for fixed $n_e^{sep} = 2.5 \times 10^{19} m^{-3}$ (pressure calculated upstream from cells at $ix = 40$, $iy = 23$, and at the divertor from cells $ix = 72$, $iy = 19$)*

detached state is, however, likely to have an even larger volume of low T_e plasma (perhaps sufficiently low for EIR to occur at higher levels), promoting neutral escape and thus in a second step a reduction in the measured neutral pressure.

5.3.4.6 Influence of C production at main chamber walls

Summarizing the above analysis, total plasma pressure is lost in the detached simulated cases through CX momentum transfer to neutrals and for this to occur it is evident that T_e must be low in the divertor volume. The decrease is strongest for case #10841, which has the lowest simulated T_e in the outer divertor volume and as a consequence the largest EIR volumetric recombination sink. In addition, it is somewhat surprising that cases #9532 and #10100, neither of which include CD_4 molecules, lead to such similar results regarding pressure loss. This would appear to practically exclude hydrocarbon MAR processes, at least in the way in which they have been included in the code, from having a strong influence on the plasma detachment in TCV.

One is thus led to ask which processes upstream in the main SOL and around the

X-point might lead to conditions in the outer divertor volume such as to promote efficient momentum removal and possibly volumetric recombination. The answer evidently lies with power balance in the main SOL (and to some extent in the divertor volume) and its consequence for the power entering the outer divertor. Only when convective radial outfluxes are combined with enhanced main chamber chemical erosion yields or CD_4 can the simulations achieve any degree of the outer target detachment. This points strongly to main SOL radiation loss as the candidate for reduction of outer divertor power influx.

Even though there is considerable scatter in chemical yield measurments from toka-maks, divertor simulators and ion beam experiments, recent attempts to compile the data and provide appropriate fitting functions [69] conclude that maximum yields for D^+ on graphite are $\sim 4\%$ for particle fluxes in the range $10^{22} - 10^{23} m^{-2} s^{-1}$, wall temperatures from $300K \rightarrow 600K$ and for particle energies typical of the tokamak edge. The key element with regard to the code simulations is to recognize that the version of SOLPS5 used here does not simulate main chamber wall ion interaction at all[18]. Neutral outfluxes do reach the walls, but as described in Chapter 3, particle recycling is simulated using a default reflection model for the ions reaching the north boundary, reinjecting them as neutral atoms or molecules. These neutrals may then be backscattered through CX or elastic collisions and propagate to the walls where they will interact chemically with the graphite protection tiles.

A very rough estimate of the simulated MCW carbon production rate compared with what might be expected in experiment is readily made. According to Fig. 5.43, RCP data show that a mean, turbulent driven flux of $\langle \Gamma \rangle \sim 2 \times 10^{21} m^{-2} s^{-1}$ arrives perpendicularly to the flux surfaces at the probe location and at a radial position corresponding to the wall surface mapped to the midplane for plasma densities at which anomalous detachment

---

[18]When using more than one molecular species, EIRENE '99' must be used. A slight modification to the code remains to be applied and retested in order to make chemical sputtering at the north boundary possible. In principle, chemical sputtering of C could be defined in B2.5. At present it is not possible to include physical sputtering at the main chamber walls (although this is considered negligible at the low SOL temperatures, charecteristic of high n_e^{sep})

is seen in the standard TCV SNL discharge. Although a new set of LFS Langmuir probes have just been installed in TCV at the time of writing, full analysis permitting a more accurate estimate of the integral MCW ion flux than can be provided by a single probe (the RCP) has not yet been performed.

Assuming that the total surface across which ions are transported perpendicularly with this flux is limited to the LFS only, gives an area of $\sim 5m^2$. The total ion flux reaching a MCW surface is therefore $1 \times 10^{22}s^{-1}$, which, with $Y_{chem} = 3\%$, would yield $3 \times 10^{20}s^{-1}$ C atoms produced by ion impact. For a typical SOLPS5 simulation with $\Gamma^{conv}_{\perp max} = 20m^{-2}s^{-1}$, the total ion outflux across the North boundary is $2 \times 10^{21}s^{-1}$ and is thus a factor 5 lower than the experimental estimate. The total D outflux in the simulations across the north boundary is $\sim 2 \times 10^{21}s^{-1}$ and is the only flux that reaches the main chamber walls to produce C, yielding 6×10^{19} atoms, with $Y_{chem} = 3\%$. This is a factor of 5 less than the estimated C production rate due to ion impact in the experiment. It could thus be argued that in order to provide a more realistic estimate of the C-production at the main chamber walls in the simulations, an 'artificial' increase of Y_{chem} to any value between 3.5% and 15% is perfectly reasonable. One should also note that chemical sputtering produces wall temperature hydrocarbon molecules, whether due to ion or neutral impact and so, unlike physical sputtering, the incoming C atoms have very low energies. The ion outflux (which the code does not simulate) may also cause physical sputtering, but ion energies and electron temperatures in the far SOL at high density are unlikely to be sufficient for much sputtering to occur in this way. Reference [197] describes the results from a similar approach in which simulated ion and neutral outfluxes have been used to compute the erosion rate of the MCW in ITER, including an estimate for erosion from physical sputtering.

In its present state, SOLPS5 cannot be simply adapted to correctly account for interaction with wall surfaces, even though it is becoming increasingly clear that such interaction must be accounted for, at least at high densities. The only apparent option therefore appears to be to compensate through adhoc adjustments such as that proposed here for wall impurity release.

Table 5.8 provides an overview of the simulated impurity radiation distributions from a series of code runs including the various transport, atomic and molecular physics models and assumptions on the magnitude of the chemical yield. The experimental data are taken from a previously published density ramp discharge [16] since good quality bolometric reconstructions are not available for the most recent detachment studies. The simulated integral outer target and strike point ion fluxes (the latter being denoted as j_{SAT}^{sep}) are also provided as an indicator of the degree of the achieved detachment.

The maximum decrease in both the total and strike point ion fluxes to the outer target is achieved in the simulations when power radiated in the main SOL above the X-point is highest. The loss of target current is far less dependent on radiation losses in the outer divertor volume. This is very similar to the experimental observation of an increase in power radiated from the main SOL with increasing $\bar{n}_e$. In addition, the simulated volumetric power loss from recycling neutrals and impurities in the outer divertor decreases with decreasing total ion flux. A similar slight tendency is observed in experiment. For simulation case #10841 with the lowest integral and strike point ion flux at the outer target, the total radiated power is $\sim 63\%$ of P_{SOL}, close to the experimental value ($\sim 70\%$).

As a crude test of the extent to which P_{SOL} and the main SOL radiation affect the divertor performance, P_{SOL} was increased to $600kW$ (case #11207), leaving all other parameters as for case #9532. The results are shown in Fig. 5.62. Although the upstream profiles change only slightly in response to the increased power (notably T_u, as expected) the ion flux to the outer target doubles and the target temperature increases. Thus, although the total radiated power in the SOL and divertor combined remains unchanged compared with the lower input power (i.e.$\sim 70\%$ of P_{SOL}), the absolute value of the power conducted into the divertor volume is higher and a degree of target flux reattachment is obtained.

Despite the encouraging approximate agreement, it should nevertheless be clear from Table 5.8, that the code is not quantitatively matching the experimental radiation distribution. Although the total power radiated in the SOL and divertor is reproduced,

196

#	Type	$P_{LCFS}^{outside}$ total [kW]	P_{X-pt}^{above} [kW]	P_{X-pt}^{below} [kW]	$\int^{ot} j_{SAT}$ [kA]	j_{SAT}^{sep} [Acm^{-2}]
#8006	$D_\perp = 0.2$	186/42%	53/12%	100/22%	2.0	16
#10433	$D_\perp = 0.2$ $Y_{chem} = 10\%$	208/47%	99/23%	114/26%	1.4	9.1
#10452	$D_\perp = 0.2$ $\Gamma_{\perp\,max}^{conv} = 20m^{-2}s^{-1}$	254/58%	80/18%	109/25%	2.6	12.8
#9532	$D_\perp = 0.2$ $\Gamma_{\perp\,max}^{conv} = 20m^{-2}s^{-1}$, $Y_{chem}^{mcw} = 10\%$	269/61%	204/46%	83/19%	1.6	7.36
#11128	$D_\perp = 0.2$, $\Gamma_{\perp\,max}^{conv} = 30m^{-2}s^{-1}$, VRM	262/60%	178/40%	66/15%	1.27	5.6
#10100	$D_\perp = 0.2$, $\Gamma_{\perp\,max}^{conv} = 20m^{-2}s^{-1}$, CD_4,	273/62%	146/#33%	98/22%	1.6	4.8
#10841	$D_\perp = 0.2$ $\Gamma_{\perp\,max}^{conv} = 20m^{-2}s^{-1}$, CD_4, $Y_{chme}^{mcw} = 10\%$	275/63%	245/56%	52/12%	0.98	1.1
Experiment #17823		300/70%	176/40%	132/30%	0.4	~ 0.5

Table 5.8: *Experimental and simulated SOL and divertor radiation fractions relative to $P_{SOL} = 440kW$ at high density in D. The experimental fractions are derived from Fig. 5.17. The last two columns provide the outer target integral and strike point ion fluxes and hence a measure of the detachment compared with experiment.*

too little is predicted (for case #10841) to occur below the X-point. This is visible in Fig. 5.63. According to the simulation, impurities are by far the largest contributors to the total radiated power, accounting for more than 70%. Nevertheless, radiation from recycling neutrals does contribute an important fraction to the total power losses in the SOL (Tables 5.9, 5.10). Whilst the agreement between code and experiment for both
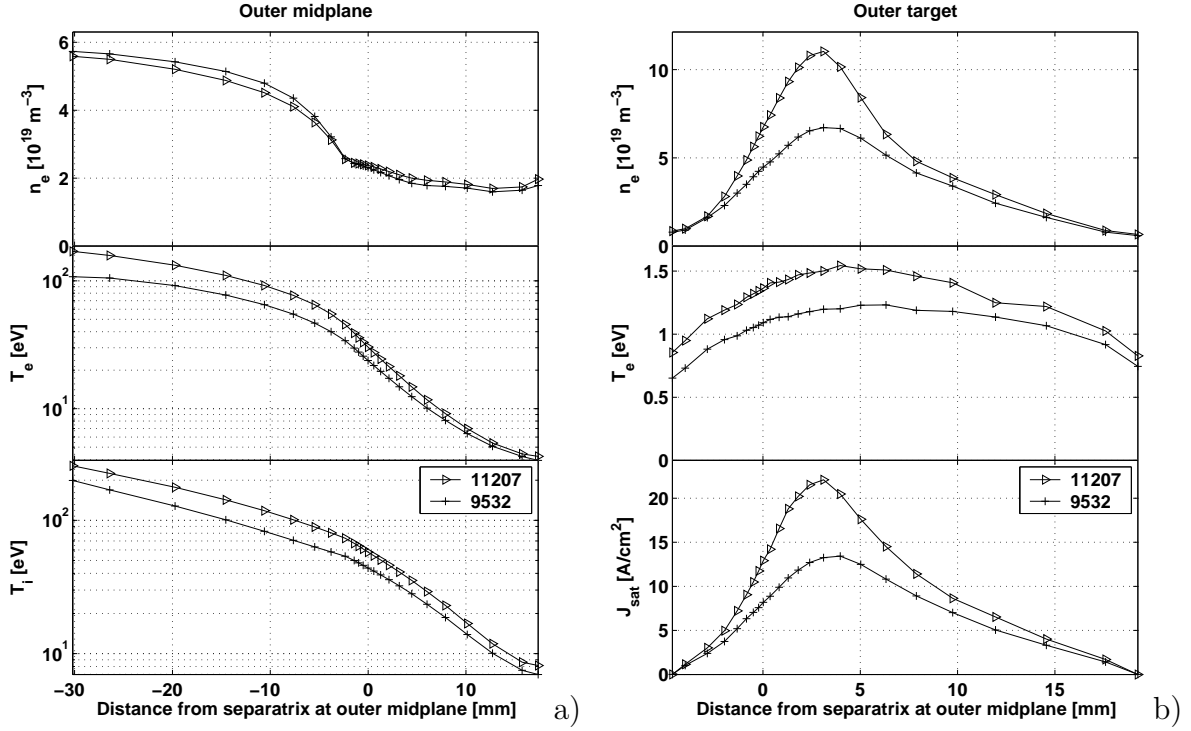
Figure 5.62: *Comparing simulated (a) upstream and (b) outer target profiles for $P_{SOL} = 600kW$ (#11207) and $P_{SOL} = 440kW$ (#9532). In each case $n_e^{sep} = 2.5 \times 10^{19}m^{-3}$, $Y_{chem}^{mcw} = 10\%$ and convective transport is activated.*

the total radiation and its distribution is good at low density, at high density, simulation case #10841, with the lowest target j_{SAT}, does not match the experimental radiation distribution. The code predicts a radiating belt around the LCFS, but in experiment, the strongest radiation losses are centered around the X-point. This is a common observation at high densities in divertor tokamaks and is known as an X-point MARFE (Multi Faceted Asymmetric Radiation from the Edge) [28]. The difference between code and experiment points strongly to the simulations incorrectly reproducing the real distribution of ion and neutral fluxes impinging on wall surfaces. In particular, imposing $Y_{chem}^{mcw} = 10\%$ on all MCW surfaces is unlikely to be an adequate represntation of the real impurity release.

In the convective scenarios the neutral flux imping on the HFS walls is a factor of 10 larger than in the pure diffusive case (see Fig. 5.61). In contrast, ion fluxes are low com-
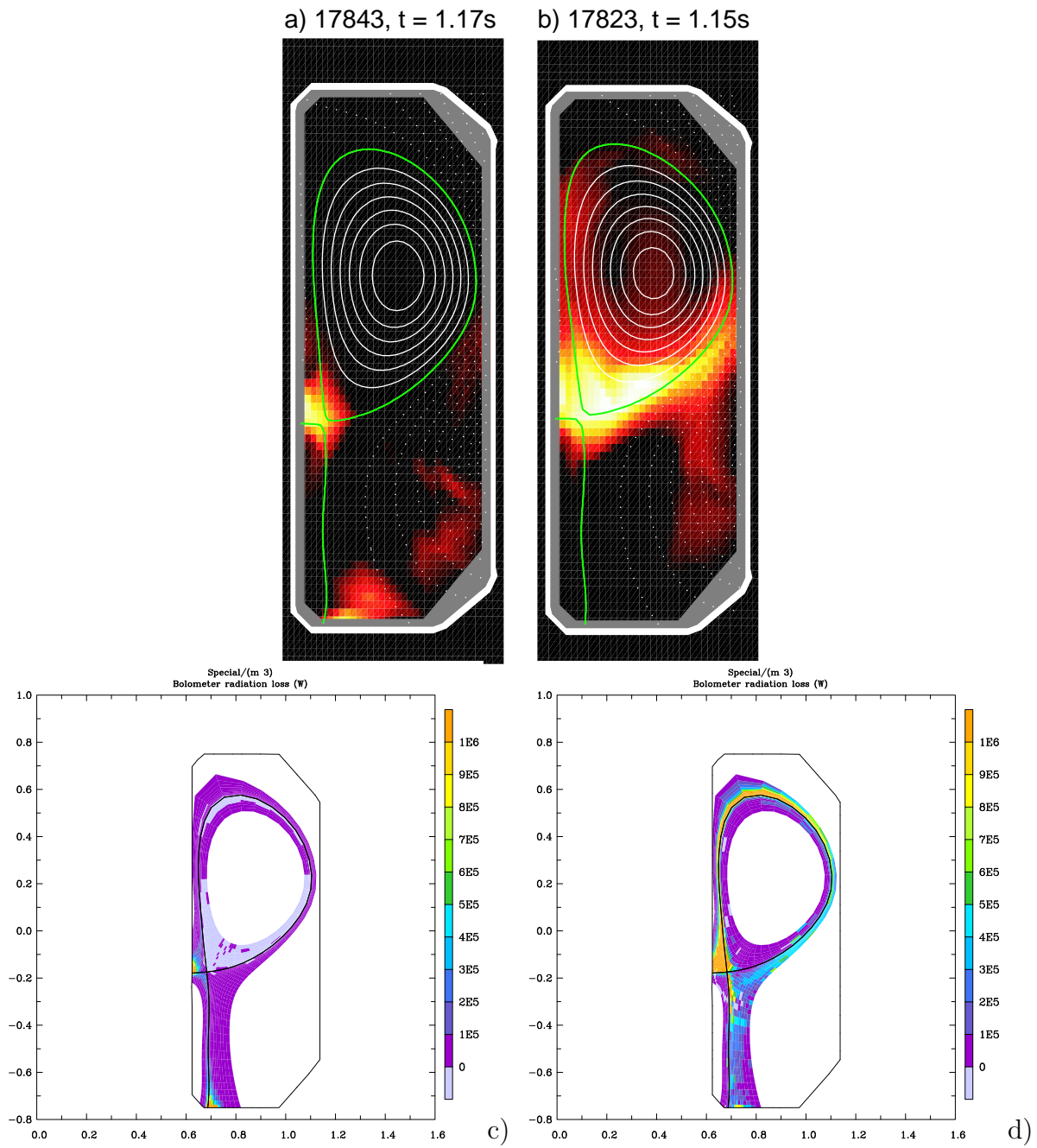
Figure 5.63: *Comparing the experimental (a,b) and simulated ((c): #8524, (d):#10841) distributions of total radiated power at low (a,c) and high (b,d) n_e^{sep}*

pared to the LFS due to the poloidally enhanced convection there (imposed at the wall). The enhanced chemical sputtering has been introduced to simulate additional ion sputter-

ing and might therefore overestimate the chemical production of C on the HFS. This effect is exacerbated by the likely enhanced neutral 'plugging' and subsequent contact with the inner wall due to the geometric proximity of the HFS separatrix along a significant length of the central column. As shown in Fig. 5.56, the enhanced C-production also results in a global decrease of the T_e profile. Cooling of the edge plasma through radiation can have a strong positive feedback effect on T_e since the power loss rate for C is maximum for $T_e \sim 10eV$ [28], due in particular to strong C^{2+} and C^{3+} line radiation. Regions of low T_e and high n_e develop, further increasing C production and radiation cooling on the HFS until a stable regime is reached, in which the HFS becomes a region of strong radiation emission.

Additional simulations confirm the marked sensitivity of the results to the total radiated power, especially that radiated in the main SOL: the ion flux can be reduced still further with increasing radiation in the main SOL, but at the cost of a stable operational window for the code being lost. During the course of simulations using higher (than 10%) chemical yields at the MCW a further decreases of the integral outer target ion flux are accompanied by a collapse in the upstream densities and temperatures.

The use of a simple chemical yield at the main wall to represent an extremely complex distribution of ion impact can clearly never hope to produce the real experimental situation - only trends can be sought with the relatively crude tools at hand. Beyond a certain point the limit of applicability of the code is reached and it makes little sense to push further when the initial approximations fall outside of the physical situation being modelled.

5.3.4.7 Influence of CD_4 dissociation chain on SOL energy balance?

Somewhat surprisingly, cases #9532 and #10100 lead to very similar results in the entire SOL, including the divertor volumes, even though $Y_{chem} = 3.5\%$ on all surfaces for case #10100 (compared with 10% in #9532) and thus less carbon is produced. That this observation excludes MAR from playing any major role as a volumetric particle sink in the present simulations has already been noted. It cannot, however, be concluded that MAR

due to higher hydrocarbons (such $C_x D_y$ with $x > 1$, $y \leq 1$), is unimportant. According to Janev [79], such species are expected to possess considerably higher plasma recombination efficiencies, being a factor $\sim 3 - 4$ stronger than that due to CD_4.

In order to understand the similarity between cases #9532 and #10100, Table 5.9 compares the distributions of radiation loss in each case, where both include radial convection. The proximity of the outer divertor parallel n_e and T_e profiles in the two cases

Case	Type	Radiation in main SOL [kW]	Radiation in outer divertor [kW]	Power into outer divertor [kW]
#9532	CRM $Y_{chem}^{mcw} = 10\%$	204/(46)	83/(20)	75
#10100	CD_4	146/(70)	98/(50)	88

Table 5.9: *Comparison of simulated radiation and conducted plus convected power into the outer divertor for two radial convection cases with and without CD_4. The second number in the 3rd and 4th columns provides the electron cooling losses from EIRENE and thus the volumetric power losses due to ionization, recombination and dissociation processes.*

would appear to be a consequence of the similarity in the power conducted into the divertor. Since case #10100 includes CD_4 it might be concluded that the dissociation break-up chain of the molecule is responsible for an increased electron energy sink in the main SOL. Closer inspection provides an alternative explanation for the different amounts of power radiated in the SOL between the two cases ($46kW$ vs. $70kW$). Table 5.10 compares the total EIRENE computed D^+ sources in the main SOL from the above two cases together with two other simulations described in Table 5.6: the electron cooling losses computed by EIRENE, the D^+ source strength and the losses from EIRENE normalized by the source strength, such as to provide a value of how much power has been radiated with respect to the number of ionization processes. Once the ionization source is normalized by the electron cooling losses provided by EIRENE, the differences between all these cases are relatively small (last two columns of Table 5.10). The difference between #9532 and #10452 is easily explained since the electron cooling losses from EIRENE also include

Case	$\int D^+$ source in main SOL $[\times 10^{21} s^{-1}]$	$\int$(electron cooling) from EIRENE $[kW]$	D^+/P $10^{20}/[kW]$	$[eV]/D^+$
8006	3.68	18	2.0	31
10452	11.2	55	2.0	31
9532	8.53	46	1.8	34
10100	12	70	1.7	36

Table 5.10: *Comparison of simulated integral D^+ sources and electron cooling losses from EIRENE, together with the numbers of D^+ produced per $[kW]$ and the electron cooling loss per D^+ produced. (see Table 5.6 for a description of the simulations)*

the energy loss due to first ionization of C, which is present in larger amounts in #9532 due to the assumption of $Y_{chem}^{mcw} = 10\%$. Comparing cases #10452 and #10100 shows that the energy needed per D^+ produced is $\sim 20\%$ higher when the ion originates from the break-up of CD_4. Since the upstream T_e and n_e profiles differ only slightly (see Fig. 5.46), so that the electron cooling loss per D^+ ionization is similar, the difference is likely to be due to the electron power loss due to CD_4 dissociation (see Table 5.8 and 5.10).

An explanation for the difference in impurity radiation level, between cases #10452 ($25kW$) and #10100 ($76kW$) has not yet been found. Both have similar upstream profiles and identical $Y_{chem}^{mcw} = 3.5\%$. The reason is likely to be associated with the poloidal distribution of the radiating impurities and requires further study.

5.4 Concluding remarks

Detachment in TCV deuterium fueled discharges is almost certainly strongly linked to impurity production from the main chamber walls. Experiments conducted in forward and reversed field have shown that at low $\bar{n}_e$, upstream, inner and outer target n_e and T_e profiles are very similar and that at the highest $\bar{n}_e$, detachment is observed independently of field direction for the highest current at which a one to one comparison is possible on TCV. Field direction appears to have a strong effect on both divertor plasmas only for intermediate densities.

Although a number of important experimental measurements with which to make detailed comparison are missing, considerable progress has been made in the simulations in demonstrating that enhanced MCW interaction, leading to increased main SOL radiation, can yield high levels of strike point detachment in deuterium. Systematic studies have included molecular vibrational levels, hydrocarbons, more sophisticated geometry and convective radial transport. Only when increased MCW impurity production is included, in conjunction with convection and/or hydrocarbons can any degree of detachment be obtained that approaches what is observed in experiment.

Using spatially constant diffusion coefficients and assuming only diffusive radial particle and energy transport, excellent agreement can be achieved between experiment and simulation for both upstream and outer target profiles for low upstream densities ($n_e^{sep} = 1.0 \times 10^{19} m^{-3}$) in D plasmas. Relatively good agreement is also obtained in low density He simulations. The inner target profiles are reasonably well matched in both D and He with spatially constant diffusive transport at all simulated densities. As plasma density increases, radial particle transport in the main SOL needs to be increased if the upstream density profiles are to be matched.

However, the introduction of a convective contribution to perpendicular transport limited to the region between the top of the machine and the X-point in simulations at high n_e^{sep} does not, by itself, decrease the ion flux to the outer target. In fact it has the opposite effect. That impurity production from areas other than the divertor targets must play

a crucial role in determining the onset of divertor detachment in TCV is implied by the relatively good agreement between code and experiment for He at high densities. In these cases, SOL temperatures are low and He ion physical sputtering of carbon will thus also be low. Since chemical sputtering does not occur in He, the enhanced C-production rate producing increased main SOL radiation in D is absent.

It thus appears that in these ohmic plasmas at relatively low power input, unconventional divertor geometry and transparent outer target divertor, TCV operates in a narrow window in which relatively small changes in main SOL radiation power loss force a transition to strong detachment. This shift in radiation balance is seen in the code only when MCW interaction is increased, mimicking ion-wall interaction (which is not accounted for in SOLPS5) through an artificial enhancement of the chemical yield at the main chamber walls. This therefore constitutes a somewhat indirect proof that the absence of a realistic wall interaction model has direct consequences on the ability to correctly simulate the divertor plasma.

The inclusion of CD_4 in simulations with main SOL convective transport also leads to a reduction in the outer target flux, contrary to findings using spatially constant transport coefficients. This is related to a slightly enhanced power loss in the main SOL due to dissociation processes through the methane chain and subsequent increased impurity radiation and is not linked to an increase in impurity production but possibly to a different distribution of radiating impurities. Further analysis is required to make more quantitative statements.

By comparing the difference in the drop of the total ion flux to the outer target in the simulated cases invoking different chemistry, it cannot be concluded that MAR through ion conversion of D_2^+ or hydrocarbons plays an important role as a particle sink during detachment. Nevertheless the simulations do not exclude higher hydrocarbon chains (not included in the simulations) from influencing the onset of divertor detachment, be it via MAR, increased total radiation or a different distribution of impurity radiation in the main SOL.

Chapter 6

Divertor detachment in JET Helium plasmas

6.1 Introduction

Chapter 5 has focused on elucidation of the processes leading to anomalous detachment in deuterium discharges in TCV. A key ingredient in providing an explanation was the observation that such detachment was not observed in TCV helium plasmas in which carbon chemistry is absent. Learning more about impurity production in D plasmas was one of the principal aims of a campaign of pure He discharges executed in JET in May 2001 [167]. By studying the differences between discharges carefully matched in everything but plasma species, the relative importance of the mechanism and location of the impurity release can be studied in the real tokamak environment.

Apart from impurity production, a second fundamental difference separates He and D plasmas. This is to be found in the atomic physics processes operating in each case. In He, molecules are absent and radiation losses, CX collision cross-sections and ionization mfp's differ substantially. Together with the impurity content, all these processes have a strong influence on divertor detachment. It might therefore be expected, and is indeed observed, that the character of detachment in He compared with D is quite different.

From the point of view of code modeling, this provides an excellent opportunity to study detachment physics in the absence of complicating factors such as molecular physics and carbon chemical sputtering. This chapter describes the simulation effort undertaken using SOLPS5.0 to reproduce the JET He detachment observed during specific density ramp experiments performed within the pure helium campaign. These discharges were matched as closely as possible to their more common deuterium counterparts. The simulation of deuterium detachment in JET, in contrast to the case in He, is a far from trivial exercise and has not yet been convincingly achieved with either the SOLPS5 or EDGE2D/NIMBUS code packages. Some preliminary attempts have been made in the context of the present work but the results are insufficiently mature to qualify for presentation in this thesis.

6.2   Experiment

A detailed description of the JET diagnostic system such as that presented for TCV in Section 5.2.1 cannot be provided here. In essence, much the same diagnostic data are used as for the TCV experiment-simulation comparison: target data from Langmuir probes and upstream profile measurements of n_e and T_e. The latter are provided by Lithium-beam (KY63), edge Thomson Scattering (KE9D) and fast reciprocating probe (KY3) systems, but more often than not are associated with quite severe spatial alignment problems in the sense that varying degrees of radial shifting seem to be required if any degree of overlap is to be obtained. The particular magnetic equilibrium used for the detachment studies is not, unfortunately, optimized for the JET edge profile diagnostics - configurations that are known as Diagnostic Optimized Configurations (DOC) provide much higher quality composite radial profiles than have been possible in the work reported here. They have recently been used by Kallenbach in a comprehensive modeling study of the Type I ELM-ing H-mode edge plasma using the EDGE2D/NIMBUS package [198].

Experiments described here are exclusively in L-mode conditions and have been performed in the JET MarkIIGB configuration with septum installed. The latter was intended to provide some separation between the inner and outer divertors and is shown

206

in Fig. 6.1 which illustrates the divertor target configuration in cross-section. Since the work of this thesis began, a new divertor design has been installed in which the septum is absent. The magnetic equilibrium (see Fig. 6.5 for an example in the form of a SOLPS5
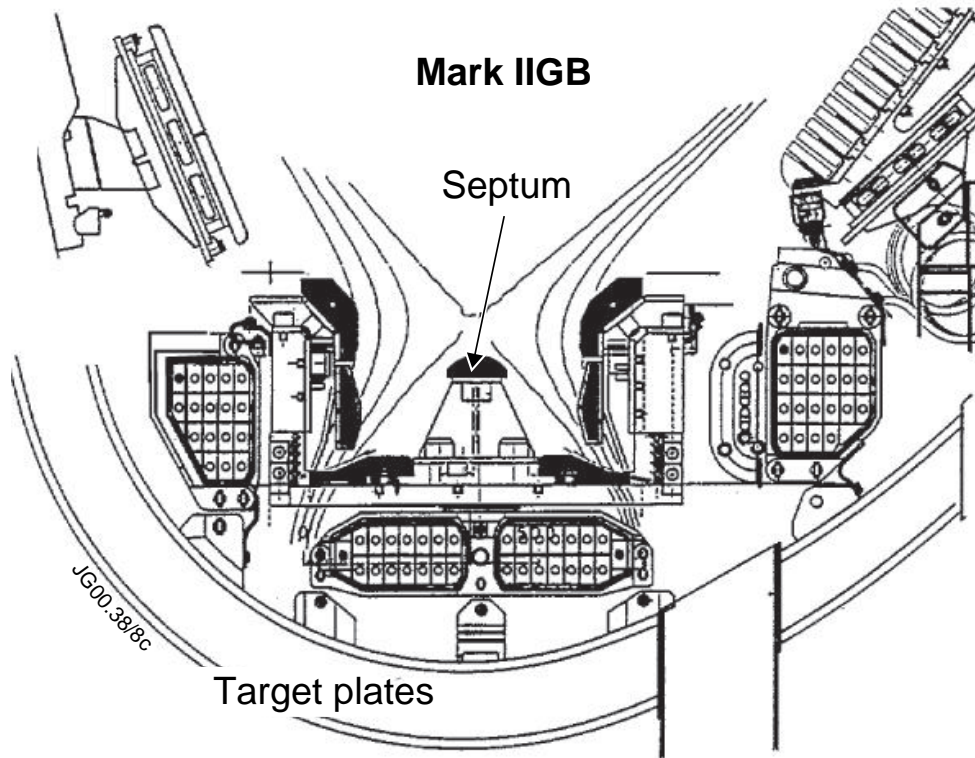

Mark IIGB

Septum

Target plates

JG00.38/8c

Figure 6.1: *Cross-section of the JET MarkIIGB divertor, illustrating the location of the septum, target plates, in-vessel divertor coils and the cryo-pump duct below the outer divertor.*

simulation grid) used for these density ramp studies is known as the 'Standard Fat' configuration and is a SNL, low wall clearance equilibrium. Similar density limit pulses in He, but in a high clearance configuration have also been performed [168] but are not modeled here. The standard fat plasma has strike points symmetrically disposed on the vertical (CFC) targets and is thus a far more 'conventional' arrangement than the TCV magnetic configuration discussed in the previous chapter. Whilst the TCV divertor is completely open, the JET gas box provides a strong degree of closure. Coupled with the large differences in machine size, this is therefore bound to have a substantial influence

on the detachment behaviour.

One of the important features of the JET pure He campaign, inside which the discharges simulated here were executed, was the conversion of the neutral beam injectors to He such that pure He plasmas could be heated with pure He beams. Unlike TCV, JET is in addition easily able to breakdown in He, so that no D-prefill is required. The discharges modelled here have $I_p = 2.5MA$, $B_\Phi = 2.4T$ and are exclusively in forward field (i.e. with $\vec{B} \times \nabla B \downarrow$). For the majority of the pure He campaign, the JET cryopump was inactive (to achieve any degree of pumping He requires intense Argon frosting). Gas fuelling for the density ramp discharges was through a toroidally continuous injection module located on the inner divertor floor (GIM 11). A high degree of He purity was achieved in these plasmas, with the ratio $He/(He + D)$ approaching 90%, as measured both by visble spectroscopy in the plasma edge and partial pressures in the sub-divertor volume [167]. Fig. 6.2 compiles some basic plasma signals for the He density ramp discharge #54029 with $3MW$ of NBI power. Also included are the same traces for a well matched deuterium discharge (#53088) demonstrating the recycled normalized Z_{eff} in helium, a consequence of the lower carbon levels in the He shown by the $CIII$ intensities measured in the inner and outer divertor legs and the main chamber. Fig. 6.2 also clearly highlights the considerably higher density limit in He compared with D (factor ~ 2.5) in this configuration [168] and that, for comparison, in TCV the density limit is only $\sim 15\%$ higher when comparing matched He and D plasmas (Section 5.2.2). This D-He density ramp comparison can be compared with the TCV equivalent in Figs. 5.8 and 5.9.

Figure 6.3 illustrates the density dependence of key strike point experimental data from both target Langmuir probes and Infrared (IR) thermography at the inner (Fig. 6.3(a)-(c)) and outer (Fig. 6.3(d)-(f)) targets. With the exception of the peak IR power (for which no data was available in D), the data are from three He discharges with varying P_{NBI} and a single D pulse for reference matched most closely to the He discharge #54001, corresponding to the mid-range power in the heating scan. Figure 6.3 shows how the observed detachment in JET is very different when comparing the two species. One may also recall that detachment is not seen at all in TCV pure He ohmic discharges
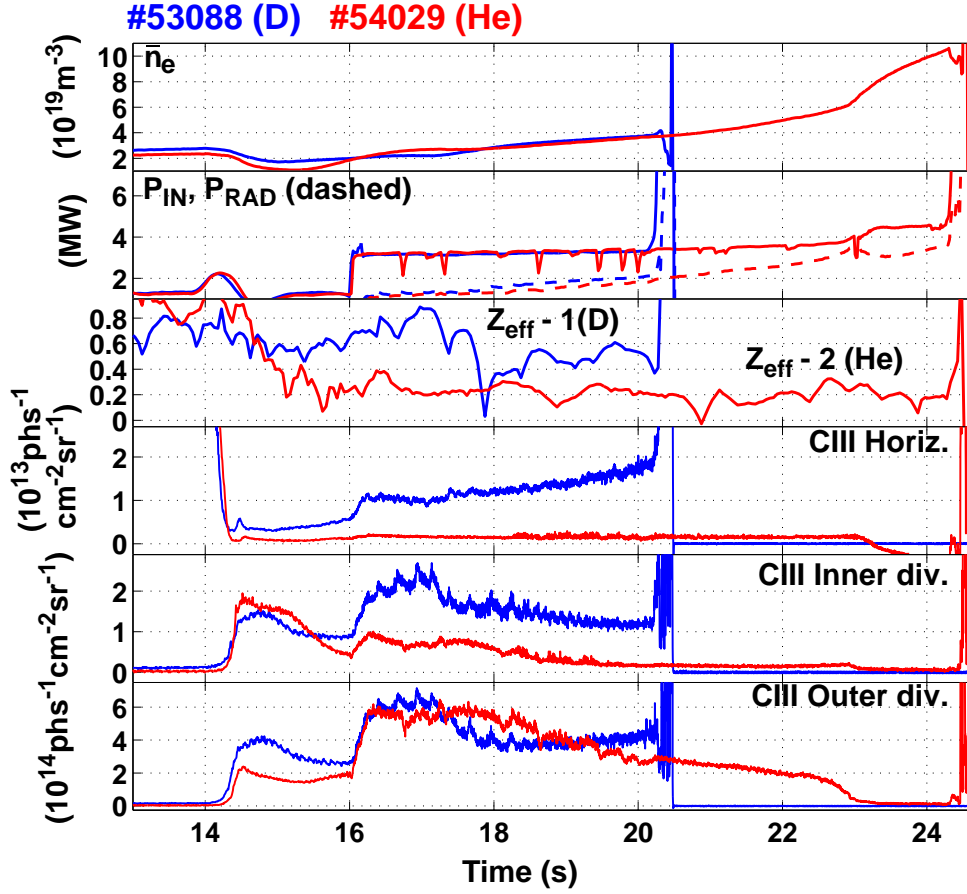
Figure 6.2: *Comparison of density ramp discharges in matched JET D (#53088) and He (#54029) plasmas. Note the He pulse #54029 is exactly equivalent to discharge #54001 used for the target probe comparison in Fig. 6.3.*

(Section 5.2.2.1, and in particular Figs. 5.15 and 5.16).

At the inner divertor, particle (Fig. 6.3(a)) and energy (Fig. 6.3(c)) detachment occurs immediately in D. This is a common observation in JET discharges with forward ion ∇B drift direction [199]. It is believed to be due both to the effects of unequal power sharing between the two divertors (as a consequence of the toroidal geometry and perhaps ballooning transport favoring LFS power exhaust) and plasma drifts, which increase power flow to the outer divertor in SNL with forward field. This favours the formation of a colder inner divertor which in turn encourages the build-up of density and further temperature decrease. In a carbon machine, it is known that the colder, more dense plasma

209
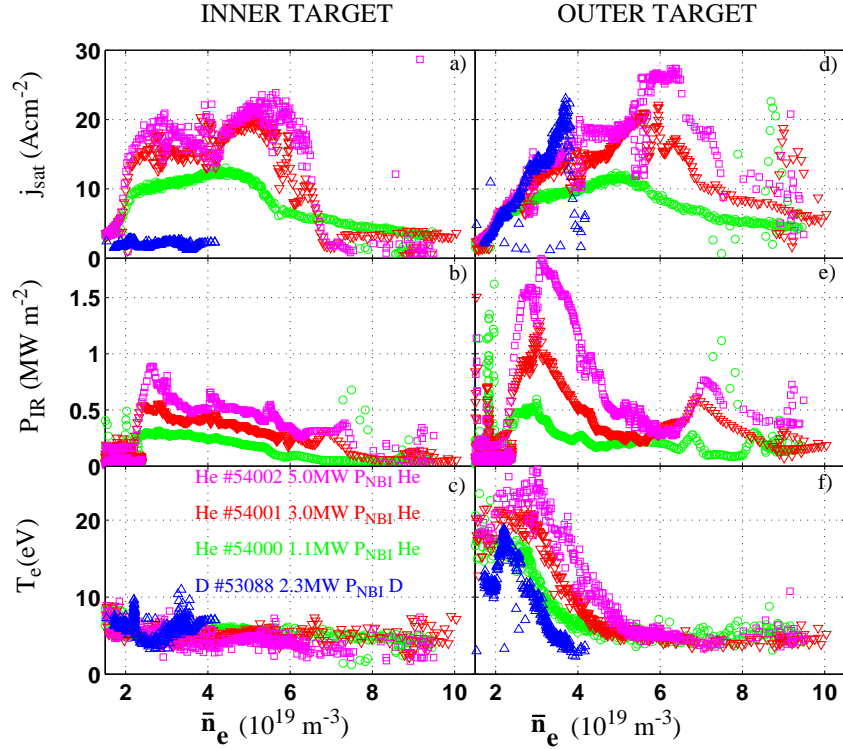
Figure 6.3: *Experimental measurements of the plasma density dependence of ion particle flux (a, d), peak surface heat flux (b, e) and T_e (c, f) at the inner (left) and outer (right) divertor targets in JET. Data are shown for three He discharges and a single comparable D pulse, with the exception of P_{IR}, for which deuterium data are unavailable [193].*

promotes the growth of amorphous C films with high chemical sputtering yields (for D impact), thus yielding high levels of carbon production at the inner target. In equivalent He plasmas, inner target ion fluxes begin to decrease only at much higher densities, with the onset of detachment coinciding with the formation of a strong X-point MARFE. This occurs earlier in density as input power is decreased. In common with D plasmas, T_e at the inner target in He appears to be collapsed at all densities for the limited power scan described here (Fig. 6.3(c)). Note also the low peak powers (Fig. 6.3(b)), only just above the experimental sensitivity of the IR camera; although particles still arrive at the target, the energy flux is low, even at the maximum P_{NBI} of $5MW$.

At the outer target, particle flux detachment in He occurs at marginally higher $\bar{n}_e$

(Fig. 6.3(d)) in comparison with the inner target and is again sensitive to the degree of input power. In D for the reference case in Fig. 6.3, the outer target remains attached almost until the density limit, where the formation of an X-point MARFE and then rapidly an inner wall MARFE occurs [168]. The outer target electron temperatures (Fig. 6.3(f)) demonstrate clearly the effect of increasing input power, decreasing in He, as in D, to values of $\sim 5eV$ as $\bar{n}_e$ increases. Unlike in D however, when T_e falls in the He plasma, the particle flux does not (as also observed in the inner divertor). Note that the known problems of Langmuir probe interpretation at low T_e (see also Section 5.2.1.1) prevent any knowledge of the true value of T_e at high $\bar{n}_e$. In He, for densities below the detachment threshold, the peak IR power at the outer target (Fig. 6.3(e)) falls in synchrony with T_e, despite the increasing ion flux (Fig. 6.3(d)).

Fig. 6.4 illustrates the behaviour, during a single discharge, of the distribution of total radiation (from bolometric inversion) in the divertor region as $\bar{n}_e$ rises. Initially located at both the inner and outer strike zones at low $\bar{n}_e$, the total radiation increasingly concentrates at the inner leg and then finally above the X-point during the MARFE phase. Likewise, the HeI emission (HeI, $706nm$, from tomographic reconstruction of tangential CCD camera images [194, 200]) is more intense in the outer divertor at lower $\bar{n}_e$ and switches to the inner leg at high density. As the density rises in He, $CIII$ emission in the divertor and main chamber is observed to decrease to progressively low levels, becoming almost negligible at the highest density. This is in sharp contrast to the case in D plasmas, where carbon emission is observed at best to remain constant or even to increase with increasing $\bar{n}_e$ [167, 168]. This is attributed to the absence of chemical sputtering in He (and the decrease of ion energy below the threshold for physical sputtering at high $\bar{n}_e$) and implies that the radiated power (Fig. 6.4) in He plasmas at elevated densities is due almost exclusively to that from He^0 and He^+.
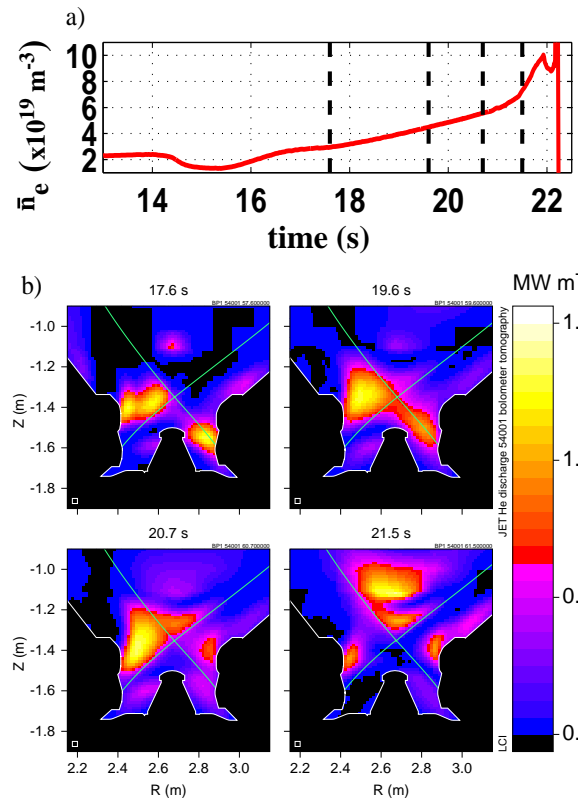
211

Figure 6.4: *Density dependence of the 2D distribution of total radiation in the divertor for He discharge #54001. The bolometric inversions in (b) correspond to the times marked by the vertical dashed lines in the density trace in (a). Note the intense emission from the inner divertor and the movement of radiation above the X-point at the highest density [193].*

6.3 Simulations

The previous section has highlighted the principle experimental differences observed in the divertor when operating at high density in pure helium compared with deuterium as working gas. Essentially, these reduce to the persistence, at both targets, of an elevated ion flux, even when the local temperature has fallen to low values and the key observation that ion flux detachment proceeds simultaneously at both targets beyond a given threshold density, relatively independently of input power (at least in L-mode). The considerably higher density limit in He compared with D for these standard fat plasmas means that detachment, when it finally occurs in He, does so at densities far higher than can be sustained in equivalent D plasmas. The challenge is to reproduce these observations in SOLPS5 simulations. In an attempt to do so, the modeling efforts reported here constitute the first ever SOL simulations with pure He in JET [193]. Since this work was first published, simulations of essentially the same discharges using the EDGE2D code package have also been reported [194]. The basic findings reported here on the simulation of pure He plasmas have much in common with those found in an earlier attempt at He plasma modeling for DIII-D discharges with the older, SOLPS4 version of the code [148].

The simulations are conducted on a grid (Fig. 6.5 and 6.6) extending from $\rho = -5.7$ to $\sim 2cm$ relative to the outer midplane separatrix. It has 96 poloidal cells (numbered ix), including the guard cells at the inner and outer target and 36 radial cells (numbered iy) including the guard cells at the inner and outer grid boundaries, with the separatrix being located between cell numbers 9 and 10. The first 24 poloidal cells cover the inner and outer divertors, whilst the remainder cover the main SOL. Ion species included in all simulations are D^+ and all charge states of C and He. Unless otherwise stated, the following assumptions have been adopted in all simulations:

- B2.5 is coupled to EIRENE '96.

- The power crossing the core boundary (south boundary connecting the core plasma to the SOL), is fixed at $P_{core} = 3.8MW$, corresponding to P_{SOL} for the experimental discharge #54001. This input power is varied appropriately when attempting to
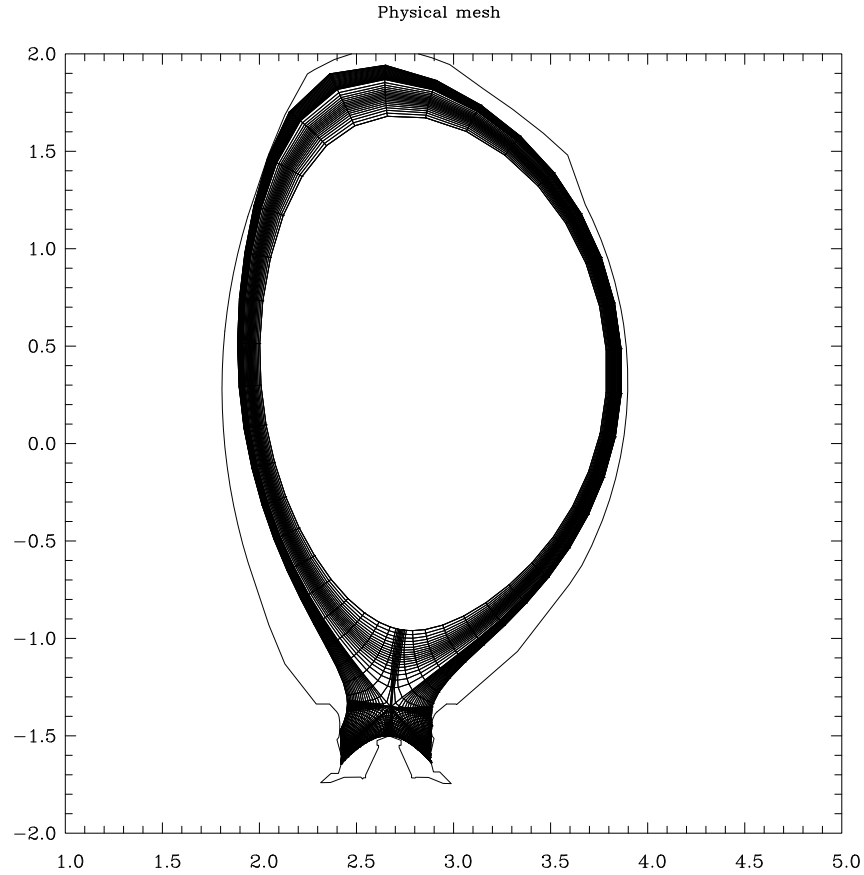
Figure 6.5: *Grid used for all the JET simulations based on the EFIT equilibrium recon-struction of discharge #54000 at 60s. See Fig. 6.6 for an expanded view of the divertor region.*

match the results of the experimental NBI scan.

- The density of He^{2+} is prescribed at the core boundary, n_e^{core}. The D^+ density is maintained constant at $4 \times 10^{17} m^{-3}$ and is set to zero for all other ions. The particle flux across the core boundary adapts to maintain the preset density. No feedback mechanism is applied and no gas puff is used.

- A particle recycling coefficient of $R = 1.0$ is fixed on all surfaces.

- The core boundary is fully absorbing for neutrals.

214
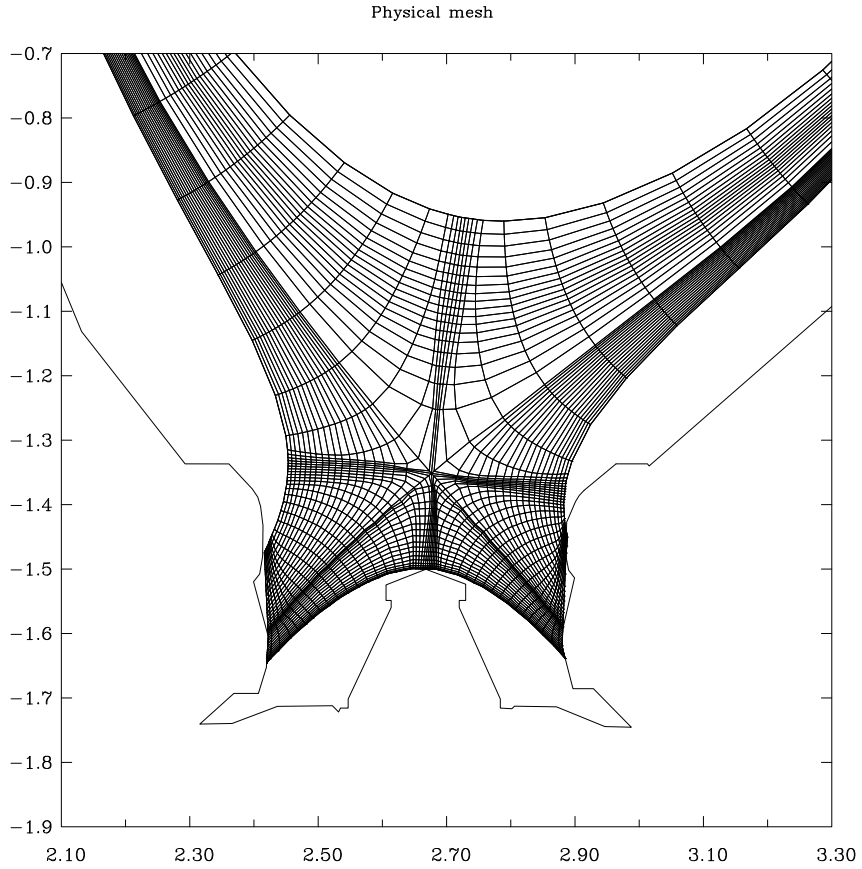
Figure 6.6: *Divertor region of the grid used for all the JET simulations (see Fig. 6.5), based on the EFIT reconstruction of discharge #54000 at 60s. Note that the real poloidal contour of the vertical target tiles is not fully reproduced by the grid.*

- Heat transmission coefficients are $\gamma_e = 4$ and $\gamma_i = 2.5$, setting them (for historical reasons) at the lower limit of the theoretically expected values (see Section 2.4). Tests have shown, in common with TCV, that variations in these coefficients have little impact on the simulation results.

- $M \geq 1$ at both targets; fixing $M = 1$ has only a negligible effect on the simulation results in He.

- A decay length of $3cm$ is fixed at the north boundary for all ion densities, T_i and T_e.

- Parallel velocities at the south and north boundaries are assumed to be zero.

- Electron and ion heat flux limits are fixed at $\alpha_e = 0.3$ and $\alpha_i = 10$ respectively. The viscous stress limiter is set to 0.5.

- Physical sputtering is implemented according to the Roth-Bodansky formula [68].

- Ion sputtering occurs only at the divertor targets.

- Chemical sputtering is fixed at 1% for D, which is a minority species in the He simulations.

- Carbon impurities at all ionized states are assumed to be deposited on material surfaces with a sticking coefficient of unity.

- All simulations are run with spatially constant values of $D_\perp$ and $\chi_\perp$, their values are given in the text for each simulation individually. There has been no attempt in this context to introduce radially dependent transport coefficients.

With regard to the percentage of D in these code runs (where the percentage is defined for the code as the ratio of the D^+/He^{2+} ion densities fixed at the core boundary), experiment shows the plasma purity to be $\sim 90\%$. Sensitivity tests have been performed in the code for constant n_e^{core} and input power, showing that whilst a change from $\sim 100\%$ He to $\sim 70\%$ He has only little effect on the upstream T_e and n_e profiles, target densities can increase by as much as 30% at the outer and 50% at the inner target. In what follows, He^{2+} is assumed to comprise essentially 100% of the core boundary density.

As for the TCV modeling in Section 5.3, an attempt is first made to match a low density case by varying the perpendicular transport coefficients, assumed fixed in space. The result for upstream profiles is shown in Fig. 6.7 where the experimental data are taken from a discharge with constant low density ($\bar{n}_e \sim 2 \times 10^{19} m^{-3}$) which is otherwise very similar to the density ramp discharge used for detachment. Unfortunately, the limited quality of data available here does not permit a convincing argument for a particular
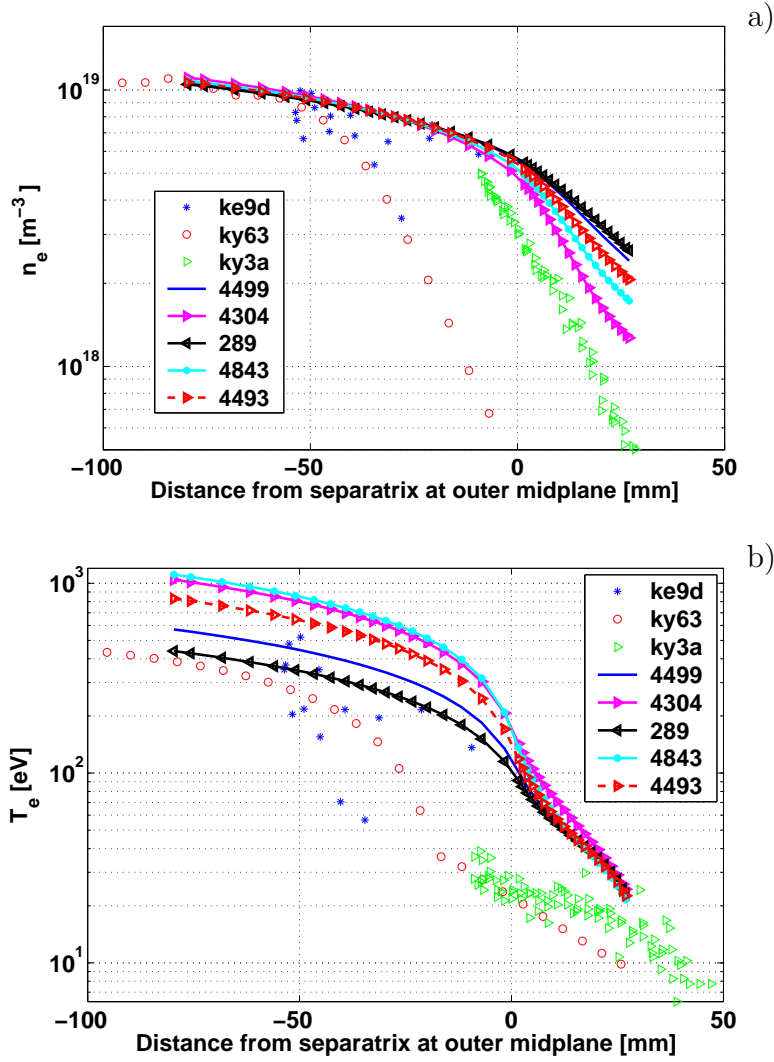
Figure 6.7: *Comparison of midplane mapped experimental (#53973) and simulated up-stream profiles. Experimental data from the EDGE-Lidar Thomson scattering system (KE9D), the fast reciprocating probe system (KY3-A) and the Li-beam diagnostic (KY63), are compiled. The simulation cases use transport coefficient pairs as follows: #4499: $D_\perp = 0.75m^2s^{-1}$, $\chi_\perp = 1.5m^2s^{-1}$ #4304: $D_\perp = 0.2m^2s^{-1}$, $\chi_\perp = 1.0m^2s^{-1}$ #289: $D_\perp = 1.0m^2s^{-1}$, $\chi_\perp = 2.0m^2s^{-1}$ #4843: $D_\perp = 0.35m^2s^{-1}$, $\chi_\perp = 0.75m^2s^{-1}$ #4493: $D_\perp = 0.5m^2s^{-1}$, $\chi_\perp = 1.0m^2s^{-1}$*

radial shift to be applied and none is attempted. On the basis of Fig. 6.7 and the comparison between Li-beam upstream density profiles and simulation at higher $\bar{n}_e$ shown

in Fig. 6.8 it can only be concluded that the transport coefficient pair $D_\perp = 0.5m^2s^{-1}$, $\chi_\perp = 1.0m^2s^{-1}$ provides a reasonable match to the data across a range of density, at least in so far as the density profile is concerned. The same pair of transport coefficients was also adopted in the EDGE2D/NIMBUS simulations and found to yield reasonable agreement with experiment upstream for the same discharge (#54001) [194]. Even though the profile shape is approximately matched, the relative radial shifts make it difficult to assess which value of n_e^{sep} to assign each $\bar{n}_e$ and thus to link a particular point in the experimental density ramp with a given simulation.

The sensitivity of target parameters to n_u (at least according to the Two-point modeling in which $\Gamma_t \propto n_u^2$, $n_t \propto n_u^3$) means that any uncertainty in upstream density as consequence of radial shifts is exacerbated at the targets. It is not therefore straightforward to compare experimental and simulated target profiles for a specific experimental density. This is attempted in Fig. 6.9 and 6.10 for the two values of $\bar{n}_e$ in Fig. 6.8 and the reference discharge, #54001. The target profile widths are of course dependent on the choice of transport coefficients, but also on n_e^{sep}, which in these simulations (in contrast to the TCV cases in which it is fixed by feedback on gas puff), is determined by the choice of core boundary density. Concerning the outer target, best agreement within the set of simulations performed is obtained with the transport coefficient pair $D_\perp = 0.35m^2s^{-1}$, $\chi_\perp = 0.75m^2s^{-1}$ which is certainly in the range of combinations producing qualitative matches with the upstream experimental profiles. Agreement remains acceptable at the inner target with increasing $\bar{n}_e$ (bearing in mind that n_e^{sep} is not well determined and that no D contamination is present in the simulations), but there is a discrepancy with the outer target j_{SAT} in both magnitude and spatial profile. This appears to worsen with increasing density. In contrast the target T_e is well matched throughout at both targets. It should be noted that the simulations indicate $T_i \sim T_e$ in the divertors at anything but the lowest densities. This means that the assumption of $T_i = T_e$ in computing densities from Langmuir probes should be valid in these cases.

The overall agreement may be judged satisfactory at least in so far as drawing conclusions on the mechanism of the detachment is concerned. It should be recalled that
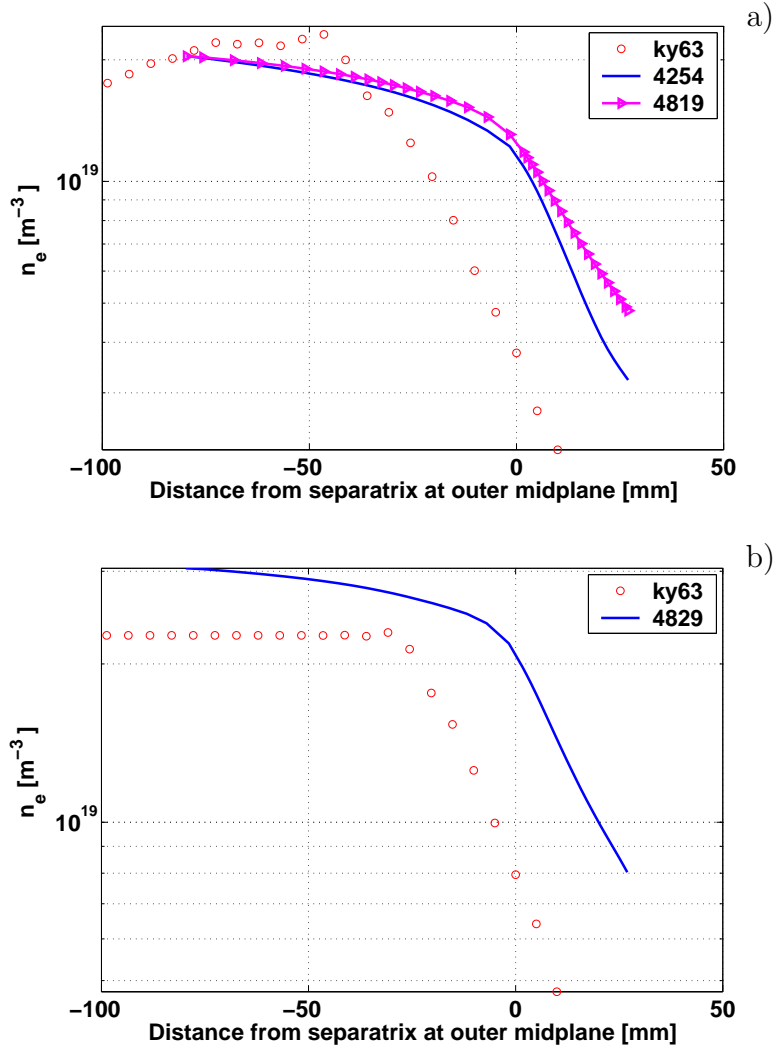
Figure 6.8: *Comparison of midplane mapped experimental (KY63, #54001) and simulated upstream profiles for (a) $\bar{n}_e \sim 4 \times 10^{19} m^{-3}$ and (b) $\bar{n}_e \sim 6 \times 10^{19} m^{-3}$. Note that at the highest density in (b) the Li-beam (KY63) attenuation at distances $< -30mm$ from the separatrix is too severe for the data to be considered credible. Simulations #4819 and #4829 use $D_\perp = 0.5m^2s^{-1}$, $\chi_\perp = 1.0m^2s^{-1}$, whilst #4254 uses $D_\perp = 0.2m^2s^{-1}$, $\chi_\perp = 1.0m^2s^{-1}$.*

drifts are not included in these simulations - any asymmetries between inner and outer target arise purely as a result of geometric and atomic physics considerations. It is not surprising therefore, that discrepancies arise at the target, particularly for the particle
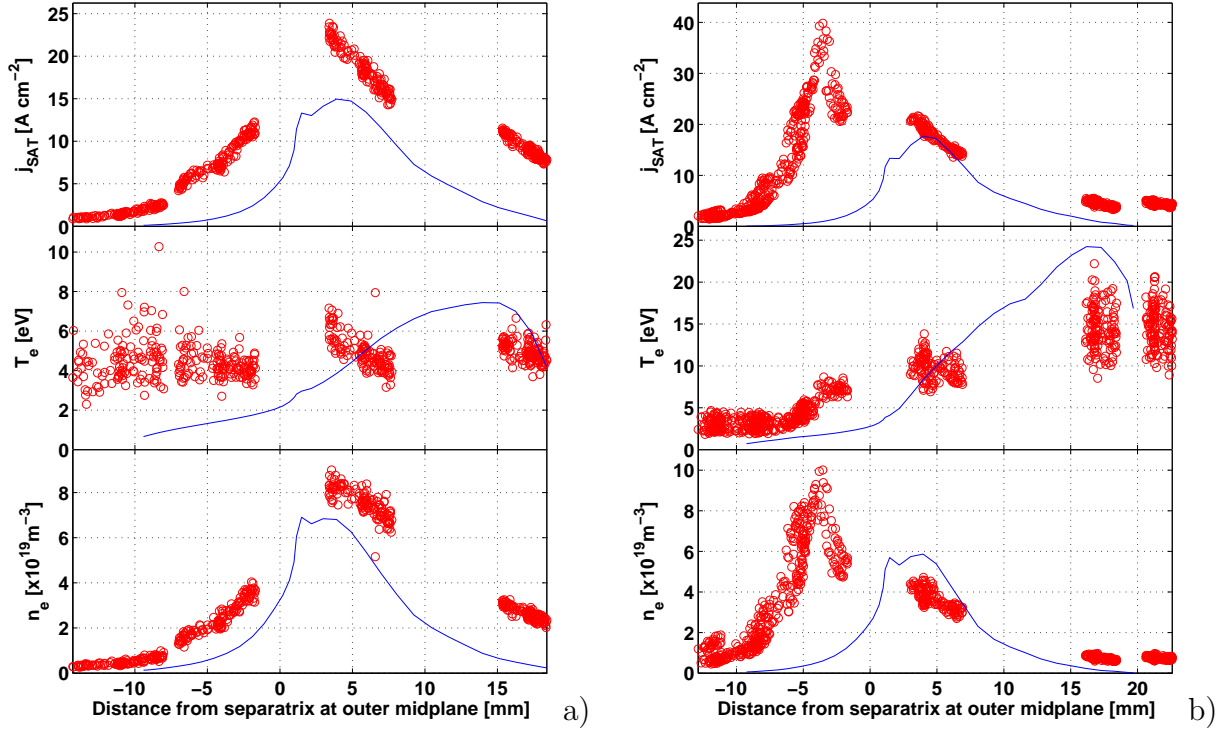
Figure 6.9: *Comparison of midplane mapped experimental (#54001) and simulated (a) inner and (b) outer target profiles using case #6110 for $\bar{n}_e = 4 \times 10^{19} m^{-3}$, $D_\perp = 0.35 m^2 s^{-1}$, $\chi_\perp = 0.75 m^2 s^{-1}$.*

flux which is known to depend strongly on the $\vec{B} \times \nabla B$ drift direction in JET, at least for deuterium plasmas [103].

Fig. 6.11 compiles the variation with n_e^{sep} of the simulated total radiation fraction, P_{rad}/P_{core} and the total ion and power fluxes to the targets and shows that the general experimental observation (Fig 6.3) in helium plasmas of power flux detachment occurring before particle loss is reproduced by the code. The simulations also demonstrate a clear tendency for lower total power flux to the inner target compared with the outer and confirm the experimental tendency for earlier detachment onset in He with decreasing power.

In the context of this study, the principle differences between He and D are the increased mean-free-path for neutral ionization ($\lambda_{mfp}^{He} \sim 6\lambda_{mfp}^{D}$ at $10eV$), the reduced CX rate coefficients (see Fig. 6.12) which reduce the efficiency for momentum transfer to
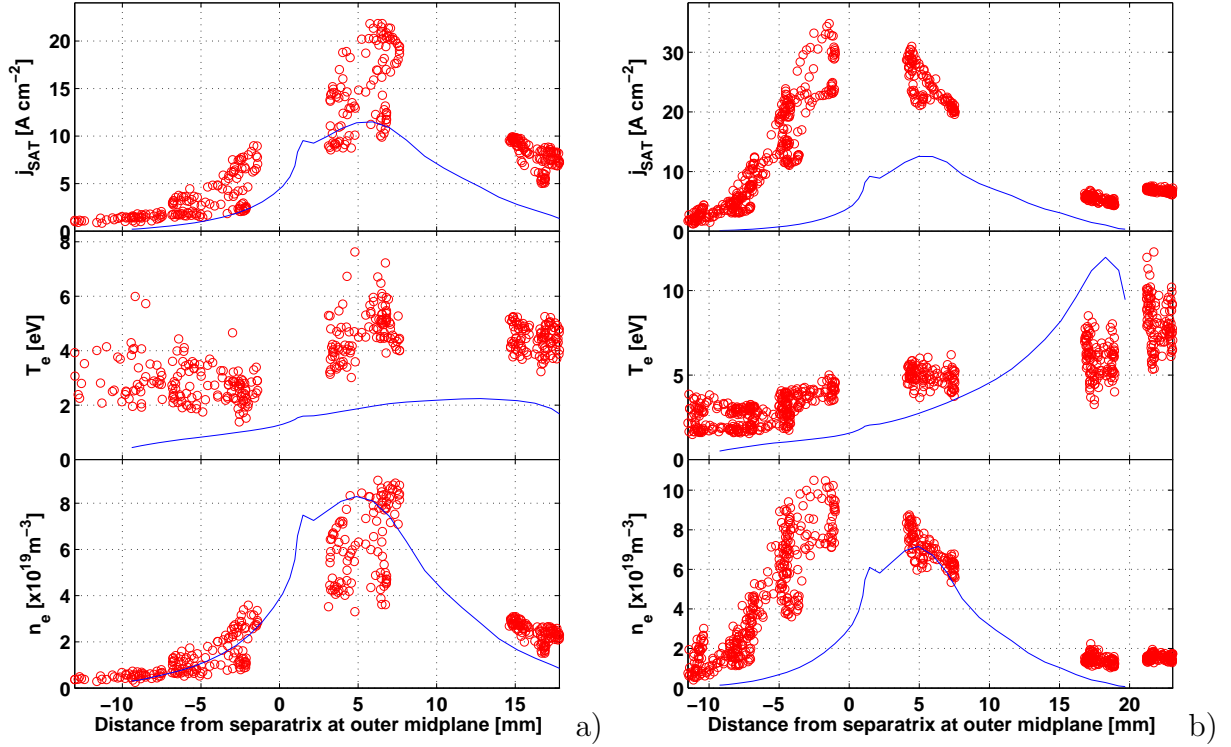
Figure 6.10: *Comparison of midplane mapped experimental (#54001) and simulated (#4496) profiles at the (a) inner and (b) outer targets for $\bar{n}_e = 6 \times 10^{19} m^{-3}$, $D_\perp = 0.35 m^2 s^{-1}$, $\chi_\perp = 0.75 m^2 s^{-1}$*

neutrals and the absence of MAR or hydrocarbon species with the potential for the provision of additional particle sinks. The first important consequence is that neutral He recycled at the targets penetrates further upstream before being ionized than would be the case for D atoms. This is graphically illustrated by the EIRENE neutral trajectories in Fig. 6.13 which compares a low and a high n_u case. Fig. 6.13 clearly demonstrates how physical sputtering of carbon at the targets is much more intense at low densities (see the blue trajectories in the strike point region) and, as in experiment [167], that overall carbon production is strongly reduced, if not nearly completely absent in the divertor at medium to high $\bar{n}_e$ in He (see also Fig. 6.2). In fact, in the simulations the percentage of power irradiated by carbon is already quite low at the lowest upstream densities. For case #4843 (corresponding to $\bar{n}_e \sim 2 \times 10^{19} m^{-3}$), carbon species account for $\sim 28\%$ of
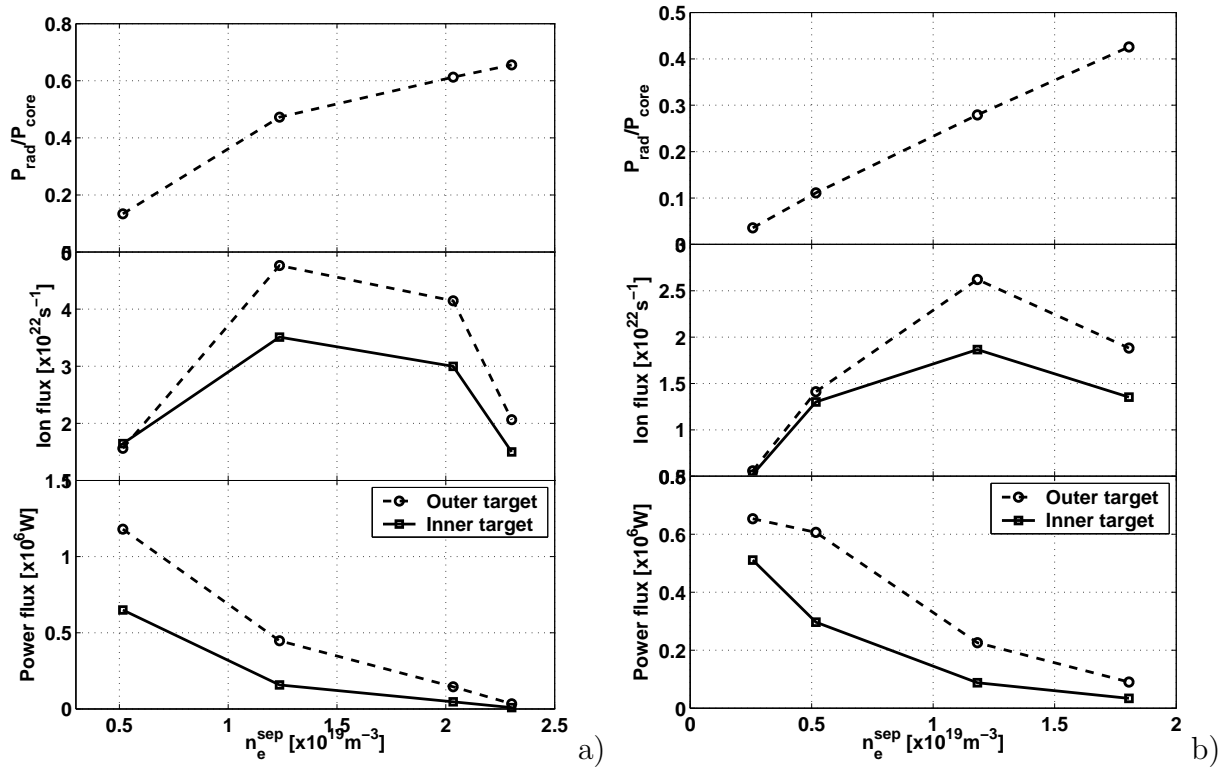
Figure 6.11: *Simulated total radiation fraction (P_{rad}/P_{core}) and integral ion and power fluxes to the inner and outer targets for simulations with (a) $P_{core} = 3.8MW$ and (b) $P_{core} = 2.2MW$. The four cases shown correspond to simulations #4843, #6110, #4496, #4494 in order of increasing n_e^{sep}.*

the total radiated power, while at the next highest simulated density (case #6110 corresponding to $\bar{n}_e \sim 4 \times 10^{19} m^{-3}$ in experiment), the fraction has dropped to only $\sim 6\%$. This trend continues until, at the highest simulated density, the radiation fraction has fallen to negligible values ($\sim 2\%$). In contrast, carbon radiation in D discharges at high density usually accounts for more than 75% of the total radiation in the SOL (see for example [12]).

As the density rises $HeII$ emission (i.e. from He^+ ions) contributes increasingly to the total radiation, making up more than 90% at the highest densities. Huber [194] has reported experimental observations of the movement of the $HeII$ radiation front from the target plates up through the divertor fan and finally to the X-point region as n_u increases.
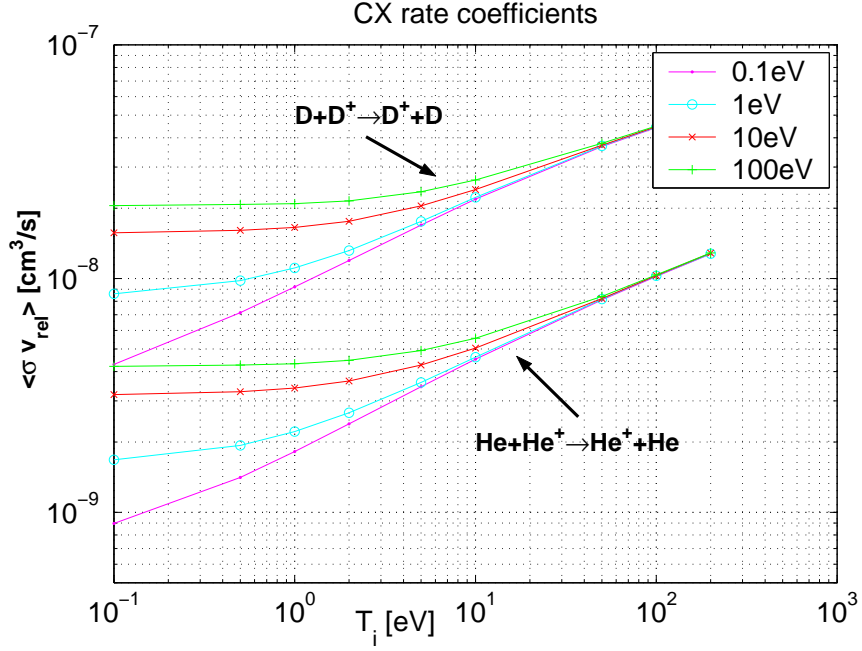
Figure 6.12: *Charge-exchange rate coefficients [65, 81] for D (HYDHEL 3.1.8) and He (HYDHEL 5.3.1) for different ion temperatures and neutral 'beam' energies (inset at top right).*

As shown in Fig. 6.13, this movement is a consequence of the increasing neutral penetration upstream as density rises. These neutrals are the source of the $HeII$ radiation, which is emitted in the course of the ionization process to fully ionized He. Fig. 6.14 shows the corresponding change in the distribution of the ionization front for $He^+ \rightarrow He^{2+}$. The fact that He^+ ions are the dominant radiators is shown by the behavior of the simulated total radiation (Fig. 6.15) which evolves in the same way as the $He^+ \rightarrow He^{2+}$ ionization front (Fig. 6.14). Both the experimentally measured spatial distribution and order of magnitude of the total radiation are qualitatively matched by the simulations, although more radiation appears in the outer divertor leg in the code than observed in experiment (see Fig. 6.4). This latter discrepancy might though be a consequence of uncertainty in the exact correspondence between simulation and experiment with regard to upstream density. Experiment and simulations are unanimous in placing the strongest radiation region inside the separatrix at the highest density when detachment occurs.
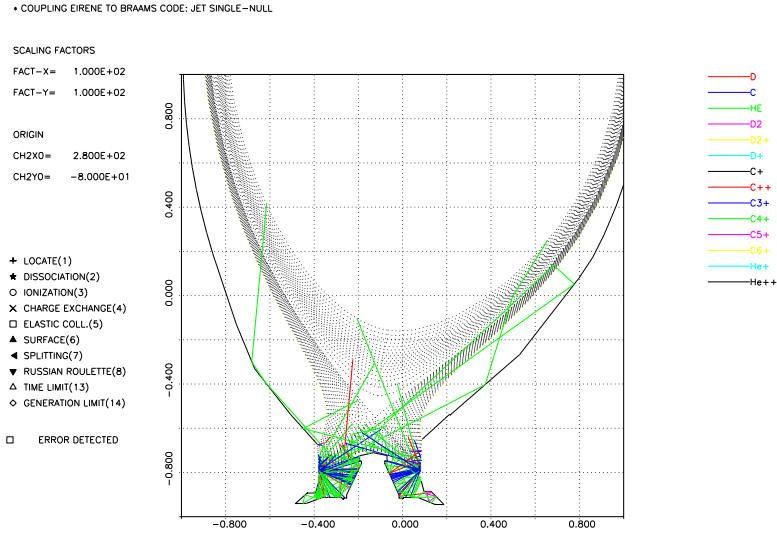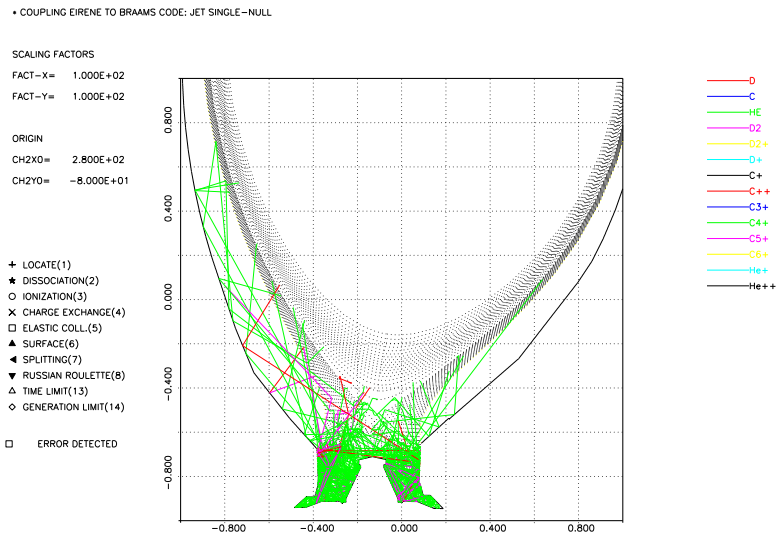
Figure 6.13: *Particle histories from EIRENE of* 100 *trajectories launched at the inner and outer targets (*50 *histories each) for (a) low density (#4843) and (b) high density (#4494,* $n_e^{core} = 4 \times 10^{19} m^{-3}$*).*

Detachment in deuterium is associated with cooling of the divertor volume, followed by momentum removal and subsequent recombination. In helium, the phenomenon begins at much higher upstream densities and is similar to that in D at most in the sense that the
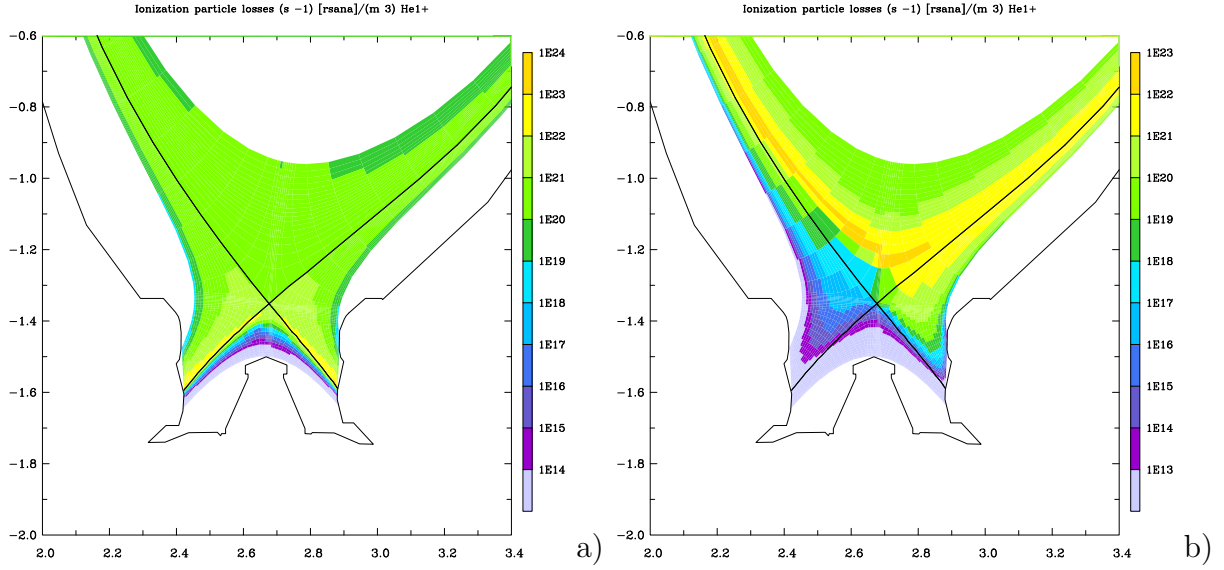
Figure 6.14: *Particle losses due to He^+ ionization at (a) low density (case #4843) and (b) high density (case #4494), corresponding to the highest n_e^{sep} in Fig. 6.11.*

inner target detaches first. For varying input power, only at the highest densities is particle detachment observed at both targets. Particle detachment occurs close to the density limit whilst 'power detachment' is observed at much lower densities. From comparison of simulations and experimental data it is clear that the power detachment is a consequence of He atoms escaping further upstream compared to the case for D neutrals, followed by power loss, mostly due to He^+ line radiation. At the highest densities a large enough fraction of the power entering the SOL is lost through line emission such that there is insufficient energy for ionization of the recycled neutrals, thereby leading to a collapse in the particle flux to the targets. This is very different to the situation in D plasmas, where a complex interdependence between CX reactions, radiative cooling due to high carbon concentrations, recombination and ionization processes lead to the observed power and particle detachments.

In He, the simulations show that recombination plays no role in the detachment process. This is a direct consequence of the plasma temperature in the divertor volume. As shown in Fig. 6.16, the rate coefficients for He^+ and D^+ recombination are very similar.
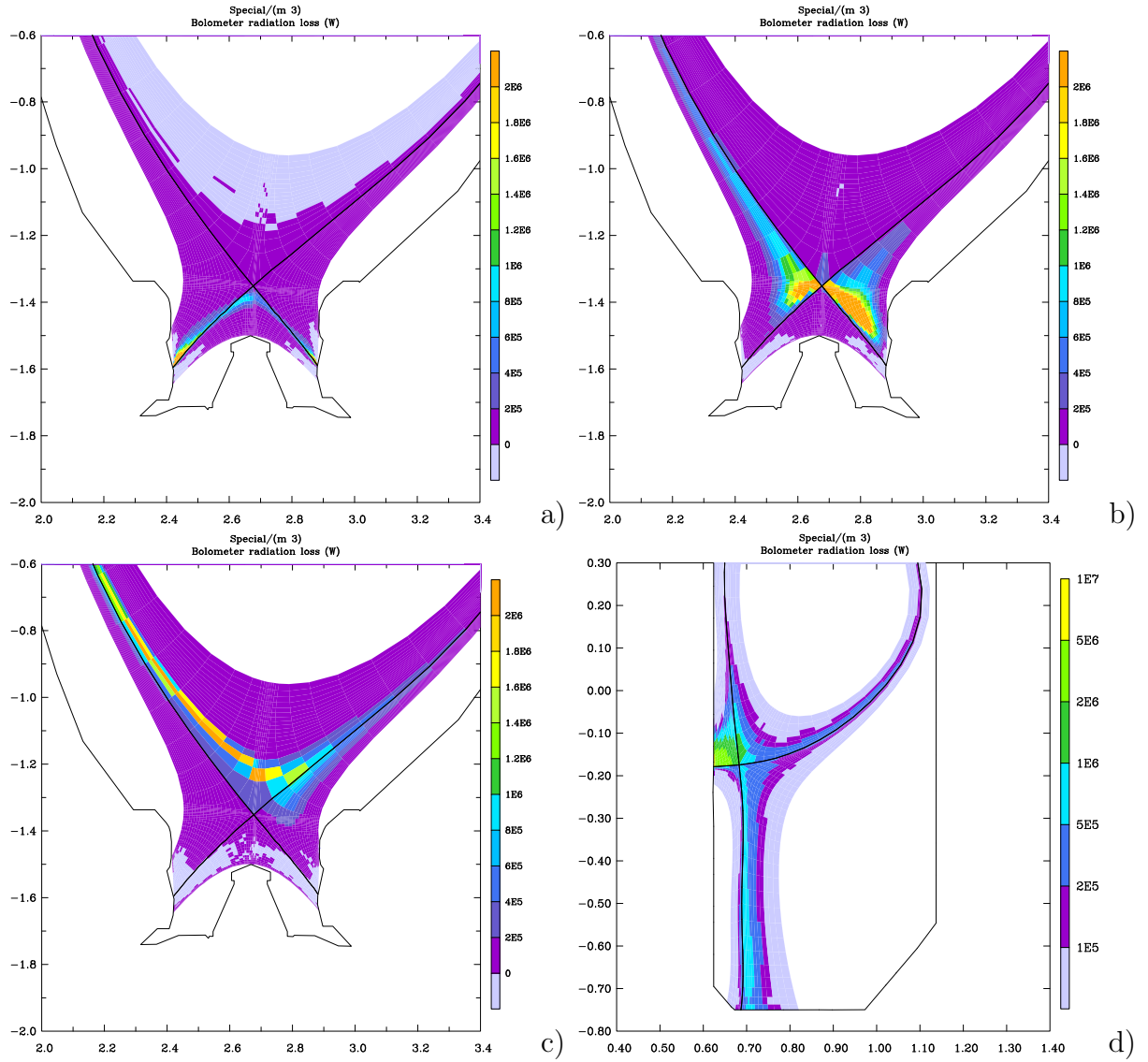
Figure 6.15: *Poloidal distribution of total radiation for (a) low density (case #4843), (b) medium/high density (case #4496) and (c) high density (case #4494), corresponding to the first, third and fourth values of n_e^{sep} in Fig. 6.11. Compare this evolution with Fig. 6.4. The total radiation distribution for a pure He simulation in TCV at the highest density considered (case #11150) is included in (d) for later comparison.*

For both species therefore, recombination will only be a significant particle sink if T_e falls below $\sim 2eV$ in a 'sufficiently' large volume in front of the target plates. The simulated
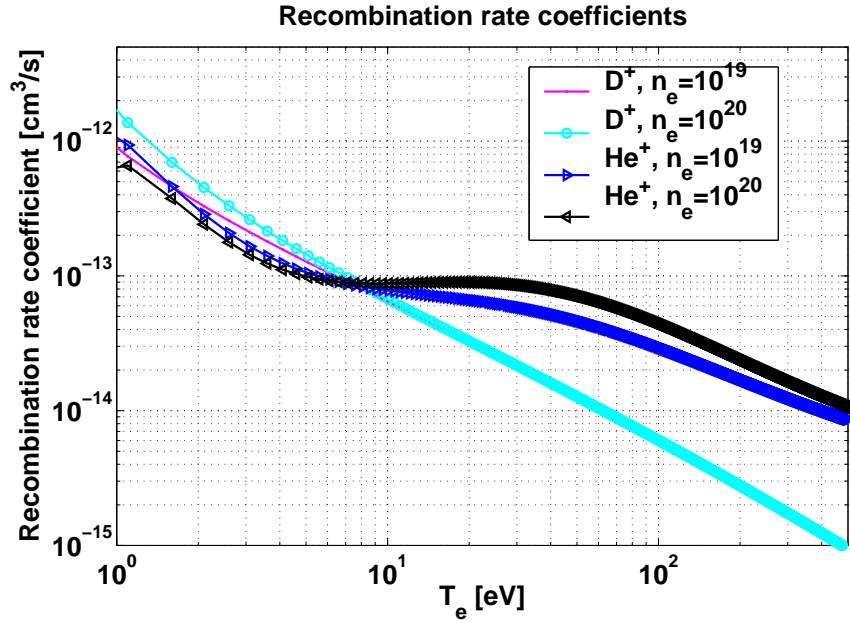
Figure 6.16: *CRM recombination rate coefficients at $n_e = 1.0 \times 10^{19} m^{-3}$ and $n_e = 1.0 \times 10^{20} m^{-3}$ for $e + He^+ \rightarrow He + h\nu$ (AMJUEL 2.3.13a) and radiative plus three body recombination for D^+ (AMJUEL 2.1.8).*
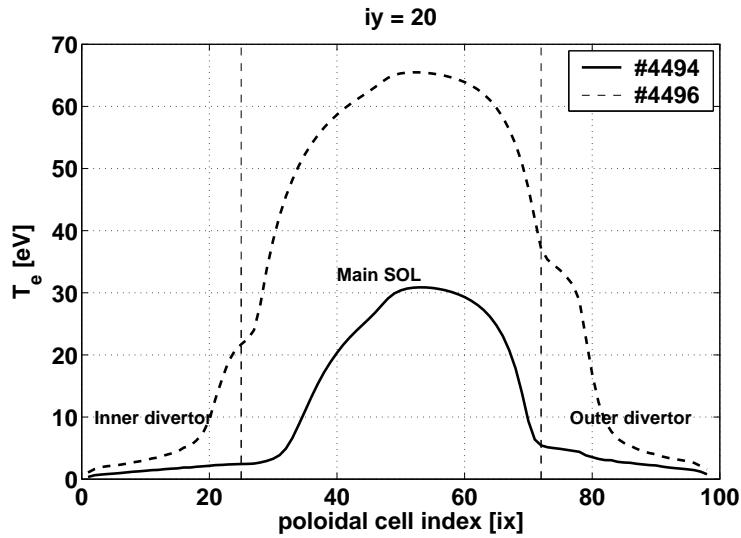

Figure 6.17: *Poloidal electron temperature profiles for cases #4496 (highest density prior to detachment) and #4494 (detached case). Profiles are shown along the second ring of the computational grid in the SOL (iy = 20).*

poloidal temperature distribution in Fig. 6.17 (see also Fig. 6.22) shows that this never really occurs in He, even at the highest density. Experimental support for this argument comes from the observation that recombination is only a negligible contributor to the HeI emission [194]. Despite the lack of recombination, the simulations demonstrate a marked decrease in the integral target ion flux (to both targets) at high n_u (Fig. 6.11). The key to understanding the He detachment is the recognition that even though the CX rate coefficients for He are approximately an order of magnitude lower than for D at low T_e (Fig. 6.12), the ionization mfp for He neutrals is about the same factor higher than in D (for $T_e \sim 5eV$). Charge-exchange processes may thus be less effective in slowing the ion fluid down but can, by virtue of the longer mfp for first ionization of He (allowing neutrals to escape the plasma in the divertor volume), be sufficient to remove enough momentum for detachment to occur. This is implied by Fig. 6.18 which shows how pressure
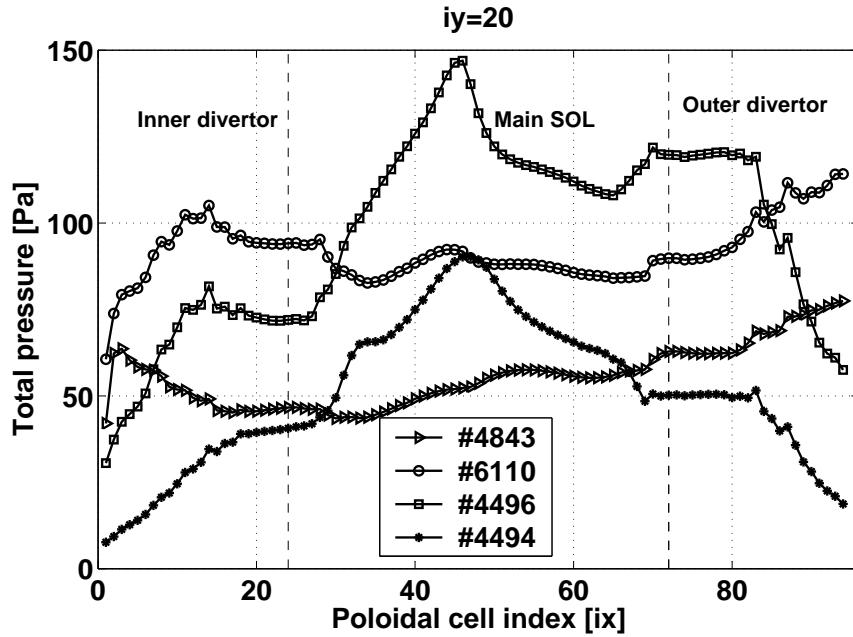

Figure 6.18: *Poloidal profiles of total pressure ($p_{tot} = p_{dyn} + p_e + p_i$) for the cases shown in Fig. 6.11 along a poloidal ring two radial cells outside the separatrix in the SOL ($iy = 20$). Upstream density increases from #4843 to #4494. Compare this with simulations for detachment of TCV D discharges (Fig. 5.53 and 5.54).*

falls (equally in both divertors) along field lines close to the separatrix with increasing density. This is a clear sign of momentum removal and thus efficient momentum transfer to neutrals.

One may therefore conclude that in He two processes lead to the observed detachment. The high recycling cycle, $He \rightarrow He^+ \rightarrow He^{2+}$, is first strongly depleted as density increases when the divertor volumes are power starved after the radiation zone moves inside the LCFS. As a consequence, the temperature in the divertor volume decreases (as do the particle fluxes), but does not reach values sufficiently low for significant recombination to occur. It is low enough, however, for the He neutral ionization mfp to be long enough for neutrals to transfer sufficient ion fluid momentum out of the divertor fans to further reduce the target ion flux, such to increase the degree of detachment.

Together with the absence of chemical sputtering, the suppression of physical sputtering due to low divertor temperatures in the high recycling and detached regimes means that carbon impurity release falls to negligible levels in helium at high density. In contrast, even if ion fluxes and energies are reduced in deuterium at high densities, neutral chemical sputtering persists at high levels and carbon production can be significant.

Figure 6.19 compares the T_e (and n_e) dependent radiation cooling curves for H, He and C computed using the ADAS database under the assumption of coronal equilibrium. For temperatures in the divertor typical of the high recycling regime prior to detachment, carbon radiates between one and three orders of magnitude more power than He or even H (thus D). Simulations and experiment demonstrate that helium alone is apparently a strong enough radiator to exhaust enough power in the JET divertor and X-point regions for power starvation (and subsequent detachment) to occur, but even small amounts of carbon (in the region of a few percent) in the same plasma volume would be as efficient in radiating power as all of the helium put together. The presence of carbon in D-fueled discharges therefore allows the temperature in the divertor volume to drop low enough for significant recombination to occur (this has also been shown in Section 5.2.2 to be the key element for understanding detachment in D in TCV). It is therefore the absence of significant amounts of carbon in He which prevents pure helium plasmas from reaching
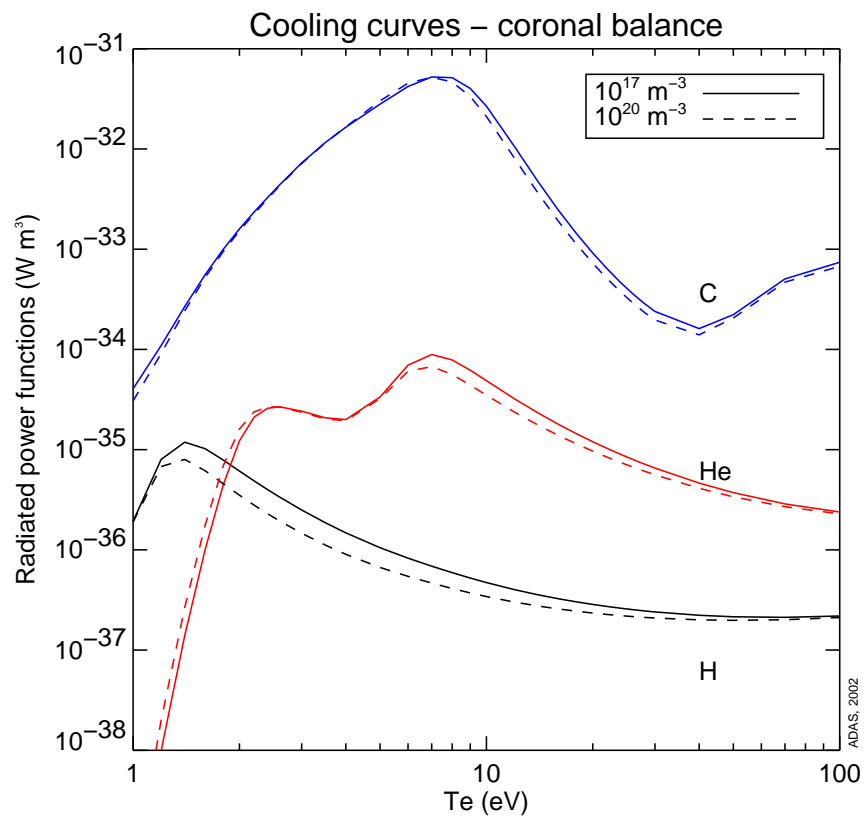
Figure 6.19: Radiated power losses for the D (H), He and C species relevant to this thesis. Curves computed using the ADAS database and supplied by M. O'Mullane [201].

low enough temperatures in a sufficiently large volume for recombination to be an important player in the reduction of target ion fluxes. One is thus naturally led to conjecture that if the experimental density limit is the value of $\bar{n}_e$ at which detachment is obtained at both targets, then the earlier density limit observed experimentally in D compared to He can simply be associated with the absence of carbon in helium plasmas at high density, preventing T_e in He to drop low enough earlier on during the density ramp for recombination to occur and from more power to be radiated than would be possible, if more carbon was present.

A further obvious implication is that the density limit in deuterium plasmas in a carbon-free tokamak might be considerably higher, at least in L-mode. The situation is less clear in the hotter edge plasmas of the H-mode nor given the fact that a future all-metal device will likely require the injection of external seed impurities to provide the additional radiation needed for the achievement of detachment that occurs naturally in a carbon machine. One may also note the recent conjecture in [166] where an edge transport based density limit is proposed. Further study is required to ascertain whether or not the results of this JET He/D comparison support such a mechanism.

6.4 Comparing JET and TCV in pure helium

The discussion of TCV detachment in Section 5.2.2 concentrated on the mechanisms at work in D plasmas, using the comparison with He simply to demonstrate how the absence of carbon chemistry, and hence the lack of a requirement to account for impurity release at the main chamber walls, allows simulations with a more conventional set of assumptions to adequately match experimental observations. But a question which naturally arises in the light of the JET helium simulations is why detachment is observed at JET in He, but is not seen at any density in TCV.

Prior to detachment at JET, upstream conditions with respect to T_e and n_e are very similar to those at the highest density reached on TCV, with $n_e^{sep} \sim 2 \times 10^{19} m^{-3}$ and separatrix temperature $\sim 40 - 50 eV$. Since, in both cases, reasonably good agreement with experiment has been obtained with the code simulations, the code results can be used comparatively in seeking an explanation. This is performed here by studying the simulation results at the highest modeled upstream density for TCV (case #11150, see Section 5.3.2.2) and the JET case (#4496) appropriate to conditions just prior to detachment. One may note that the experimental comparison is made here between pure He plasmas in forward field for JET and reversed field for TCV. Some differences are therefore to be expected due to divertor asymmetries provoked by drifts. The JET data show, however, that the marked asymmetries seen in D plasmas are not observed in He, implying that the switch of plasma species is a more important factor in modifying the in/out asymmetry than the drifts themselves.

In both tokamaks, radiation from He^+ is the dominant contributor to the total volumetric power exhaust. The poloidal distribution of the simulated total radiation for the two cases mentioned above is shown in Fig. 6.15(b) and (d). Before the onset of detachment it is clear that most of the radiation in both machines is concentrated in the divertor volumes and X-point regions. It might therefore be expected that, as in JET (seen both in experiment and simulations), the radiation front in TCV should also move inside the separatrix with further increase in density. But this does not occur even in

simulations in which n_e^{sep} is $\sim 20\%$ higher than in the highest JET case. This different behavior is linked to the very different divertor geometries between the two machines. In JET the inner and outer divertor radiation fronts move toward the X-point as $\bar{n}_e$ increases such that, just before the onset of detachment, both radiation fronts can contribute to power exhaust in the X-point region, power starving the rest of the divertor. This is not the case in TCV, where the divertor is highly asymmetric. Although the total radiation in the outer leg is higher than at the inner, in part due simply to the larger divertor volume, the radiation is distributed almost uniformly along the divertor leg, exhausting power continuously from the X-point to the outer target (Fig. 6.15(d)). This is a result of the unbaffled divertor geometry allowing neutrals to escape the target zone easily. At the inner target, conditions are very different - the escape probability for neutrals is much lower and the radiation zone is confined to a small region close to the X-point.

At first sight therefore, concerning the relative proximity of the radiating zones in the inner divertors to the X-point, JET and TCV appear reasonably similar. But this similarity no longer holds when the radiation, or ionization efficiency of the two divertors is compared. To see this, the average plasma energy consumed per ionization event of He and He^+ in the different regions of the two tokamaks is compared in Table 6.1. The average energy consumed per ionization event of He^0 is very similar in both machines and in both ionization of He^0 contributes little to the total energy consumption. In addition, there do not appear to be large differences in the relative neutral behavior with respect to overall plasma parameters in both inner divertors. Fig. 6.20 compares parallel profiles of the relative neutral density (normalized to the background electron density) computed 2 radial cells outward from the separatrix in the SOL for both machines and plotted in normalized distance from the X-point to the inner target. Interestingly, the relative normalized density decay lengths are very similar, although the relative He^0 density in the JET inner divertor is uniformly a factor of ~ 2 higher than in TCV. This is partly due to the higher degree of divertor closure at JET and also to the differing T_e values (see Fig. 6.22). Relative to the background plasma, the He neutral density is thus similar for both machines in the inner divertor volume. It should not, however, be forgotten that

Region	$[eV]/He^+$ TCV, #11150	$[eV]/He^+$ JET, #4496	$[eV]/He^{2+}$ TCV, #11150	$[eV]/He^{2+}$ JET, #4496
Inner divertor	31	44	348	1579
Outer divertor	36	37	329	849
Main SOL	33	33	233	415
Core	31	30	139	149

Table 6.1: *Simulation results for the ratio of total radiated energy (thus energy consumed) to the total number of ionization events of He and He^+, resulting respectively in He^+ and He^{2+}, providing a measure for the energy efficiency in ionizing particles in the different zones. Values are listed for the inner and outer divertors, main SOL and the computational region inside the separatrix of TCV and JET in He at high density.*

the absolute value of the neutral density is of course much higher in JET (compare for example Fig. 6.10 with Fig. 5.42).

An important and striking difference between the two machines is to be found in the energy radiated per ionization event resulting in He^{2+}. A factor ~ 5 more energy is consumed per ionization event in the JET inner divertor than in TCV. It would appear that in JET, He^+ ions simply have more time to radiate in the inner divertor volume before either reaching the target or being ionized. Fig. 6.21 compares the parallel velocity profiles of the He^+ fluid along the inner divertors of both machines. As expected, the TCV inner divertor exhibits the typical signature of an attached plasma, with the parallel velocity increasing towards the target. In contrast, there is a strong decrease of $v_\parallel$ in JET. This is due to momentum removal by neutrals and is the principal cause of the drop in total pressure discussed earlier in the context of detachment.

It is now clear that this momentum removal also plays an important role in determining radiation balance. As $v_\parallel$ decreases, the dwell time for He^+ ions increases. Assuming that the He^+ originates mostly from regions close to the X-point (since in both machines radiation there is largest), and (crudely) that on average fluid velocity $v_\parallel \sim 1.4 \times 10^{-4} ms^{-1}$,
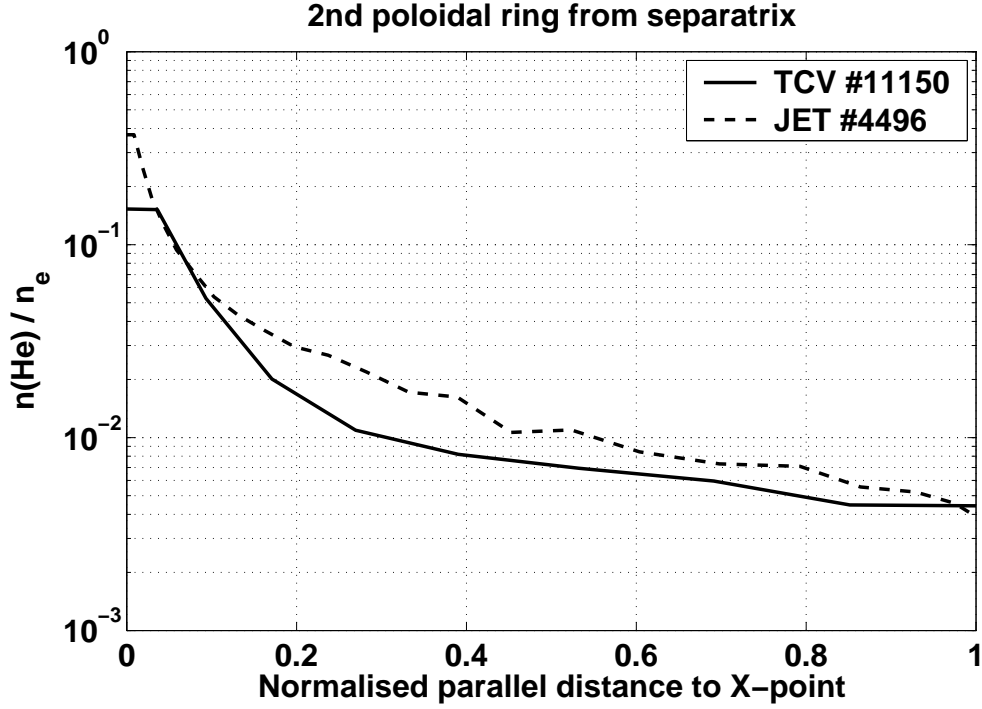
Figure 6.20: *Neutral He density along the inner divertor normalized to the local electron density. The parallel distance has been normalized to the distance from the inner target to the X-point and the data are extracted from the second computational cell on the SOL side of the separatrix.*

the dwell times are $\tau_{dwell}^{TCV} \sim 2.5 \times 10^{-4} s$ and $\tau_{dwell}^{JET} \sim 7.5 \times 10^{-4} s$ using the parallel distances shown in Fig. 6.21. In addition, Fig. 6.22 shows the parallel T_e profiles along the second radial cell from the separatrix in the inner divertor. The temperature is clearly lower in JET than in TCV, strongly reducing the ionization probability for neutrals and especially for He^+. In fact, the rate coefficient for the ionization of He^+ falls by over an order of magnitude as T_e decreases from $10eV$ to $5eV$. At the same time, Fig. 6.19 illustrates that for the temperature range encountered in the divertors of TCV and JET, the radiative cooling loss from helium remains rather uniform. It may therefore be concluded that it is simply the larger size of JET (i.e. larger divertor volume and X-point to divertor connection length) which permits He^+ to radiate more power in the inner divertor volume before being ionized or lost to the target. Similar conclusions can be drawn on the basis
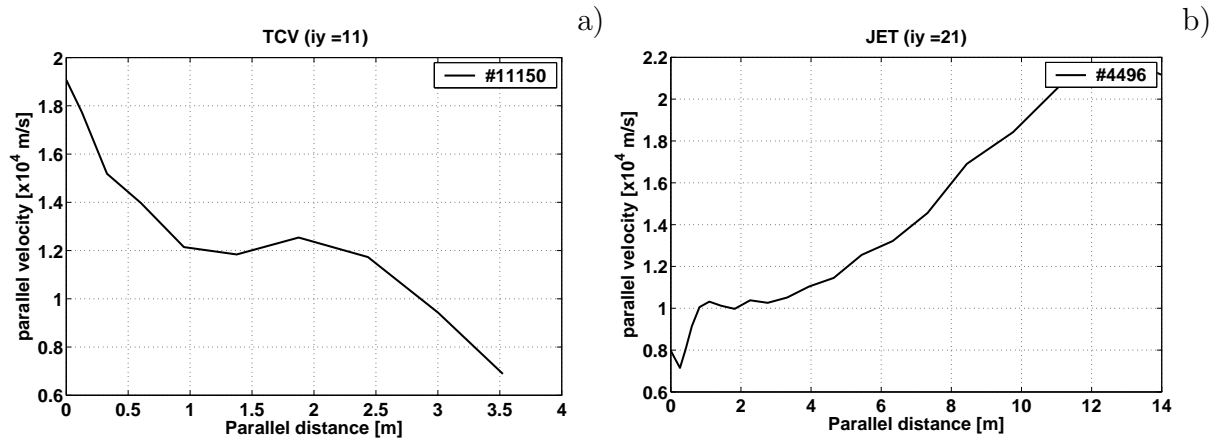
Figure 6.21: *Parallel He^+ fluid velocity in the inner divertors of (a) TCV and (b) JET, as function of the parallel distance from the inner target (located at the origin of the abscissa).*
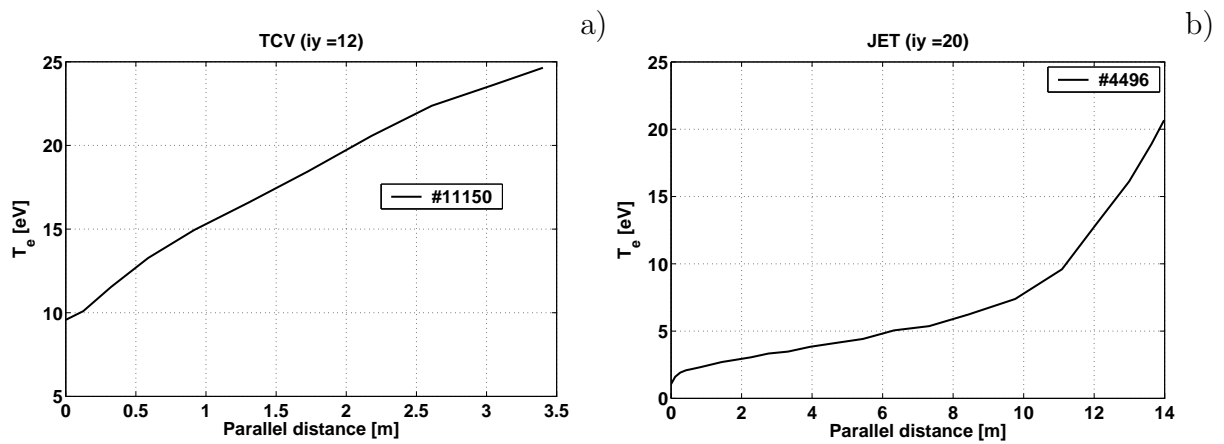

Figure 6.22: *Parallel T_e profiles in the inner divertors of (a) TCV and (b) JET in both cases as a function of the parallel distance from the inner target.*

of the outer target parallel T_e profiles in Fig. 6.23. In this case, both divertors extend over similar connection length and the parallel T_e profiles are similar, with TCV having higher values in regions close to the target. Since the rate coefficient for $He^+ \rightarrow He^{2+}$ ionization is a strong function of T_e, He^+ ions in front of the target plates at JET are less likely to be fully ionized compared with those in TCV and can therefore radiate more power before being ionized. The fact that radiation losses normalized to the number of
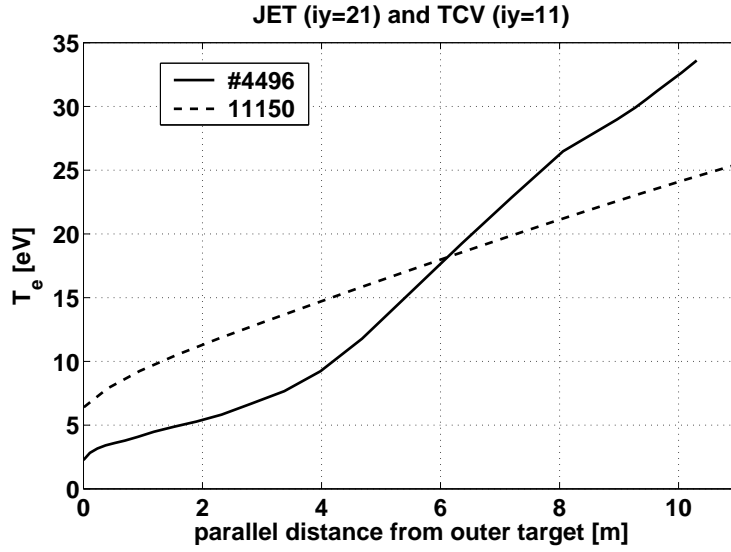
Figure 6.23: *Simulated parallel T_e profiles in the outer divertor of TCV (case #11150) and JET (case #4496).*

He^+ ionizations are quite similar between the two machines for the outer divertor may be linked to the similarity in the T_e profiles. But for the radiation pattern that ultimately leads to power starvation, there is also a major difference between the two machines. At JET the outer divertor (vertical) target to X-point distance is approximately half as long in the poloidal plane as in TCV. It is this distance which is relevant to neutral helium leaving the target plates, since their motion is not confined by the magnetic field. As a consequence of the divertor geometry it is more likely in JET than in TCV for neutrals to reach regions upstream close to the X-point, be ionized there and then radiate as He^+. In TCV they would have to travel either along the entire outer divertor leg or 'bypass' it and enter the X-point region from the LFS main chamber walls, where fluxes are considerably lower than at the target.

6.5 Concluding remarks

Experiments on JET have shown that detachment does occur in pure He discharges, but that it does so in a way which is very different than in deuterium plasmas. The SOLPS5 code has been used to simulate this detachment and reasonable agreement has been found with experimental data. Such comparison leads to a picture in which helium detachment in JET is due to momentum transfer to neutrals, combined with sufficiently long dwell times of the He^+ fluid in the divertor volume and X-point region that enough radiation occurs to starve the divertors of power. The subsequent reduction in the ionization rate both of recycled neutrals and He^+ ions in the divertor volume and the ultimate formation of a strong MARFE inside the LCFS in turn starves power and causes detachment.

Comparing JET with TCV, the simulation results indicate that an important factor in the absence of detachment during He plasma operation in TCV is the smaller machine size, coupled with very different divertor geometries (disposition of target plates, open versus closed divertor). Less radiation is emitted by He^+ in the TCV divertor compared with JET so that lower volumetric radiation losses cannot cool the divertor sufficiently to allow neutral mfp's to increase to the point at which neutral escape inside the separatrix becomes significant. It may be therefore expected that in principle, $\bar{n}_e$ could be further increased in TCV before detachment occurs. Only when recycling fluxes from the inner and outer targets exceed the values at which a large enough fraction of neutrals can penetrate the LCFS will detachment begin. Preliminary simulations, running into a numerically unstable situation, indicate that something very similar may very well occur, at least in the code. This though seems to be more linked to radiation occurring along the entire SOL than to an X-point MARFE.

Finally, and perhaps most importantly, it appears that a major reason for the absence of volumetric recombination in He plasmas is the lack of plasma radiative cooling, compared to D plasmas, prior to the radiation front moving inside the separatrix. This would seem to be linked to the very low carbon concentrations at high density in pure He (due to notably the absence of carbon chemistry). The implication is therefore that the

deuterium density limit, at least in L-mode, might be expected to be considerably higher in a carbon-free tokamak.

Chapter 7

Summary and conclusions

Tokamak divertor detachment, though expected to play a major role in allowing the high power fluxes expected in reactor grade devices to be tolerated, is still not completely understood. Predictive modeling of the phenomena and how it influences the physics design of the next step international tokamak, ITER, is based on the complex two dimensional, coupled plasma fluid-Monte Carlo neutral code package, SOLPS. The aim of this thesis has been to apply the most recent version of this code (SOLPS5) to the numerical simulation of experimentally observed divertor detachment on two very different tokamaks, TCV and JET, and, through the use of both deuterium and helium as working gas, in two very different plasma environments. Specific experiments have been performed on each tokamak to provide input for this modeling exercise. Switching from deuterium to helium in a tokamak containing significant amounts of carbon first wall material (as do both TCV and JET), dramatically modifies the nature of plasma-wall interaction since carbon chemical sputtering, a demonstrably important source of carbon impurity for the deuterium plasma, is absent in helium. Through close comparison of simulation results with experimental data regarding detachment onset in these very different situations, progress has been made concerning the relative importance of the various physics components determining how and under what conditions it occurs. This work also constitutes a contribution to the ongoing effort towards building confidence in the predictive ability of the codes when applied to experiments still to be constructed.

In TCV, the simplest of ohmically heated plasmas exhibit totally anomalous divertor detachment in deuterium at the outer target, a situation which was first observed clearly when the graphite first wall protection was extended to cover an area accounting for nearly 90% of the vacuum vessel internal surface area. Early efforts at modeling this detachment, attempted before this thesis began, could not account for the effect. Experiments in pure helium, conducted during this research show that detachment does not occur in this instance. Moreover, although having some impact on the divertor performance at intermediate densities (presumably as a consequence of drift effects), reversal of the toroidal field is not observed to influence detachment. Among the initial potential candidates thought to be at the origin of the anomaly was the possibility of strong molecularly activated recombination through reaction chains involving hydrogenic and even hydrocarbon molecular species. This was partly motivated by measurements of the in-vessel neutral pressure made by ASDEX-type fast pressure gauges, installed as part of this thesis work, and additional experimental data from the divertor region, all of which indicated that the divertor neutral and plasma density were far too low, even at high plasma density, to permit electronic volumetric recombination processes to remove significant ion flux.

Systematic SOLPS5 simulations have been conducted in attempt to understand this deuterium detachment, progressively activating more sophisticated options in the EIRENE neutral code, including a collision radiative model, more realistic toroidal geometry, molecular vibrational levels and, for the first time in an integrated tokamak edge simulation, hydrocarbons in the form of CD_4. In no case was any degree of detachment observed in the code. This observation, coupled with the fact that the code is found to match experimental data for very low plasma density (when the divertor is far from detachment) in both deuterium and helium, suggested that the description of upstream cross-field transport, previously assumed to be described by diffusion coefficients for particles and energies constant everywhere in space and fixed for all densities, might require some revision at high densities. Further evidence in favor of this supposition has also been recently supplied on TCV by measurements of density fluctuations and turbulent driven cross-field fluxes in the SOL plasma. At high density, cross-field transport in the far SOL becomes

increasingly convective, flattening the density profile and making the description in terms of a diffusive process alone inadequate. A slight modification to SOLPS5 allowing for the specification of such a convective component on the low field side of the SOL poloidal cross-section and its activation at high density did not, however, improve the situation with respect to producing detachment in the simulations.

The key to producing significant loss of target ion flux in the code has been found to be the coupling of upstream convective transport with enhanced main chamber wall chemical sputtering and the presence of hydrocarbons. The chemical yields ($\sim 10\%$) specified at the all-carbon walls are far above the values currently believed to be reasonable under the conditions most favorable for chemical sputtering in tokamaks. The justification for such an enhancement in the code comes from the recognition that SOLPS5 (in common with all existing tokamak SOL codes) contains no realistic model of the ion flux interaction with the main chamber walls - in diverted plasmas, only at the target plates is the ion interaction correctly specified. In contrast, the real neutral-main wall interaction is reasonably well approximated by the code. By increasing the main wall chemical yield in deuterium at high density (when cross-field ion fluxes are high due to the increased convective transport), the additional impurity production due to impinging wall ion fluxes is accounted for in a crude, adhoc manner. This increased impurity influx, together with the energy loss to the plasma electron fluid as a result of CD_4 dissociation is just sufficient, in these relatively low power ohmic discharges, to modify the SOL radiation balance such that the divertor is starved of power and outer target detachment can occur. In helium, even though increased convection is also present at high densities, there is no carbon chemistry and carbon release occurs only through physical sputtering. The reduced charge-exchange collision cross-sections in helium compared with deuterium, coupled with the low far SOL ion energies at high densities mean that physical sputtering due to both ions and neutrals in helium is reduced and main wall carbon production is considerably lower. Radiation losses are then confined to what can be dissipated through helium excitation only and this is insufficient, even at the highest densities, to detach the divertor in the simulations. There is thus perfect consistency between code and experiment. In addition to providing

an explanation for the TCV outer target detachment anomaly, these simulations have also demonstrated that, at least in some cases, the lack of a more realistic model of the plasma-main chamber wall interaction can have serious consequences for the outcome of simulation results in the divertor.

Regarding the application of SOLPS5 to the simulation of JET plasmas, efforts have concentrated on a study of divertor detachment observed in pure helium alone, with emphasis once again on the comparison of code and experimental results. This modeling constitutes the first ever application of an edge code to the simulation of helium plasmas in JET. Unlike in pure helium TCV ohmic plasmas, divertor detachment is observed in JET L-mode He discharges. But this detachment is very different to that in deuterium. The SOLPS5 modeling has successfully reproduced experiment and detachment in helium has been identified as the result of synergy between radiation losses due to He^+ ionization and momentum losses of the ion fluid through CX reactions with neutrals in the nearly complete absence of volumetric recombination processes. This is a direct consequence of an insufficiently low divertor plasma temperature, itself due to the massively reduced carbon concentrations in comparison with deuterium plasmas (as a result of carbon chemical sputtering, absent in helium) which provide for much lower levels of total radiation loss.

This constitutes, therefore, a striking demonstration of the utility of carbon as a natural, extremely powerful radiator, in any tokamak divertor. Unfortunately, carbon is also associated with increased levels of fuel retention which are currently thought to exclude its use in next step devices. The experimental and simulation results described here imply that one of the envisaged solutions to the retention problem, an all-metal machine, may well also be associated with a much higher density limit for operation with hydrogenic fuel.

Bibliography

[1] U.S. Department of Energy. *International Energy Outlook 2004*, April 2004. DOE/EIA-0484(2004), URL: http://www.eia.doe.gov/oiaf/ieo/index.html.

[2] National Academy of Sciences, Washington. *The hydrogen economy*, 2001. URL: http://www.nap.edu.

[3] G. Van Oost. Energy for future centuries. *Transactions of Fusion Technology*, **29**:9, 1996. Second Carolus Magnus Summer School on Plasma Physics.

[4] L. Spitzer. The stellarator concept. *Phys. Fluids*, **1**:253, 1958.

[5] J.A. Wesson. *Tokamaks*. Clarendon Press, Oxford, 2nd edition, 1997.

[6] *ITER*. URL: http://www.iter.org.

[7] N.A. Krall and A.W Trivelpiece. *Principles of plasma physics*. San Francisco Press, Inc., 1986.

[8] P. C. Stangeby et al. A tutorial on some basic aspects of divertor physics. *Plasma Phys. Control. Fusion*, **42**:B271, 2000.

[9] ITER Physics Basis. Chapter 4: Power and particle control. *Nucl. Fusion*, **39**:2391, 1999.

[10] G. Federici et al. Plasma-material interactions in current tokamaks and their implications for next step fusion reactors. *Nucl. Fusion*, **41**:1967, 2001.

[11] A. Loarte et al. Plasma detachment in JET MARK I divertor experiments. *Nucl. Fusion*, **38**:331, 1998.

[12] M. E. Fenstermacher et al. Physics of the detached radiative divertor regime in DIII-D. *Plasma Phys. Control. Fusion*, **41**:A345, 1999.

[13] B. Lipschultz et al. Modification and control of divertor detachment in Alcator C-Mod. *Journal of Nuclear Materials*, **241-243**:771, 1997.

[14] R. Schneider et al. Role of divertor geometry on detachment in ASDEX Upgrade. *Journal of Nuclear Materials*, **266-269**:175, 1999.

[15] N. Asakura et al. Role of divertor geometry on detachment and core plasma performance in JT60U. *Journal of Nuclear Materials*, **266-269**:182, 1999.

[16] R. A. Pitts et al. Divertor geometry effects on detachment in TCV. *Journal of Nuclear Materials*, **290-293**:940, 2001.

[17] C. S. Pitcher and P. C. Stangeby. Experimental divertor physics. *Plasma Phys. Control. Fusion*, **39**:779, 1997.

[18] C. S. Pitcher et al. Routes to divertor detachment in ASDEX Upgrade. *Journal of Nuclear Materials*, **241-243**:1696, 1997.

[19] S. I. Krasheninnikov et al. Plasma recombination and divertor detachment. *Physics Letters A*, **214**:285, 1996.

[20] D.P. Coster et al. Automatic evaluation of edge transport coefficients with SOLPS5.0. *Contributions to Plasma Physics*, **40**:334, 2000.

[21] J. A. Boedo et al. Transport by intermittent convection in the boundary of the DIII-D tokamak. *Phys. Plasmas*, **8**:4826, 2001.

[22] S. I. Krasheninnikov. On scrape off layer plasma transport. *Physics Letters A*, **283**:368, 2001.

[23] J. P. Graves et al. Self-similar density turbulence in the tcv tokamak scrape-off layer. *Plasma Phys. Control. Fusion*, . accepted.

[24] R. A. Pitts and others. Detachment in variable divertor geometry on TCV. *Proc. 18th IAEA Fusion Energy Conference (Sorrento, Italy)*, IAEA-CN-77-EXP/P4-23, 2000.

[25] G. Haas et al. Measurements on the particle balance in diverted ASDEX discharges. *Journal of Nuclear Materials*, **121**:151, 1984.

[26] C. C. Klepper et al. Neutral presure studies with a fast ionization gauge in the divertor region of the DIII-D tokamak. *J. Vac. Sci. Technol. A*, **11**(2):447, 1993.

[27] R. A. Pitts et al. The design of central column tiles for the TCV tokamak. *Nucl. Fusion*, **39**:1433, 1999.

[28] P. C. Stangeby. *The plasma boundary of magnetic fusion devices.* Institute of physics publishing, Bristol and Philadelphia, 2000.

[29] G. D. Porter et al. Analysis of separatrix plasma parameters using local and multi-machine databases. *Journal of Nuclear Materials*, **266-269**:917, 1999.

[30] D. Tskhakaya and others. *Kinetic simulations of the tokamak scrape-off layer.* Editrice Compositori, Societá italiana di Fisica, Bologna. Varenna (2004), Int. Workshop in Theory of Fusion Plasmas (2004), submitted, to be published,.

[31] F. Subba et al. Kinetic and fluid study of classical transport phenomena in scrape-off layer plasmas. *Contributions to Plasma Physics*, **42**(2-4):372, 2002.

[32] O. V. Batishchev et al. Kinetic effects in tokamak scrape-off layer plasmas. *Phys. Plasmas*, **4**(5):1672, 1997.

[33] S. K. Erents et al. Simple relations between scrape-off layer parameters of high recycling divertors Part I: The relation between 'upstream' density and temperatures. *Nucl. Fusion*, **40**:295, 2000.

[34] S. I. Braginskii. Transport processes in plasma. In M.A. Leontovich, editor, *Reviews of plasma physics*. Consultants Bureau New York, 1965.

[35] E. Zawaideh et al. Generalized fluid equations for parallel transport in collisional to weakly collisional plasmas. *Phys. Fluids*, **29**(2):463, 1986.

[36] L. Spitzer and R. Härm. Transport phenomena in a completely ionized gas. *Physical Review*, **89**(5):977, 1953.

[37] W. Fundamenski. Kinetic and gyro-kinetic parallel heat flux limits. *Plasma Phys. Control. Fusion*, , 2004. to be submitted.

[38] R. Chodura. Plasma flow in the sheath and the presheath of a scrape-off layer. In D. E. Post, editor, *Physics of plasma-wall interactions in controlled fusion*, page 99. Plenum Press New York, 1984.

[39] P. C. Stangeby and A. V. Chankin. The ion velocity (bohm-chodura) boundary condition at the entrance to the magnetic presheath in the presence of diamagnetic and $\vec{E} \times \vec{B}$ drifts in the scrape-off layer. *Phys. Plasmas*, **2**(3):707, 1995.

[40] D. Tskhakaya and S. Kuhn. Effect of $\vec{E} \times \vec{B}$ drift on the plasma flow at the magnetic presheath entrance. *Contributions to Plasma Physics*, **42**(2-4):302, 2002.

[41] R. H. Cohen and D. D. Ryutov. Sheath physics and boundary conditions for edge plasmas. *Contributions to Plasma Physics*, **44**(1-3):111, 2004.

[42] B. LaBombard et al. Cross-field plasma transport and main-chamber recycling in diverted plasmas on Alcator C-Mod. *Nucl. Fusion*, **40**(12):2041, 2000.

[43] D. Bohm. In A. Guthrie R. K. Wakerling, editor, *The characteristics of electrical discharges in magnetic fields*. McGraw-Hill New York, 1949.

[44] R. J. Goldston and P. H. Rutherford. *Introduction to plasma physics*. Bristol: Institute of Physics Publishing, 1997.

[45] P. C. Stangeby. Modelling plasma contact with the main vessel walls of a divertor tokamak. *Phys. Plasmas*, **9**(8):3489, 2002.

[46] G. D. Porter et al. Simulation of experimentally achieved DIII-D detached plasmas using the uedge code. *Phys. Plasmas*, **3**(5):1967, 1996.

[47] G. D. Porter et al. Detailed comparison of simulated and measured plasma profiles in the scrape-off layer and edge plasma of DIII-D. *Phys. Plasmas*, **7**(9):3663, 2000.

[48] A. Loarte. Understanding the edge physics of divertor experiments by comparison of 2D edge code calculations and experimental measurments. *Journal of Nuclear Materials*, **241-243**:118, 1997.

[49] R. Simonini et al. *Journal of Nuclear Materials*, **196-198**:369, 1992.

[50] R. Schneider et al. B2-EIRENE simulation of ASDEX and ASDEX-Upgrade scrape-off layer plasmas. *Journal of Nuclear Materials*, **196-198**:810, 1992.

[51] A. Loarte. Comparison of B2-EIRENE calculations with multi-machine experimental measurments. *Journal of Nuclear Materials*, **266-269**:1123, 1999.

[52] B. LaBombard et al. Particle transport in the scrape-off layer and its relations to discharge density limit in Alcator C-Mod. *Phys. Plasmas*, **8**(5):2107, 2001.

[53] M. V. Umansky et al. Comments on particle and energy balance in the edge palsma. *Phys. Plasmas*, **5**(9):3373, 1998.

[54] M. V. Umansky et al. Modelling of particle and energy transport in the edge plasma of Alcator C-Mod. *Phys. Plasmas*, **6**(7):2791, 1999.

[55] M. Endler. Turbulent SOL transport in stellarators and tokamaks. *Journal of Nuclear Materials*, **266-269**:84, 1999.

[56] D. A. D'Ippolito et al. Cross-field blob transport in tokamak scrape-off-layer plasmas. *Phys. Plasmas*, **9**(1):222, 2002.

[57] S. I. Krasheninnikov and A. I. Smolyakov. On neutral wind and blob motion in linear devices. *Phys. Plasmas*, **10**:3020, 2003.

[58] A. V. Nedospasov et al. Plasma convection in the poloidal limiter shadow of a tokamak. *Nucl. Fusion*, **25**:21, 1985.

[59] A. Y. Pigarov et al. Tokamak edge plasma simulation including anomalous cross-field convective transport. *Phys. Plasmas*, **9**(4):1287, 2002.

[60] A. Y. Pigarov et al. DIII-D edge plasma simulations with UEDGE code including non-diffusive anomalous cross-field transport. *Journal of Nuclear Materials*, **313-316**(1-3):1076, 2003.

[61] A. Y. Pigarov et al. Multi-fluid code simulations including anomalous non-diffusive transport of plasma and impurities in the tokamak sol. *Contributions to Plasma Physics*, **44**(1-3):228, 2004.

[62] P. C. Stangeby. Scrape-off layers in which ionisation is important. *Journal of Nuclear Materials*, **121**:55, 1984.

[63] W. Fundamenski and S. Sipilä. Boundary plasma energy transport in JET ELMy H-modes. *Nucl. Fusion*, **44**(1):20, 2004.

[64] I. H. Hutchinson. A fluid theory of ion collection by probes in strong magnetic fields with plasma flow. *Phys. Fluids*, **30**(12):3777, 1987.

[65] *EIRENE manual*, 2004. URL: http://www.eirene.de.

[66] W. Eckstein and D. B. Heifetz. Data sets for hydrogen reflection and their use in neutral transport calculations. *Journal of Nuclear Materials*, **145-147**:332, 1987.

[67] D. Reiter et al. Database for recycling and penetration of neutral helium atoms in the boundary of a fusion plasma. Report, Jül-2605, 1992.

[68] J. Roth. Chemical erosion of carbon based materials in fusion devices. *Journal of Nuclear Materials*, **266-269**:51, 1999.

[69] J. Roth et al. Flux dependence of chemical erosion and its implication for ITER. *Journal of Nuclear Materials*, . presented at PSI-16 Portland (ME), 2004, accepted for publication.

[70] R. A. Pitts. Private communications.

[71] B. V. Mech et al. Isotopic effects in hydrocarbon formation due to low-energy H^+/D^+ impact on graphite. *Journal of Nuclear Materials*, **241-243**:1147, 1997.

[72] J. Roth et al. Flux dependence of carbon chemical erosion by deuterium ions. *Nucl. Fusion*, **44**, 2004.

[73] D. R. Bates et al. Recombination between electrons and ions II. *Proc. Roy. Soc. A*, **270**:155, 1962.

[74] D. R. Bates et al. Recombination between electrons and ions I. *Proc. Roy. Soc. A*, **267**:297, 1962.

[75] T. Fujimoto et al. Ratio of Balmer line intensities resulting from dissociative excitation of molecular hydrogen in an ionizing plasma. *J. Appl. Phys.*, **66**:2315, 1989.

[76] T. Fujimoto et al. Effective ionization and dissociation rate coefficients of molecular hydrogen in plasmas. *J. Appl. Phys.*, **78**:2913, 1995.

[77] A. Y. Pigarov. Collisional radiative kinetics of molecular assisted recombination in edge plasmas. *Phys. Scripta*, **T96**:16, 2002.

[78] R. K. Janev et al. Survey of atomic processes in edge plasmas. *Journal of Nuclear Materials*, **121**:10, 1984.

[79] R. K. Janev and others. Catalytic mechanism of divertor plasma recombination provided by hydrocarbon impurities. *Phys. Plasmas*, **7**(11):4364, 2000.

[80] Janev R. K, D. Reiter, and U. Samm. Collision processes in low temperature hydrogen plasmas. Report, Jl-4105 2003, 2003.

[81] R. K Janev and W. D. Langer. *Elementary processes in hydrogen helium plasmas.* Springer Verlag, Heidelberg, 1987.

[82] Keilhacker et al. *Plasma Physics and Controlled Nuclear Fusion Research*, **III**:183, 1982. Vienna:IAEA.

[83] S. I. Krasheninnikov. Divertor plasma detachment: present status of understanding. *Contributions to Plasma Physics*, **36**:293, 1996.

[84] Y. Shimomura et al. *Nucl. Fusion*, **23**:869, 1983.

[85] P. C. Stangeby. Can detached divertor plasmas be explained as self-sustained gas targets. *Nucl. Fusion*, **33**(11):1695, 1993.

[86] S. I. Krasheninnikov and others. Plasma recombination and molecular effects in tokamak divertors and divertor simulators. *Phys. Plasmas*, **4**(5):1638, 1997.

[87] B. Lipschultz et al. The role of particle sinks and sources in Alcator C-Mod detached divertor discharges. *Phys. Plasmas*, **6**(5):1907, 1999.

[88] U. Fantz et al. Hydrogen molecules in the divertor of ASDEX Upgrade. *Journal of Nuclear Materials*, **290-293**:367, 2001.

[89] N. Ohno et al. Experimental evidence of molecular activated recombination in detached recombining plasmas. *Phys. Rev. Lett.*, **81**(4):818, 1998.

[90] S. I. Krasheninnikov et al. Molecular effects in plasma recombination. *ECA*, **24B**:21, 2000. 27th EPS Conference on Controlled Fusion an Plasma Physics, Budapest, 2000, Europhysics Conference Abstract.

[91] G. M. McCracken et al. Evidence for volume recombination in JET detached plasmas. *Nucl. Fusion*, **38**(4):619, 1998.

[92] J. L. Terry et al. The experimental determination of the volume recombination rate in tokamak divertors. *Journal of Nuclear Materials*, **266-269**:30, 1999.

[93] U. Wenzel et al. Volume recombination in the ASDEX Upgrade divertor. *ECA*, **22C**:504, 1998. 25th EPS Conference on Controlled Fusion an Plasma Physics, Praha, 1998, Europhysics Conference Abstract.

[94] D. Lumma and others. Radiative and three-body recombination in the Alcator C-Mod divertor. *Phys. Plasmas*, **4**(7):2555, 1997.

[95] R. C. Isler and others. Signatures of deuterium recombination in the DIII-D divertor. *Phys. Plasmas*, **4**(8):2989, 1997.

[96] A. Niemczewski. *Neutral particle dynamics in the Alcator C-Mod tokamak*. PhD thesis, Massachusetts Institute of Technology, Cambrdige (MA), 1995.

[97] A. S. Kukushkin et al. Scaling laws for edge plasma parameters in ITER from two-dimensional edge modelling. *Nucl. Fusion*, **43**:716, 2003.

[98] A. W. Leonard et al. Distributed divertor radiation through convection in DIII-D. *Phys. Rev. Lett.*, **78**(25):4769, 1997.

[99] M. E. Fenstermacher et al. The two-dimensional structure of radiative divertor plasmas in the DIII-D tokamak. *Phys. Plasmas*, **4**(5):1761, 1997.

[100] J. A. Boedo et al. Electric field-induced plasma convection in tokamak divertors. *Phys. Plasmas*, **7**:1075, 2000.

[101] S. K. Erents et al. Parallel flow in the JET scrape-off layer. *Plasma Phys. Control. Fusion*, **42**:905, 2000.

[102] N. Asakura et al. Driving mechanism of sol plasma flow and effects on divertor performance in JT-60U. *Nucl. Fusion*, **44**:503, 2004.

[103] R. A. Pitts et al. Edge and divertor physics with reversed toroidal field in JET. *Journal of Nuclear Materials*, . Presented at the PSI-16, Portland (ME), 2004, accepted for publication.

[104] J. Horacek et al. Overview of edge electrostic turbulence experiments on TCV. *Czechoslovak Journal of Physics*, , 2004. to be submitted.

[105] S. K. Erents et al. A comparison of experimental measurements and code results to determine flows in the JET SOL. *Plasma Phys. Control. Fusion*, **46**:1757, 2004.

[106] D. P. Coster and others. Integrated modelling of material migration and target plate power handling at JET. *Proc. 20th IAEA Fusion Energy Conference (Vilamura, Portugal)*, IAEA-CN-116-TH/P5-18, 2004.

[107] M. Baelmans. *Code improvements and applications of a two-dimensional edge plasma model for toroidal devices*. PhD thesis, Ecole Royale Militaire, Belgium, 1994. KMS-Rep. No 100.

[108] P. C. Stangeby and A. V. Chankin. Simple models for the radial and poloidal $\vec{E} \times \vec{B}$ drifts in the scrape-off layer of a divertor tokamak: effects on in/out asymmetries. *Nucl. Fusion*, **36**(7):830, 1996.

[109] A. V. Chankin. Classical drifts in the tokamak SOL and divertor: models and experiment. *Journal of Nuclear Materials*, **241-243**:199, 1997.

[110] J. Hugill et al. Density limits in helium plasmas at JET. *Journal of Nuclear Materials*, **196-198**:918, 1992.

[111] W. Fundamenski et al. Effect of $B \times \vec{\nabla} B$ direction in SOL energy transport in JET. *Journal of Nuclear Materials*, . presented at PSI-16, accepted for publication.

[112] G. S. Kirnev et al. EDGE2D code simulations of SOL flows and in-out divertor asymmetries in JET. *Journal of Nuclear Materials*, . presented at PSI-16 Portland (ME), 2004, submitted to JNM.

[113] D. Reiter. Progress in two-dimensional plasma edge modelling. *Journal of Nuclear Materials*, **196-198**:80, 1992.

[114] D. Reiter et al. Radiation transfer in dense edge plasmas and divertors: experimental and recent computational results. *Journal of Nuclear Materials*, **313-316**:845, 2003.

[115] T. D. Rognlien et al. *Contributions to Plasma Physics*, **34**:362, 1994.

[116] G. J. Radford et al. *Contributions to Plasma Physics*, **36**:187, 1996.

[117] B. J. Braams. A multi fluid code for simulation of the edge plasma in tokamaks. EUR-FU/XII-80/87/68, 1987.

[118] D. P. Coster. Simulation of the edge plasmas in tokamaks. *Phys. Scripta*, **T100**:7, 2004.

[119] D. P. Stotler et al. Coupling of parallelized DEGAS 2 and UEDGE codes. *Contributions to Plasma Physics*, **40**(3-4):221, 2000.

[120] M. E. Rensink et al. *Contributions to Plasma Physics*, **38**:325, 1998.

[121] R. Simonini et al. *Contributions to Plasma Physics*, **34**:368, 1994.

[122] D. Reiter et al. *Plasma Phys. Control. Fusion*, **33**:1579, 1991.

[123] D. P. Stotler and C. F. F. Karney. *Contributions to Plasma Physics*, **34**:392, 1994.

[124] E. Cupini et al. NIMBUS-Monte Carlo simulation of neutral particle transport in fusion devices. EUR-FU/XII-324/9, 1984.

[125] R. Simononi et al. Monte Carlo modelling of edge re-cycle fueling on JET. *Plasma Phys. Control. Fusion*, **33**(6):653, 1991.

[126] D. Reiter. *Randschicht-Konfiguration von Tokamaks: Entwicklung und Anwendung stochastischer Modelle zur Beschreibung des Neutralgastransports*. PhD thesis, Heinrich Heine Universität Düsseldorf, Germany, 1984. KFA-Report, Jül-1947.

[127] W. Fundamenski. *Tokamak edge plasma modelling using an improved onion skin method.* PhD thesis, University of Toronto, Canada, 1999.

[128] D. P. Coster and others. Further developments of the edge transport simulation package, SOLPS. *Proc. 19th IAEA Fusion Energy Conference (Lyon, France),* IAEA-CN-94-TH/P2-13, 2002.

[129] R. Marchand et al. *Comp. Phys. Commun.,* **96**:232, 1996.

[130] R. Schneider et al. B2-SOLPS5.0: SOL transport code with drifts and currents. *Contributions to Plasma Physics,* **40**(3-4):328, 2000.

[131] V. A. Rozhansky et al. Simulation of tokamak edge plasma including self-consistent electric fields. *Nucl. Fusion,* **41**(4):387, 2001.

[132] X. Bonnin et al. Improved modelling of detachment and neutral-dominated regimes using the SOLPS B2-EIRENE code. *Journal of Nuclear Materials,* **313-316**:909, 2003.

[133] *SOLPS, homepage by D. Coster.* URL: http://www.rzg.mpg.de/dpc/solps.html.

[134] L. L. Lao et al. Reconstruction of current profile parameters and plasma shapes in tokamaks. *Nucl. Fusion,* **25**(11):1611, 1985.

[135] F. Hoffmann and G. Tonetti. Tokamak equilibrium reconstruction using Faraday rotation measurments. *Nucl. Fusion,* **39**(10):1871, 1988.

[136] X. Bonnin et al. The two-mesh grid refinement method for the B2 code. *Contributions to Plasma Physics,* **42**(2-4):175, 2002.

[137] R. Schneider. Scrape-off layer physics: an introduction. Report, IPP Garching 12-1 2004.

[138] P. L. Bhatnagar, E. P. Gross, and M. Krook. A model for collision processes in gases. I. Small amplitude processes in charged and neutral one-component systems. *Physical Review,* **94**(3):511, 1954.

[139] C. May. *Neutralgasströmungen in Fusionsexperimenten bei endlichen Knudsenzahlen.* PhD thesis, Heinrich Heine Universität, Germany, 1997. **Jül-3486**.

[140] A. S. Kukushkin. Private communications.

[141] E. D. Cashwell and C. J. Everett. *A practical manual on the Monte Carlo method for random walk problems.* Pergamon Press, New York, 1959.

[142] J. Spanier and E. M. Gelbard. *Monte Carlo principles and neutron transport problems.* Addison-Wesley, 1969.

[143] A. B. Erhardt and W. D. Langer. Collisional processes of hydrocarbons in hydrogen plasmas. Report, PPPL-2477, Princeton, 1987.

[144] C. F. F. Karney and D. P. Stotler. Modelling of neutral plasma in a divertor in the fluid-kinetic transition. *Contributions to Plasma Physics*, **38**:319, 1998.

[145] *OPENMOSIX clustering software.* URL: http://www.openmosix.sourceforge.net.

[146] D. P. Coster. Time dependent SOL modelling with SOLPS. In R. Koch and S. Lebedev, editors, *Europhysics Conference Abstracts (CD-ROM, Proc. of the 30th EPS Conference on Controlled Fusion and Plasma Physics, St. Petersburg, 2003)*, volume 27A, pages P–1.169, Geneva, 2003. EPS.

[147] F. Hoffmann et al. Creation and control of variably shaped plasmas in TCV. *Plasma Phys. Control. Fusion*, **36**:B277, 1994.

[148] A. Loarte et al. Influence of plasma composition on divertor detachment. *Contributions to Plasma Physics*, **40**(3-4):508, 2000.

[149] R. A. Pitts et al. Experimental investigation of the effects of neon injection in TCV. *Journal of Nuclear Materials*, **266-269**:648, 1999.

[150] M. Wischmeier et al. The influence of molecular dynamics on divertor detachment in TCV. *Contributions to Plasma Physics*, **44**(1-3):268, 2004.

[151] J. Horacek et al. Predicted effects of parallel temperature gradients on the over-estimation of TCV divertor target Langmuir probe T_e measurements. *Journal of Nuclear Materials*, **313-316**:931, 2001.

[152] R. D. Monk et al. Interpretation of ion flux and electron temperature profiles at the JET divertor target during high recycling and detached discharges. *Journal of Nuclear Materials*, **241-243**:396, 1997.

[153] G. F. Matthews. Tokamak plasma diagnostic by electrical probes. *Plasma Phys. Control. Fusion*, **36**:1595, 1994.

[154] J. A. Boedo et al. Fast scanning probe for tokamak plasmas. *Review of Scientific Instruments*, **69**(7):2663, 1998.

[155] P. C. Stangeby. Measuring plasma drift velocities in tokamak edge plasmas using probes. *Phys. Fluids*, **27**(11):2699, 1984.

[156] I. H. Hutchinson. Ion collection by probes in strong magnetic fields with plasma flow. *Phys. Rev. A*, **37**(11):4358, 1988.

[157] R. Behn et al. A Thomson scattering diagnostic foe measurements in the divertor region of tcv. *Review of Scientific Instruments*, **70**(10):768, 1999.

[158] G. Haas and H-S. Bosch. In vessel pressure measurements in nuclear fusion experiments with ASDEX type gauges. *Vacuum*, **51**(1):39, 1998.

[159] G. Haas et al. Neutral gas diagnostic for ITER. In P. E. Stott, editor, *Diagnostics for experimental thermonuclear fusion reactors* 1, page 571. Plenum Press, New York, 1996.

[160] G. Haas et al. Pressure gauges and neutral pressure measurements in ITER. In P. E. Stott, editor, *Diagnostics for experimental thermonuclear fusion reactors* 2, page 559. Plenum Press, New York, 1998.

[161] A. W. Degeling et al. AXUV bolometer and Lyman-α camera systems on the TCV tokamak. *Review of Scientific Instruments*, **75**(10):4139, 2004.

[162] R. A. Pitts et al. Divertor detachment in TCV ohmic plasmas. *ECA*, **23J**:1085, 1999. 26th EPS Conference on Controlled Fusion an Plasma Physics, Maastricht, 1999, Europhysics Conference Abstract.

[163] R. A. Pitts et al. Divertor target profiles and recycling studies in TCV single null lower standard discharges. *Journal of Nuclear Materials*, **241-243**:867, 1997.

[164] I. Condrea et al. Helium discharge operation in TCV. *29th EPS Conference on Controlled Fusion an Plasma Physics, Montreux, 2002, Europhysics Conference Abstract*, **26B**:P2.079, 2002.

[165] M. Greenwald. *Nucl. Fusion*, **28**:2199, 1988.

[166] M. Greenwald. Density limits in toroidal plasmas. *Plasma Phys. Control. Fusion*, **44**:R27, 2002.

[167] R. Pitts et al. Comparing scrape-off layer and divertor physics in JET pure He and D discharges. *Journal of Nuclear Materials*, **313-316**:777, 2003.

[168] J. Rapp et al. Density limits in helium plasmas at JET. *Journal of Nuclear Materials*, **313-316**:524, 2003.

[169] H. Weisen et al. Effect of plasma shape on confinement and MHD behaviour in the TCV tokamak. *Nucl. Fusion*, **37**(12):1741, 1997.

[170] K. Sawada and T. Fujimoto. Effective ionization and dissociation rate coefficients of moleuclar hydrogen in plasma. *J. Appl. Phys.*, **78**(5):2913, 2002.

[171] D. Reiter. Private communications.

[172] R. A. Pitts. Private communications.

[173] K. H. Hellwege. *Einführung in die Physik der Molekeln.* Springer-Verlag, Berlin Heidelberg New York, 1974.

[174] P. J. Eenshuistra et al. Observation of exceptionally high vibrational excitation of hydrogen molecules formed by wall recombination. *Phys. Rev. Lett.*, **60**(4):341, 1988.

[175] B. Heger and U. Fantz. Modification of the ground state vibrational population of molecular hydrogen and deuterium by different wall materials in low temperature plasmas. *28th EPS Conference on Controlled Fusion an Plasma Physics, Funchal, 2001, Europhysics Conference Abstract*, **25A**:261, 2001.

[176] B. Heger et al. Vibrational population of the ground state of H_2 and D_2 in the divertor of ASDEX Upgrade. *Journal of Nuclear Materials*, **290-293**:413, 2001.

[177] U. Fantz. Emission spectroscopy of hydrogen molecules in technical and divertor plasmas. *Contributions to Plasma Physics*, **42**:675, 2002.

[178] U. Fantz et al. Using the radiation of hydrogen molecules for electron temperature diagnostics of divertor plasmas. *Plasma Phys. Control. Fusion*, **43**:907, 2001.

[179] U. Fantz et al. Photon efficiency $(S+D)/XB$ of hydrogen molecules at low electron temperatures. *Journal of Nuclear Materials*, **313-316**:743, 2003.

[180] S. Brezinsek et al. Identification of molecular carbon sources in the JET divertor by means of emission spectroscopy. *Journal of Nuclear Materials*, . presented at the PSI-16, Portland (ME), 2004, accepted for publication.

[181] S. Brezinsek et al. Chemical erosion measurements in tokamaks by spectroscopy. *Phys. Scripta*, **111**:42, 2004.

[182] S. Kado et al. Experimental investigations on hydrocarbon-enhanced MAR processes in low temperature plasma divertor simulator MAP-II. *Journal of Nuclear Materials*, **313-316**:754, 2003.

[183] K. Matyash et al. Modeling of hydrocarbon species in ECR methane plasmas. *Journal of Nuclear Materials*, **313-316**:434, 2003.

[184] R. K. Janev and D. Reiter. Unified analytic representation of hydrocarbon impurity collision cross sections. *Journal of Nuclear Materials*, **313-316**:1202, 2003.

[185] R. Janev and D. Reiter. Collision processes of hydrocarbon species in hydrogen plasmas: I. The Methane Family. Report, IPP Jülich 3966, ISSN 0944-2952, 2002.

[186] R. Janev and D. Reiter. Collision processes of hydrocarbon species in hydrogen plasmas: II. The Ethane & Propane Families. Report, IPP Jülich 4005, ISSN 0944-2952, 2002.

[187] V. Philipps et al. Impurity release and deposition processes close to limiter surfaces in TEXTOR-94. *Journal of Nuclear Materials*, **241-243**:105, 1997.

[188] B. V. Mech et al. Chemical erosion of pyrolitic graphite by low-energy H^+ and D^+ impact. *Journal of Nuclear Materials*, **241-243**:1147, 1997.

[189] J. W. Davis et al. Hydrocarbon formation due to combined H^+ ion and atom impact on pyrolytic graphite. *Journal of Nuclear Materials*, **155-157**:234, 1988.

[190] A.A. Haasz et al. Methane yield of pyrolitic graphite due to low-energy D^+ impact. *Journal of Nuclear Materials*, **231**:170, 1996.

[191] J. Roth and C García-Rosales. Analytic description of the chemical erosion of graphite by hydrogen ions. *Nucl. Fusion*, **36**(12):1647, 1996.

[192] T. Fujimoto. A collisional-radiative model for helium and its application to a discharge plasma. *J. Quant. Spectrosc. Radiat. Transfer*, **21**:439, 1979.

[193] M. Wischmeier et al. Divertor detachment during pure helium plasmas in JET. *Journal of Nuclear Materials*, **313-316**:980, 2003.

[194] A. Huber et al. Tomographic reconstruction of 2-D line radiation distribution in the JET MKIIGB divertor in pure *he* and *d* discharges. *30th EPS Conference on Controlled Fusion an Plasma Physics, St. Petersburg, 2003, Europhysics Conference Abstract*, **27A**:P3.199, 2003.

[195] N. Tsois et al. A fast scanning langmuir probe system for ASDEX-Upgrade divertor. *Journal of Nuclear Materials*, **266-269**:1230, 1999.

[196] A. Hatayama et al. High mach flow associated with X-point MARFE and plasma detachment. *Nucl. Fusion*, **40**(12):2009, 2000.

[197] R. Behrisch et al. Material erosion at the vessel walls of future fusion devices. *Journal of Nuclear Materials*, **313-316**:388, 2003.

[198] A. Kallenbach et al. EDGE2D modelling of edge profiles obtained in JET diagnostic optimized configuration. *Plasma Phys. Control. Fusion*, **46**:431, 2004.

[199] G. McCracken et al. Volume recombination and detachment in JET divertor plasmas. *Journal of Nuclear Materials*, **266-269**:37, 1999.

[200] A. Huber et al. Tomographic reconstruction of 2D line radiation distribution in the JET MkIIGB divertor. *Journal of Nuclear Materials*, **313-316**(1-3):925, 2003.

[201] *ADAS, Atomic Data and Analysis Atructure*. URL: http://adas.phys.strath.ac.uk/.

Acknowledgements

Before thanking any particular person I owe my gratitude to all the people of CRPP as a whole. CRPP as such has provided me with an, I'd consider, ideal environment for undertaking my thesis work, being challenging and stimulating from a scientific point of view, while remaining humane and pleasant in doing so.

I will always remember the first time I met my thesis adviser Richard Pitts in his office and the way he talked to me about the possible subject of my thesis which resulted in this document. I shall not forget the confidence he had in me and the trust he has put into me since the very beginning. His passion for the subject, his broad knowledge, ever growing efficiency and, not to underestimate, network of people to which he is scientifically connected have made the finalization of my thesis only possible. His enthusiasm for science and ability to motivate have helped me pass through some particularly difficult moments throughout my thesis work, keeping me moving forward. I very much enjoyed our long and sometimes drifting discussions all along my thesis, even in times during which he was buried under more work than he had been on average anyways, finding in those discussions a strong drive to pursue my work. And I believe that I nearly always walked out of his office with a new question to answer as a result of our discussions. I am particularly indebted to him for the long hours he spent carefully reading this manuscript. Above all I wish to preserve for my professional future the scientific ethics and honesty in doing research, which he has over and over tried to convey.

The carrying out and completion of my thesis, being dominated by work involving modelling for which there was little or no knowledge at CRPP before my arrival, would have been absolutely impossible without the strong and inexhaustible support by David Coster (IPP Garching), Xavier Bonnin (now CNRS-LIMHP, Paris) and last but not least Detlev Reiter (IPP Jülich). In this context my thanks go also to A. S. Kukushkin and Alberto Loarte (CSU Garching) who always found time to explain to me in detail many aspects of

At last I thank my family and friends, not only those in Lausanne but also those spread around for their support in all these years despite the distance. I dedicate this thesis to my parents Hein-Dieter and Marisa, who have accompanied my education ever since with great support and who, I know, suffered with me when times got rough, never ceasing to believe in me. It is not only my dream that is now fulfilled. My thank also goes to Kristina who has been so patient with me, in particular in the last months of writing the thesis and who made great efforts in supporting me in that particularly stressful period. Even during my last weeks she kept saying "you will finish"...

Curriculum Vitae

Personal data:

Name: Marco Wischmeier

Date of birth: August, 15th, 1973

Place of birth: Porz am Rhein (Köln), Germany

Nationality: German and Italian

Professional and educational background:

1979 - 1983   Elementary School, Deutsche Schule, New Delhi, India

June 1992   Abitur in Korschenbroich, Germany.

1992 - 1993   Compulsory military service, Luftwaffe, Germany.

1993 - 1994   Astronomy at the Universitá degli Studi di Padova, Italy.

1994 - May 2000 Diplom in Physik at the Heinrich-Heine Universität Düsseldorf, Germany.

1996 - 2000   Teaching Assistant in Experimental Physics at the Physics Department of the Heinrich-Heine Universität Düsseldorf, Germany.

Since July 2000 Assistant and Doctoral Student at the Centre de Recherches en Physique des Plasmas (CRPP), Ecole Polytechnique Fédérale de Lausanne (EPFL), Lausanne, Switzerland.

List of publications:

1. **M. Wischmeier** et al., *The influence of molecular dynamics on divertor detachment in TCV*, Contributions to Plasma Physics, **44**, 268 (2004)

2. A. W. Degeling et al. (incl. M. Wischmeier), *AXUV bolometer and Lyman-α camera systems on the TCV tokamak*, Review of Scientific Instruments, **75**, 4139 (2004)

3. D. Coster et al. (incl. M. Wischmeier), *Integrated modelling of material migration and target plate power handling at JET*, proceedings of the 20th IAEA Fusion Energy Conference, Vilamura, Portugal, 2004

4. D. Tskhakaya et al. (incl. M. Wischmeier) *Kinetic simulations of the tokamak scrape-off layer*, Varenna, Int. Workshop in Theory of Fusion Plasmas (2004), submitted, to be published by Editrice Compositori, Societá italiana di Fisica, Bologna

5. E. Tsitrone et al. (incl. M. Wischmeier) *Divertor modelling of septum assessment experiments in JET MkIIGB*, Contributions to Plasma Physics, **44**, 241 (2004)

6. **M. Wischmeier** et al., *Divertor detachment during He plasmas in JET*, J. Nucl. Mater., **313-316**, 980 (2003)

7. R. A. Pitts et al. (incl. M. Wischmeier), *Comparing scrape-off layer and divertor physics in JET pure He and D discharges*, J. Nucl. Mater., **313-316**, 777 (2003)

8. D. Coster et al. (incl. M. Wischmeier), *An overview of JET modelling activities*, J. Nucl. Mater., **313-316**, 868 (2003)

9. A. Huber et al. (incl. M. Wischmeier), *Tomographic reconstruction of 2-D line radiation distribution in the JET MKIIGB divertor in pure He and D discharges*, 30th EPS Conference on Controlled Fusion and Plasma Physics, St. Petersburg, 2003, Europhysics Conference Abstract **27A**, P3.199 (2003)

10. I. Condrea et al. (incl. M. Wischmeier), *Helium discharge operation in TCV*, 29th EPS Conference on Controlled Fusion and Plasma Physics, Montreux, 2002, Europhysics Conference Abstract **26B**, P2.079 (2002)